

HZDR-071

MEASUREMENT OF THE PHOTODISSOCIATION OF THE DEUTERON AT ENERGIES RELEVANT TO BIG BANG NUCLEOSYNTHESIS

Roland Hannaske

Wissenschaftlich-Technische Berichte
HZDR-071 · ISSN 2191-8708

WISSENSCHAFTLICH-
TECHNISCHE BERICHTE

HZDR

 HELMHOLTZ
ZENTRUM DRESDEN
ROSSENDORF

Druckausgabe: ISSN 2191-8708

Elektronische Ausgabe: ISSN 2191-8716

Die elektronische Ausgabe erscheint unter Creative Commons License (CC BY 4.0):

<https://www.hzdr.de/publications/Publ-23501>

<urn:nbn:de:bsz:d120-qucosa-201284>

Die vorliegende Arbeit wurde sowohl als Dissertation an der Fakultät Mathematik und Naturwissenschaften der Technischen Universität Dresden sowie als Wissenschaftlich-Technischer Bericht des Helmholtz-Zentrum Dresden – Rossendorf mit der Berichtsnummer **HZDR-071** veröffentlicht.

2016

Herausgegeben vom

Helmholtz-Zentrum Dresden - Rossendorf

Bautzner Landstraße 400

01328 Dresden

Germany

**Measurement of the photodissociation
of the deuteron at energies relevant
to Big Bang nucleosynthesis**

DISSERTATION

zur Erlangung des akademischen Grades

Doctor rerum naturalium
(Dr. rer. nat.)

vorgelegt

der Fakultät Mathematik und Naturwissenschaften
der Technischen Universität Dresden

von

Dipl.-Phys. Roland Hannaske

geboren am 23.01.1984 in Eisenhüttenstadt

eingereicht am 06.10.2014

verteidigt am 26.05.2015

Die Dissertation wurde in der Zeit von 10/2008 bis 09/2014 am Institut für Strahlenphysik am Helmholtz-Zentrum Dresden-Rossendorf angefertigt.

Für Ariane und Lotta

*Maybe I didn't treat you
Quite as good as I should have
Maybe I didn't love you
Quite as often as I could have
Little things I should have said and done
I just never took the time
You were always on my mind
You were always on my mind*

*Maybe I didn't hold you
All those lonely, lonely times
And I guess I never told you
I'm so happy that you're mine
If I make you feel second best
Girl, I'm so sorry I was blind
You were always on my mind
You were always on my mind*

[W. Carson, J. Christopher, M. James - 1972]

Die Promotionskommission bestand aus:

Prof. Dr. Thomas Cowan, Technische Universität Dresden
(1. Gutachter der Dissertation)

Prof. Dr. René Reifarth, Goethe-Universität Frankfurt am Main
(2. Gutachter der Dissertation)

Prof. Dr. Burkhard Kämpfer, Technische Universität Dresden
(Prüfer im Fach Kosmologie)

Prof. Dr.-Ing. Antonio Hurtado, Technische Universität Dresden
(Prüfer im Fach Grundlagen der Kernenergietechnik)

Prof. Dr. Dominik Stöckinger, Technische Universität Dresden
(Vorsitzender)

Zusammenfassung

Zwischen 10 und 1000 s nach dem Urknall bildeten sich während der Big Bang Nukleosynthese (BBN) die ersten leichten Elemente aus Protonen und Neutronen. Die primordialen Häufigkeiten dieser Elemente hingen von den Wirkungsquerschnitten der beteiligten Kernreaktionen ab. Vergleiche zwischen den Ergebnissen nuklearer Netzwerkrechnungen mit astronomischen Beobachtungen bieten eine einzigartige Möglichkeit, etwas über das Universum zu dieser Zeit zu erfahren.

Da es für die $p(n,\gamma)d$ -Reaktion, die eine Schlüsselreaktion der BBN ist, kaum Messungen im relevanten Energiebereich gibt, beruht deren Reaktionsrate in Netzwerkrechnungen auf theoretischen Berechnungen. Darin fließen auch experimentelle Daten der Nukleon-Nukleon-Streuung, des Einfangquerschnitts für thermische Neutronen sowie (nach Anwendung des Prinzips des detaillierten Gleichgewichts) der $d(\gamma,n)p$ -Reaktion mit ein. Diese Reaktion, die Photodissoziation des Deuterons, ist bei BBN-Energien ($T_{\text{cm}} = 20\text{--}200$ keV) ebenfalls kaum vermessen. Die großen experimentelle Unsicherheiten machen Vergleiche mit den präzisen theoretischen Berechnungen schwierig. In den letzten Jahren wurde die $d(\gamma,n)p$ -Reaktion und insbesondere der M1-Anteil des Wirkungsquerschnitts mit quasi-monoenergetischen γ -Strahlen aus Laser-Compton-Streuung oder durch Elektrodesintegration untersucht. Üblicherweise verwendete man für Messungen des $d(\gamma,n)p$ -Wirkungsquerschnitts entweder die auf wenige diskrete Energien beschränkte Strahlung des γ -Zerfalls oder Bremsstrahlung, für die aber eine genaue Photonenflussbestimmung sowie der Nachweis von einem der Reaktionsprodukte und dessen Energie nötig ist. Da diese Energie im Bereich der BBN relativ gering ist, gab es bisher noch keine absolute Messung des $d(\gamma,n)p$ -Wirkungsquerschnitts bei $T_{\text{cm}} < 5$ MeV mit Bremsstrahlung.

Das Ziel dieser Dissertation ist eine solche Messung mit einer Unsicherheit von 5 % im für die BBN relevanten Energiebereich und darüber hinaus bis $T_{\text{cm}} \approx 2.5$ MeV unter Verwendung gepulster Bremsstrahlung an der Strahlungsquelle ELBE. Dieser supraleitende Elektronenbeschleuniger befindet sich am Helmholtz-Zentrum Dresden-Rossendorf und stellt einen Elektronenstrahl hoher Intensität bereit. Die kinetische Elektronenenergie von 5 MeV wurde mit einem Browne-Buechner-Spektrometer präzise gemessen. Die Energieverteilung der in einer Niob-Folie erzeugten Bremsstrahlungsphotonen wurde berechnet. Die Photonenflussbestimmung nutzte die Kernresonanzstreuung an ^{27}Al , das sich mit deuteriertem Polyethylen in einem mehrschichtigen Target befand. Die ^{27}Al -Abregungen wurden mit abgeschirmten, hochreinen Germanium-Detektoren nachgewiesen, deren Effektivität mit GEANT4 simuliert und durch Quellmessungen normiert wurde. Die Messung der Energie der Neutronen aus der $d(\gamma,n)p$ -Reaktion erfolgte mittels deren Flugzeit in Plastikszintillatoren, die an zwei Seiten von Photoelektronenvervielfachern mit hoher Verstärkung ausgelesen wurden. Die Nachweiseffektivität dieser Detektoren wurde in einem eigenen Experiment in den Referenz-Neutronenfeldern der PTB Braunschweig kalibriert. Die Nachweisschwelle lag bei etwa 10 keV kinetischer Neutronenenergie. Wegen der guten Zeitauflösung der Neutronendetektoren und des ELBE-Beschleunigers genügte eine Flugstrecke von nur 1 m. Die Energieauflösung betrug im $d(\gamma,n)p$ -Experiment 1–2 %. Leider gingen viele Neutronen bereits durch Streuung in dem großen Target verloren oder sie wurden erst durch Teile des kompakten Experimentaufbaus in die Detektoren gestreut. Beide Effekte wurden mit Hilfe von FLUKA simuliert um einen Korrekturfaktor zu bestimmen, der aber bei niedrigen Energien relativ groß war.

Der $d(\gamma,n)p$ -Wirkungsquerschnitts wurde daher nur im Bereich 0.7 MeV $< T_{\text{cm}} < 2.5$ MeV bestimmt. Die Ergebnisse stimmen mit anderen Messungen, Daten-Evaluierungen sowie theoretischen Rechnungen überein. Die Gesamtunsicherheit beträgt circa 6.5 % und kommt zu fast gleichen Teilen von den statistischen und systematischen Unsicherheiten. Die statistische Unsicherheit könnte durch eine längere FLUKA Simulation noch von 3–5 % auf 1 % verringert werden. Die systematische Unsicherheit von 4.5 % ist vorrangig auf die Photonenflussbestimmung, die Neutronen-Nachweiseffektivität und die Target-Zusammensetzung zurückzuführen.

Abstract

Between 10 and 1000 s after the Big Bang the first light nuclei were produced from protons and neutrons during Big Bang nucleosynthesis (BBN). The primordial abundances of these nuclei depended on the cross sections of the involved nuclear reactions. Comparisons between results of nuclear network calculations and astronomic observations offer a unique probe of the universe at that time.

Experimental data for the $p(n,\gamma)d$ reaction, which is one of the BBN key reactions, are scarce at the relevant energies. Its reaction rate used in network calculations relies on theoretical models constrained by nucleon-nucleon scattering data, by the capture cross section for thermal neutrons, and (via the principle of detailed balance) by experimental data of the $d(\gamma,n)p$ reaction. The latter reaction, the photodissociation of the deuteron, is also only sparsely measured at BBN energies ($T_{\text{cm}} = 20\text{--}200$ keV). Large experimental uncertainties make a comparison of measurements with precise theoretical calculations difficult. In recent years, the $d(\gamma,n)p$ reaction and especially the M1 contribution to its cross section have been studied using quasi-monochromatic γ rays from Laser-Compton scattering or electrodisintegration. Traditionally, $d(\gamma,n)p$ cross sections were measured with γ -decay radiation, which is limited to a few discrete energies, or with bremsstrahlung, which requires an accurate photon flux normalization as well as the detection of one of the reaction products and its energy. Because this energy is relatively low in the BBN range, there has not yet been an absolute $d(\gamma,n)p$ cross section measurement at $T_{\text{cm}} < 5$ MeV that used bremsstrahlung.

The objective of this dissertation is such a measurement with a total uncertainty of about 5 % in the energy range relevant to BBN and up to $T_{\text{cm}} \approx 2.5$ MeV with pulsed bremsstrahlung at the radiation source ELBE. This superconducting electron accelerator is located at Helmholtz-Zentrum Dresden-Rossendorf and delivered a high-intensity electron beam with a kinetic energy of 5 MeV, which was measured precisely with a Browne-Buechner spectrometer. The energy distribution of the bremsstrahlung photons produced in a thin niobium foil has been calculated. The photon flux was determined by nuclear resonance fluorescence on ^{27}Al , which was combined with deuterated polyethylene in a multilayer target. The ^{27}Al transitions have been measured with shielded high-purity germanium detectors, of which the detection efficiency was simulated with GEANT4 and normalized to source measurements. The energy of the neutrons from the $d(\gamma,n)p$ reaction has been measured using the time-of-flight method with plastic scintillators read out on two sides by high-gain photomultipliers. The efficiency of these detectors has been calibrated in a separate experiment in the neutron reference fields of PTB Braunschweig. The detection threshold was at a kinetic neutron energy of about 10 keV. The excellent time resolution the neutron detectors and the ELBE beam allowed a short flight path of about 1 m. The neutron energy resolution in the $d(\gamma,n)p$ experiment was 1–2 %. Unfortunately, many neutrons were lost due to reactions in the large target or they scattered from parts of the compact experimental setup into the detectors. Both effects were studied with FLUKA simulations to determine a correction factor, which was rather large at low energies.

Therefore, the absolute $d(\gamma,n)p$ cross section has only been determined in the energy range of $0.7 \text{ MeV} < T_{\text{cm}} < 2.5 \text{ MeV}$. The results are consistent with other measurements, data evaluations, and theoretical calculations. The total uncertainty of about 6.5 % has nearly equal contributions from statistical and systematic uncertainties. The statistical uncertainty could be decreased from 3–5 % to about 1 % if longer FLUKA simulations were carried out. The systematic uncertainty of 4.5 % comes mainly from the photon flux normalization, the neutron detection efficiency, and the target composition.

Contents

Zusammenfassung / Abstract	iii
A historical and anecdotal preface	1
1 Introduction and motivation	3
1.1 Standard model of cosmology	3
1.2 Observed primordial abundances	4
1.3 Big Bang nucleosynthesis	5
1.4 Objective of this dissertation	8
2 Photodissociation of the deuteron and its inverse reaction	9
2.1 The deuteron	9
2.2 Kinematics of the $d(\gamma,n)p$ reaction	10
2.3 Reciprocity relation	12
2.4 Cross section calculations	13
2.5 Differential cross section	15
2.6 Previous measurements of the $p(n,\gamma)d$ cross section	16
2.7 Previous measurements of the $d(\gamma,n)p$ cross section	20
3 Photodissociation measurement at ELBE	25
3.1 Experimental setup	25
3.2 Production of bremsstrahlung	32
3.2.1 Measurement of the electron energy	33
3.2.2 Stability of the electron beam	34
3.2.3 Size and position of the photon beam	36
3.2.4 Calculation of the photon energy distribution	37
3.3 Target	39
3.4 Photon flux determination	42
3.4.1 Nuclear resonance fluorescence	42
3.4.2 Analysis of HPGe spectra	47
3.4.3 HPGe efficiency	52
3.4.4 Normalization and uncertainties	56
3.5 Neutron detection	58
3.5.1 Detection principle	58
3.5.2 Data acquisition and dead time	60
3.5.3 Background subtraction, energy resolution, and solid angle	64
4 Efficiency calibration of neutron detectors	65
4.1 Motivation and previous studies	65
4.2 Experimental setup	66
4.3 Reference neutron flux	69
4.4 Data analysis and background	70
4.5 Detection efficiency and uncertainties	72

5	Simulation of neutron interactions	77
5.1	Neutron interactions in the target	77
5.2	Neutron interactions in the whole setup	79
5.2.1	Primary particle source	79
5.2.2	Geometry	79
5.2.3	Detection and tracking	81
5.2.4	Correction factor for the $d(\gamma,n)p$ measurement	83
5.2.5	Outlook on improvements of the simulation	85
6	Results and discussion	87
6.1	Cross section of the $d(\gamma,n)p$ reaction	87
6.2	Systematic uncertainties	90
6.3	Conclusions and outlook	91
A	Constant values used in this work	93
B	Kinematics of the $d(\gamma,n)p$ reaction	94
C	Neutron sources	97
	List of Acronyms and Abbreviations	98
	List of Figures	99
	List of Tables	100
	Bibliography	101
	Danksagung / Acknowledgement	114
	Erklärung / Declaration	115

A historical and anecdotal preface

In the first half of the 20th century there were the first astronomical observations of distant galaxies and their redshifts by Slipher and Hubble, which allowed the interpretation that there is an expansion of the universe. About at the same time, Friedmann and Lemaître proposed a model for this expansion based on Einstein's theory of general relativity and the cosmological principle, which says that on large scales matter is distributed homogeneously and isotropically in the universe. If the expansion started in a singularity, then there should have also been a phase, in which the temperatures were even higher than inside of stars. Although the stellar generation of energy and helium by fusion processes (proton–proton chain, CNO cycle) was explained by Eddington, Bethe, and von Weizsäcker, the production of heavier elements in stellar environments was out of the question at that time. Therefore, it was tried to explain “The Origin of Chemical Elements” by imagining

“the early stage of matter as a highly compressed neutron gas [...] which started decaying into protons and electrons when the gas pressure fell down as the result of universal expansion. The radiative capture of still remaining neutrons by the newly formed protons must have led first to the formation of deuterium, and the subsequent neutron captures resulted in the building up of heavier and heavier nuclei” [Alpher1948a, with Bethe and Gamow].

This idea became popular as the $\alpha\beta\gamma$ theory named after their authors, whereas Bethe's name was only jocularly included by Alpher's advisor Gamow. As another consequence of the expanding universe, the present temperature of the primordial radiation was estimated to be 5 K by Gamow, Herman, and [Alpher1948b]. They are shown in figure 0.1, which was again a joke by Gamow. The first network of nuclear reactions was calculated by Fermi and Turkevich based on the $\alpha\beta\gamma$ theory [Alpher1950]. Later it was recognized that the initial gas must have already consisted of neutrons and protons [Hayashi1950, Alpher1953]. However, the $\alpha\beta\gamma$ idea of producing *all* elements by successive neutron capture reactions was questioned by the absence of elements with mass numbers five and eight. Salpeter and Hoyle suggested, that in stars these mass gaps could be skipped by the resonant formation of ^{12}C in a 3α process, which turned out to be true. With this and other nuclear reactions in stars, the production of nearly all elements in the universe by stellar nucleosynthesis was explained by [Burbidge1957, with Burbidge, Fowler, and Hoyle] as well as independently by [Cameron1959].



Figure 0.1: “A 1949 composite picture with Robert Herman on the left, Ralph Alpher on the right, and George Gamow in the center, as the genie coming out of the bottle of “Ylem,” the initial cosmic mixture of protons, neutrons, and electrons from which the elements supposedly were formed.”

Figure and caption taken from [Hetherington2014].

Gamow commented Hoyle's discovery humorously with a "New Genesis":

"In the beginning God created radiation and ylem. And ylem was without shape or number, and the nucleons were rushing madly over the face of the deep.

And God said: "Let there be mass two." And there was mass two. And God saw deuterium, and it was good.

And God said: "Let there be mass three." And there was mass three. And God saw tritium and tralphiium [Gamow's nickname for the helium isotope He-3], and they were good.

And God continued to call number after number until He came to transuranium elements. But when He looked back on his work He found that it was not good. In the excitement of counting, He missed calling for mass five and so, naturally, no heavier elements could have been formed.

God was very much disappointed, and wanted first to contract the universe again, and to start all over from the beginning. But it would be much too simple. Thus, being almighty, God decided to correct His mistake in a most impossible way.

And God said: "Let there be Hoyle." And there was Hoyle. And God looked at Hoyle... and told him to make heavy elements in any way he pleased.

And Hoyle decided to make heavy elements in stars, and to spread them around by supernovae explosions. But in doing so he had to obtain the same abundance curve which would have resulted from nucleosynthesis in ylem, if God would not have forgotten to call for mass five.

And so, with the help of God, Hoyle made heavy elements in this way, but it was so complicated that nowadays neither Hoyle, nor God, nor anybody else can figure out exactly how it was done." [Hetherington2014]

Hoyle supported the steady-state theory and rejected the singularity hypothesis, which today is known by the name he introduced for it in 1949:

"[The Big Bang] is an irrational process that cannot be described in scientific terms [... nor] challenged by an appeal to observation." [Hetherington2014]

The Big Bang theory was revived when large primordial helium abundances were observed that became a problem for stellar nucleosynthesis [Hoyle1964] and eventually became widely accepted after the predicted cosmic microwave background radiation was detected at a temperature of about 3 K [Penzias1965, with Wilson]. Refined nuclear network calculations by [Peebles1966] and [Wagoner1967, with Fowler and Hoyle] successfully showed that Big Bang nucleosynthesis (BBN) can explain the observed helium abundance.

BBN became a cornerstone of modern cosmology and a unique probe of the physics of the early universe. It contributed to the questions of the number of light neutrino species as well as of the fraction of dark matter. New observations led to a concordance between the four most-abundant nuclei composed during the Big Bang (^2H , ^3He , ^4He , ^7Li) [Boesgaard1985]. Until the end of the 20th century improvements of observational and laboratory data as well as of modeling and calculations helped BBN to enter a precision era [Schramm1998].

Conventions in this dissertation

Unless otherwise stated uncertainties refer to 68 % confidence level (CL).

If a compound is split after the interaction with a photon, then the term "photodisintegration" is mostly used for nuclei, while the term "photodissociation" usually refers to molecules. To keep the nomenclature of the feasibility study [Beyer2005] and the proposal [Junghans2007] of this dissertation, the $d(\gamma,n)p$ reaction will be called "photodissociation of the deuteron" throughout this work. The common term "deuteron breakup" may also refer to reactions not induced by photons.

1 Introduction and motivation

1.1 Standard model of cosmology

The current knowledge about the evolution of the universe and the standard model of cosmology, the Λ CDM model, is summarized in this section based on references [Weinberg2008], [Pdg2013, chapters 21, 22, and 26], and [Planck2013]. According to the Λ CDM model, the universe is flat and consists today of 69 % dark energy (denoted by the cosmological constant Λ), 26 % cold dark matter (CDM), and only 5 % baryonic matter. With only six parameters, the Λ CDM model explains several important phenomena such as the abundance of light nuclei, the temperature and the structure of the cosmic microwave background radiation (CMB), the accelerating expansion of the universe, and the large-scale structures in the distribution of matter.

In a strict definition, the Big Bang is the appearance of space-time 13.8×10^9 years ago. In a wider definition, the term Big Bang is also used for the hot, dense phase in the minutes following the singularity at the time $t = 0$. Because of the high energy density (infinite at $t = 0$) all four fundamental forces (gravitational, strong, weak, and electromagnetic interaction) are assumed to be unified until the end of the Planck epoch at $t \approx 10^{-43}$ s. It is assumed that an inflationary epoch followed, in which the universe expanded much faster than the speed of light and which ended at $t \approx 10^{-32}$ s. This inflation would solve several problems of cosmology. It was possibly followed by processes that caused the matter-antimatter asymmetry observed in the present universe.

The following, much slower expansion is described by the Hubble parameter H that today has the value $H_0 = 100h \text{ km s}^{-1} \text{ Mpc}^{-1}$, in which $h = 0.678$ is the scaled Hubble constant. The dominant influence on the expansion of the early universe after inflation was radiation (including relativistic particles) in local thermal equilibrium. Therefore, the equation of state of a gas of radiation can be used to describe the thermodynamic behavior. The energy density depends on the effective number of degrees of freedom $N(T)$, which takes the production of particle-antiparticle pairs and the freeze-out of particles from the thermal bath into account. $N(T)$ depends on the temperature and the particle physics model, e.g., on the number of light neutrino families. In the standard model of particle physics $N(T)$ is 10.75 for energies below the myon mass and decreases to 3.36 for energies below the electron mass. Using the reduced Planck constant \hbar , the speed of light in vacuum c , the gravitational constant G , and the Boltzmann constant k_B , the relation between the age of the radiation-dominated universe t and the temperature T is

$$t = \sqrt{\frac{45\hbar^3 c^5}{16\pi^3 G N(T)}} (k_B T)^{-2} \quad \Rightarrow \quad \frac{t}{\text{s}} \approx \frac{2.4}{\sqrt{N(T)}} \left(\frac{k_B T}{\text{MeV}} \right)^{-2}. \quad (1.1)$$

At $t \approx 10^{-12}$ s all four fundamental forces were separated and the universe was filled with a quark-gluon plasma, leptons, antileptons and photons. After $t \approx 10^{-6}$ s the quarks formed hadrons and antihadrons, which mostly annihilated each other. While all remaining mesons were unstable and decayed, protons and neutrons were the only baryons that had not decayed yet. The number of both baryons was kept in an equilibrium by weak interactions with leptons. At $t \approx 1$ s electrons and positrons started to annihilate. Between $t \approx 10$ s and $t \approx 10^3$ s the first light nuclei were produced during the Big Bang nucleosynthesis (BBN). The final abundances (75 % ^1H and 25 % ^4He by

mass, traces of ^2H , ^3He , ^3H , ^7Be , ^7Li , ^6Li , and others) of some of them can still be observed in the present universe, see section 1.2. A detailed description of BBN is given in section 1.3. After BBN the universe was filled by a plasma of nuclei, electrons, neutrinos, antineutrinos, and photons. The baryon-to-photon ratio stayed constant at $\eta < 10^{-9}$. It is related to the present relative baryon density by $\eta \times 10^{10} \approx 274 \Omega_b h^2$. Some of the produced nuclei were unstable. The β^- decay of ^3H to ^3He has a half life of about 12 years. In its ionized form, ^7Be decayed much slower by electron capture to ^7Li than it is the case for neutral atoms (53 days half life).

The plasma was opaque due to Thomson scattering of photons off free electrons. 380000 years after the Big Bang the photons decoupled from matter when electrons and nuclei formed electrically neutral atoms. Since then, these photons have traveled freely through the expanding universe and have been red-shifted. Today, they can be observed as the CMB, which has a black-body spectrum with $T = 2.725$ K. Measurements of the tiny anisotropies of the CMB by satellites such as [Planck2013] allowed a precise determination of the parameters (η, H_0, \dots) of the Λ CDM model.

70000 years after the Big Bang matter became the dominant influence on the expansion of the universe and first gravitational structures have build up. The formation of the first stars from gravitational collapses of matter a few hundred million years after the Big Bang released radiation that reionized the atoms. Although the universe was then filled by a plasma again, it stayed transparent due to the low density. The different phases in the evolution of stars of different masses are the astrophysical sites of stellar nucleosynthesis, which is responsible for the production of nearly all other nuclei. Some specific nuclei were also produced in spallation reactions of cosmic rays. Galaxies and large-scale structures such as galaxy groups, clusters, and superclusters formed gradually from smaller structures. Five billion years after the Big Bang dark energy started to dominate and accelerate the expansion of the universe.

1.2 Observed primordial abundances

The determination of primordial abundances of light nuclei outlined here is discussed in [Pdg2013, chapter 22]. The quantity to be measured is the abundance ratio of two nuclides in the same gas. For the primordial nuclei, ^1H is usually used as reference because it is the easiest to measure. At many astrophysical sites the primordial abundances changed during the chemical evolution of the universe. Stellar burning can destruct light nuclei and produce ^3He , ^4He , and ^7Li . Cosmic-ray spallation can produce ^6Li and ^7Li . Sites with a lower metallicity (mass fraction of elements larger than helium) are considered as being less chemically evolved. Therefore, the observed abundance ratios can be correlated with the metallicities to determine the primordial abundance ratio by an extrapolation to zero metallicity. At sites with exclusive production (destruction) the observed abundance is an upper (lower) limit for the primordial abundance.

The used instruments and methods are strongly dependent on the observed site. In the solar system, the deuterium–hydrogen ratio D/H ($= ^2\text{H}/^1\text{H}$), for example, has been determined from infrared spectra of rotational lines of HD molecules of Neptune and Uranus, and with the mass spectrometer of the Galileo probe in the atmosphere of Jupiter [Tytler2000]. The most precise method for the determination of the primordial D/H ratio is the detection of Lyman absorption lines, which are found in spectra of quasars when their light passes the gas in the interstellar medium on its way to earth [Kirkman2003]. To observe chemically unprocessed matter, the absorption had to happen at large distances. Typically, the absorption lines are red-shifted with $z = 2 - 4$ (corresponding to $t \approx 1.5 - 3$ billion years) and the line of deuterium is also isotope-shifted. Such observations in the range of visible and ultraviolet light are only possible at large telescopes with high resolution. In the last two decades there were about a dozen D/H determinations from quasar absorption systems.

The primordial abundance of ^3He has not been determined yet with sufficient precision because the only observations were made in chemically evolved systems and are in conflict with stellar

nucleosynthesis models. The ${}^4\text{He}$ mass fraction Y is determined from the observation of emission lines related to the recombination of ionized He and H in certain, very metal-poor extragalactic regions. There is a large number of observed objects, but the modeling of the astrophysical sites is rather complex. Therefore, the uncertainties are dominated by systematic effects and different evaluations came to different results [Olive2004]. The same is true for the lithium-to-hydrogen ratio [Fields2011], for which the absorption lines observed in the atmospheres of certain metal-poor stars in the spheroid of the galaxy are best suited. The ratio of both stable lithium isotopes was recently estimated from the tiny isotopic shift to ${}^6\text{Li}/{}^7\text{Li} < 0.05$.

The primordial values (indexed by p) given in the topical evaluation [Pdg2013, chapter 22] are

$$Y_p = 0.2465 \pm 0.0097, \quad \text{D/H}|_p = (2.53 \pm 0.04) \times 10^{-5}, \quad \text{and} \quad \text{Li/H}|_p = (1.6 \pm 0.3) \times 10^{-10}.$$

1.3 Big Bang nucleosynthesis

This section summarizes, how BBN predicts the abundance of light nuclei. Elaborate reviews are given by [Steigman2007, Iocco2009, Pospelov2010]. In the hadron epoch, which started at $t \approx 10^{-6}$ s, protons and neutrons were converted into each other through weak-interaction processes with electrons, positrons, electron neutrinos, or electron antineutrinos. The equilibrium value of the neutron–proton ratio $n/p = \exp(-\Delta m/k_B T)$ depended on the temperature and the mass difference between both nucleons $\Delta m = m_n - m_p = 1.293$ MeV. Because the weak interaction rate became slower than the expansion of the universe, the neutrinos decoupled from the thermal bath at $k_B T \approx 0.7$ MeV ($t \approx 1$ s) with $n/p \approx 1/6$. Although the mean photon energy was already below the deuteron binding energy $B_d = 2.225$ MeV, there was still a large number of photons above this threshold in the high-energy tail of the black-body spectrum. Therefore, the deuterons formed by the $p(n,\gamma)d$ reaction at that time were immediately destroyed by the $d(\gamma,n)p$ reaction. The density was too low for three-body reactions. An efficient deuteron production started only later at $t \approx 10$ s. The $p(n,\gamma)d$ reaction provided the raw material and fixed the start conditions (t, T, η) for all following nuclear reactions (the most important are shown in figure 1.1) and is therefore the bottleneck reaction of BBN. Tritium (${}^3\text{H}$) and ${}^3\text{He}$ were produced by d–p and d–d reactions and then reacted with deuterons to form α particles, i.e., ${}^4\text{He}$ nuclei. Nearly all neutrons ended up in ${}^4\text{He}$ for three reasons: It is the most tightly bound of all BBN nuclei, there are no stable nuclei with mass number five, and there is a stronger Coulomb-suppression for the production of heavier nuclei. Until $t \approx 200$ s ($k_B T \approx 0.08$ MeV) the neutron destruction rate was dominated by the decay (life time $\tau_n = 880$ s [Pdg2013]), which resulted in $n/p \approx 1/7$, before nuclear reactions took over. From that value, the primordial ${}^4\text{He}$ mass fraction can be estimated by

$$Y_p = \frac{2n}{p+n} = \frac{2n/p}{1+n/p} \approx 0.25.$$

Tiny amounts of ${}^7\text{Li}$ ($\text{Li/H} \approx 10^{-10}$) were produced directly by ${}^3\text{H}-\alpha$ reactions, which was the dominant reaction path at $\eta < 3 \times 10^{-10}$, or via the production of ${}^7\text{Be}$ by ${}^3\text{He}-\alpha$ reactions. ${}^6\text{Li}$ was produced with an even lower abundance during BBN. Because there are no stable nuclei with mass number eight, the BBN abundances of the stable isotopes of beryllium, boron, or carbon were again orders of magnitude lower and thus negligible compared to other nucleosynthesis mechanisms. Figure 1.2 summarizes the time line of the BBN by showing the evolution of the mass fractions. At $t \approx 1000$ s there were almost no nuclear reactions anymore due to the reduction of density and temperature ($k_B T \approx 0.037$ MeV) caused by the expansion. After the decay of the unstable nuclei (${}^3\text{H}$, ${}^7\text{Be}$, see section 1.1), the abundances of the light nuclei were fixed at their primordial values.

The calculation of the primordial abundances that are predicted by BBN is a nontrivial task [Serpico2004, Cyburt2004, Fields2006]. However, such calculations are much less complicated for BBN than for stellar nucleosynthesis, because of the homogeneity, the simpler thermodynamic

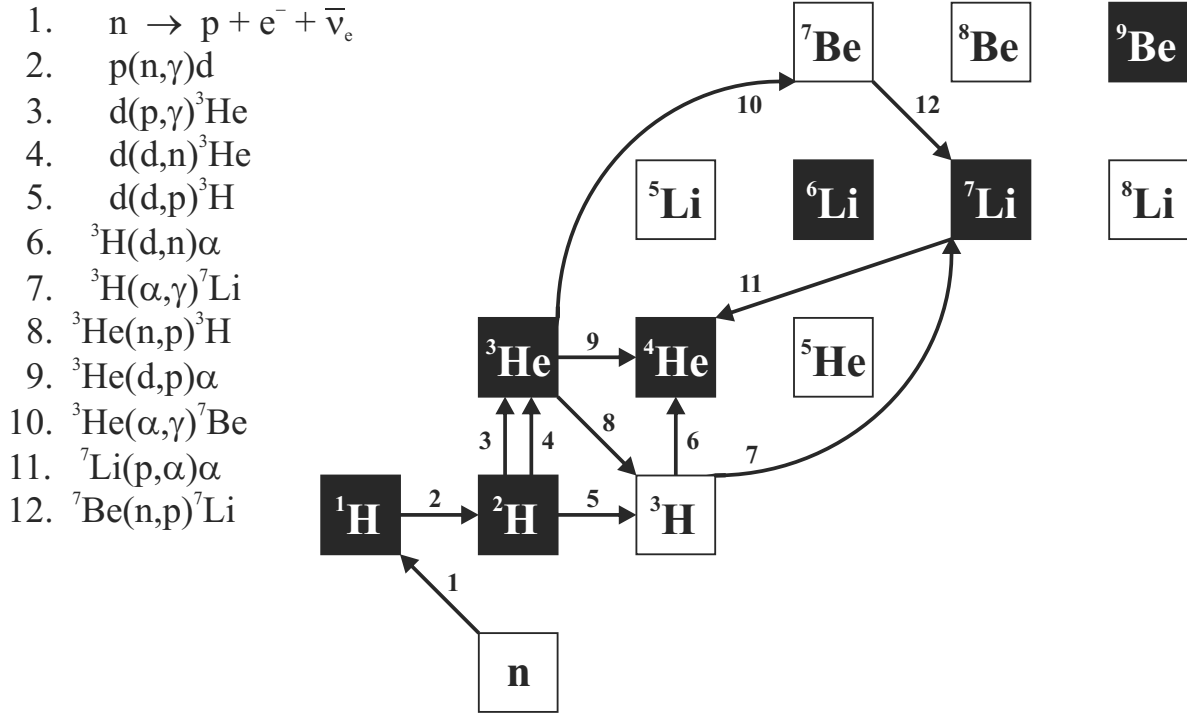


Figure 1.1: Nuclear reaction network of BBN. The black and white boxes denote stable and unstable nuclei, respectively, sorted by proton (vertical) and neutron number (horizontal). The numbered arrows represent the nuclear reactions listed on the left, which are most important for the primordial abundances of ${}^1\text{H}$, ${}^2\text{H}$, ${}^3\text{He}$, ${}^4\text{He}$, and ${}^7\text{Li}$.

evolution, and the small number of key reactions, which are directly measurable in the laboratory at the relevant energies. Apart from the measured nuclear data (reaction cross sections and neutron life time), the main inputs for BBN are the particle physics model, the physical constants, and the baryon-to-photon ratio η . If the standard model of particle physics is applied, then BBN depends only on one parameter. Therefore, a comparison of the predicted and the observed primordial abundances makes BBN a unique probe of η in the early universe.

Figure 1.3 shows that deuterium is best suited to determine η because the BBN prediction of the D/H abundance ratio is a monotonic function with a steep slope and both the observation and the prediction have small uncertainties. Within the large systematic uncertainty of its observed abundance, ${}^4\text{He}$ is consistent with the baryon-to-photon ratio obtained from ${}^2\text{H}$, which is already a great success for BBN. Some years ago, when the observed D/H_p and ${}^7\text{Li}/\text{H}_p$ abundance ratios were known less precise, there was a clear concordance of ${}^2\text{H}$, ${}^4\text{He}$, and ${}^7\text{Li}$, i.e., BBN predicted the abundances correctly over ten orders of magnitude. In the current precision era of cosmology there are tensions with ${}^6\text{Li}$ and ${}^7\text{Li}$ known as the *lithium problems* [Cyburt2008, Fields2011]. However, the agreement between recent BBN and CMB results [Pdg2013, chapter 22] remains remarkable:

$$5.7 \leq \eta_{\text{BBN}} \times 10^{10} \leq 6.7 \quad \eta_{\text{CMB}} \times 10^{10} = 6.05 \pm 0.15 \quad (\text{both at 95 \% CL}).$$

These results show that the ΛCDM model provides a concordant description of the universe at ages of a few minutes and 380000 years. By using η_{CMB} as a constant for BBN, it became possible to test “new physics” hypotheses such as particle physics models beyond the standard model or the variation of fundamental constants [Malaney1993, Cyburt2005, Steigman2007, Iocco2009, Pospelov2010], which may offer solutions to the lithium problems. With the same intention, the influence of nuclear physics was studied by including new reactions to the network [Fuller2010, Coc2012] or by sensitivity studies that evaluate the impact of the key reactions (see below).

For all these approaches a further reduction of the uncertainties is very important, both of the observed abundances, which dominates in the case of ${}^4\text{He}$, and the BBN predictions. The relative uncertainties of the BBN predictions by [Pdg2013, chapter 22], which are based on [Cyburt2008],

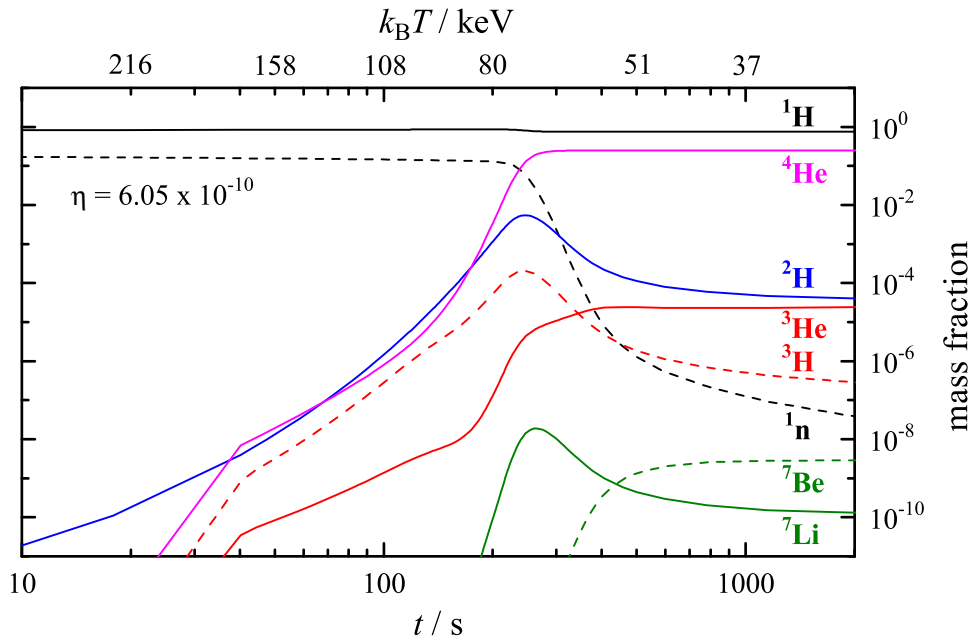


Figure 1.2: Time-dependent mass fractions during BBN calculated with the code by [Timmes2009] with the input parameters as measured by [Planck2013]. Dashed lines are used for nuclides that decay to the stable nuclide of the same color.

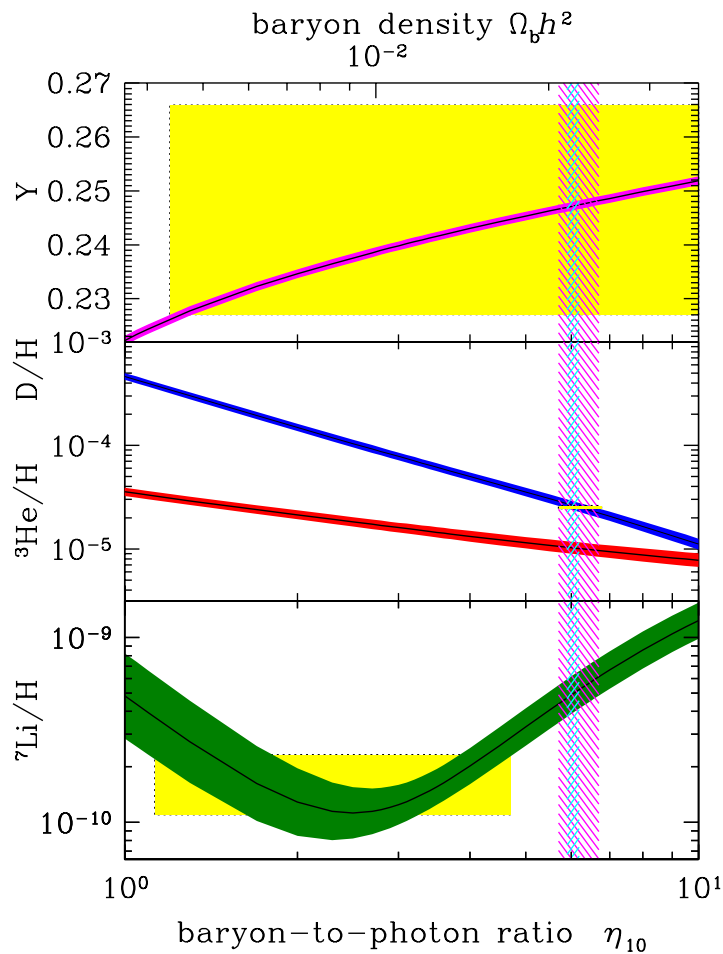


Figure 1.3: Primordial abundance ratios of light nuclei. The filled bands are the ranges of BBN calculations as function of the baryon-to-photon ratio $\eta \times 10^{10} = \eta_{10}$. The yellow boxes indicate the ranges of η_{10} resulting from observations, see section 1.2. The vertical hatched bands indicate the range of η_{10} from BBN (magenta) and CMB (cyan, from [Planck2013]). In this figure taken from [Pdg2013, chapter 22] all ranges are at 95 % CL.

are less than 0.3 % for ${}^4\text{He}$, about 4 % for ${}^2\text{H}$, and about 12 % for ${}^7\text{Li}$ at η_{BBN} . Due to evolving nuclear data bases or different methods for data evaluation and uncertainty treatment, the results of other calculations [Smith1993, Fiorentini1998, Nollett2000, Cyburt2001, Serpico2004, Descouvemont2004, Cyburt2004, Fields2006] are slightly different but consistent. From several sensitivity studies [Fiorentini1998, Nollett2000, Cyburt2004, Coc2010] it is known, that Y_p is most sensitive to the neutron life time τ_n , $D/H|_p$ to the reactions 2–5 from figure 1.1, and ${}^7\text{Li}/H|_p$ to the reactions 2, 9, 10, and 12.

Therefore, the $p(n,\gamma)d$ reaction is a key reaction for the prediction of $D/H|_p$ and ${}^7\text{Li}/H|_p$. The energy range, for which its cross section is relevant for BBN, is at total kinetic energies in the center-of-mass system T_{cm} of 20–200 keV [Burles1999, Wustmann2006]. Unlike for all other reactions in the BBN network, the $d(\gamma,n)p$ reaction rate is not directly based on experimental data:

“Experimentally, this reaction is quite difficult to measure in the relevant energy range for BBN. We thus rely on theory-based cross sections which are normalized to the available experimental data. [...] Evaluating all of the relevant data, np scattering, deuteron ground state properties as well as the radiative capture and photo-dissociation data using a Markov chain Monte Carlo algorithm, a best fit with propagated uncertainties [Ando2006] finds $\lesssim 1\%$ errors in the capture rate. We adopt this rate in our network.” [Cyburt2008]

Although the precision calculations of the $p(n,\gamma)d$ cross section do not contribute considerably to the uncertainties of the present BBN predictions [Serpico2004, Cyburt2008], this will become important again, when the uncertainties of other nuclear reactions, observed abundances, and cosmological parameters can be reduced in the future.

1.4 Objective of this dissertation

While the different cross section calculations deviate only by a few percent from each other, the experimental uncertainties are usually much larger. Precision measurements of the $p(n,\gamma)d$ or $d(\gamma,n)p$ cross sections would therefore be desirable both for constraining theoretical calculations and to allow BBN network calculations that are solely based on experimental data.

Calculations and previous measurements of $p(n,\gamma)d$ and $d(\gamma,n)p$ cross sections are reviewed in chapter 2. In the energy range relevant to BBN ($T_{\text{cm}} \approx 20\text{--}200$ keV) there is a lack of absolute cross section measurements: there are eight data points of the $p(n,\gamma)d$ cross section, which were all measured at one facility, two data points of the total $d(\gamma,n)p$ cross section, and a few data points of the M1 contribution to the $d(\gamma,n)p$ cross section. So far, there has been no absolute $d(\gamma,n)p$ cross section measurement at $T_{\text{cm}} < 5$ MeV that used bremsstrahlung, because apart from an accurate photon flux normalization such measurements require an efficient detection of one of the reaction products and its relatively low energy.

The objective of this dissertation is an absolute $d(\gamma,n)p$ cross section measurement with a total uncertainty of about 5 % in the energy range relevant to BBN and up to $T_{\text{cm}} \approx 2.5$ MeV with pulsed bremsstrahlung at the radiation source ELBE. To achieve this, the experimental setup features a photon flux determination using nuclear resonance fluorescence and an energy determination using neutron time-of-flight detectors with low detection threshold and well known efficiency, see chapter 3. Further important parts of this work are the calibration of the neutron detection efficiency in a separate experiment in the neutron reference fields of PTB Braunschweig as well as the simulation of interactions of neutrons with the setup, see chapters 4 and 5.

2 Photodissociation of the deuteron and its inverse reaction

2.1 The deuteron

Deuterium is the naturally occurring, stable hydrogen isotope with mass number two. Its nucleus is called deuteron, has the mass $m_d = 1875.612859(41) \text{ MeV } c^{-2}$ [Mohr2012], and consists of one proton and one neutron. The binding energy $B_d = (m_n + m_p - m_d) c^2 = 2.22456614(41) \text{ MeV}$ has been determined precisely by measuring the wavelength of the γ ray emitted after the thermal-neutron capture on hydrogen [Kessler1999]. The parity $\pi = (-1)^l$ of the deuteron is positive, which is known from n-p scattering experiments [Landau1958, p. 15], and limits the orbital angular momentum l to integral multiples of two. From the total angular momentum $J = |l + S| = 1$, which is known from the hyperfine-structure splitting [Kellogg1936], one can deduce the deuteron spin $S = 1$ (proton and neutron spins parallel) and that $l = 0$ or $l = 2$. Proton and neutron can be described by the isospin formalism. The isospin I is a quantum number of the strong interaction, which has the value $1/2$ for nucleons and different third components $I_z = \pm 1/2$ for proton and neutron. The nucleon–nucleon (NN) system must have an antisymmetric wave function (Pauli principle). The spatial and spin components of the deuteron’s wave function are symmetric, so the isospin component must be antisymmetric and thus the deuteron has isospin $I = 0$. The other three possible configurations (n–n, p–n, p–p) form an isospin triplet with $I = 1$ and with opposite nucleon spins ($S = 0$). Figure 2.1 illustrates the possible low-energy states of the NN system.

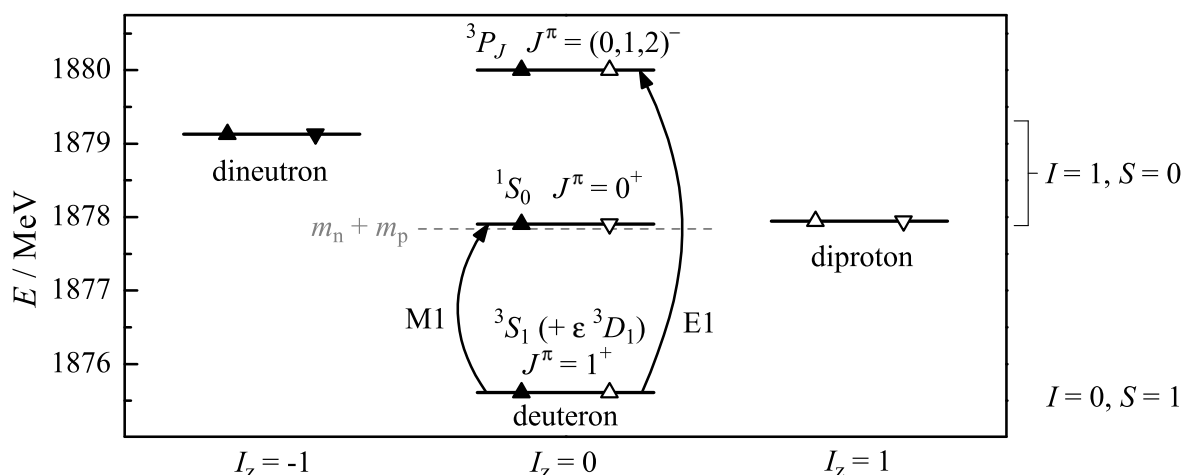


Figure 2.1: Low-energy states of the NN system sorted by isospin direction I_z . The symbols stand for protons (empty) or neutrons (filled) and their spin direction $S_z = \pm 1/2$ (up- and down-pointing triangle). The total energy E is shown by horizontal lines for each state and includes rest masses and binding energy, which was assumed to be 0 for the dineutron, -1.4 MeV for the diproton (Coulomb repulsion), -66 keV for the 1S_0 state, and -2.2 MeV for the 3P_J state (maximum of the E1 cross section). For $I_z = 0$ the quantum numbers are shown by the spectroscopic notation $^{2S+1}L_J$. The curved arrows show electromagnetic transitions.

From n-p- and p-p-scattering experiments it is known that dineutron, diproton, and the 1S_0 state of the deuteron are unbound, the latter with a binding energy of $B'_d \approx -66$ keV. From measurements of the magnetic dipole moment and the electric quadrupole moment of the deuteron it can be deduced that its ground state has the configuration $^1S_0 + \varepsilon^3 D_1$, i.e., there is a small contribution ($|\varepsilon|^2 \approx 0.04$) from higher angular momentum [Evans1955].

Figure 2.1 also shows the electromagnetic transitions from the deuteron ground state to the two lowest unbound p-n states. The changes of total angular momentum and parity result in the following multipolarities: The transition to the 1S_0 state is a magnetic dipole (M1, $|\Delta J = 1|, \Delta P = +1$) and the transition to the 3P_J state is an electric dipole (E1, $|\Delta J = 1|, \Delta P = -1$).

2.2 Kinematics of the $d(\gamma, n)p$ reaction

The kinematics of the $d(\gamma, n)p$ reaction will be described in two reference frames. On the one hand, the laboratory (**lab**) frame is defined by a resting observer, i.e., all quantities are measured in this frame. It is assumed that the photon beam is parallel to the z -axis and that the deuteron is at rest in the **lab** frame. On the other hand, the center-of-mass (**cm**) frame is defined by a resting center of mass, i.e., the total momentum vanishes in this frame. This is the natural frame of the reaction. In this section the most important relations between angles and energies in the two different frames will be declared, while some derivations and all definitions are given in appendix B. The following conventions will be used: The speed of light $c = 1$. If the frame is not denoted by an index, the prime symbol $'$ denotes the **cm** frame. Particles and coordinates are denoted by indices, too. The particle masses that have been used are listed in appendix A.

The equations (2.1)–(2.6) show, that the velocity of the **cm** frame in the **lab** frame β , the **lab** photon energy E_γ , the **cm** photon energy E'_γ , the **cm** total energy \sqrt{s} , the **cm** kinetic energy T_{cm} , the **cm** total momentum p' , and the **cm** total neutron energy E'_n can be calculated, if one of these variables is known:

$$\beta = E_\gamma / (E_\gamma + m_d) \quad (2.1)$$

$$E'_\gamma = E_\gamma (1 + 2E_\gamma / m_d)^{-0.5} \quad (2.2)$$

$$\sqrt{s} = E'_\gamma + (m_d^2 + E'^2_\gamma)^{0.5} = m_d (1 + 2E_\gamma / m_d)^{0.5} \quad (2.3)$$

$$T_{\text{cm}} = \sqrt{s} - m_p - m_n \quad (2.4)$$

$$p'^2 = [s - (m_p + m_n)^2][s - (m_p - m_n)^2] / (4s) \quad (2.5)$$

$$E'_n = (m_n^2 + p'^2)^{0.5} = (s + m_n^2 - m_p^2) / \sqrt{4s} \quad (2.6)$$

Depending on the frame, in which neutron energy and angle are given, three cases are considered:

1. E'_n and ϑ' are given:

$$E_n = \gamma(E'_n + \beta p' \cos \vartheta') = \gamma[(m_n^2 + p'^2)^{0.5} + \beta p' \cos \vartheta'] \quad (2.7)$$

$$\cos \vartheta_n = \gamma[p' \cos \vartheta' + \beta(m_n^2 + p'^2)^{0.5}] / (E_n - m_n)^{0.5} \quad (2.8)$$

2. E'_n and ϑ_n are given:

$$p_n^\pm = \frac{\cos \vartheta_n E'_n \beta / \gamma \pm \sqrt{E_n'^2 / \gamma^2 - m_n^2 (1 - \beta^2 \cos^2 \vartheta_n)}}{1 - \beta^2 \cos^2 \vartheta_n} \quad (2.9)$$

$$E_n = (m_n^2 + p_n^2)^{0.5} \quad (2.10)$$

$$\cos \vartheta' = \gamma(p_n \cos \vartheta_n - \beta E_n) / p' \quad (2.11)$$

If $T_{\text{cm}} \geq 1.323$ keV then p_n^+ is the only solution, so p_n^- is irrelevant for BBN. The figures 2.2 and 2.3 show ϑ'_n and the **lab** kinetic neutron energy $T_n = E_n - m_n$ as functions of T_{cm} and ϑ_n .

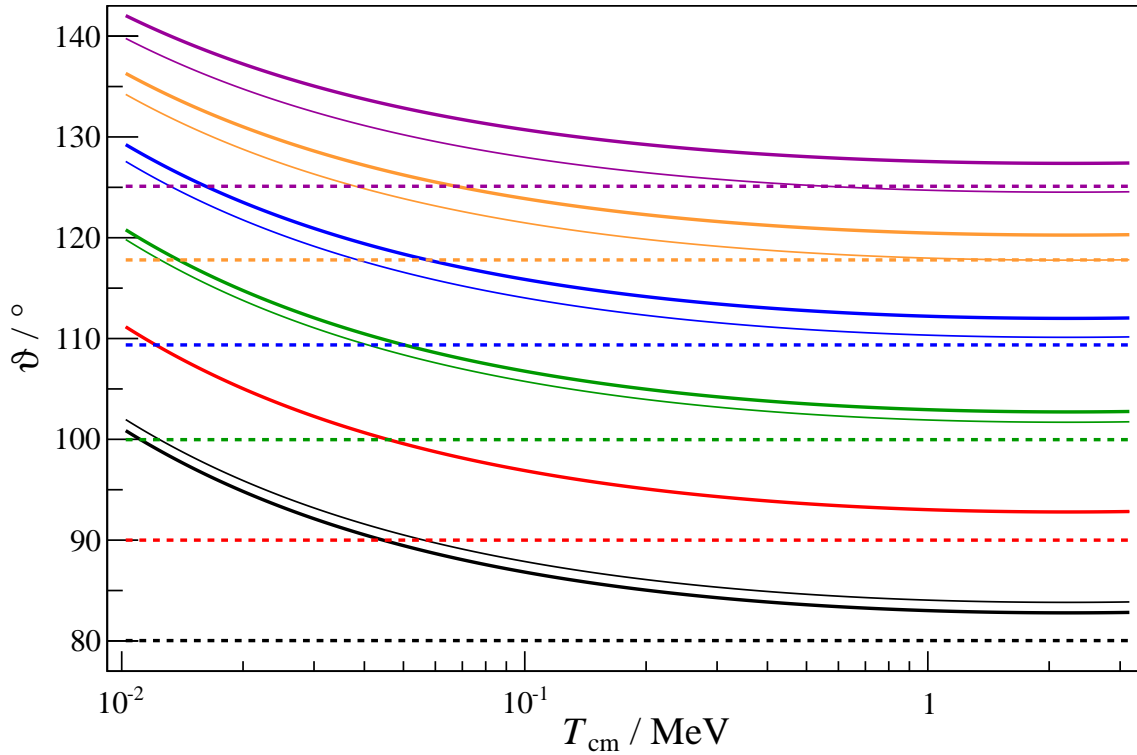


Figure 2.2: Neutron angle as function of cm kinetic energy T_{cm} . The colors represent the position of the six neutron detectors described in section 3.1. The thick and thin solid lines show ϑ'_n at the center ($x = 0$) and the edge ($x = \pm 500$ mm) of the detectors, respectively. The dashed lines show ϑ_n at the detector center.

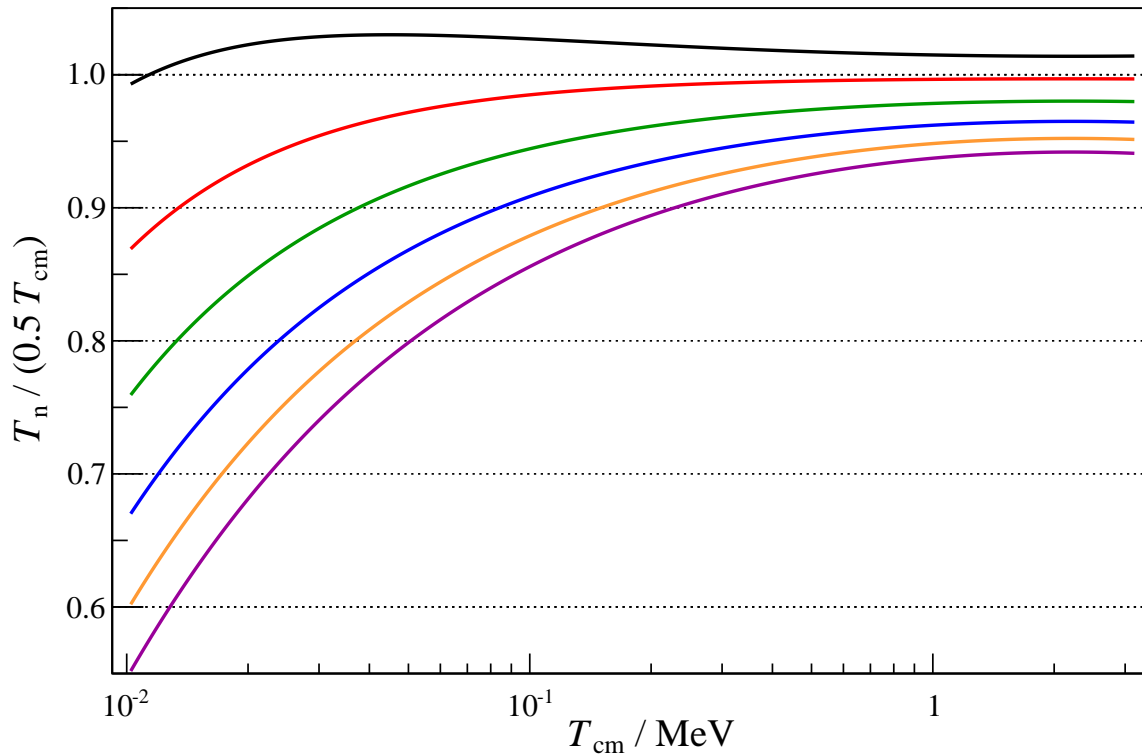


Figure 2.3: Kinetic neutron energy T_n in the lab frame as function of T_{cm} . The colors are related to ϑ_n as described in figure 2.2. The plot is normalized to the often used approximation $T_n \approx 0.5 T_{\text{cm}}$ to demonstrate the importance of an exact calculation of kinematic quantities especially close to the threshold or at angles not close to 90° .

3. E_n and ϑ_n are given and $T_{\text{cm}} \geq 1.323$ keV:

E'_n and ϑ' can be calculated using equations (2.5), (2.6), and (2.11) with

$$\begin{aligned} s &= m_d (Y_1 + Y_2) / Y_3 & (2.12) \\ Y_1 &= p_n^2 (1 + \cos^2 \vartheta_n) m_d + p_n \cos \vartheta_n (m_p^2 - m_n^2 + m_d^2) + m_d m_p^2 \\ Y_2 &= \sqrt{p_n^2 + m_n^2} (2p_n \cos \vartheta_n m_d + (m_p^2 - m_n^2 + m_d^2)) \\ Y_3 &= p_n^2 (\cos^2 \vartheta_n - 1) + 2p_n \cos \vartheta_n m_d - m_n^2 + m_d^2. \end{aligned}$$

In all three cases, the relations between time of flight t_n , kinetic energy T_n , and flight path l of a neutron are given by

$$t_n = l \frac{E_n}{p_n} = l \frac{T_n + m_n}{\sqrt{(T_n + m_n)^2 - m_n^2}} \Leftrightarrow T_n = m_n \left(\left(1 - \frac{l^2}{t_n^2} \right)^{-0.5} - 1 \right). \quad (2.13)$$

The kinematic relations for the transformations of the differential quantities $d\sigma/d\Omega \rightarrow d\sigma/d\Omega'$, $d\Phi_\gamma/dE_\gamma \rightarrow d\Phi_\gamma/dT_{\text{cm}}$, $d\Phi_\gamma/dE_\gamma \rightarrow d\Phi_\gamma/dT_n$, and $d\Phi_\gamma/dE_\gamma \rightarrow d\Phi_\gamma/dt_n$ are given in equations (B.1)–(B.4) in appendix B.

2.3 Reciprocity relation

The reciprocity relation [Mayer-Kuckuk2002] for the cross sections of the reaction $A + a \rightarrow b + B$ and the time-reversed reaction $B + b \rightarrow a + A$ takes kinematic factors (momentum vector in the **cm** frame \vec{p}') and statistical weights (related to total angular momenta J) into account and is given by

$$(2J_A + 1)(2J_a + 1) |\vec{p}'_A - \vec{p}'_a|^2 \sigma_{Aa \rightarrow bB} = (2J_b + 1)(2J_B + 1) |\vec{p}'_b - \vec{p}'_B|^2 \sigma_{Bb \rightarrow aA}.$$

It is also called *principle of detailed balance* and care must be taken, that it applies only if the reaction channels are the same in both reaction directions. This is usually not the case if several energy levels can be populated in the final states [Musiol1988]. In the case of the $d(\gamma, n)p$ reaction and its inverse reaction there are no excited states that can be populated and thus the principle of detailed balance can be applied to the total cross sections. The statistical weight for unpolarized photons is 2 because there are two possible directions of polarization once the direction of propagation is fixed. Using $J_d = 1$, $J_n = J_p = 1/2$, and equations (2.3) and (2.5) one finds

$$\sigma_{d\gamma \rightarrow np} = \frac{2}{3} \frac{[s - (m_p + m_n)^2][s - (m_p - m_n)^2]}{(s - m_d^2)^2} \sigma_{pn \rightarrow \gamma d}. \quad (2.14)$$

For the $p(n, \gamma)d$ reaction in the **lab** frame with a neutron kinetic energy T_n^* and a resting proton one finds $s = 2m_p T_n^* + (m_p + m_n)^2$.

2.4 Cross section calculations

The $d(\gamma,n)p$ cross section can be calculated based on the coupling of photons to the deuteron ground state. Because the deuteron is one of the simplest nuclear systems, it served as a test case for any new theoretical concept. The historical development of cross section calculations is summarized in [Arenhoevel1991], where three periods are distinguished:

1. The *primitive period*, in which only simple wave functions and forces (effective range theory) have been used and only the lowest multiplicities (E1, M1) have been considered [Bethe1935, Fermi1935, Bethe1950, Evans1955].
2. The *classic period*, which still uses conventional nuclear physics, but with realistic forces, elaborate wave functions, and higher multiplicities [Partovi1964].
3. The *post-classic period*, with an explicit treatment of subnuclear physics (meson, isobar, and quark-gluon degrees of freedom) and relativistic effects [Riska1972, Schmitt1991].

The cross sections calculated by [Bethe1950] can be expressed analytically by

$$\sigma_{E1}(T_{cm}) = 19.2405 \frac{(T_{cm}/B_d)^{1.5}}{(T_{cm}/B_d + 1)^3} \quad \sigma_{M1}(T_{cm}) = 0.6938 \frac{1.026(1 + 0.045T_{cm})T_{cm}^{0.5}}{(T_{cm} + B_d)(T_{cm} + 0.0736)}, \quad (2.15)$$

in which T_{cm} and B_d are to be inserted in MeV to obtain the cross section in mb. The factors are not model-dependent, but can be calculated using measurable quantities. A discrepancy to experimental values of $\sigma_{pn \rightarrow \gamma d}$ at thermal neutron energies was solved by including meson-exchange effects. This resulted in a correction factor of 1.097 to σ_{M1} [Riska1972]. Figure 2.4 shows the cross sections from equation (2.15) with and without this correction. The maximum of σ_{M1} is at $T_{cm} = 65$ keV, the maximum of σ_{E1} is at $T_{cm} = 2.2$ MeV, and equal strength ($1.097\sigma_{M1} = \sigma_{E1}$) is found at $T_{cm} = 0.24$ MeV.

A model independence was also found in calculations with modern realistic nucleon–nucleon (NN) potentials like *CD-Bonn*, *Nijmegen I*, or *Argonne v18*, which gave very similar results for the $d(\gamma,n)p$ cross section [Schiavilla2005, p. 2] [Marcucci2006, p. 124]. These precision models were constructed in the mid 1990’s and use about 45 parameters, which are fitted to measured cross sections of NN elastic scattering [Machleidt2001]. Figure 2.4 also shows a calculation provided by [Arenhoevel2005], which is based on the Bonn potential and includes multiplicities of higher order. For $T_{cm} < 0.01$ MeV and $T_{cm} > 1$ MeV it is between 1 and 2 % lower than the calculation by [Riska1972], whereas in the energy range between there is a deviation of up to 5 %.

The last twenty years can be considered as a *precision period* not only because of the precision NN potentials, but also due to the development of techniques of effective field theory (EFT) in the NN sector. EFT calculations solved discrepancies that had been observed between theory (using NN potentials) and measurements of the $d(e,e'n)p$ reaction [Ryezayeva2008]. A calculation of the $p(n,\gamma)d$ cross section using the pionless nucleon-nucleon EFT up to NLO (next-to-leading order) for the M1 contribution and up to N³LO (next-to-next-to-next-to-leading order) for the E1 contribution reached an uncertainty of $\lesssim 4$ % [Chen1999]. Thereby the E1 amplitude depended only on NN phase shift data, whereas the M1 amplitude was determined from the thermal $p(n,\gamma)d$ cross section. A similar calculation with a theoretical uncertainty of about $\lesssim 1$ % has been done by [Rupak2000], in which the next-higher orders (M1: N²LO, E1: N⁴LO) were included. As the coupling at N⁴LO is constrained by $d(\gamma,n)p$ cross section data measured in the energy range $2.6 \text{ MeV} < E_\gamma < 7.3 \text{ MeV}$, an experimental uncertainty of $\lesssim 1$ % is given, too. Similar uncertainties are estimated for a calculation using the pionless EFT with dibaryon fields up to NLO [Ando2006]. These three EFT calculations agree very well to each other and to the calculation by [Arenhoevel2005] as can be seen in figure 2.4. The figure also shows that

at $T_{\text{cm}} = 0.1$ MeV and $T_{\text{cm}} = 1$ MeV there is some tension between these calculations and the R-Matrix fit by [Johnson2001], which uses experimental data from the $p(p,p)p$, $p(n,n)p$, $d(\gamma,n)p$, and $p(n,\gamma)d$ reactions between 0 and 30 MeV.

Recent developments are *ab initio* calculations of the $p(n,\gamma)d$ cross section on the lattice using EFT, which were able to reproduce the continuum result in leading order [Rupak2013], and contributions of the two-pion exchange currents to the $d(\gamma,n)p$ cross section, which have been studied in the framework of chiral EFT and are found to be important especially at photon energies higher than the BBN energy range [Epelbaum2013].

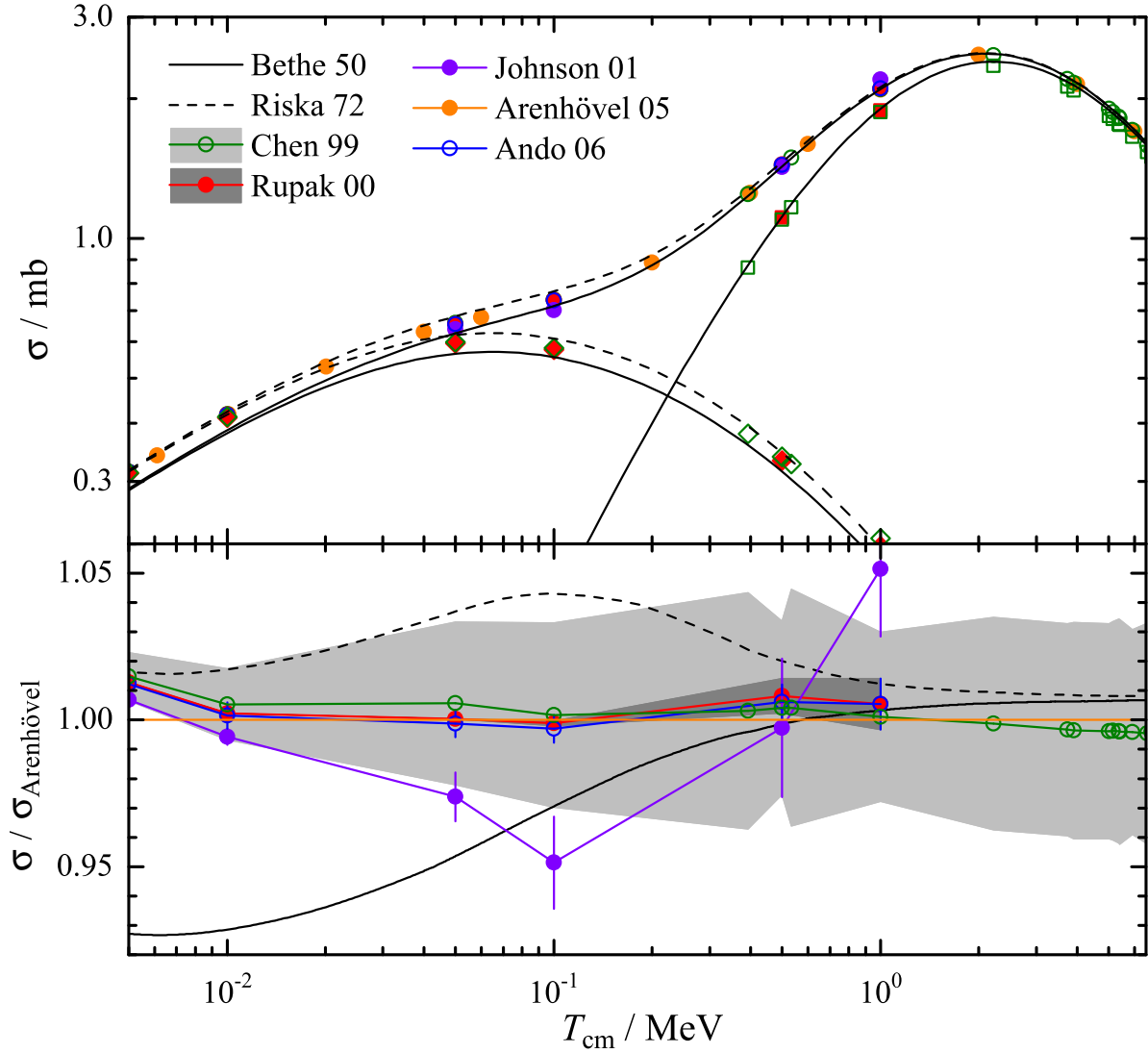


Figure 2.4: Calculated $d(\gamma,n)p$ cross sections at energies relevant to BBN. The upper panel shows the total cross section and for the black, red, and green data sets separately the M1 and E1 contributions (for red and green as diamonds and squares). The black lines are calculated analytically with equation (2.15) with and without the correction factor of [Riska1972] while the other data sets are from tables. The lower panel shows the total cross sections normalized to the calculation of [Arenhoevel2005]. Error bars or bands are only shown in the lower panel, but not for the orange and black curves. The structures in the light gray error band are from rounding.

2.5 Differential cross section

Close to the threshold the $d(\gamma,n)p$ reaction is dominated by E1 and M1 transitions and the differential cross section can be parametrized as in [Evans1955, p. 337] by

$$\frac{d\sigma}{d\Omega'}(T_{\text{cm}}, \vartheta') = \frac{1}{4\pi} \left(\sigma_{\text{M1}}(T_{\text{cm}}) + \frac{3}{2} \sigma_{\text{E1}}(T_{\text{cm}}) \sin^2 \vartheta' \right), \quad (2.16)$$

which is a rather accurate low-energy approximation of the parametrization used in the cross section calculation of [Partovi1964]. Figure 2.5 shows the differential cross sections for three different energies and four theoretical data sets. It can be seen that higher multiplicities can be neglected at energies relevant to BBN. There is no dependence on the azimuth angle ϕ , if beam and target are unpolarized. An expansion of the differential cross section in Legendre polynomials given by

$$\frac{d\sigma}{d\Omega'}(T_{\text{cm}}, \vartheta') = \sum_{n=0}^{\infty} A_n(T_{\text{cm}}) P_n(\cos \vartheta')$$

has the advantage that orthogonal functions are used, which have uncorrelated coefficients when fitted to data. To obtain equation (2.16), the only non-zero coefficients are $A_0 = (\sigma_{\text{E1}} + \sigma_{\text{M1}})/4\pi$ and $A_2 = -\sigma_{\text{E1}}/4\pi$. Further relations between the Legendre polynomial expansion and the coefficients of the parametrization of [Partovi1964] can be found in [Arenhoevel1991, p. 160].

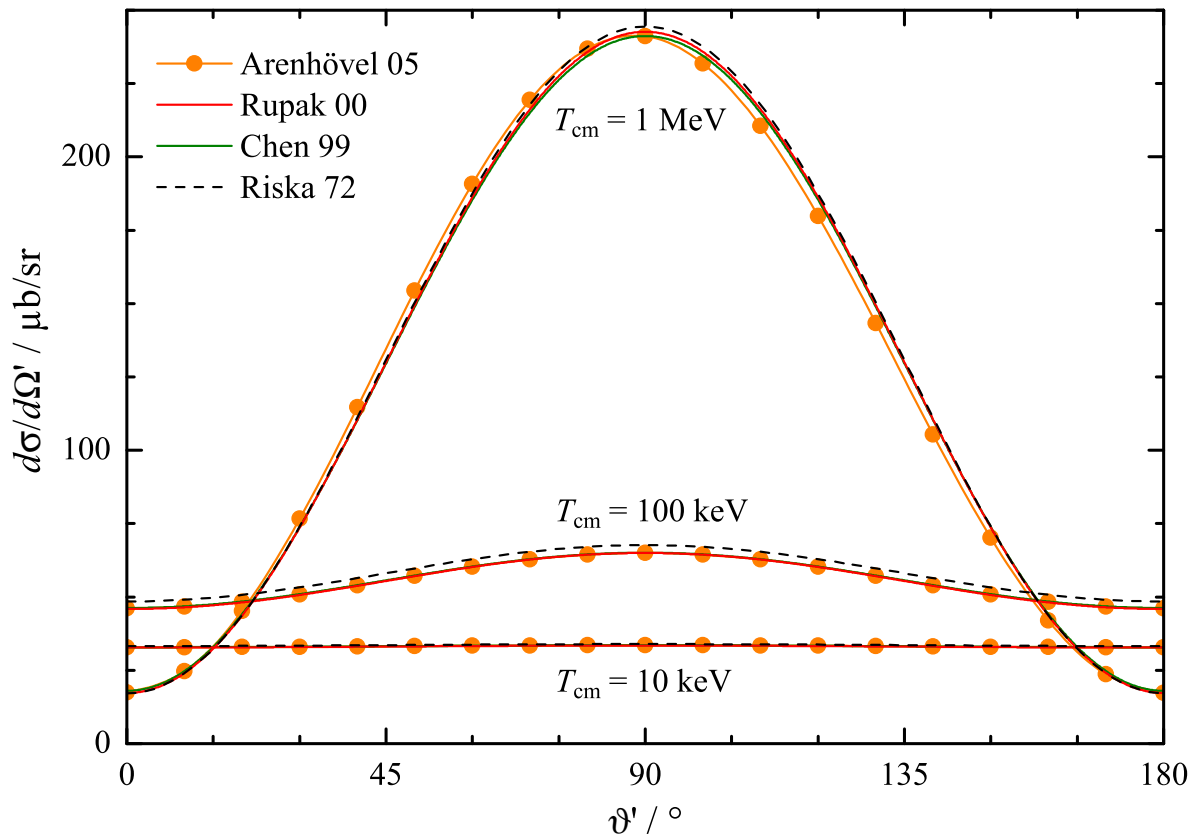


Figure 2.5: Calculated $d(\gamma,n)p$ differential cross sections at energies relevant to BBN. The orange data set is from tables while the other curves are calculated with equation (2.16) using the cross section data shown in figure 2.4. This explains, why the curves are nearly identical. At $T_{\text{cm}} = 1 \text{ MeV}$ the orange curve does not look symmetric to $\vartheta' = 90^\circ$ anymore, which is related to multiplicities of higher orders.

2.6 Previous measurements of the $p(n,\gamma)d$ cross section

Measurements of the $p(n,\gamma)d$ cross section can be divided chronologically and by kinetic neutron energy range into three groups.

Thermal energies (25 meV)

Measurements with thermal neutrons have been performed from the end of the 1930s [Amaldi1936, Frisch1938], i.e., only a few years after the neutron and the deuteron were discovered, until the late 1970s [Cox1965, Cokinos1977, and references therein]. The neutron sources utilized radionuclides (Ra/Be) or particle accelerators (spallation, (p,n) or (d,n) reactions). Liquids or solids containing hydrogen served at the same time as a target, in which the neutron capture occurred, and as a moderator, in which the neutrons were slowed down by elastic scattering. At room temperature ($T = 293$ K) such neutrons can be described by a Maxwell-Boltzmann distribution with a most probable velocity of about 2200 m/s, which is equivalent to a kinetic energy of 25 meV. At this energy the cross section is about 330 mb, which is rather high and thus easier to measure compared to the cross section at higher energies, see figure 2.6. Although the elastic scattering cross section of neutrons on protons is two orders of magnitude higher, this does not disturb these measurements, because the energy distribution of the thermalized neutrons is not changed. There was usually no angular sensitivity in these experiments and thus differential cross sections could not be determined. The different methods applied in these experiments, among them the

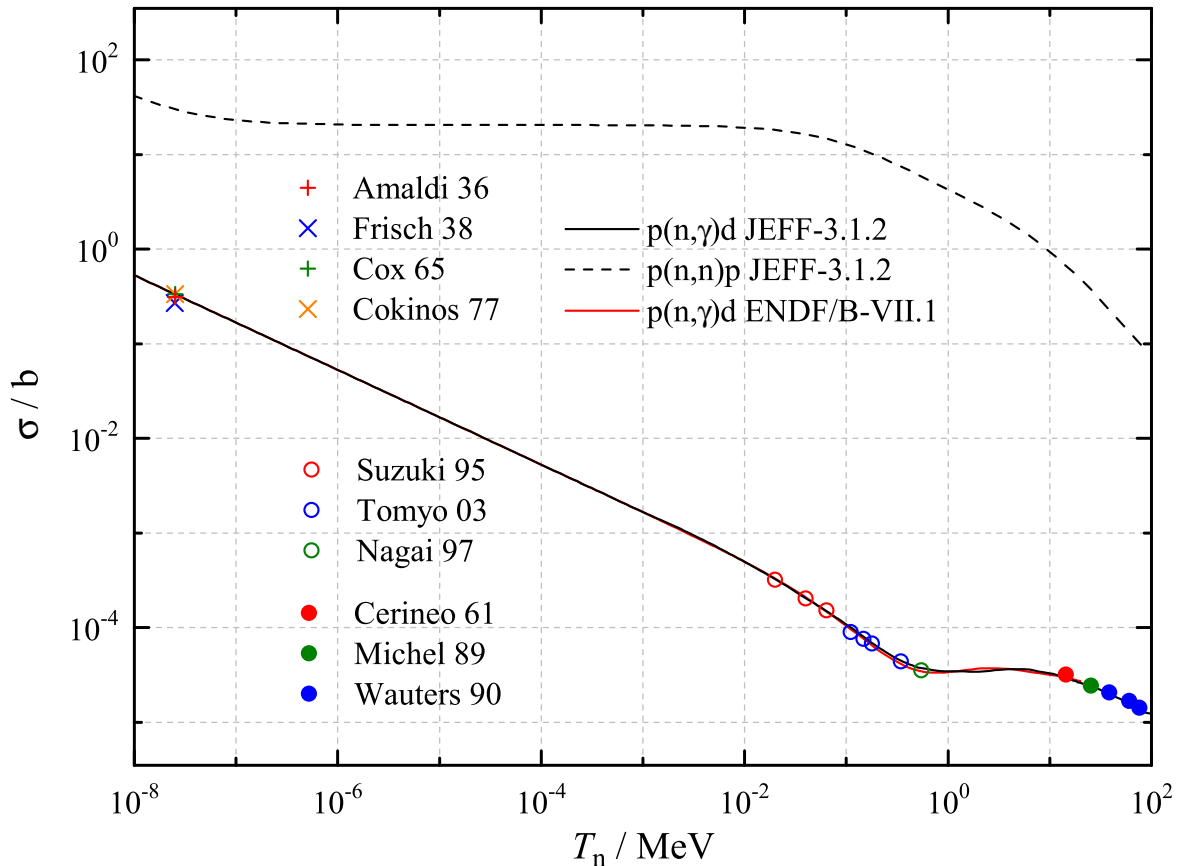


Figure 2.6: $p(n,\gamma)d$ cross section measurements (symbols) mentioned in the text compared to data evaluations (lines) of neutron capture and neutron elastic scattering on protons. Other $p(n,\gamma)d$ data evaluations are nearly identical to ENDF/B-VII.1 (ENDF/B-VII.0, ROSFOND-2010, JENDL-4.0u2) or JEFF-3.1.2 (JEFF-3.1.1, JEFF-3.0, ENDF/B-VI.8, ENDF/B-V.2, JENDL-3.3) [Nds]. At thermal energies and at $T_n > 14$ MeV there are more measurements of the $p(n,\gamma)d$ cross section than shown here.

measurement of spatial distribution, diffusion length or life time of the neutrons, are discussed in [Cox1965, Cokinos1977]. These later experiments achieved relative statistical uncertainties of about 0.2 % and had negligible systematic uncertainties.

High energies (> 14 MeV)

The general problem of measurements of the $p(n,\gamma)d$ cross section using non-thermalized neutrons is the competing elastic scattering of neutrons on protons. The $p(n,n)p$ cross section is between two and five orders of magnitude larger (see figure 2.6) and the loss of kinetic energy makes the capture of the neutron more probable. To determine the capture cross section and the neutron energy at which the capture occurred, the counting of the number of capture reactions has to be complemented by spectroscopic information of the ejected photon or the recoiling deuteron.

Capture experiments with neutrons in the MeV range benefit from the reaction kinematics. On the one hand, there are capture γ rays with energies $E_\gamma \approx 0.5 T_n + B_d$ that allow a discrimination of thermal-neutron capture events. Unfortunately, typical compact photon detectors are limited by their full-energy efficiency, which decreases above a few MeV. At higher energies large, electromagnetic calorimeters would be required. Because the capture γ rays are emitted at all laboratory angles, either a 4π detector or knowledge of the angular distribution is required to determine the cross section. On the other hand, the recoiling deuterons are moving in a forward cone of small aperture and have sufficient energy to apply spectroscopic and particle-discrimination methods like $\Delta E/E$ telescopes or the time-of-flight technique. Charged-particle detectors with high intrinsic efficiency allow using gaseous or thin solid targets of hydrogen-containing material. By this, both the moderation problem and the energy loss of the deuteron in the target were reduced. The identification of recoil protons is not only an effective background suppression, but at the same time serves as normalization without changing the setup. This helps to reduce systematic uncertainties, but also limits this method to energy ranges in which the elastic-scattering cross section is known with sufficient precision. Measurements of the neutron capture cross section based on the detection of the recoiling deuteron have been performed in the neutron energy range from 14.4 MeV to 76 MeV from the beginning of the 1960s [Cerineo1961] to the end of the 1980s [Michel1989, and references therein] [Wauters1990]. The relative statistical and systematic uncertainties achieved in the later experiments were below 2 % and in the range 2–5 %, respectively.

Differential capture cross sections, which do not cover all angles, have been determined in measurements at even higher energies up to several 100 MeV [Edwards1992, and references therein]. At these energies measurements complicate because the pionic neutron capture $n(p,\pi^0)d$ can become more probable than the radiative neutron capture and because the nearly exclusive decay of neutral pions into two photons has a very similar experimental signature. Using polarized neutrons or protons, asymmetries between different polarization states have been studied in this energy range [Xu1995], too, as well as at the other energetic extreme using cold neutrons [Gericke2011]. Angular distributions and polarization observables are discussed in detail in [Arenhoevel1991].

Big Bang energies

A measurement of the $p(n,\gamma)d$ cross section at energies relevant to Big Bang nucleosynthesis is very difficult. Until now, the Tokyo Institute of Technology (TIT) was the only facility, at which experiments at neutron energies between 10 and 600 keV were performed successfully. In the beginning, the $p(n,\gamma)d$ reaction served as a test case for a simulation code for multiple-scattering effects of neutrons between 10 and 80 keV in thick targets [Senoo1994]. Based on that, experimental results had been presented at a conference in 1994 for the energy range between 10 and 280 keV [Suzuki1995a], but in a following letter only cross sections at mean neutron energies of 20 keV, 40 keV and 64 keV were published, while a previously mentioned data point at 185 keV

was not included [Suzuki1995b]. Both publications are rather short and do not explain all analysis steps in detail. More information about the experimental technique and the data analysis as well as a new data point at a mean neutron energy of 550 keV was later published by [Nagai1997]. Finally, in 2002, four more data points in the energy range between 100 and 350 keV were presented on a conference poster [Tomyo2003].

The neutrons in these experiments were produced by the ${}^7\text{Li}(p,n){}^7\text{Be}$ reaction, which is described to some extent in chapter 4 about the efficiency calibration of neutron detectors. A comparison of selected parameters of this and other facilities can be found in appendix C. The protons were provided by a Pelletron in pulsed mode to apply time-of-flight (tof) methods. This allowed to characterize and monitor the neutron spectrum by a ${}^6\text{Li}$ -glass detector. The neutron energy width, which was taken as energy uncertainty, increased from 10 to 33 keV from the lowest to the highest neutron energy. Furthermore, the tof method allowed a separation of foreground and background by setting gates on the timing signals of the γ -ray detector. This detector was an anti-Compton spectrometer made of thallium-doped sodium iodide (NaI(Tl)) offering a good compromise between energy and time resolution. Knowing both observables accurately was crucial to discriminate the large amounts and different kinds of background signals. To keep the background signals at a moderate level, the NaI(Tl) had to be shielded against neutrons with borated paraffin or ${}^6\text{LiH}$ and against γ with lead. Without shielding, neutrons could reach the detector directly from the uncollimated production target or scattered from the sample, get captured inside the detector by ${}^{127}\text{I}$ and produce prompt γ rays and the β -unstable nuclide ${}^{128}\text{I}$. Furthermore, γ rays were produced in the Li target by the ${}^7\text{Li}(p,\gamma){}^8\text{Be}$ reaction (up to 17 MeV) and by the neutron capture reactions in parts of the shielding. Another problematic background source was the ${}^{12}\text{C}(n,\gamma){}^{13}\text{C}$ reaction in the polyethylene sample and in parts of the shielding, which can emit γ rays with energies similar to the $p(n,\gamma)d$ reaction at certain neutron energies.

Polyethylene samples with different thicknesses were used to study the effects of shielded incident neutrons and multiple-scattered neutrons as well as to study the validity of the Monte Carlo code [Senoo1994] calculating correction factors for these effects. Depending on neutron energy and sample thickness the correction factors varied between 1.1 and 6 for neutron multiple scattering and between 0.72 and 0.93 for incident-neutron shielding. Further correction factors for the absorption of photons in the sample and for the finite size of the sample were calculated by Monte Carlo codes, too. Gold, which has a well known neutron capture cross section, was used as normalization for the neutron yields. From the differential cross section at 125.3° , which was measured, the angle-integrated cross section was calculated assuming there were only dipole transitions.

The $p(n,\gamma)d$ cross sections measured at TIT and their uncertainties are shown in figure 2.7. The relative uncertainties are 5–10 % [Suzuki1995b], 7 % [Nagai1997], and 9–18 % [Tomyo2003]. Contributions to the uncertainties are the response function of the NaI(Tl) detector, the γ -ray yield statistics, the γ -ray yield low-energy extrapolation for Au, and the absolute cross section of Au, which is 3 % [Suzuki1995b, Nagai1997]. The published data imply, that in measurements at one energy with samples of different thickness the cross sections were combined by taking the simple average and that the variance was chosen as the larger value of the variance of the weighted mean and the weighted sample variance. Thereby the authors erroneously included systematic uncertainties of the normalization, which are equal for all sample thicknesses, and thus calculated a total uncertainty that is too low. The values from [Tomyo2003] had to be taken from the corresponding EXFOR data-base entry, because the authors neither offer any values nor discuss the uncertainties of their measurement.

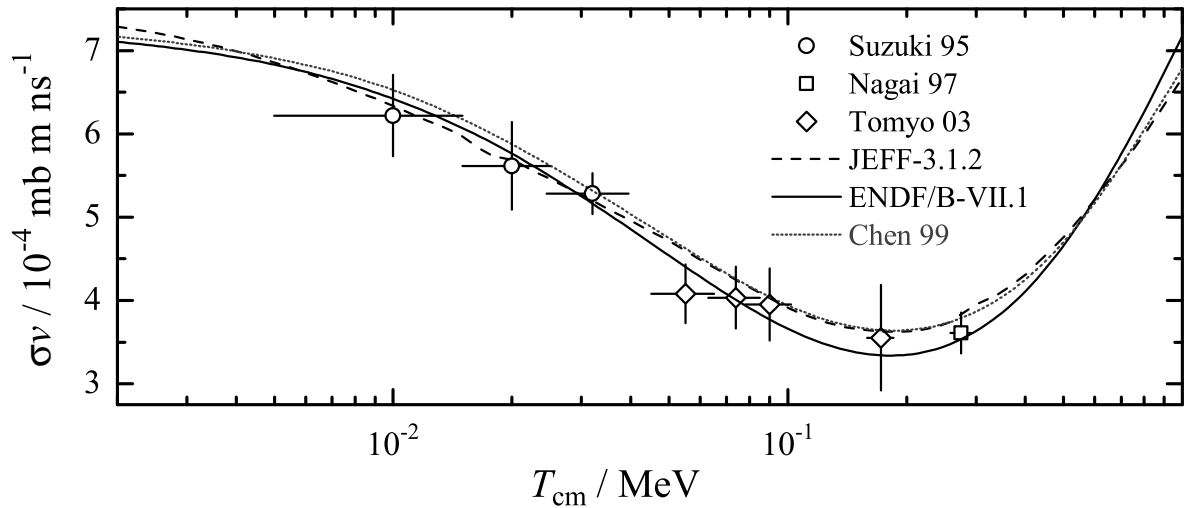


Figure 2.7: The product of cross section and neutron velocity σv , which is proportional to the reaction rate and nearly constant below 1 keV, is plotted for $p(n,\gamma)d$ cross section measurements at TIT (symbols), data evaluations (solid and dashed black splines) [Nds], and a cross section calculation (dotted gray spline). There are further, nearly identical $p(n,\gamma)d$ data evaluations (see caption of figure 2.6). The calculation is normalized to the thermal value of $(7.352 \pm 0.011) \times 10^{-4} \text{ mb m ns}^{-1}$ taken from [Cox1965]. The uncertainty of σv does not include the uncertainty of v , but only the published uncertainty of σ . The energy uncertainty of [Tomyo2003] is an interpolation between the other two measurements.

Recent developments

Feasibility studies for a measurement of the $p(n,\gamma)d$ cross section have been recently carried out at Los Alamos Neutron Science Center (LANSCE) and University of Kentucky (UKY) [Daub2012]. The spallation neutron source at LANSCE produced neutrons with energies up to 800 MeV, while the Van de Graaff accelerator at UKY produced neutrons via the ${}^7\text{Li}(p,n){}^7\text{Be}$ reaction (see appendix C for details). The neutron flux was measured by a uranium fission chamber at LANSCE and by elastic n - p scattering at UKY. A BC-418 plastic scintillator with known light response to low-energy protons [Daub2013] was read out on two sides by each one PMT and used as an active target for the $p(n,\gamma)d$ reaction. Time and energy of the γ rays have been measured by detectors made of cerium-doped lanthanum bromide ($\text{LaBr}_3(\text{Ce})$) or bismuth germanate (BGO). Although it has the worse energy resolution, the BGO detector gave better results due to its higher efficiency. Only by cuts on the neutron *tof*, the deuteron recoil energy, the γ -ray *tof*, and the γ -ray energy it was possible to extract a small signal. The conclusion of the studies is that a measurement using the setup tested at LANSCE is not feasible due to the large background of high-energy neutrons, while it would need one month of beam time and more detectors at UKY to reach a statistical uncertainty of 5 % at $T_n = (425 \pm 25) \text{ keV}$.

A similar experiment planned at the neutron time-of-flight facility at ELBE (nELBE) was part of the project, which also proposed the experimental work of this dissertation [Junghans2007]. At the moment, a $p(n,\gamma)d$ experiment at nELBE is not pursued anymore due to limited neutron beam intensity available with the current thermionic injector. There are also plans to study the $p(n,\gamma)d$ reaction at the recently developed neutron source FRANZ [Reifarth2009], which is designed for small target samples by producing a high neutron flux with energies up to 500 keV via the ${}^7\text{Li}(p,n){}^7\text{Be}$ reaction (see appendix C for details).

2.7 Previous measurements of the $d(\gamma,n)p$ cross section

In this section, $d(\gamma,n)p$ experiments in the energy range relevant to Big Bang nucleosynthesis (BBN) as well as advantages and disadvantages of experimental methods at γ -ray energies below 20 MeV shall be discussed. It is not a complete review of all experiments but rather a compilation of pioneering and the most precise experiments.

Data of the reviewed experiments are plotted in figures 2.8 and 2.9. For comparison, these figures also include $p(n,\gamma)d$ data that has been converted with equation (2.14) (principle of detailed balance), theoretical curves, and data evaluations. Surprisingly, the ENDF/B-VII.1 evaluations of the $d(\gamma,n)p$ and $p(n,\gamma)d$ data do not fulfill the principle of detailed balance, see figure 2.8. Reviews of the $d(\gamma,n)p$ cross section at higher energies can be found in [Arenhoevel1991, Jenkins1994].

Experiments with decay radiation

The $d(\gamma,n)p$ cross section was estimated for the first time in an experiment that studied the “nuclear photo-effect“ to measure the binding energy of the deuteron and thus to determine the neutron mass [Chadwick1935]. In this absolute measurement of the total cross section an ionization chamber, which was filled with deuterium gas and which detected protons with almost 100 % efficiency, was irradiated with 2.62 MeV γ rays from a radiothorium¹ source of known activity. Based on this method, many experiments with different γ -ray sources, targets (heavy water), detection methods for protons (e.g., cloud chambers, proportional counters) or neutrons (e.g. activation, BF₃ counter) followed [Collie1950, Snell1950]. Measurements of the angular distribution were independent of absolute normalization and detection efficiency. This allowed a more accurate determination of the ratio of σ_{MI}/σ [Bishop1951, Smit1987]. Besides ²⁰⁸Tl (2.62 MeV), the nuclides ⁷²Ga (2.51 MeV) and ²⁴Na (2.76 MeV) emit γ rays close above the $d(\gamma,n)p$ threshold, but their half-life is only 14 h and 15 h, respectively. The total cross sections of [Bishop1950] measured at that energies have later been revised due to corrections of the source calibration and reached a precision of 2–3 % [Marin1954, McMurray1955]. By using γ rays from proton-induced reactions, total cross sections have been measured in the range 4.45–17.6 MeV with a precision of 5–12 % [Barnes1952]. The main advantage of monoenergetic γ rays is that there is no need to measure the energy of the reaction products. A problem is the lack of suitable γ -ray sources and their calibration.

A different approach that allows the absolute determination of the total $d(\gamma,n)p$ cross section without knowing the absolute flux or the detection efficiency is the *photon absorption method*, in which the transmission of photons through samples of normal and heavy water is compared. The $d(\gamma,n)p$ cross section is less than 1 % of the atomic cross section and therefore the samples are rather long (1 m – 2 m). The small difference in the atomic interaction of photons with normal and heavy water must be corrected based on assumptions or atomic data. The precision of the sample-length determination, the target purity, and the counting statistics limit the overall precision. An early measurement with γ rays from ²⁰⁸Tl (2.62 MeV) reached a precision of 15 % [Colgate1951]. This improved in later experiments at research reactors with γ rays from neutron-induced reactions (5.97–11.4 MeV, 1–4 %) [Birenbaum1985] or ²⁴Na (2.76 MeV, 3 %) [Moreh1989].

¹ The 2.62 MeV γ ray is emitted after the β^- decay of ²⁰⁸Tl, which is a decay product of ²²⁸Th. The historic names of these nuclides of the thorium series are thorium C'' (ThC'') and radiothorium (RdTh).

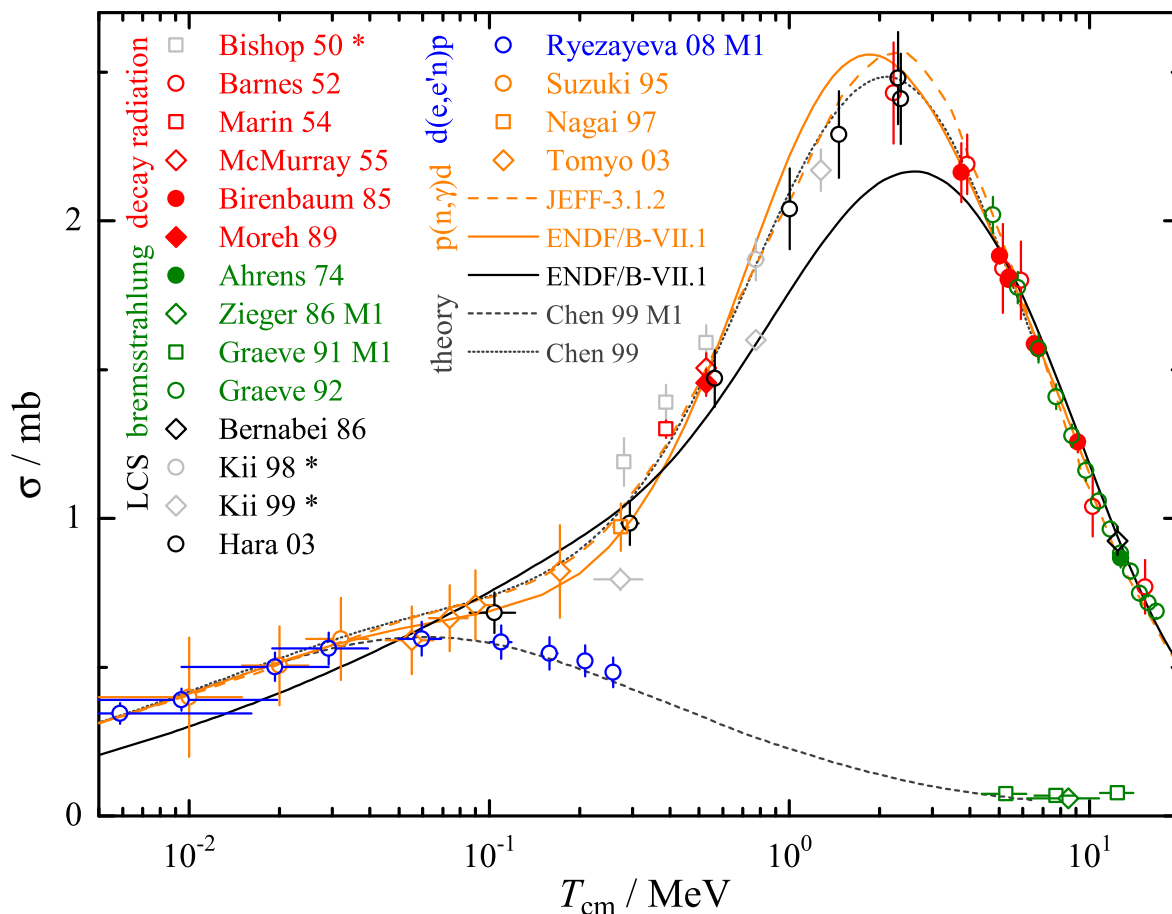


Figure 2.8: Absolute $d(\gamma,n)p$ cross section measurements (symbols) mentioned in the text compared to data evaluations (orange and black splines) and cross section calculations (dark gray splines). Similar experiments share the same symbol color (see legend), except for those known to have some problems (light gray symbols, marked with * in the legend, see text for explanations). Full symbols denote photon absorption measurements. Measured or evaluated $p(n,\gamma)d$ data (orange) has been converted with equation (2.14) (principle of detailed balance). There are further, nearly identical $p(n,\gamma)d$ data evaluations (see caption of figure 2.6) and one more $d(\gamma,n)p$ data evaluations (ENDF/B-VII.0), which is identical to ENDF/B-VII.1 [Nds].

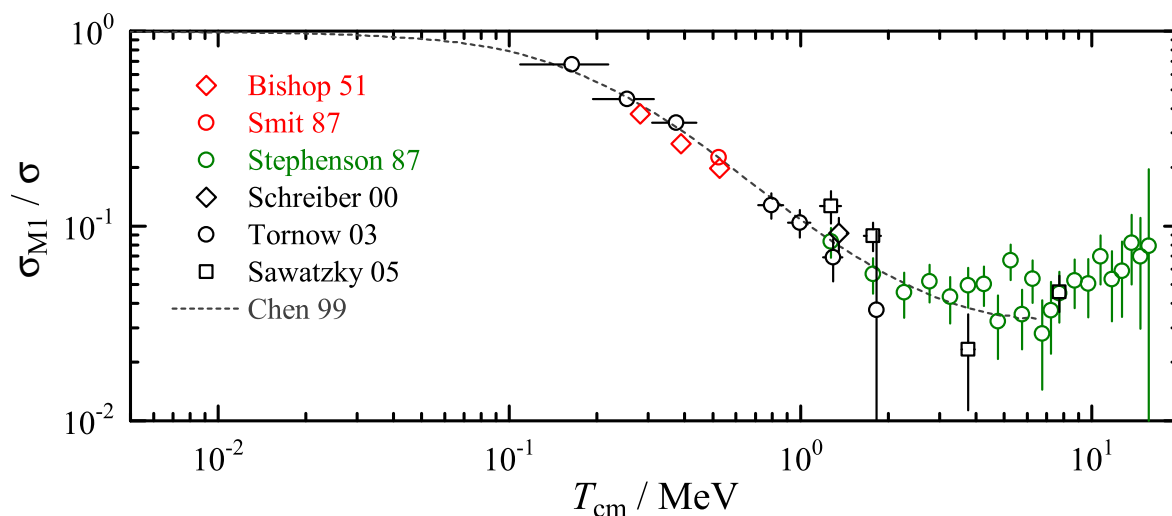


Figure 2.9: Measurements of the relative M1 contribution to the $d(\gamma,n)p$ cross section (symbols) mentioned in the text compared to a cross section calculation (spline). The colors are explained in the legend of figure 2.8.

Bremsstrahlung

Photons from electron bremsstrahlung have a continuous energy spectrum from zero to a maximum energy. Thus, a wide energy range can be covered, but an energy measurement is necessary. For absolute measurements both the shape and the normalization of the spectrum are needed. In many experiments the shape is calculated, but especially near the maximum energy different bremsstrahlung models can have large differences, see section 3.2.4.

The photon absorption method mentioned before is independent of shape and flux normalization. Using this method and a magnetic Compton spectrometer to measure the photon energy, the absolute $d(\gamma,n)p$ cross sections was determined at a photon energy of 15 MeV with uncertainties of 3 % (statistical) and 2 % (systematic, dominated by target composition) [Ahrens1974]. The Compton cross section can also serve as normalization. The differential cross section at 0° , which is proportional to σ_{MI} (see equation (2.16)), was determined in a photon energy interval 8.4–13.4 MeV with a precision of 20 % by detecting photoprotons and Compton electrons from a thin deuterated polyethylene (CD_2) foil in a magnetic spectrometer, whose acceptance was simulated [Zieger1986]. Using the same method, but an ionization chamber for the photon flux normalization, the total cross section at photon energies between 7 and 19 MeV has been determined with a precision of 3 % from measurements of the differential cross sections at 0° , 90° , and 180° [Graeve1991, Graeve1992]. If pulsed bremsstrahlung can be produced, then the energy of the photoneutrons can be determined by the time-of-flight method. In thick targets, multiple scattering of neutrons has to be taken into account and can be corrected with the help of Monte Carlo simulations. If the detection efficiency of the neutron detectors is unknown, only relative angular distributions can be determined. For example, the cross sections at 45° , 135° , and 155° were measured relative to 90° with this method using a 3 mm thick CD_2 target in the photon energy range 4–18 MeV with a typical precision of 2–5 % [Stephenson1987].

For *tof* measurements of photoneutrons from the $d(\gamma,n)p$ reaction close to the threshold, detectors with low threshold, good time resolution, and high efficiency are necessary. A characterization of scintillation detectors made of different materials showed that compared to lithium glass, zinc sulfide, lithium borate, or barium fluoride only plastic fulfills all these requirements [Beyer2005]. A part of that detector characterization was a feasibility study of an absolute $d(\gamma,n)p$ cross section measurement in the photon energy range 3–5 MeV with pulsed bremsstrahlung at ELBE, in which nuclear resonance fluorescence on ^{11}B was used as photon flux normalization. On the basis of that work and a proposal [Junghans2007] resulting from it, the experiment carried out in this dissertation was planned, see section 3.

The $d(\gamma,n)p$ reaction has also been used to study the shape and the endpoint of the ELBE bremsstrahlung spectrum and the degree of polarization by detecting photoprotons from a thin CD_2 foil [Schwengner2005, Rusev2006, Erhard2009, Nair2009]. At energies relevant to BBN a large background due to photon scattering and electron production in the CD_2 foil was observed.

In connection with bremsstrahlung two methods are to be mentioned that provide quasi-monoenergetic photons: *positron annihilation in flight* and *tagged bremsstrahlung*. Both methods are reviewed in [Arenhoevel1991, pp. 51–57], but they have not been used to study the $d(\gamma,n)p$ reaction at energies relevant to BBN, yet. Below 10 MeV, positron annihilation in flight suffers from too small currents of available positron sources [Leicht1981]. The bremsstrahlung photon tagger NEPTUN was recently developed at the Superconducting Darmstadt Linear electron Accelerator (S-DALINAC) to provide tagged photons with an energy resolution of less than 50 keV in the photon energy range 5–20 MeV [Schnorrenberger2014], but in principle NEPTUN should be able to reach the $d(\gamma,n)p$ threshold.

Laser-Compton scattering (LCS)

Photons scattered from electrons can either lose (Compton scattering) or gain (inverse Compton scattering) energy. Inverse Compton scattering can be used to produce polarized quasi-monoenergetic photons at energies interesting for nuclear physics by scattering laser light on high-energetic electrons [Arenhoeve1991, pp. 55–65]. The photon energy can be tuned by changing the energy of the laser light (typically a few eV), the total electron energy (typically several 100 MeV) or the scattering angle. Therefore, the energy resolution of the LCS photon beam depends on the energy resolution of the electron beam and the collimation of the LCS photon beam.

Using the LCS γ -ray source in Frascati called LADON, a deuterium gas target, a liquid scintillator as a 4π detector for photoprotons and a NaI(Tl) detector to measure the photon flux, the absolute $d(\gamma,n)p$ cross section was determined with an energy resolution of 400 keV at a photon energy of 15 MeV with uncertainties of 2 % (statistical) and 5 % (systematic) [Bernabei1986]. The efficiencies of both detectors used have been simulated.

Measurements of the absolute $d(\gamma,n)p$ cross section have been performed close to the threshold at the LCS γ -ray source of the National Institute of Advanced Industrial Science and Technology (AIST) in Tsukuba. In a first approach, photoprotons were detected in a time projection chamber [Kii2005], which was filled with deuterium gas, and the photon flux was determined with a BGO detector. Cross sections at γ -ray energies of 2.5 MeV, 3.0 MeV and 3.5 MeV have been measured with an energy resolution of 50 keV and uncertainties of 2–5 %. These results and experimental details are not easily accessible (one preliminary data point was published in a conference proceeding [Kii1998] and three data points can be extracted from a PhD thesis written in Japanese language [Kii1999]) and are hardly noticed by the scientific community. Both publications are in disagreement and are even not mentioned in publications of related experiments, in which the same co-authors were involved [Tomyo2003, Hara2003], and thus its quality must be regarded critically. In a later experiment at the LCS γ -ray source at AIST, photoneutrons from a heavy-water target were detected by ^3He detectors embedded in a polyethylene moderator, while a NaI(Tl) detector measured the photon flux [Hara2003]. Although a moderator was used, it was possible to reject background signals by using the *tof* method. Cross sections have been measured with uncertainties of 1–8 % (statistical) and 6 % (systematic) at seven γ -ray energies between 2.33 and 4.58 MeV with a relative energy uncertainty of 1–2 %. Until today, no other absolute $d(\gamma,n)p$ cross section measurement was closer to the threshold.

Polarized photons from the High-Intensity Gamma-ray Source (HIGS) located in Durham have been used for several experiments to study the angular distribution (azimuthal and polar) of photoneutrons from the $d(\bar{\gamma},n)p$ reaction. From that, the relative M1 contribution to the total $d(\gamma,n)p$ cross section can be determined. To measure the azimuthal neutron asymmetry, each two liquid scintillators with pulse-shape-discrimination capabilities have been positioned in the γ -ray polarization plane and perpendicular to it. A C_6D_{12} scintillator served as an active target, which allowed *tof*-based background discrimination. The finite geometry and multiple neutron scattering in the target were corrected using simulations. At a photon energy of 3.58 MeV and a neutron polar angle of 150° a precision of 20 % was reached [Schreiber2000]. A follow-up experiment measured at seven energies from 2.39 to 4.05 MeV and a neutron polar angle of 90° reaching 3 % total uncertainty at the lowest energy [Tornow2003]. In both experiments the photon energy resolution was less than 3 %. The validity of these results was questioned after an experiment, which used a large array of 88 liquid scintillators to measure 11 polar angles from 22.5 to 157.5° and 8 azimuthal angles simultaneously, found an unexpected large forward-backward asymmetry [Sawatzky2005], but this finding could not be confirmed later in a more precise HIGS experiment [Ahmed2008]. The measurement of [Sawatzky2005] used LCS γ rays of 3.5 MeV, 4 MeV, 6 MeV, and 10 MeV, active C_6D_{12} , and passive D_2O targets, while detection efficiencies and scattering of neutrons in the target or from one detector to the other were simulated. Although an absolute $d(\gamma,n)p$ cross

section measurement was aimed for, none of the available flux monitors turned out to be reliable enough. In measurements of other reactions at higher energies at HIGS, the $d(\gamma,n)p$ cross section has been used as normalization [Perdue2011].

Other methods

An experiment in Osaka demonstrated that the shape of the M1 contribution of the $d(\gamma,n)p$ cross section close to the threshold can be deduced with a very low energy resolution of 800 keV from the *charge-exchange spin-flip reaction* $d(^7\text{Li}, ^7\text{Be})$ [Nakayama2005].

In contrast to experiments with real photons from decay radiation, bremsstrahlung, or LCS, the $d(\gamma,n)p$ reaction can also be studied using virtual photons. The virtual-photon theory has been tested by comparing the *electrodisintegration* of the deuteron $d(e,e'n)p$ and the photodissociation, e.g., by comparing the neutron yields from both reactions in the energy range 4–11 MeV [Phenneger1974]. The only electrodisintegration measurement relevant to BBN was performed at S-DALINAC [Ryezayeva2006, Ryezayeva2008]. Two settings with an initial electron energy of 28 MeV (74 MeV) allowed a deuteron excitation energy up to 4 MeV (7 MeV) with a resolution of 45 keV (140 keV). The electrons were backscattered from thin CD_2 foils and detected at 180° in a magnetic spectrometer. This data was normalized either by the collected electron charge or by structure functions of the elastic scattering cross section. Based on the latter method, the two energy settings, which were consistent for excitation energies below 3 MeV, were combined to deduce absolute M1 cross sections of the $d(\gamma,n)p$ reaction. The result are nine data points at photon energies between 2.23 and 2.49 MeV with uncertainties of 10 keV (energy) and 10 % (cross section).

In *Coulomb dissociation* experiments, virtual photons from the Coulomb field of a high-Z material are used as target and thus reactions can be measured in inverse kinematics [Baur1986]. Ion beams (even of radioactive nuclei) with energies up to several 100 MeV per nucleon can be used to study reactions at *cm* energies of down to 100 keV. On the one hand, such kinematic conditions allow an efficient detection of the reaction products, which have rather high energy and are strongly focused in beam direction in the *lab* frame. On the other hand, the *cm* energy resolution of a few hundred keV is usually worse than in experiments in normal kinematics. It is an experimental challenge that the *cm* energy can only be calculated, if the kinematic quantities of incoming beam and outgoing reaction products have been determined completely. A fundamental difficulty is the disentangling of dissociations due to Coulomb interaction, nuclear interaction, and the interference of both. A calculation of these contributions for the reaction $^{208}\text{Pb}(d,pn)^{208}\text{Pb}$ can be found in [Bertulani1988, p. 349]. Although the Coulomb breakup of the deuteron was studied close to the threshold [Baur1976, Okamura1994], so far no absolute $d(\gamma,n)p$ cross section has been determined at BBN energies using this method. At the heavy-ion research center (GSI) in Darmstadt, deuteron dissociation reactions have been used to study properties of the large-area neutron detector (LAND) [Blaich1993] and its successor called NeuLAND [R3b2011].

3 Photodissociation measurement at ELBE

The absolute measurement of the $d(\gamma,n)p$ cross section at ELBE was planned on the basis of the feasibility study [Beyer2005] discussed on page 22 and a proposal [Junghans2007] resulting from it. The principle ideas of

- a measurement over a wide energy range using **pulsed bremsstrahlung**,
- a thick target made of **deuterated polyethylene**,
- a photon flux determination using **nuclear resonance fluorescence**,
- and an energy determination using **neutron time-of-flight detectors** with low detection threshold and well known efficiency

were maintained and further developed to get closer to the reaction threshold and to reach a total uncertainty of about 5 %.

3.1 Experimental setup

Electron accelerator ELBE

The *Electron Linac for beams with high Brilliance and low Emittance* (ELBE) is located at Helmholtz-Zentrum Dresden-Rossendorf (HZDR) and is in operation since 2001. The layout of ELBE is shown in figure 3.1. The electron beam is mainly used to generate secondary radiation such as coherent infrared radiation from free-electron lasers, (unpolarized or partially polarized) bremsstrahlung up to 20 MeV, neutrons in the energy range from about 10 keV to 10 MeV (at the neutron time-of-flight facility nELBE), and monoenergetic positrons. In the past, a quasi-monochromatic X-ray source based on electron channeling was available and there are plans to offer coherent terahertz radiation in the future. Together with high-power lasers used for particle acceleration and laser-electron interaction, ELBE forms the *Center for High-Power Radiation Sources*. Apart from the variety of secondary radiation, the main features of ELBE are the high average power and the excellent time structure of the beam [Elbe2013].

At ELBE, electrons are accelerated in standing-wave radio-frequency (rf) cavities, which are made of superconducting niobium and are cooled by superfluid helium to temperatures of 1.8 K. Each of the two cryomodules houses two nine-cell cavities and allows an electron acceleration up to 20 MeV. Normal-conducting rf cavities made of copper have small duty cycles in the % range because much power is dissipated into heat due to ohmic losses. The superconducting technology used at ELBE allows a nearly complete conversion of rf energy into kinetic projectile energy and thus a free adjustment of the time structure and a high duty cycle up to 100 % [Gabriel2000].

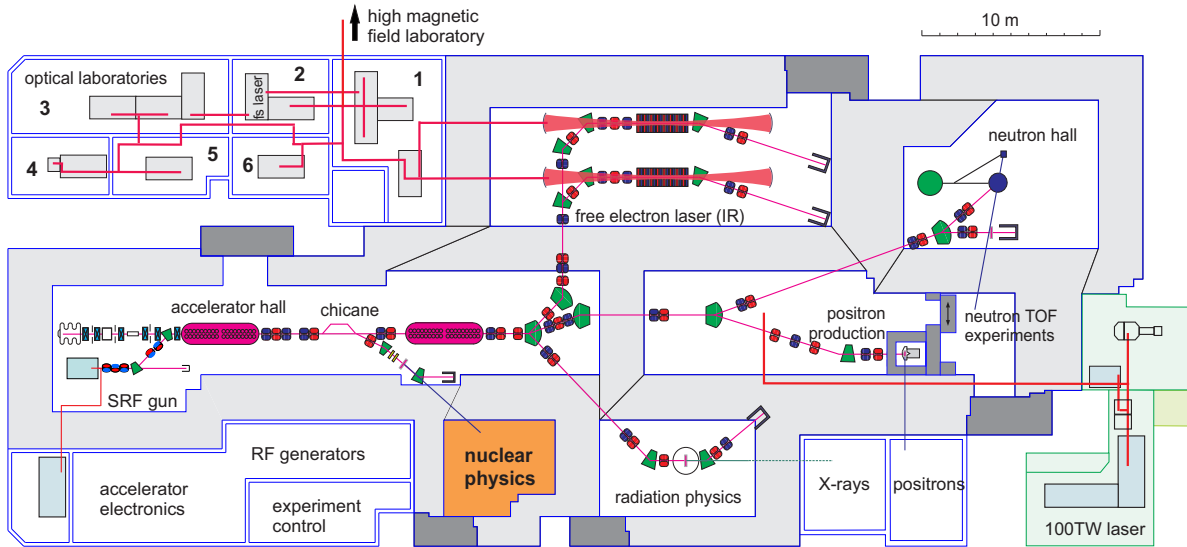


Figure 3.1: Layout (top view) of the radiation source ELBE in 2010. The $d(\gamma,n)p$ reaction was measured in the bremsstrahlung facility, which is labeled with “nuclear physics” in the figure. Figure by courtesy of H. Büttig, HZDR.

The cavities are operated at a radio frequency of 1.3 GHz, but the time structure of the beam is defined in the electron injector. It consists of a thermionic electron source, a buncher system, a macro-pulse generator, and beam optics. In the source, electrons are extracted from a thermionic cathode and are electrostatically accelerated to an energy of 250 keV. Bunches with a length of about 500 ps and a charge of up to 77 pC are formed by a subsequent grid that is modulated with high-voltage pulses of a variable micro-pulse frequency between 100 kHz and 260 MHz. After passing two bunchers, electron bunches with a length of a few ps enter the first cavity. After the first cryomodule there is a magnetic chicane, which can be used for further bunch compression or to reduce the energy spread of the beam. Selected ELBE parameters and their values in the $d(\gamma,n)p$ experiment are summarized in table 3.1.

Table 3.1: Range of selected parameters [Gabriel2000, Teichert2003, Elbe2013] of the Electron Linac for beams with high Brilliance and low Emittance (ELBE) and specific values of the $d(\gamma,n)p$ experiment. The bremsstrahlung facility uses electrons from the first cryomodule accelerated up to 20 MeV while all other experiments use electrons accelerated in both cryomodules up to 40 MeV. The micro-pulse frequency can either be 260 MHz or $26 \text{ MHz} / 2^n$ ($0 \leq n \leq 8, n \in \mathbb{N}$). In the $d(\gamma,n)p$ measurement the continuous-wave (cw) mode with its duty cycle of 100 % was used, which can be reduced in the macro-pulse mode.

parameter	symbol	ELBE	$d(\gamma,n)p$	unit
kinetic electron energy	T_e	5 – 40		5 MeV
energy resolution (FWHM)		35 – 55		≈ 50 keV
micro-pulse frequency	f_{acc}	0.1 – 260		1.625 MHz
micro-pulse period	$t_{\text{acc}} = f_{\text{acc}}^{-1}$	$3.8 - 10^4$		615 ns
bunch length		2 – 5		≈ 2 ps
bunch charge		0.10 – 77		≈ 50 pC
current		< 1000		$\approx 80 \mu\text{A}$
power		< 25		0.6 kW
macro-pulse frequency		1 – 25		- Hz
macro-pulse length		0.1 – 36		- ms

Bremsstrahlung facility

At the bremsstrahlung facility at ELBE a variety of photon-induced experiments have been carried out in the past, see table 3.2. Technical details of the facility are discussed extensively in [Schwengner2005, Rusev2006]. So far, the only experiment at the facility, in which neutrons have been detected, was the feasibility study for this work [Beyer2005].

To produce bremsstrahlung, the ELBE beam can be deflected out of the main beam line after the first cryomodule and the chicane using two dipole magnets and a quadrupole magnet between the dipoles. Further beam optics are a doublet of quadrupole magnets and a doublet of dipole magnets used to focus the beam on a radiator and to steer the angle between beam and radiator, respectively. With the steerer magnets, it would be possible to produce partly polarized photon beams using off-axis bremsstrahlung. The thin radiator foil made of niobium, the production of bremsstrahlung, and also the measurement of the electron energy are described in section 3.2. As shown in figure 3.2, the radiator is followed by a purging magnet that deflects the all electrons that have not interacted with the thin foil into a beam dump.

The bremsstrahlung photons created in the foil pass the magnet unaffected and enter the photon beam line. A 3 mm thick quartz window separates the vacuum in the electron beam line (10^{-10} mbar) from the vacuum in the photon beam line (10^{-6} mbar). It is followed by a device that can move 10 cm thick metal cylinders into the beam to attenuate low-energy photons (beam hardener made of aluminum, which was not used here) or the whole beam (beam shutter). The photons leave the accelerator hall through a collimator in the 1.6 m thick heavy-concrete wall and enter the experimental area. The collimator is mainly made from aluminum to avoid neutron production. It starts 972 mm behind the radiator and is 2600 mm long. The diameter of the collimator

Table 3.2: Selected experiments carried out at the ELBE bremsstrahlung facility.

photon scattering	$^{92,98,100}\text{Mo}(\gamma, \gamma')$	[Schwengner2005, Rusev2006]
	$^{136}\text{Ba}(\gamma, \gamma')$	[Massarczyk2012]
	$^{86}\text{Kr}(\gamma, \gamma')$	[Schwengner2013a]
photo-activation	$^{92}\text{Mo}(\gamma, n/\alpha), ^{144}\text{Sm}(\gamma, n/p/\alpha)$	[Nair2009, Erhard2009]
photodissociation	$d(\gamma, n)p$	[Beyer2005]
photo-fission	$^{238}\text{U}(\gamma, ff)$	[Kosev2007]
positron spectroscopy	(γ, e^+e^-)	[Wagner2013a]

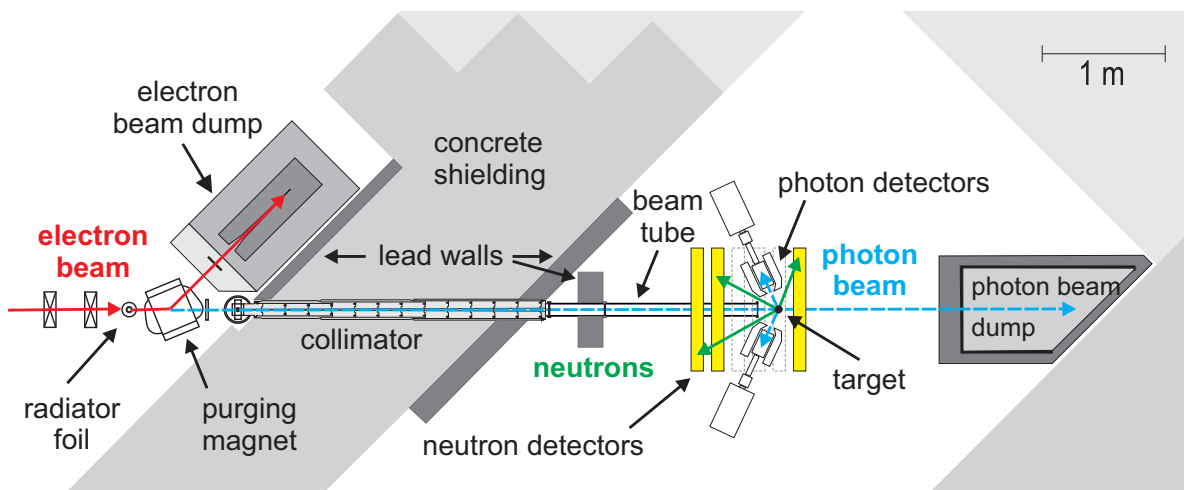


Figure 3.2: Layout (top view) of the $d(\gamma,n)p$ setup at ELBE. Three of the six neutron detectors are indicated by dashed rectangles to see the underlying setup parts.

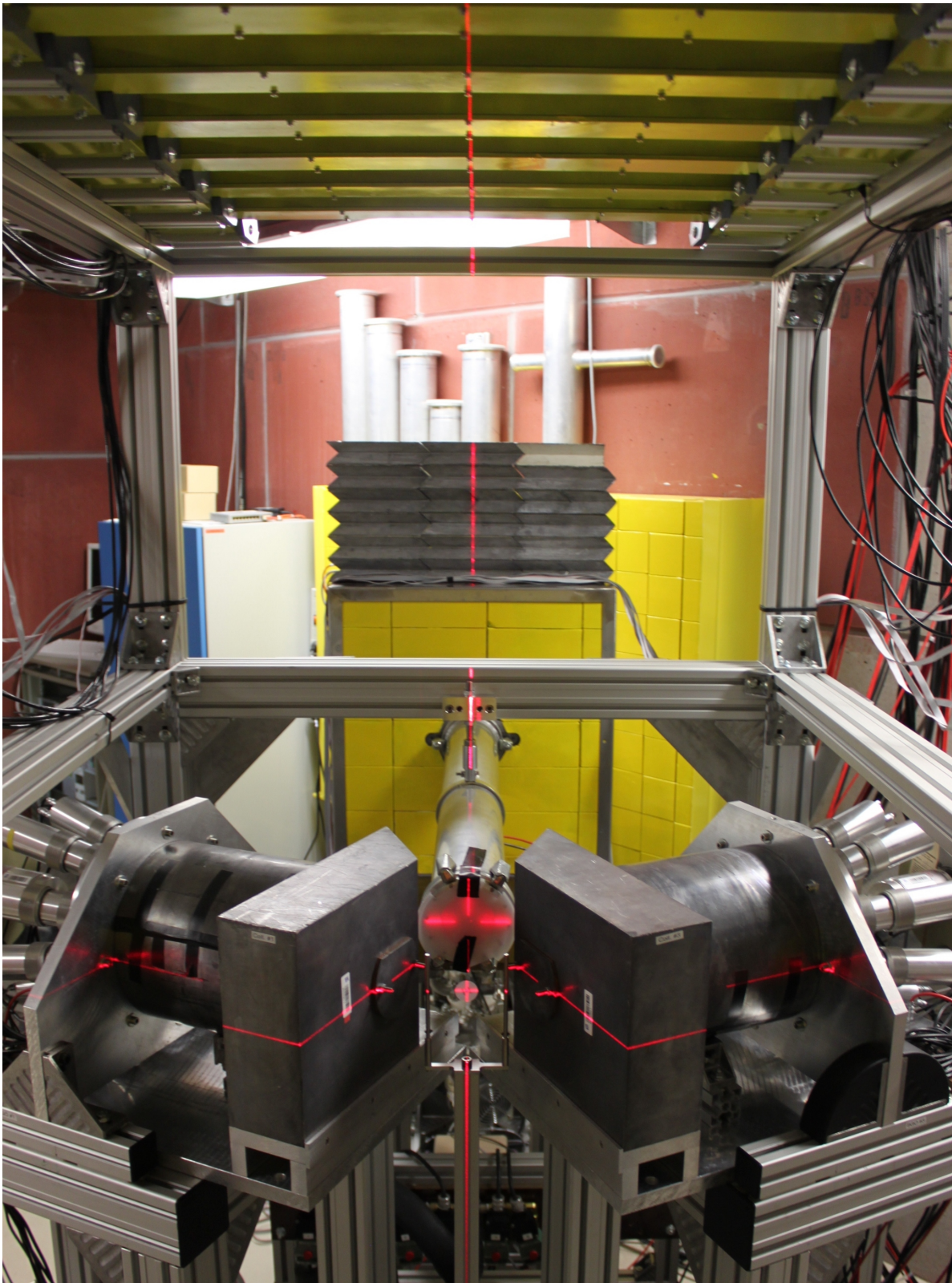


Figure 3.3: Setup of the $d(\gamma,n)p$ experiment at ELBE. The camera was placed close to the photon beam dump approximately 0.5 m directly above the beam axis and looked in opposite beam direction. The six neutron and two photon detectors can be seen in the upper and lower part, respectively. The red laser lines helped to adjust the positions of detectors and target. In this picture, the titanium window of the beam tube is covered and the target is replaced by a radioactive source.

opening is 5 mm at the entrance and 24 mm at the exit. Thus, the opening angle between the radiator center and the collimator entrance is 5.1 mrad and between the entrance and the exit of the collimator it is 7.3 mrad. A cross section of the collimator is also shown later in figure 3.10.

The collimator exit is connected to a polarization monitor, which is based on the $d(\gamma,n)p$ reaction (see page 22) and which has not been used in this work for the following reasons: First, it was tried to avoid polarization by proper beam adjustments. Second, it would be an additional neutron source. And last, there is too much background in the detectors of the polarization monitor to determine such a low endpoint energy of a bremsstrahlung spectrum of about 5 MeV.

The target position is about 2.1 m behind the collimator exit and about 5.7 m behind the radiator. An evacuated aluminum beam tube ends about 25 cm before the target position and is sealed with a 25 μm thick titanium window, see figures 3.3 and 3.4. The distances from the photon beam axis to the floor and the ceiling are 1.4 m and 2.2 m, respectively.

Finally, the bremsstrahlung beam enters a photon beam dump starting 1.3 m behind the target position and ending at a heavy-concrete wall, see figures 3.2 and 3.5. The photons are stopped in a large polyethylene block with a 60 cm \times 60 cm sized front face and a base with the shape of right trapezoid with 0.7 m and 1.3 m long parallel sides. Except for the entrance hole, the block is surrounded by 0.5 mm thick cadmium sheets to absorb neutrons and a lead shield with a thickness of 10 cm (20 cm at the front face) to absorb γ rays. The entrance hole has cylindrical shape with a diameter of 12 cm and length of 39 cm measured from the front face of the lead shield.

Permanently installed lead walls on both sides of the heavy-concrete wall between accelerator hall and experimental area shield the setup from radiation created in the electron beam dump. Scattered photons created near the collimator exit or in the polarization monitor are shielded by a 20 cm thick lead wall with a 60 cm \times 60 cm sized front face, which is permanently installed about 60 cm behind the collimator exit. In the $d(\gamma,n)p$ measurement, such photons were also detected in the neutron detectors by their time of flight, so the wall was raised with a 60 cm wide, 10 cm thick, and 30 cm high wall made of lead bricks to shield the neutron detectors, too, see figure 3.3.

A spirit level and a self-leveling cross-line laser, which is shown in the figures 3.3, 3.4 (laser lines), and 3.5 (device), has been used to align target and detectors to each other and to the beam line. The width of the laser lines was about 2 mm. Because of their wide opening angle, the laser lines continued to the walls and the floor, where markings have been set. Distances between the markings have then been measured with steel rulers and angles have been calculated from the distances.

Target

The target consisted of alternating layers of aluminum and deuterated polyethylene (CD_2). It had cylindrical shape with a diameter and a total thickness of about 20 mm, which was smaller than the beam diameter (see section 3.2.3). The target production and the choice of the materials and their masses are discussed in section 3.3 in detail. The choice of materials also influenced the choice of some ELBE parameters listed in table 3.1. ^{13}C , which amounts naturally to about 1 % of the carbon in the CD_2 , has a neutron separation energy of 4.95 MeV. To avoid photoneutrons from that nuclide, an electron energy of about 5 MeV was used, which is the lower limit for the ELBE electron beam diagnostics. As ^{27}Al is used for the photon flux determination, the aluminum beam hardener could not be used.

The target and the target holder are shown in figure 3.4. The holder consisted of two steel poles with 5 mm diameter screwed to a 5 mm thick steel plate located about 10 cm below the beam axis. It was mounted on top of an 125 cm long, 30 mm thick, quadratic aluminum strut profile. At its bottom, the profile was connected to a metal disc with three, height-adjustable feet. A thin nylon string connected to the steel poles formed a cross at the target position, where the target or radioactive sources have been clamped.

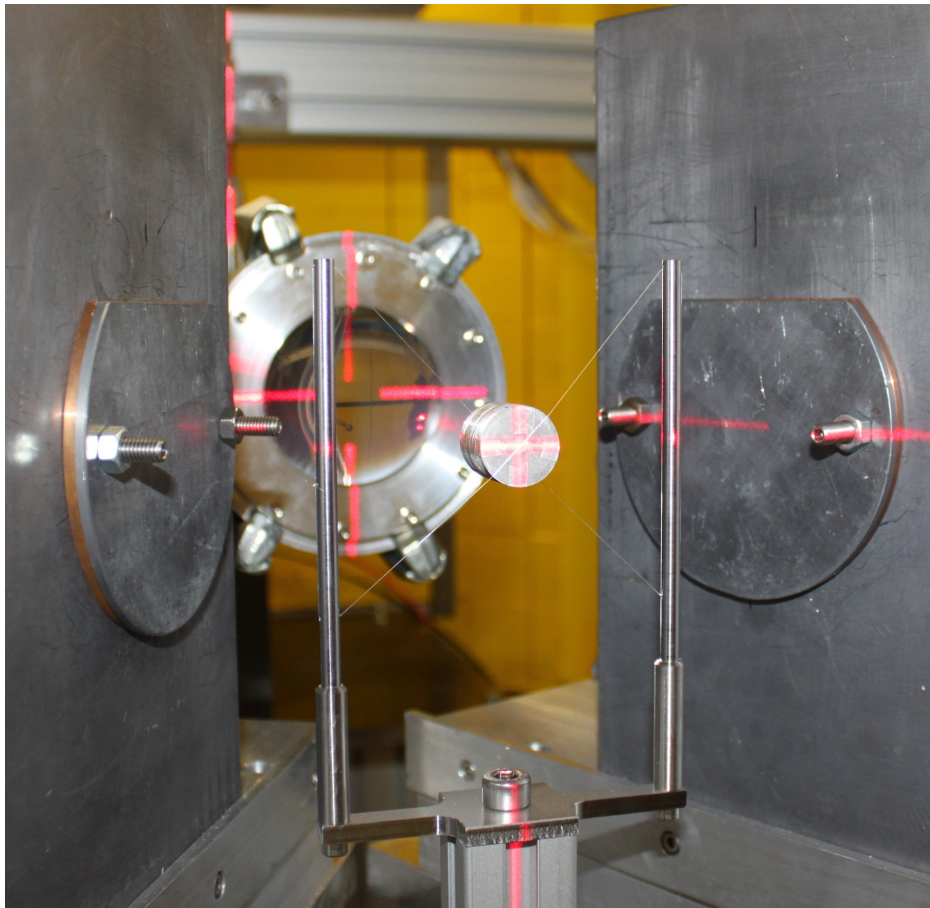


Figure 3.4: Target and target holder. In the background the beam tube sealed with the titanium window is shown. The red laser lines have been used for alignment.

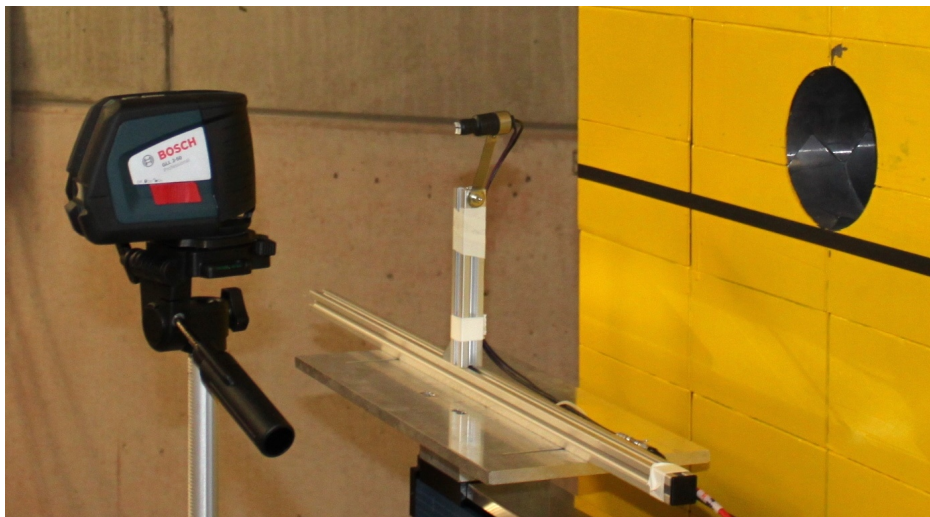


Figure 3.5: Self-leveling cross-line laser used for alignment (removed before experiment), movable scintillation detector, and photon beam dump (from left to right).

Photon detectors

Approximately 1.1 m behind the target position and 0.2 m before the photon beam dump a small scintillation detector was installed that could be moved remote-controlled in the plane perpendicular to the beam axis, see figure 3.5. Beam profiles measured with this detector are discussed in section 3.2.3.

For the photon flux determination two n-type high-purity germanium (HPGe) detectors with a relative efficiency² of about 100 % have been used, which were routinely used in many experiments at the bremsstrahlung facility, e.g., in those mentioned in table 3.2. The HPGe crystal is surrounded by scintillation detectors made of bismuth germanate (BGO) working as an escape suppression. Both the HPGe and the BGO are encased in aluminum³ separately. Passive shielding is realized by a 10 cm thick lead collimator between the target position and the HPGe crystal and by a 2 cm thick radial lead shield surrounding the BGO detector array. The collimator hole has a conical shape with diameters of 50 mm at the detector side and 34 mm at the target side. At the latter, it was covered by one copper disk and one lead disk of each 3 mm thickness to reduce the beam-on background. A computer model of the detector geometry is shown later in figure 3.22.

The two detectors have been positioned horizontal to the photon beam axis at polar angles of 115° and a distance of 245 mm between the centers of HPGe detector surface and target, see figures 3.2 and 3.3. The distance between target center and collimator front was 91.2 mm. To increase the geometric efficiency, the smallest possible distance was chosen, at which no flight path from the target to the neutron detectors was blocked by the shielding. To minimize the background from Compton-scattered photons from the target, the largest possible polar angles were chosen, at which the frames of the two detectors just began to block each other. Unfortunately, only after the $d(\gamma,n)p$ experiment a misalignment of one HPGe detector was recognized, which was related to a shifted reference point at the detector frame. In the result, the axis of this detector did not cross the photon beam axis at the target center but 5 mm behind.

As seen in table 3.1, the ELBE electron bunch charge was only 65 % of its maximum. This was done to keep the total count rates of the HPGe detectors, which are difficult to estimate precisely before the experiment, at a level at which pile-up of signals is unproblematic. Using the full intensity of ELBE would have allowed the same count rates at a target–detector distance increased to 300 mm and would have lead a reduction of the problem of neutron scattering at matter close to the CD₂ target (compare section 5).

The photon flux determination is discussed in section 3.4, which includes measurements and simulations of the efficiency of the HPGe detectors and the analysis of the measured spectra.

Neutron detectors

The neutrons from the $d(\gamma,n)p$ reaction were detected in six plastic scintillators that have been placed above the beam axis. The neutron energy was determined by the time-of-flight (tof) method. The detectors have originally been build for experiments at the neutron tof facility at ELBE (nELBE) [Beyer2005]. Their construction and their properties are reviewed and discussed in section 3.5, followed by the data analysis of the neutron spectra and the efficiency determination.

In direction of the beam (z -axis), the detectors were 42 mm wide and the center of the detectors numbered with i ($1 \leq i \leq 6$) was positioned at $z = (i - 2) \times 176$ mm with respect to the target position at $x = y = z = 0$. In direction of the other axis in the horizontal plane (x -axis) the detectors were 1000 mm long and centered at $x = 0$. In the vertical direction (y -axis), the detectors 1–4 were 11 mm thick, the detectors 5 and 6 were 2×11 mm thick (two scintillators combined), and the position of the detector center was at $y = (1001.5 \pm 1.0)$ mm, which is still 1.2 m below the ceiling. Each scintillator was read out by two photomultiplier tubes (PMTs) at $x = \pm 500$ mm. This allows a low neutron detection threshold and a position-sensitive measurement along the x -axis. Each detector was surrounded by a 10 mm thick lead shield to absorb bremsstrahlung photons that have been Compton-scattered in the target and ambient γ rays.

² Photopeak efficiency at 1.333 MeV relative to a 3" × 3" cylindrical NaI(Tl) detector [Knoll1999, p. 450].

³ There is no resonant absorption of NRF transitions from the target in the aluminum casing (see section 3.4.1). A nuclear excitation of aluminum nuclei in the casing is very unlikely because the flux of suitable high-energy photons is strongly suppressed due to kinematics and shielding.

The flight path $l = (x^2 + y^2 + z^2)^{0.5}$ between target and the six detectors was between 1.0 and 1.35 m and the polar angle in the lab frame $\vartheta = \arccos(z/l)$ was between 80° and 125° , see figure 2.2. While the differential $d(\gamma,n)p$ cross section given by equation (2.16) has its maximum at 90° , there is a lower background from photons that have been Compton-scattered in the target at larger angles. The vertical distance between beam axis and detectors was a compromise between energy resolution (compare section 3.5.3) and statistical uncertainty. To minimize the effect of neutron scattering between adjacent detectors the distance between them was chosen based on experiences from experiments at nELBE. The maximum neutron *tof*, which can be calculated from the flight path and the detection threshold of the detectors, determined the ELBE micro-pulse frequency of 1.625 MHz (see table 3.1) that had to be used to avoid the detection of neutrons from the previous pulse.

Setup development

Some alternative approaches have been tested before the setup developed into the form described above. In experiments with separated target positions for CD_2 and aluminum, two problems had to be faced. First, it turned out to be difficult to align the targets with the same diameter on the beam axis with sufficient precision. Second, the target that was hit by the beam first caused a high background at detectors close to the other target position coming behind. One solution would have been a setup, in which the photon flux is measured at a first target position using close photon detectors followed by a second CD_2 target in sufficient distance and far neutron detectors. In the bremsstrahlung facility this was hard to realize due to limited space. In retrospect (compare section 5), this solution also seems favorable regarding the problem of neutron scattering at matter close to the CD_2 target, e.g., at the lead collimators of the HPGe detectors. A “naked“ HPGe detector (without BGO detectors and lead shield) has been used in the feasibility study [Beyer2005] and has been tested for this setup again, but here suffered from the large background at the second target position.

3.2 Production of bremsstrahlung

As described in section 3.1, the bremsstrahlung is produced when the electron beam passes a thin radiator foil. In general, an ideal radiator has a high atomic number, which gives a high production cross section (compare equation 3.1), and a high melting point to cope with the thermal load. The thicker the radiator, the higher the photon yield, but the higher the probability for multiple interactions and small-angle scattering of electrons, which can lead to deviations from the calculated spectral shape.

The radiator foils at the ELBE bremsstrahlung facility are made of niobium and are described in detail in [Schwengner2005]. Niobium is a metal with a medium atomic number ($Z = 41$) and a high melting point of over $2400^\circ C$. The radiator foils have a diameter of 16 mm. Six foils with areal densities of 1.7, 2.6, 3.4, 4.3, 6.0, and 10.6 mg cm^{-2} , which correspond to thicknesses between 2.0 and $12.4 \mu\text{m}$ and about $2\text{--}10 \times 10^{-4}$ radiation lengths, are mounted in a movable, water-cooled holder integrated in the evacuated electron beam line. In the $d(\gamma,n)p$ experiment the thickest radiator has been used to maximize the photon flux. Even if the electron bunch charge had been increased to its maximum (compare table 3.1), the second-thickest radiator would have produced a less intense photon beam.

For the absolute measurement of the $d(\gamma,n)p$ cross section, knowledge of the endpoint energy, the shape, and the normalization of the bremsstrahlung spectrum is required. The endpoint energy, i.e., the electron energy, must be measured to calculate the spectral shape. Both is discussed in this section together with the geometric shape of the photon beam and its stability. The normalization is discussed later in section 3.4.

3.2.1 Measurement of the electron energy

The kinetic electron energy T_e was measured with a precision spectrometer, that was added to the ELBE beam diagnostics only a few weeks before the $d(\gamma,n)p$ experiment. Earlier, less precise methods to determine T_e used the polarization monitor (see pages 22 and 29) [Erhard2009] or the dipole magnet of the ELBE beam line [Lehnert2007, Nair2009]. The lowest observed neutron time of flight can also be used to estimate T_e (compare figure 3.26). The basic components of the spectrometer, which is shown in figure 3.6 and is discussed in detail in [Rudolph2012], are

- an entrance slit, which transform the extended beam approximately to a point source,
- a dipole magnet, which has a very good field homogeneity as well as a long-term-stable power supply and whose field profile was measured precisely,
- a screen made of yttrium aluminum garnet (YAG) placed in the focal plane,
- and a CCD camera, which is shielded against radiation and views the screen using a mirror.

By using the 90° Browne-Buechner geometry [Browne1956] the spectrometer can perform energy measurements, which are independent of the spot position on the screen, the transverse offset of the entrance slit, or the entrance angle of the beam, if the exact field strength is known. The expected overall energy resolution is $< 1 \times 10^{-4}$ and the energy spread accuracy 4×10^{-3} .

During the $d(\gamma,n)p$ experiment at ELBE, five measurements of the electron energy have been performed by the operators of the accelerator. The spectrometer software calculated the energy distribution from the spatial intensity distribution on the screen and from the magnetic field, which was measured with a hall probe. The spectra are shown in figure 3.7 and corresponding parameters are listed in table 3.3. The peak width in the spectra is lower than the energy resolution of the

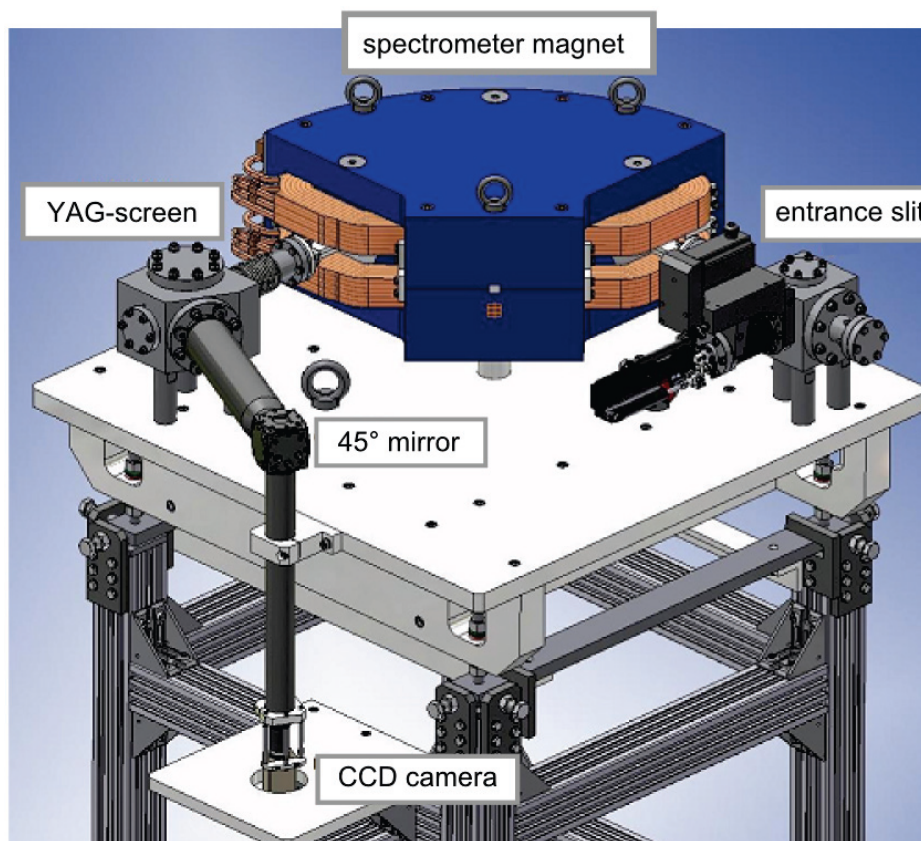


Figure 3.6: Technical drawing of the electron spectrometer. Figure taken from [Rudolph2012].

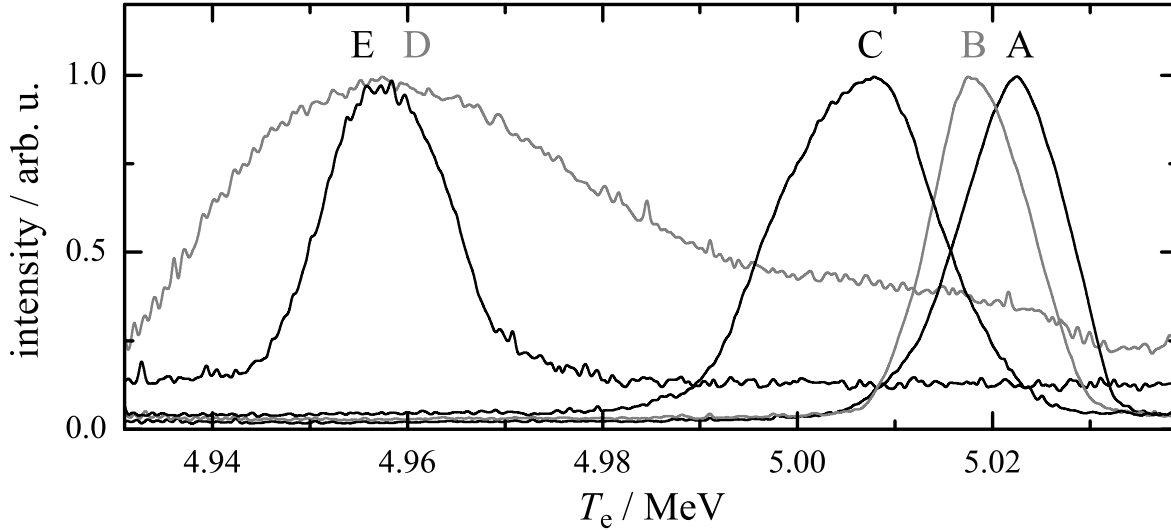


Figure 3.7: Measured spectra of the electron energy (labeled from A to E). See table 3.3 for the corresponding parameters. Except for measurement D, in which the slit was wide open to search for the peak, parameters were obtained from gaussian fits of the peaks. For comparison, the maximum intensity of each measurement was normalized to 1 in this figure.

Table 3.3: Parameters of the measurements with the electron spectrometer. The first column refers to the labels in figure 3.7. The fit uncertainties were below 0.1 keV.

	date, time	entrance slit		magnetic	gaussian fit	
		center (mm)	width (mm)	field (mT)	mean (MeV)	FWHM (keV)
A	08.06.2010 16:03	0.4	4.3	56.1	5.022	13
B	09.06.2010 15:32	0.0	2.0	56.1	5.019	12
C	10.06.2010 15:45	-0.2	3.5	56.2	5.006	19
D	14.06.2010 09:58	0.4	19.3	56.2	(no fit)	(≈ 50)
E	14.06.2010 10:06	-5.7	2.5	56.2	4.958	15

electron beam of about 50 keV, if the width of entrance slit is reduced. The mean electron energy obtained by a Gaussian fit of the measured peaks has a negligible uncertainty of less than 0.1 keV, but due to the obvious drift of the mean value, its uncertainty over the whole measurement time will be much larger. Assuming a linear drift between the measurements B and E results in a drift rate of about -13 keV per day. Because the analyzed data was mainly recorded in this period, its mean value of 4.988 MeV and its uncertainty of $61 \text{ keV} / \sqrt{12} = 18 \text{ keV}$ are used in the following.

3.2.2 Stability of the electron beam

In addition to the precision measurements with the electron spectrometer, the stability of the energy and the intensity of the beam has also been monitored. The electron energy depended on the acceleration gradients of the cavities (first cavity: constant at 3.378 kV m^{-1} , second cavity: variable), the cathode voltage ($\approx 250 \text{ kV}$), and the phase between the cavities. ELBE has an automatic energy stabilization, which is based on beam position measurements before and after the dipole magnet deflecting the beam into the photon beam line. The stability of the beam intensity at ELBE is less important for the $d(\gamma,n)p$ experiment, as the data from neutron and photon detectors are accumulated over the same period. However, it was important that the count rates became neither too high (problems: dead time, pile up) nor too low (problem: higher statistical uncertainty). Accelerator parameters and detector count rates, which have been logged during the whole experiment in intervals of 5–15 s, are shown in figures 3.8 and 3.9.

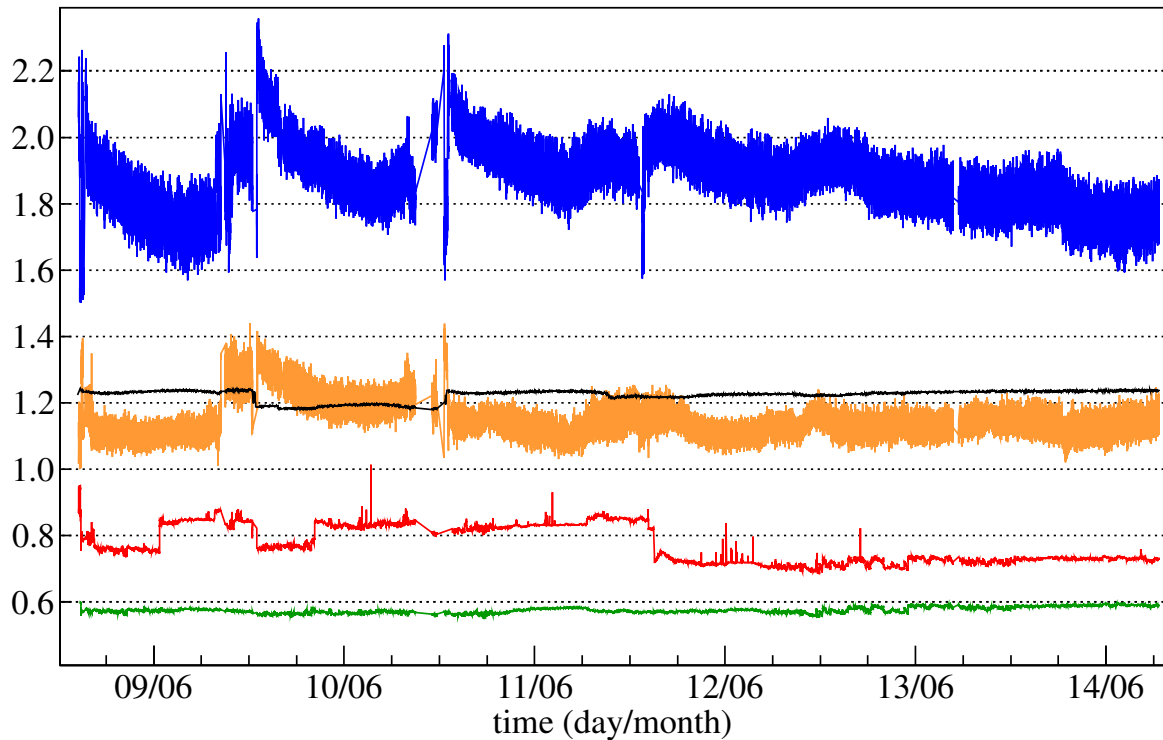


Figure 3.8: Accelerator parameters logged during the $d(\gamma,n)p$ experiment. The orange and the blue curve are the x - and y -coordinates (in mm) measured by a beam position monitor in the main beam line before the dipole magnet. The current (in $100 \mu\text{A}$) measured at this beam position monitor and at the cathode are shown in green and red, respectively, whereas the cathode measurement suffers from some artifacts in the offset determination (sharp steps). Although the acceleration gradient of the second cavity is not constant (black curve, in kV m^{-1}), the total kinetic electron energy was kept stable (see text and figure 3.7).

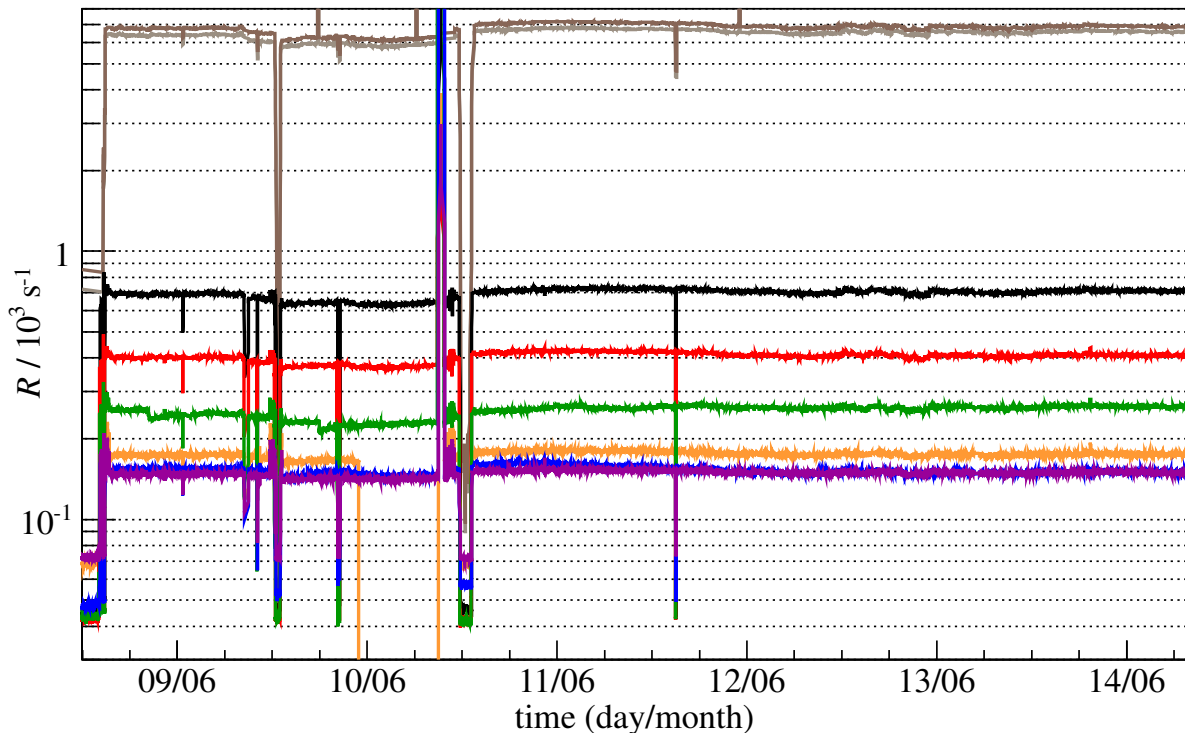


Figure 3.9: Detectors rates logged during the $d(\gamma,n)p$ experiment. The brown curves are from the two HPGe detectors. The black, red, green, blue, orange, and magenta curves are (in that order) from the neutron detectors 1–6. Except for short beam failures and beam tuning periods, which were excluded from the data analysis, the stability was very good.

3.2.3 Size and position of the photon beam

The size of the photon beam at the target position is an important criterion for the target design. In previous measurements and simulations of the beam intensity profile along the horizontal x -axis, a symmetric distribution with a flat plateau for $|x| < 10$ mm has been found close to the target position [Rusev2006, p. 20]. Increasing the target radius above that value would require a very good target homogeneity, but would not increase the reaction rate significantly and would deteriorate the energy resolution of the neutron time-of-flight measurement. Decreasing the target radius would either decrease the reaction rate or require a longer target, which makes larger corrections of the HPGe detector efficiency necessary, see figure 3.23.

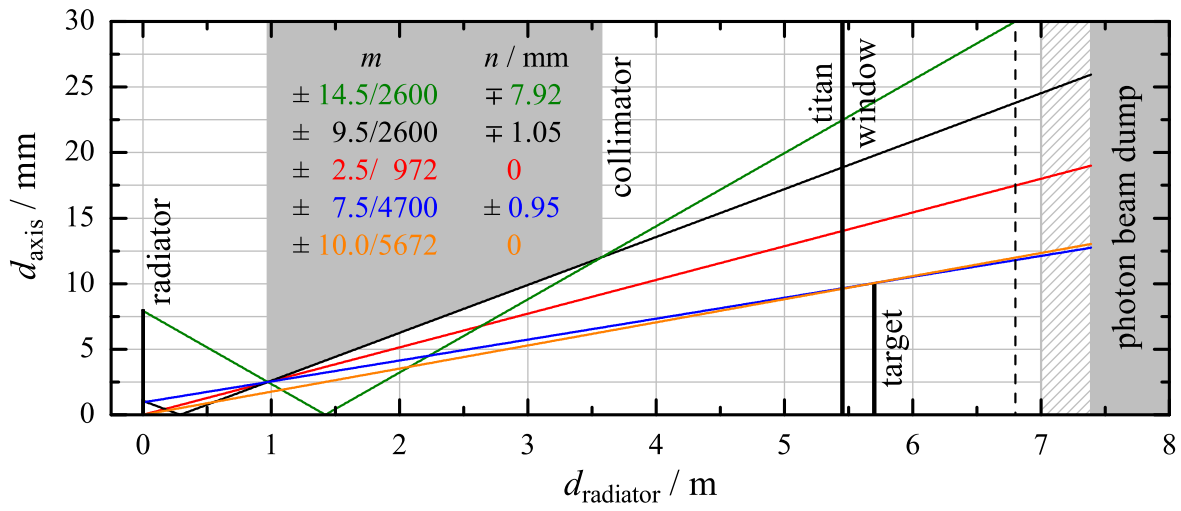


Figure 3.10: The distance from the beam axis d_{axis} is plotted as a function of the distance to the radiator d_{radiator} for five geometrically possible photon envelopes (colored lines). Each envelope consists of two linear functions $d_{\text{axis}} = m d_{\text{radiator}} + n$ calculated with the parameters given in the figure (upper or lower sign). Because of the cylinder symmetry, the part with $d_{\text{axis}} < 0$ is not shown. The position of the beam profile measurements is indicated by the dashed line. The hatched area is the entrance hole of the photon beam dump.

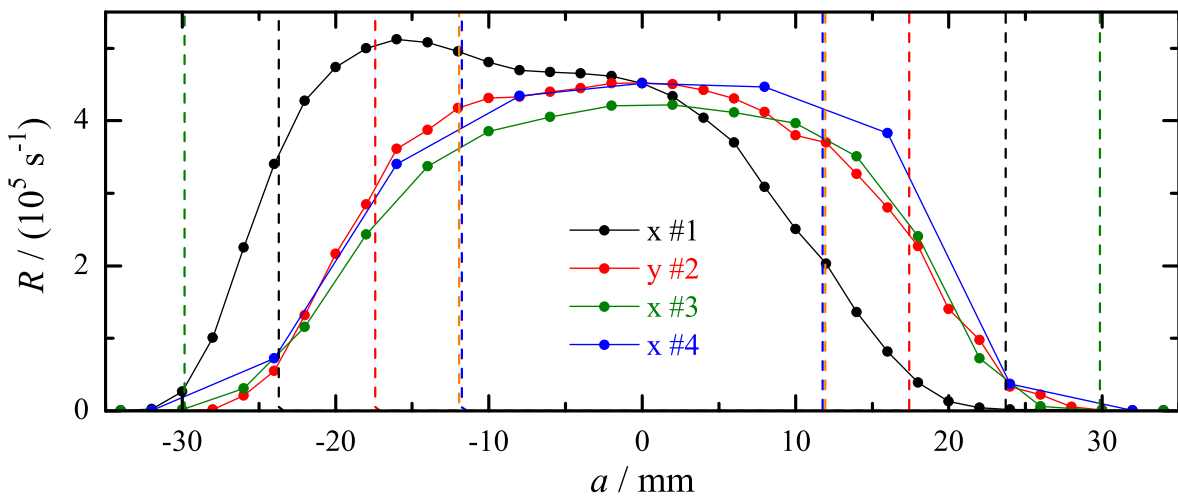


Figure 3.11: Measurement of the count rate R of a small scintillation detector (10 mm diameter) as a function of the detector position a on the x -axis ($y = 0$, black, green, and blue points) or the y -axis ($x = 0$, red points). The dashed vertical lines indicate the size of the beam envelopes from figure 3.10.

The position of the bremsstrahlung beam should be optimal if the electron beam hits the radiator foil perpendicular at its center. The diameter of the electron beam spot on the radiator is typically 2 mm. The paths that bremsstrahlung photons can take are confined by the geometry of the setup as described in section 3.1, especially by the entrance and the exit of the collimator. Figure 3.10 shows the photon beam size for five geometrically possible photon envelopes. For the electron beam size given above, the photons, which reach the target position with $|d_{\text{axis}}| < 10$ mm, are not blocked by the collimator.

The correct position of the photon beam was verified by measurements. Approximately 1.1 m behind the target position (and thus approximately 6.8 m behind the radiator) a small scintillation detector was installed that could be moved remote-controlled in the xy -plane perpendicular to the beam axis, see figure 3.5. The small size (≈ 10 mm diameter and length) and the fast decay time of the scintillator combined with a fast data acquisition allowed to measure count rates up to $5 \times 10^5 \text{ s}^{-1}$. At each position the count rate was measured for 5 s. Four beam profiles are shown in figure 3.11 and their parameters are listed in table 3.4. If the profile was too asymmetric (measurement #1), the operators of the accelerator were asked to change the position of the electron beam on the radiator foil. The y -profiles were very stable, but the optimization of the x -profiles needed more effort because the deflecting magnets in the electron beam line affect mainly the horizontal beam position.

The beam profile measurements took place behind the target, which influenced the beam in two ways: First, the beam intensity was attenuated by about 10–20 % depending on the photon energy (see section 3.4.1), and second, the beam was effectively widened by photons scattered out of the beam. The attenuation is visible in measurement #1 in figure 3.11, in which the beam center was shifted and the flat plateau turned into a step. In the other beam profile measurements the plateau was fully covered by the photon beam envelopes, which just touched the target edges (blue and orange dashed lines in figure 3.11).

Table 3.4: Parameters of the photon-beam profile measurements #1 - #4 shown in figure 3.11. The position of the electron beam on the radiator foil was changed until a symmetric profile (weighted mean $\bar{a} = \Sigma(aR)/\Sigma(R) \lesssim 1$ mm) could be measured.

#	date, time	x	y	\bar{a} / mm
1	09.06.2010 13:15	scan	0	-7.1
2	09.06.2010 14:00	0	scan	-0.9
3	09.06.2010 15:00	scan	0	-0.3
4	10.06.2010 13:00	scan	0	0.0

3.2.4 Calculation of the photon energy distribution

The production of bremsstrahlung is a process well defined in quantum electrodynamics. Typically, an incoming fast electron (charge number $z = 1$) is slowed in the coulomb field of an atomic nucleus (atomic number Z) and a bremsstrahlung photon is emitted. Electron-electron bremsstrahlung contributes only to a much smaller extend. The calculation of the bremsstrahlung cross section is complicated by the fact that the Dirac equation cannot be solved in closed form for an electron in a Coulomb field [Koch1959]. In the energy range of some MeV to several tens of MeV typically a Born approximation formula is used with a correction for the screening of the field of the nucleus by atomic electrons and with approximative wave functions in the Coulomb field (Coulomb correction). Reviews of bremsstrahlung cross section calculations are given by [Koch1959, Haug2004a].

The differential cross section for the creation of a bremsstrahlung with an energy E_γ in a thin target by an electron having the total energy E_0 can be calculated [Schiff1951] by

$$\frac{d\sigma}{dE_\gamma} = \frac{2\alpha Z^2 r_e^2}{E_\gamma} \left[\left(\frac{E_0^2 + E_e^2}{E_0^2} - \frac{2E_e}{3E_0} \right) \left(\ln M + 1 - \frac{2}{b} \arctan b \right) + \frac{E_e}{E_0} \left(\frac{2}{b^2} \ln(1+b^2) + \frac{4}{3} \frac{2-b^2}{b^3} \arctan b - \frac{8}{3b^2} + \frac{2}{9} \right) \right] \quad (3.1)$$

$$M = \left[\left(\frac{m_e E_\gamma}{2E_0 E_e} \right)^2 + \frac{Z^{2/3}}{C^2} \right]^{-1} \quad b = \frac{2E_0 E_e Z^{1/3}}{C m_e E_\gamma}.$$

Here, $E_e = E_0 - E_\gamma$ is the total energy of the electron after the photon is created and $C = 111$ is a screening constant. The numerical values used for the fine-structure constant α , the classical electron radius r_e , and the electron mass m_e can be found in appendix A. The shape of the bremsstrahlung spectrum of the $d(\gamma,n)p$ experiment was calculated with $Z = 41$ (niobium radiator) and $E_0 = m_e + 4.988$ MeV.

In figure 3.12, the analytic formula (3.1) is compared to the tabulated results of the calculation by [Seltzer1986] and to the result of a numerical computer program [Haug2004b] based on a calculation by [Haug2008]. Close to the endpoint the spectrum is most difficult to describe. The formula by [Schiff1951], e.g., predicts photons with $E_\gamma > E_0$. The three approaches differ by 3–10 % over the most relevant photon energy range 2–4 MeV and show even larger deviations closer to the endpoint energy. However, as the spectral distributions are normalized using the measured photon

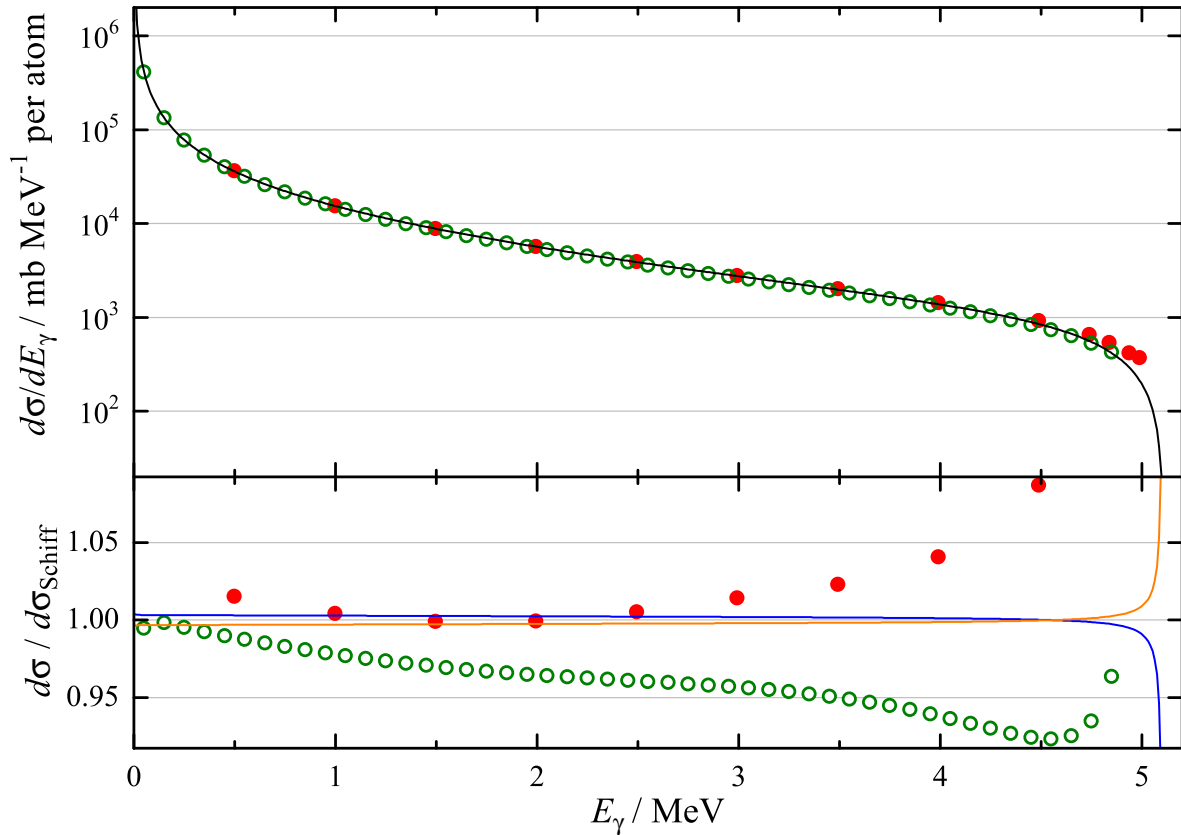


Figure 3.12: The upper panel shows the differential cross section for the production of bremsstrahlung with a photon energy E_γ from electrons with a total energy $E_0 = m_e + 4.988$ MeV in niobium calculated like [Schiff1951] (black line), [Seltzer1986] (red points) and [Haug2008] (green points). In the lower panel, the relative deviations between the calculations are shown as well as calculations by [Schiff1951], in which E_0 was decreased (blue line) or increased (orange line) by 18 keV.

flux, these deviations are effectively reduced to about 3 %. Figure 3.12 also shows that a difference in the total electron energy as large as its estimated uncertainty of 18 keV results in cross section deviations of less than 0.25 % between 2 and 4.5 MeV.

On its way from the radiator to the target, the bremsstrahlung photons with energies between 2 and 5 MeV are attenuated in the 3 mm thick quartz window by 3–2 %. The influence of the titanium foil is negligible. The energy-dependent transmission factor c_{window} was calculated with photon cross sections for atomic interactions from [Berger2010] and was taken into account to determine the spectral shape of the bremsstrahlung correctly.

3.3 Target

As outlined on page 29, the target consisted of alternating layers of aluminum and deuterated polyethylene (CD_2). The choice of these target materials for the used energy range is justified by the following considerations.

Different target materials containing deuterium have already been mentioned in the review of earlier $d(\gamma,n)p$ experiments in section 2.7. If photoprotons are to be detected, then their energy loss has to be minimized by using thin foils (e.g., CD_2) or deuterium gas as a target, which means a relative low number of target atoms and thus a longer measurement time to reach a certain statistical uncertainty. Furthermore, photoprotons require vacuum between the target and the detector. In contrast to that, the detection of photoneutrons is also possible with a few meters of air between a thick target and a detector. Typical materials for thick targets are liquids like heavy water (D_2O), plastics like polyethylene ($[-\text{CD}_2 - \text{CD}_2-]_n$, short notation CD_2) or liquid scintillators (e.g., C_6D_{12}), which are all produced using hydrogen with isotopically enriched deuterium content (up to 100 %). In these substances the number density of deuterons is quite similar and relatively large. Thick targets have the drawback that the photoneutrons have a much higher probability of unwanted secondary target interactions, in which the desired original information (energy and direction) is lost. This problem can become worse, if the target needs massive holders, containers or (in the case of active targets) detectors for scintillation light from the recoiling photoprotons. Only gaseous and liquid targets need containers. High-pressure gas targets using steel spheres as containers have recently been used in photon scattering experiments at the ELBE bremsstrahlung facility and caused time-consuming empty-target measurements [Schwengner2013a].

Nuclides used as nuclear resonance fluorescence (NRF) calibration standards for the photon flux are ^{11}B , ^{13}C , and ^{27}Al [Rusev2006, p. 91]. ^{13}C has two relatively strong NRF transitions at 3.1 MeV and 3.7 MeV, which are quite far away from the $d(\gamma,n)p$ threshold. Furthermore, the natural abundance of ^{13}C in the carbon of the CD_2 target of about 1 % would be too low for a precise photon flux determination. Highly enriched ^{11}B samples with masses of about 0.1 g have been used in nearly all NRF experiments at the ELBE bremsstrahlung facility to determine the photon flux. In these experiments, the endpoint energy of the photon spectrum was usually large enough to use NRF transitions from excitations of the levels at 4.4 MeV and 5.0 MeV, whose level widths are known with uncertainties of about 4 %. In the $d(\gamma,n)p$ experiment with an endpoint energy of 5 MeV, one mainly has to rely on the NRF transitions from the 2.1 MeV level. This allows to measure the photon flux very close to the threshold on the one hand, but its level width has an unacceptable high uncertainty of 7.5 % on the other hand [AjzenbergSelove1990]. Finally, ^{27}Al was chosen because it has levels close to the deuteron breakup threshold (2.2 MeV and 3.0 MeV) with precisely known level widths (1.7 % and 2.6 %, respectively [Pietralla1995]). Unfortunately ^{27}Al has a three times smaller integrated absorption cross section compared to ^{11}B so that for the same count rate a larger target is required. As ^{27}Al is the only stable isotope of aluminum no enrichment is necessary, so it is a relatively cheap solution.

Unexpended CD_2 raw material from the feasibility study [Beyer2005] has been used for the target production. The material's manufacturer (Trace Sciences International Corp.) stated that the isotopic abundance of deuterium is 98 % without giving an uncertainty. The raw material consisted of small grains that could easily be pressed into a solid form like a cylinder.

In a first approach to produce a homogeneous target, a mix of fine aluminum powder and the CD_2 grains was pressed together, but finally most of the powder was located at the bottom of the target. In another approach a layered target based on aluminum powder resulted in aluminum layers, whose thickness was not constant along the layer.

For the final target design, 0.5 mm thick aluminum plates with a chemical purity of 99.5 % have been used. To form disks with a diameter of 20 mm, a pile of several plates was lathed to cylindrical shape. The first and the last disk received a scratch to prevent slipping from the nylon strings of the target holder. The complete target was produced by alternately piling up aluminum disks and CD_2 grains in a cylindrical form with a diameter of 20 mm and press the pile with a force of 200 kN. The sequence was: fill Al layer #1, grains for CD_2 layer #1, and Al layer #2 to the form and press, then add grains for CD_2 layer #2 and Al layer #3 and press again, and so on. Underlying layers have not been removed, but new layers were pressed on top of them. Finally, CD_2 layer #11 and Al layer #12 were added and pressed. During the pressing, the aluminum disks were slightly deformed and the CD_2 changed its color from white to light green. The complete, 19.4 mm thick target is shown in figure 3.13. There was no bonding between the layers, but the target is hold together by four slim strips of adhesive tape.

The masses necessary to reach the desired statistical precision within the available measurement time have been estimated from experiences of the feasibility study. Masses have been determined using a digital analytic balance, whose precision was 10^{-4} g (last digit). The weight in air of all twelve aluminum layers together was 4.9955 g and the weight of the air displaced by them was 2.3 mg. The weight of the single aluminum layers differed by less than 0.3 mg. According to the standard DIN EN 573-3, aluminum with a mass fraction of at least 99.50 % can also include up to 0.40 % iron, up to 0.25 % silicon, up to 0.07 % zinc, each up to 0.05 % copper, manganese, magnesium or titanium, and each up to 0.03 % of other elements. Assuming a composition of 99.50 % aluminum, 0.31 % iron, and 0.19 % silicon, the number of ^{27}Al nuclei in the target was $N_{\text{Al}} = 1.109 \times 10^{23}$. This value increases by less than 0.5 %, if these three mass fractions are varied in their limits. For each CD_2 layer, 0.3800 g (weight in air) of the raw material has been turned into an 1.2 mm thick disk. The thickness variation along each layer was sufficiently small. The weight of the air displaced by all eleven CD_2 layers was 5.0 mg.

When the complete target was weighed before and after the experiment, a significant mass decrease was found, but the mass of the aluminum layers was still the same within the precision of the balance. The decrease of the initial weight in air of all eleven CD_2 layers of 4.1800 g was measured 4, 19, and 180 days after the layer production to be 25 mg, 167 mg, and 216 mg, respectively, see figure 3.14. The inset of that figure shows that all layers have a quite similar mass decrease and that the differences do not depend significantly on the order of layer numbers.

To study the mass decrease with a better time resolution, a test layer with the same amount of the same raw material like the CD_2 layers in the experiments was manufactured. The test layer was stored between two Al layers, which were similar to the Al target layers, in a glass container under the same condition as the target (except for the irradiation). The test layer showed a more rapid mass decrease in the first few days, in which also the target layers have not yet been irradiated, see figure 3.14. Therefore, the plan to use the mass decrease of the test layer to interpolate the mass of the target layers in the $d(\gamma, n)p$ measurement had to be rejected. On the contrary, the mass decrease after 20 and 200 days was nearly the same in the test layer and in the target layers.

As the irradiation seems not to be the reason for the mass decrease, either the inherent chemical stability of the raw material or the layer production remain as explanations. In polyethylene there

Figure 3.13: Photo of the Al- CD_2 -multilayer target. The numbering of the CD_2 layers is #1 to #11 from top to bottom, which was also the order in the production as well as in the positioning, i.e., layer #1 was produced and hit by the beam first.

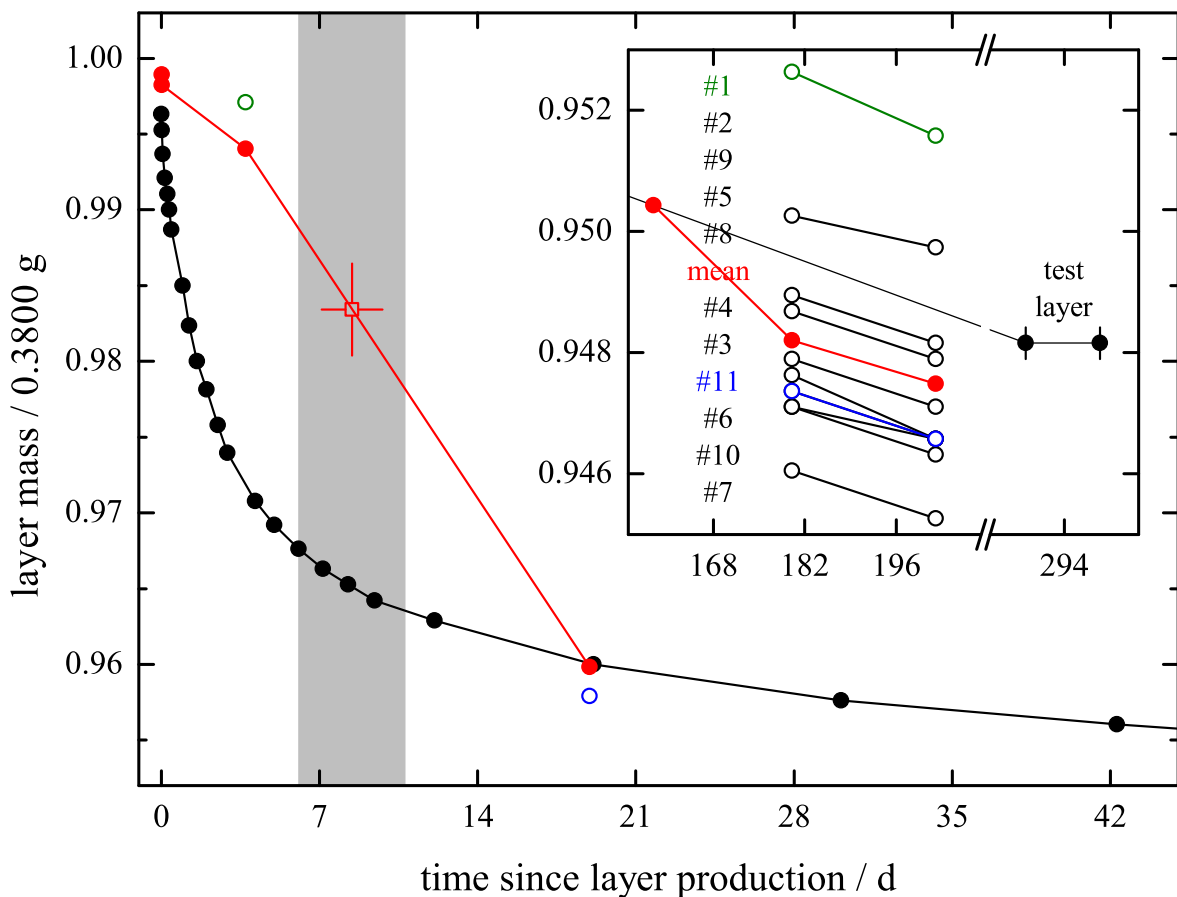
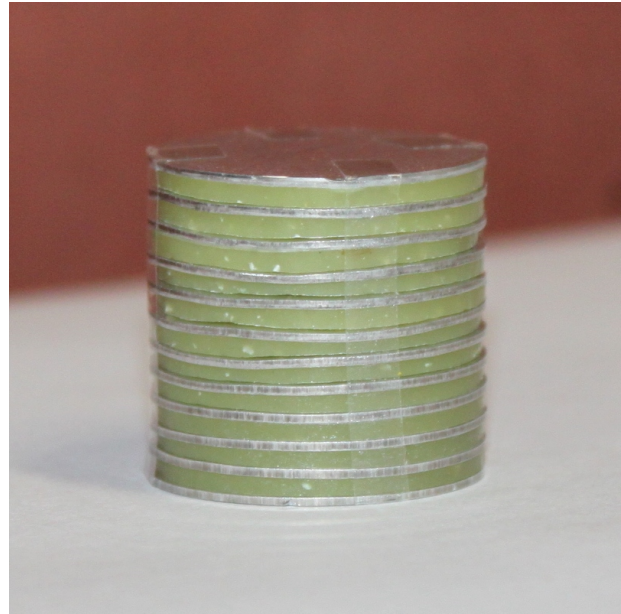


Figure 3.14: Decrease of CD_2 layer mass over time. The gray area indicates the $d(\gamma,n)p$ data taking time, while much later times are shown in the inset. Lines are linear interpolations. Empty circles result from weighing one of the eleven CD_2 layers used in the experiment. The filled red circles are the mean values calculated from weighing all eleven layers together. The filled black circles result from weighing a test layer, which was manufactured later to monitor the mass decrease with higher resolution. The error bars in the inset show the precision of the balance (\pm last digit of 10^{-4} g). The empty red square is an interpolated value used as the mean mass of the experiment.

are chemical bonds between two carbon atoms or one carbon and one hydrogen atom. The polymer chains are typically long enough so that breaks of C–C bonds should seldom lead to the formation of gaseous hydrocarbons. Breaks of C–H bonds can lead to double bonds or cross-linking between two carbon atoms of the same chain or two adjacent chains, respectively [Makosky1969, p. 25]. Broken C–H bonds usually lead to free hydrogen which can leave the material. It is therefore reasonable to assume that the mass decrease is related to an evaporation of hydrogen caused by the pressing during the layer production, which also caused the color change of the material.

Finally, the mass of the eleven CD₂ layers was linearly interpolated from the weighings before and after the d(γ ,n)p data taking time resulting in a mean mass of (4.106 ± 0.013) g. The mass uncertainty is calculated from the standard deviation of the uniform time distribution ($\text{width}/\sqrt{12}$) using the same interpolation function. Under the assumption discussed above, that the number of carbon atoms has not changed since the production, the stoichiometric C:H ratio of 2:x would change from 4 to 3.73. Using $x = 3.86 \pm 0.13$ as a conservative estimate, the number of deuterons in the target at the time of the d(γ ,n)p measurement was $N_d = 2.949 \times 10^{23}$. The relative uncertainty of this number is 2.5 % due to the stoichiometry, 0.3 % due to the mass interpolation and 0.9 % due to an assumed uncertainty of 1.0 % of the isotopic deuterium abundance. The combination of all effects results in a relative uncertainty of 2.7 %. The number of ¹²C, ¹³C, and ¹H atoms in the target at the time of the d(γ ,n)p measurement was 1.54×10^{23} , 1.71×10^{21} , and 6.02×10^{21} , respectively.

Interactions of the incoming photon beam with the target material are discussed in section 3.4 and interactions of the d(γ ,n)p photoneutrons with the target material and with other parts of the experimental setup are discussed in chapter 5.

3.4 Photon flux determination

The photon flux of the bremsstrahlung in the relevant energy range is determined from γ transitions in ²⁷Al, whose strength is well known. The time-averaged differential photon flux, i.e., the rate of photons per unit area in a small energy interval ($E_\gamma, E_\gamma + dE_\gamma$) divided by the interval width, is

$$\frac{d\Phi_\gamma(E_\gamma)}{dE_\gamma} = \frac{1}{c_{\text{loss}} t_{\text{real}} N_{\text{Al}}} \frac{c_{\text{feed}} A}{c_{\text{trans}} \epsilon I_S W}, \quad (3.2)$$

in which only the quantities in the first fraction do not depend on E_γ . The number of aluminum atoms N_{Al} was determined in section 3.3. The energy-integrated scattering cross section I_S , the angular correlation function W , the feeding-correction factor c_{feed} , and the transmission coefficient c_{trans} are described in section 3.4.1. These quantities depend on the properties of the levels, which are involved in the emission of a γ ray with the energy E_γ . The area A of the peak in the energy spectrum, the real time t_{real} , and the correction factor for event losses c_{loss} are determined experimentally as described in section 3.4.2. The detection efficiency ϵ was calibrated with radioactive sources and compared to a Monte Carlo simulation as described in section 3.4.3.

3.4.1 Nuclear resonance fluorescence

Nuclear resonance fluorescence (NRF) is the absorption and re-emission of photons by nuclei. The absorption of the incident γ ray brings the target nucleus from its ground state to an excited level. This level decays with a mean lifetime τ , which can also be expressed by the total level width

$$\Gamma = \hbar/\tau = \sum_f \Gamma_f + \Gamma_p. \quad (3.3)$$

The total level width is the sum of the partial level widths for the radiative decay to final states in the same nucleus (Γ_f) and for the emission of particles (Γ_p). The latter is zero for the excitation of ²⁷Al

with bremsstrahlung with an endpoint energy of 5 MeV because the particle separation energies are about 8 MeV (proton) and 13 MeV (neutron). An excitation from the ground state that decays back to the ground state ($\Gamma_f = \Gamma_0$) is called elastic photon scattering, while a decay to intermediate states leaves the nucleus in a lower excited state, which then also decays, and is called inelastic photon scattering. From the theory of the NRF method (see reviews in [Metzger1959, Kneissl1996]) one can derive the energy-integrated scattering cross section for photon scattering leading to the final state f by multiplying the integral over a Breit-Wigner resonance with the branching ratio $B = \Gamma_f/\Gamma$. One obtains

$$I_S = \frac{2J_x + 1}{2J_0 + 1} \cdot \left(\frac{\pi \hbar c}{E_x} \right)^2 \cdot \frac{\Gamma_0 \Gamma_f}{\Gamma}, \quad (3.4)$$

in which J_0 , J_x , and E_x are the total angular momenta and the energy of the ground state and the excited level, respectively.

In figure 3.15 all 14 levels in ^{27}Al below 5 MeV and their known 36 decays are shown and the corresponding nuclear data is listed. Not all of the shown transitions are equally well suited for the photon flux determination. The levels at 4055 keV and 4510 keV cannot get excited because their ground-state decay widths are zero, which is related to the large spin difference. Very low scattering cross sections are found for the level at 3680 keV due to its low ground-state decay width and for the levels at 844 keV and 1014 keV due to their low total level widths. There are seven transitions with relatively large scattering cross sections ($I_S > 10$ eVb). With increasing energy, a lower statistical precision is expected because of the decreasing photon flux and the decreasing detection efficiency (compare sections 3.2 and 3.4.3, respectively). The ground-state transitions of the levels at 2212 keV and 2982 keV seem to be most appropriate. Although they will need a correction for the *feeding* from higher-lying states, they should have the highest count rates and are very close to the energy region relevant for the $d(\gamma, n)p$ cross section measurement.

Due to the transfer of recoil energy to the ^{27}Al nucleus with mass $M = 25133.142 \text{ MeV } c^{-2}$, the energy of the absorbed bremsstrahlung photon is

$$E_{\gamma, \text{abs}} \approx E_x + \frac{E_x^2}{2Mc^2}. \quad (3.5)$$

Because $E_x/Mc^2 \ll 1$ is valid, the non-relativistic approximation is used. The excited state decays before the nucleus can lose its recoil energy, so there is a Doppler shift of the emitted γ energy, which depends on the angle ϑ of photon emission (relative to the beam). The photon emission also causes a recoil of the nucleus. One finds

$$E_{\gamma, \vartheta} \approx E_{\gamma, 0} + \frac{E_{\gamma, 0}^2}{Mc^2} \cos \vartheta \quad E_{\gamma, 0} \approx E_x - E_f - \frac{(E_x - E_f)^2}{2Mc^2}. \quad (3.6)$$

The widths of excited levels are affected by the thermal motion of the nuclei, which leads to a Doppler broadening of the emitted γ -ray energy distribution with the width

$$\Delta E_D = E_{\gamma, 0} \sqrt{\frac{2k_B T_{\text{eff}}}{Mc^2}} \quad T_{\text{eff}} = \frac{3T_1^4}{\Theta^3} \int_0^{\Theta/T_1} t^3 \left(\frac{1}{e^t - 1} + \frac{1}{2} \right) dt = 323.5 \text{ K}, \quad (3.7)$$

in which k_B is the Boltzmann constant. For the effective temperature T_{eff} given by [Metzger1959], the room temperature $T_1 = 293 \text{ K}$ and the Debye temperature of aluminum $\Theta = 428 \text{ K}$ are used. The Doppler widths of the ground-state transitions of the levels at 2212 keV, 2982 keV, and 3957 keV are 3–6 eV, which is one order of magnitude larger than the level width, but still two orders of magnitude smaller than the recoil shift of 100–300 eV and the Doppler shift, whose maximum shift is twice that large. Because the separation between the absorption and emission energy is much larger than the width, the emitted photons of these transitions cannot be absorbed again, except for $\vartheta \approx 0$ where the Doppler shift just compensates the recoil losses.

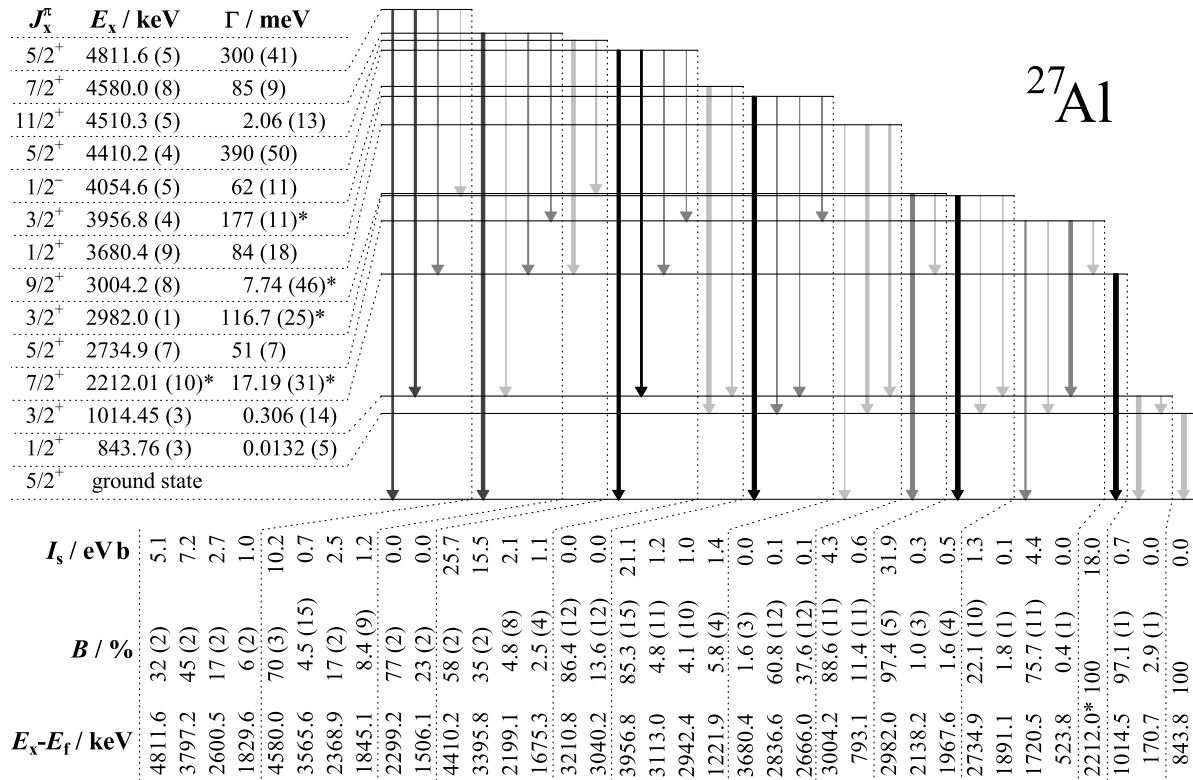


Figure 3.15: Level scheme of ^{27}Al , which shows all known levels (horizontal lines) with $E_x < 5 \text{ MeV}$. The level properties spin J_x , parity π , energy E_x , and width Γ are listed left of the scheme. The vertical arrows indicate the known transitions between these levels. The arrow width is related to the branching ratio B and the arrow's shade of gray is related to the energy-integrated scattering cross section I_s . Both are listed below the scheme together with the transition energy $E_x - E_f$. Data was taken from [Endt1990] and (if marked with *) from [Pietralla1995].

Angular correlation

The angular correlation function W was calculated as described in [Kneissl1996] using a computer program [Schwengner2013b]. The input parameters are the total angular momenta of ground state, excited level, and final level as well as the γ -ray mixing ratios [Endt1990], the angle between beam and detector $\vartheta = 115^\circ$, and its opening angle of 7.4° . A de-excitation via an intermediate level can be calculated, too. The results range from 0.92 to 1.06 with typical uncertainties of less than 0.005.

Attenuation of photons

The intensity I_0 of the photon beam is attenuated to I after propagating through the target on a path of length l . In general, the transmission coefficient is $c_{\text{trans}} = I/I_0 = \exp(-\mu l)$, with μ being the material-specific linear attenuation coefficient for photons with energy E_γ . Atomic interactions such as Compton scattering, photoelectric absorption, and pair production affect incoming bremsstrahlung photons as well as photons emitted from excited nuclei in the target. Linear attenuation coefficients μ_a were calculated with atomic cross section data of polyethylene (CH_2), which should be equal to CD_2 , and aluminum taken from [Berger2010]. The nuclear absorption due to photodissociation of the deuteron in the CD_2 can be estimated from the $d(\gamma, n)p$ cross section. It is by three orders of magnitude smaller than the atomic absorption and thus negligible. At the energies $E_{\gamma, \text{abs}}$ that allow a resonant excitation of the target nuclei, the intensity of the incoming bremsstrahlung beam is also reduced due to nuclear self absorption. As mentioned before, the emitted NRF γ rays are not attenuated by this process because the difference between the absorption and emission energy is much larger than the width. A linear attenuation coefficient $\mu_n = R/l$ was

calculated using the relative resonance absorption of a thin target [Skorka1975]

$$R = \sqrt{\frac{\pi^3 (\hbar c)^2}{2 E_{\gamma, \text{abs}}^2} \frac{2J_i + 1}{2J_0 + 1} n l \frac{\Gamma_0}{\Delta E_D}} \quad (3.8)$$

with the number density of aluminum atoms n . The comparison in table 3.5 shows, that at the three energies with strong resonances the nuclear absorption in aluminum is stronger than the atomic absorption. The atomic absorption of CD_2 is more than two times smaller than the one of aluminum, but as the CD_2 layers are more than two times thicker, the effect on the correction will be similar.

Coefficients have been calculated and simulated for the mean transmission of incoming bremsstrahlung photons ($c_{\text{trans}, \text{in}}$), for the transmission of NRF photons emitted in the target in direction of detector ($c_{\text{trans}, \text{out}}$), and for both effects together ($c_{\text{trans}} = c_{\text{trans}, \text{in}} \cdot c_{\text{trans}, \text{out}}$):

$$\begin{aligned} c_{\text{trans}, \text{in}}^{\text{sim}} &= N_{\text{in}}/N_{\text{start}} & c_{\text{trans}, \text{out}}^{\text{sim}} &= N_{\text{out}}/N_{\text{in}} \\ c_{\text{trans}, \text{in}}^{\text{calc}} &= \frac{1 - e^{-x}}{x} & x &= (\mu_{\text{Al}, \text{n}} + \mu_{\text{Al}, \text{a}}) n_{\text{Al}} l_{\text{Al}} + \mu_{\text{CD}_2, \text{a}} n_{\text{CD}_2} l_{\text{CD}_2} \\ c_{\text{trans}, \text{out}}^{\text{calc}} &= e^{-y} & y &= \frac{\mu_{\text{Al}, \text{a}} n_{\text{Al}} l_{\text{Al}} + \mu_{\text{CD}_2, \text{a}} n_{\text{CD}_2} l_{\text{CD}_2}}{n_{\text{Al}} l_{\text{Al}} + n_{\text{CD}_2} l_{\text{CD}_2}} \frac{r}{\sin \vartheta}. \end{aligned} \quad (3.9)$$

These formulas use the numbers of layers $n_{\text{Al}} = 12$ and $n_{\text{CD}_2} = 11$, the layer thicknesses $l_{\text{Al}} = 0.5$ mm and $l_{\text{CD}_2} = 1.2$ mm, the target radius $r = 10$ mm, and the detector angle $\vartheta = 115^\circ$. In the simulation, the γ rays were emitted isotropically from start positions that were distributed uniformly in the aluminum layers. The number of γ rays moving in direction of the detector was counted (N_{start}). The path lengths l_{att} of these γ rays through aluminum and CD_2 was calculated separately from the target front side to the start position as well as from the start position to the point, at which the target was left. The attenuation was described separately for these four cases by exponential distributions, whose mean values were calculated from the linear attenuation coefficients. From these distributions the attenuation lengths l_{att} were sampled randomly for each photon. If $l_{\text{att}} > l_{\text{path}}$, then the photon was transmitted and the numbers of such incoming (N_{in}) and outgoing (N_{out}) photons were counted. Some results of the simulation are listed in table 3.5. The results of the calculation are systematically higher. For $c_{\text{trans}, \text{in}}$ the difference is on average only 0.003, but for $c_{\text{trans}, \text{out}}$ a average difference of 0.02 is found. As the calculation uses mean values, whereas the simulation uses the whole distribution of the start positions, the differences seem to be a result of the non-linearity of the exponential attenuation. For the photon flux determination the simulated transmission coefficients were used.

The atomic attenuation of the incoming bremsstrahlung photons with an energy E_γ was determined to be approximately 5 %. Depending on the type of interaction, this can increase the number of photons at lower energies $E'_\gamma < E_\gamma$, which can then interact in the target again. Photons with $E'_\gamma > B_d$ are of particular interest because they can still trigger $d(\gamma, \text{n})\text{p}$ reactions, which in addition have a different reference angle. The contribution of the photo effect is negligible above B_d , while pair production contributes about 10 % to the atomic interactions at 5 MeV. The energy of electrons created by pair production is less than 2 MeV and their bremsstrahlung will not be

Table 3.5: The correction factors for the attenuation of photons in the target have been determined using the linear attenuation coefficients for atomic (a) and nuclear (n) interactions of photons with CD_2 and aluminum.

E_γ / keV	$\mu_{\text{Al}, \text{n}} / \text{cm}^{-1}$	$\mu_{\text{Al}, \text{a}} / \text{cm}^{-1}$	$\mu_{\text{CD}_2, \text{a}} / \text{cm}^{-1}$	$c_{\text{trans}, \text{in}}^{\text{sim}}$	$c_{\text{trans}, \text{out}}^{\text{sim}}$	$c_{\text{trans}}^{\text{sim}}$
2212	0.134	0.111	0.047	0.905	0.950	0.860
2982	0.169	0.096	0.040	0.904	0.958	0.866
3956	0.096	0.084	0.034	0.929	0.963	0.895

above B_d . The energy of recoil electrons from Compton scattering is up to 4.7 MeV. Because the target consists of low- Z materials (D, C, Al) the electrons lose their energy mainly by ionization. The fraction of radiative losses can be estimated to be less than 8 % [Knoll1999, p. 44] and the contribution of bremsstrahlung photons with energies above 2.225 MeV to the total radiative energy is about 30 % (see equation (3.1)). Therefore, it is estimated that the probability of a Compton electron leading to a photon in the relevant energy range can be neglected. The angle, for which the energy of the Compton-scattered photon is equal to B_d , and the differential cross section integrated over the cone defined by that angle are given by

$$\vartheta_B = \arccos\left(1 - m_e \frac{E_\gamma - B_d}{E_\gamma B_d}\right) \quad \sigma_{cs}(\vartheta_B) = 2\pi \int_0^{\vartheta_B} \left(\frac{d\sigma}{d\Omega}\right)_{\text{Klein-Nishina}} \sin\vartheta d\vartheta. \quad (3.10)$$

The fraction of photons with $E'_\gamma > B_d$ that are scattered into the cone is shown in figure 3.16. Up to one third of the Compton-scattered photons can still trigger $d(\gamma,n)p$ reactions. Because ϑ_B is less than 30° , most of the photons in the cone should stay in the target. Finally, the total probability of an incoming photon with 5 MeV that interacts with the target and leads to a photon with $E'_\gamma > B_d$ can be estimated to be about 1.5 %. To determine the effect on the photon spectrum it would be necessary to include the energy distribution of the Compton-scattered photons and also the position in the target.

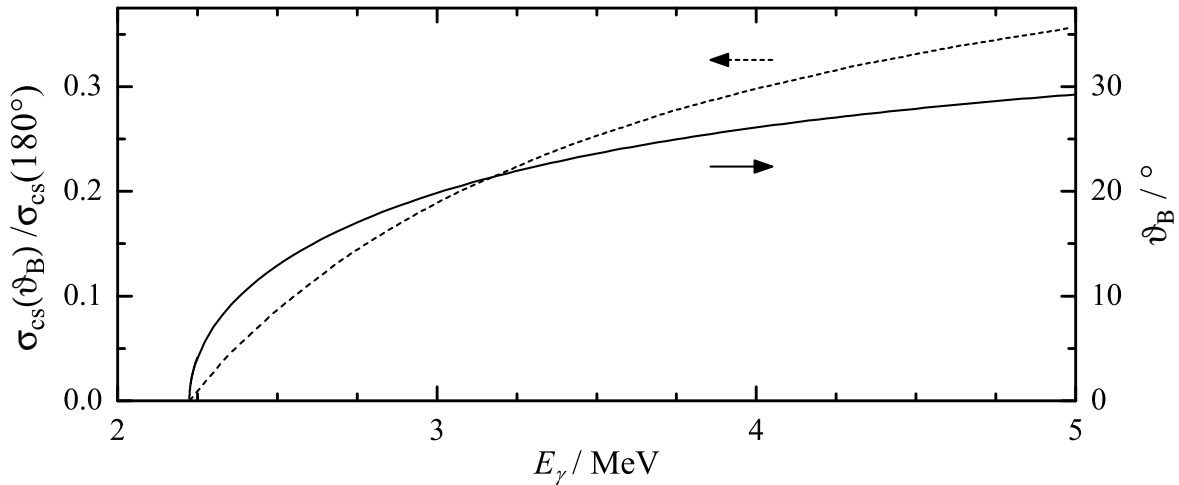


Figure 3.16: Fraction (dashed line, left axis) and maximum angle (solid line, right axis) of Compton-scattered photons with $E'_\gamma > B_d$ as a function of the incoming photon energy E_γ .

Feeding correction

The feeding-correction factor is defined by $c_{\text{feed}} = N_{\text{g.s.}} / (N_{\text{g.s.}} + N_{\text{feed}})$ for each transition. The number of elastically scattered photons reaching the position of the detector can be calculated by $N_{\text{g.s.}} = C \cdot W \cdot I_S \cdot c_{\text{trans,in}} \cdot d\sigma / dE_\gamma$ with equations (3.1) and (3.4) and an arbitrary normalization constant C . N_{feed} is the number of transitions reaching the detector position after the decay of the final level of an inelastic photon scattering event. It is calculated using $N_{\text{g.s.}}$, B , and W of the higher levels. Because N_{feed} is proportional to C , the feeding-correction factor is independent of this normalization constant. It is also independent of the efficiency, as the emitted γ -ray energy does not depend on the excitation mechanism. The uncertainty of the feeding-correction factor is dominated by the uncertainties of the branching ratios, while uncertainties of the bremsstrahlung cross section and the angular correlation functions have only a small influence. The feeding-correction factor c_{feed} ranges from 0.09 at 844 keV to 1.0 above 3 MeV. For the transitions that are relevant for the photon flux determination at 1014 keV, 1720 keV, 2212 keV, 2735 keV, and 2956 keV one finds 0.215 (6), 0.832 (10), 0.921 (5), 0.820 (13), and 0.995 (2), respectively.

3.4.2 Analysis of HPGe spectra

Data acquisition

The photons scattered from the target were detected with two high-purity germanium (HPGe) detectors labeled as detector 1 and 3 in the following. The components (escape suppression, collimator, absorber) and the position of the detectors are described on page 31. The data acquisition (DAQ) system of the HPGe detectors was described in detail in [Rusev2006, Trompler2009]. The total detector count rates with and without escape suppression were about 6600 and 7500 s⁻¹, compare figure 3.9. The real time t_{real} was measured by counting the signals of a pulser, while for the measurement of the live time t_{live} only pulses that were anti-coincident to the DAQ busy signal were counted. For practical reasons, the DAQ was halted during the d(γ ,n)p experiment about every 90 minutes and a new file for storing the data was opened. The neutron detectors had a separate DAQ system, which was started and stopped synchronously. Data was acquired over 136 h. Excluding beam tuning periods, beam energy and position measurements, short beam and DAQ failures, and repair breaks, the analyzed data was acquired over $t_{\text{real}} = 123.0$ h.

Determination of peak areas

The response of an HPGe detector to γ rays causes a characteristic peak shape. The interactions of MeV photons with the detector material are mainly Compton scattering and pair production. This leads to a cascade of secondary particles (γ , e^+ , e^-) with lower energy and (because germanium is a semiconductor) finally to the creation of electron–hole pairs. If all secondary particles are absorbed in the detector volume, then the spectrum contains a so-called full-energy peak at the energy of the incoming photon. Towards lower energies this peak has a tail and a higher background level caused by escaping low-energy particles, electron-hole pairs not reaching the electrodes (trapping by crystal defects), or discharging of the preamplifier before all charge carriers have been collected (ballistic deficit). Electronic noise, statistical fluctuations of the number of charge carriers, and ballistic deficit cause a peak width of a few keV, which is three orders of magnitude larger than the Doppler width of γ rays emitted from the ²⁷Al nuclei in the present experiment.

Two examples for peak shapes measured in the d(γ ,n)p experiment are shown in figure 3.17, in which one can see that it also depends on the number of counts, i.e., on the statistical uncertainty, how well the low-energy tail can be recognized. One method for the determination of the peak area is to fit a model function to the data. A common parametrization describes the background by a linear polynomial plus a step function and the peak by a Gaussian function plus a skewed Gaussian [Erhard2009, pp. 84-86]. The software ROOT [Brun1997] has been used to perform a log-likelihood fit of this model to the data. It was found that the fit convergence was strongly dependent on the fit range as well as on the start values and limits set to the parameters. The goodness of the fit was usually not satisfactory ($\chi^2/\text{ndf} > 1$) and the parameter errors were rather large. The left panel of figure 3.17 shows such a fit to a peak at 2615 keV resulting in $\chi^2/\text{ndf} = 1.9$ and a peak area $A = 25200 \pm 1500$. The figure also shows a fit omitting the skewed Gaussian, which only gives a poor description of the tail and the constant background towards lower energies ($\chi^2/\text{ndf} = 7.4$). Due to the missing tail, the peak area from this method $A = 23920 \pm 160$ is significantly smaller, although the area uncertainty seems to be more realistic as it is closer to the uncertainty of the simpler and more robust integration method. For the integration method the peak area $A = 25050 \pm 180$ is the total number of counts in an interval containing the peak and the tail, from which the background to the left and to the right of the peak center was subtracted separately. The background was estimated from two adjacent, peak-free intervals indicated by vertical lines in the left panel of figure 3.17. The other example in the right panel of this figure shows a background peak from ²¹⁴Bi at 2204 keV and the important NRF transition from ²⁷Al at 2212 keV, which are very close to each other. Here the integration method can be applied to the sum of both

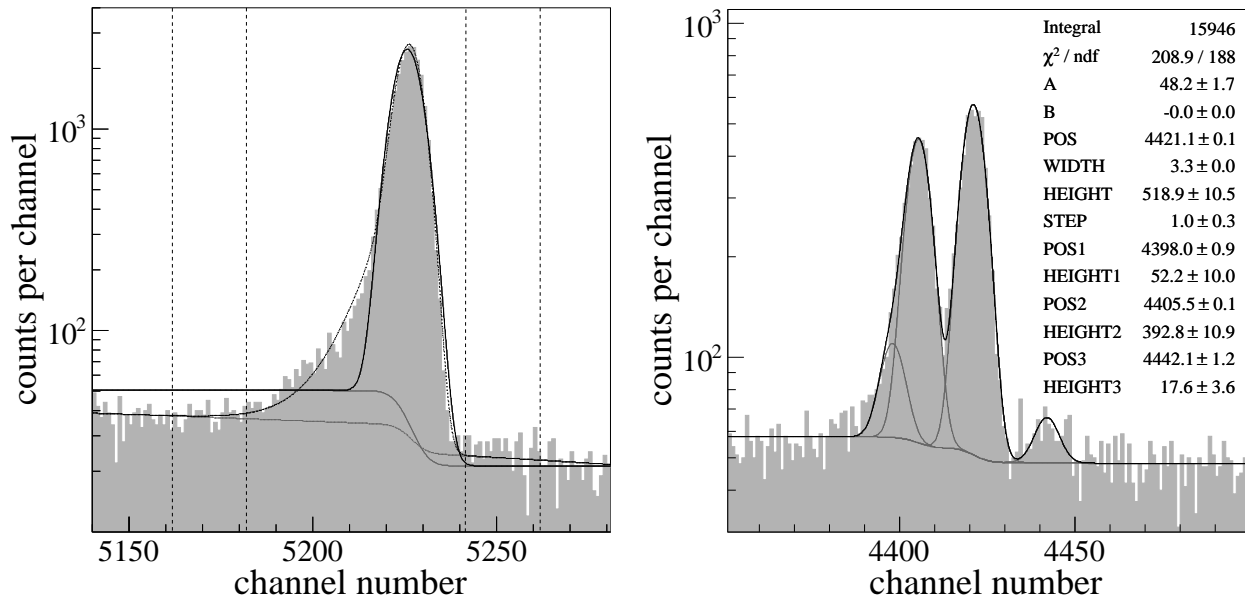


Figure 3.17: Peaks in the γ -ray energy spectrum measured with an HPGe detector with beam on (gray histogram). The left panel shows a peak at 2615 keV from the ^{208}Tl decay together with fit curves using models with (dotted) and without (solid) a skewed Gaussian. The gray curves are the belonging background contributions. The four vertical dashed lines limit the three intervals of the simpler peak integration method. The right panel shows a background peak at 2204 keV from the ^{214}Bi decay and the NRF transition from ^{27}Al at 2212 keV. The black curve and the listed parameters are from a fit (without skewed Gaussian) of four peaks that have the same width and step. The gray curves are the background plus each one peak.

peaks. Due to the statistical precision of the background measurement, the subtraction of the contribution of the background peak would result in a relative area uncertainty of about 5 % for the NRF transition. A fit including the skewed Gaussian results in unrealistic parameters and large uncertainties. If two more smaller peaks are assumed at 2199 keV (weak NRF transition from ^{27}Al) and at 2225 keV (from the $p(n,\gamma)d$ reaction), a fit without the skewed Gaussian gives a satisfactory result of $A = 4347 \pm 75$. As mentioned before, this fit model can underestimate the area. For all peaks except the NRF transition at 2212 keV the integration method has been used.

Observed γ rays

Figure 3.18 shows the measured spectrum with the beam on and off. In the beam-off spectrum several peaks from the natural background radiation of the room can be identified, which come mainly from ^{40}K (1461 keV), from ^{208}Tl (2615 keV), and from several other isotopes of the decay chains of ^{232}Th and ^{238}U (e.g., 1764 keV, 2204 keV). On the one hand, the full-energy peaks, escape peaks, or Compton continua of these γ rays can disturb the measurement of the ^{27}Al transitions. On the other hand, their count rate offers a monitor for event losses due to dead time and pile-up, if a constant background event rate is assumed. For the same purpose, a ^{60}Co source was placed below each HPGe detector, which is also visible in the spectra (1173 keV, 1332 keV, sum of both). The background events above 2615 keV are mainly caused by cosmic radiation. The beam-on spectrum also contains background events. Especially below 1 MeV there is a large continuum stemming from photons scattered from the bremsstrahlung beam by the target. The peaks at 511 keV and 1022 keV are due to the detection of one or two photons from the annihilation of electrons with positrons, which have most likely been created in the target, the absorber plates, or the collimator. All other peaks can be assigned to NRF transitions from the target, i.e., mainly from ^{27}Al , but also from the first excited levels of ^{12}C (4439 keV) and ^{13}C (3089 keV, 3685 keV). The observed count rates of the peaks are listed in table 3.6.

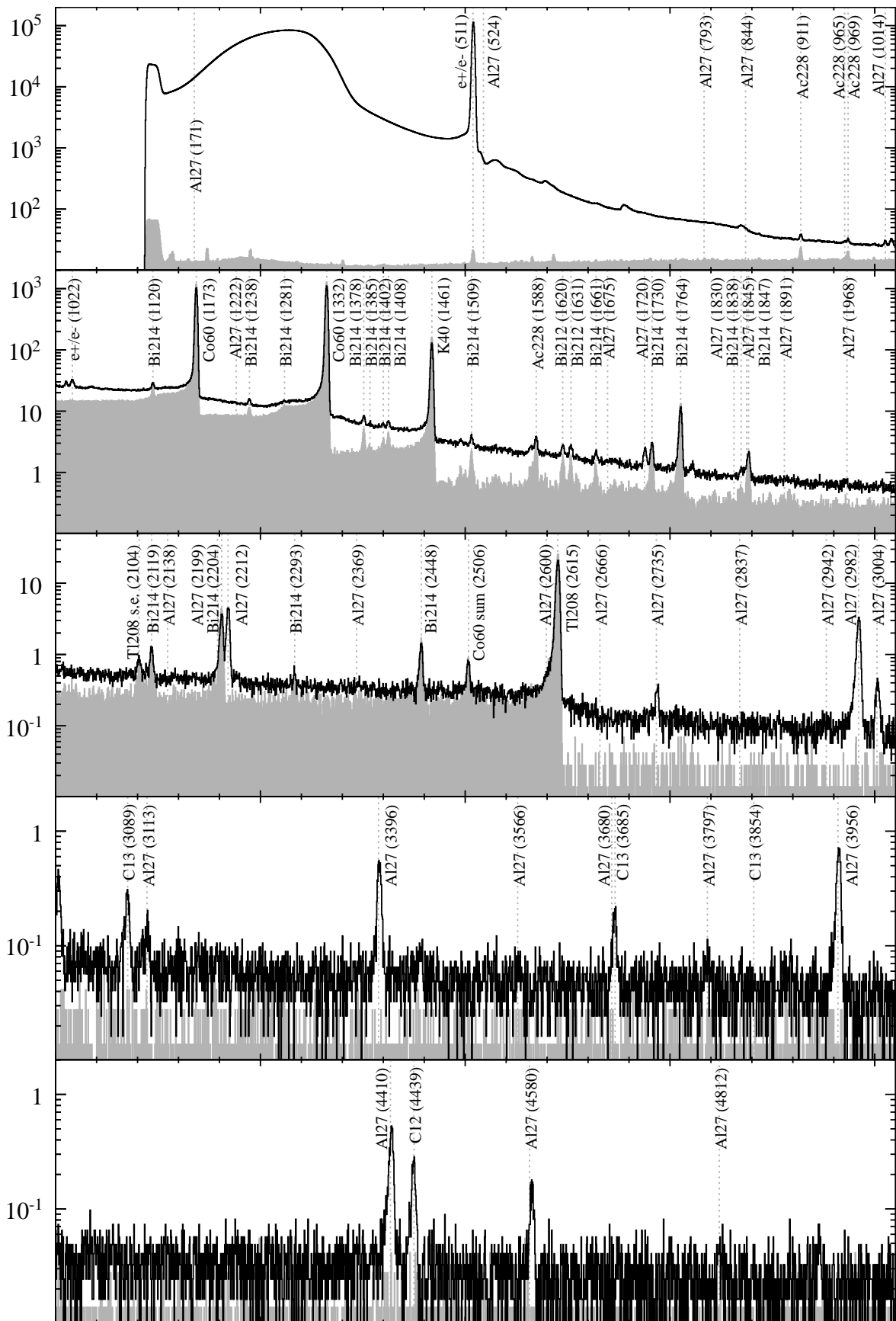


Figure 3.18: Spectrum of the γ -ray energy measured with an HPGe detector with beam on (black) and off (gray). The counts per channel per hour real time are plotted versus the ADC channel. The uppermost panel goes from channel 0 to 2050. The range of the others panels is shifted by 2000 channels compared to the upper neighbor. Vertical lines indicate the position of expected γ rays and are labeled with origin and energy in keV. See text for details.

Table 3.6: Observed count rates $R = A/t_{\text{real}}$ with beam on and off (upper table). Relative uncertainties are given in parentheses. The peak areas A have been determined with the integration method, only for the 2212 keV γ ray a Gaussian fit was used, see figure 3.17. The beam-on rates of the 2204 keV γ ray include the events at 2212 keV. The lower table lists real time, relative live time, correction factor for event losses, and total detector count rate.

E_γ / keV	R_1 / h^{-1}		$R_{1,\text{bg}} / \text{h}^{-1}$		R_3 / h^{-1}		$R_{3,\text{bg}} / \text{h}^{-1}$	
^{60}Co 1173	6712	(0.1 %)	8609	(0.2 %)	6979	(0.1 %)	9221	(0.2 %)
^{60}Co 1332	7648	(0.1 %)	9807	(0.1 %)	7944	(0.1 %)	10393	(0.1 %)
^{40}K 1461	900	(0.4 %)	1294	(0.4 %)	1083	(0.4 %)	1561	(0.4 %)
^{214}Bi 1764	80.9	(0.2 %)	114.2	(1.4 %)	78.6	(1.6 %)	115.7	(1.4 %)
^{214}Bi 2204	67.5	(2.0 %)	39.2	(3.5 %)	63.7	(2.1 %)	39.3	(3.8 %)
^{208}Tl 2615	203.7	(0.7 %)	276.2	(0.8 %)	220.6	(0.7 %)	309.4	(0.8 %)
^{13}C 3089	2.5	(14 %)			2.7	(13 %)		
^{13}C 3685	1.7	(16 %)			1.8	(14 %)		
^{12}C 4439	2.6	(8 %)			2.3	(10 %)		
^{27}Al 1014	13	(32 %)			17	(25 %)		
^{27}Al 1720	8.3	(12 %)			8.2	(13 %)		
^{27}Al 2212	35.3	(1.7 %)			33.8	(1.9 %)		
^{27}Al 2735	2.9	(15 %)			1.6	(28 %)		
^{27}Al 2982	32.7	(1.9 %)			29.6	(2.1 %)		
^{27}Al 3004	3.6	(7 %)			3.1	(8 %)		
^{27}Al 3113	1.0	(20 %)			0.8	(26 %)		
^{27}Al 3396	5.2	(7 %)			5.5	(6 %)		
^{27}Al 3956	7.6	(5 %)			6.7	(5 %)		
^{27}Al 4410	5.7	(6 %)			5.9	(5 %)		
^{27}Al 4580	1.4	(16 %)			1.4	(16 %)		
	det. 1, beam on		det. 1, beam off		det. 3, beam on		det. 3, beam off	
$t_{\text{real}} / \text{h}$	123.0		64.3		123.0		64.3	
$t_{\text{live}}/t_{\text{real}} / \%$	90.5		99.9		89.9		99.9	
$c_{\text{loss}} / \%$	78.0 (0.1 %)				76.1 (0.1 %)			
$R_{\text{total}} / \text{s}^{-1}$	7400		53		7800		59	

Peak-position stability and event losses

To analyze the peaks with high statistical precision the spectra from all measured files are added up. If the relation between γ -ray energy and peak position μ in the ADC spectrum changes during the measurement, e.g., due to changes of the signal amplification, then the peaks are further broadened in the sum spectra and each file would require its own energy calibration. To check if this was the case in the $d(\gamma,n)p$ experiment, the peak positions of the strong peaks from ^{60}Co , ^{40}K , and ^{208}Tl were obtained by a Gaussian fit for each file. The result, which is shown in the upper panel of figure 3.19, is a negligible drift of less than half a channel.

Using the integration method, the areas A of these four peaks were determined for each file. The observed count rates $R = A/t_{\text{real}}$ normalized to the observed background count rates R_{bg} are shown for HPGe detector 1 in the lower panel of figure 3.19. The changes from one file to the next are due to intensity variations of the bremsstrahlung beam and due to statistical fluctuations. The variations are sufficient small to correct event losses for the sum of all files rather than for each single file. The count rate reduction compared to the background measurement cannot be explained by dead time alone but is related to pile-up of events, which are by chance coincident within the shaping time

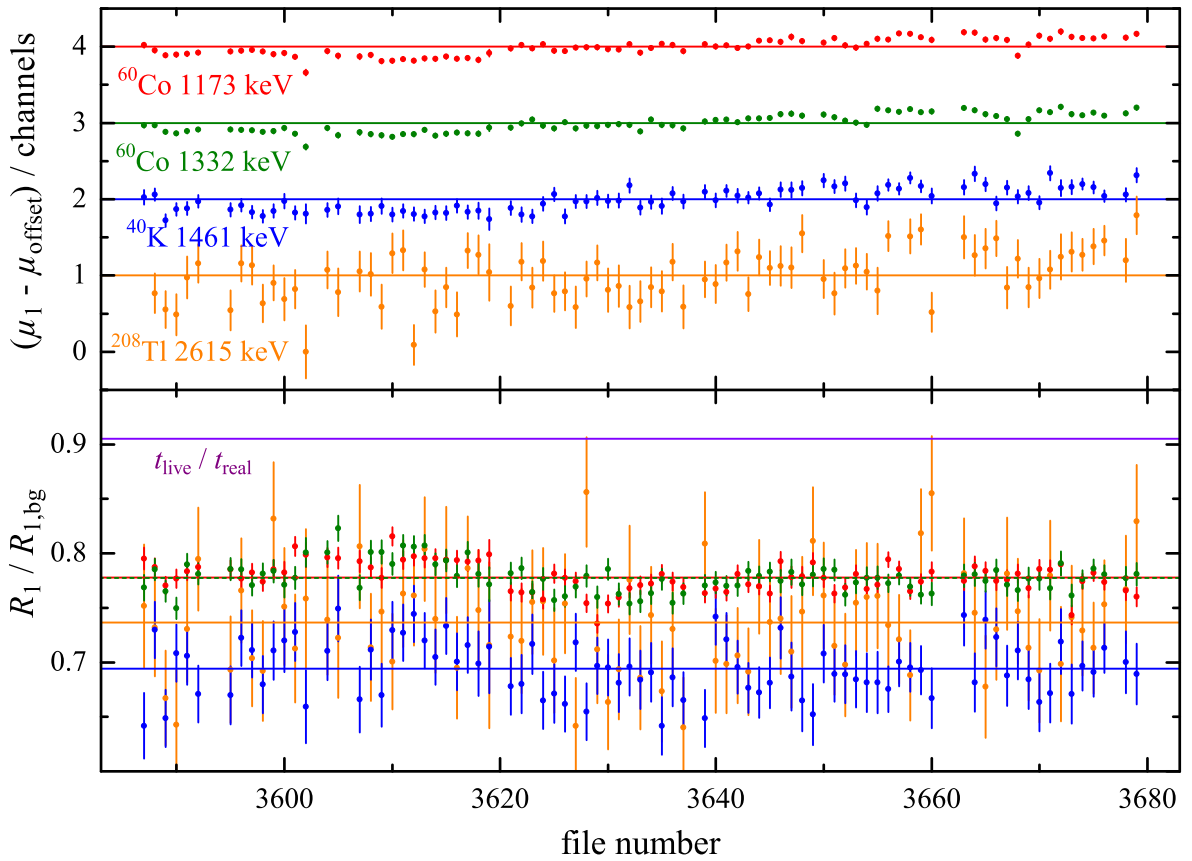


Figure 3.19: The upper panel shows the peak position μ of certain γ rays (see labels) for each data file to demonstrate the good long-term gain stability. An offset was chosen for each peak position for better visualization. The lower panel shows the observed count rate normalized to the background count rate. For comparison, the relative live time is also shown. For the vertical lines the sum of all files was analyzed. The index 1 is the detector number.

of the main amplifier. For the natural occurring γ rays and those from ^{60}Co sources the reduction seems to be different. It turned out that the background count rate of ^{40}K and ^{208}Tl depends on the position of the door of the experimental area. As this door was not closed all the time during the background measurement, the correction factor for event losses c_{loss} was calculated from both ^{60}Co γ rays. This correction factor depends on the total detector count rate and is assumed to be 1 for the beam-off measurement, in which the total rate was very low, see table 3.6.

A coincidence of events can also be the result of two (or more) γ rays that were emitted during the same decay. This decreases the count rate at the energies of the involved γ rays (summing out), but increases the count rate at the sum of their energies (summing in). A correction of these effects is important for measurements with high detection efficiency, e.g., in close geometry. The summing-in count rate, which is the product of the count rate of the first γ ray with the emission probabilities (≤ 1), the angular correlations (≈ 1), and the full-energy-peak efficiencies ε (≈ 0.001 , see section 3.4.3) of the following γ rays, is negligible in this work. The relative event loss due to summing-out is the product of the angular correlation with the probabilities for the deposition of energy in the HPGe or BGO detectors ($< 0.5\%$, estimated from efficiency simulation, see section 3.4.3) and for having correlated γ rays. For NRF transitions to the ground state the probability for having correlated γ rays can be estimated as $1 - c_{\text{feed}}$ (see feeding correction in section 3.4.1) multiplied with the average number of steps of the feeding cascade (see figure 3.15). For the ground-state transitions from the levels at 2212 keV and above 2956 keV summing-out can be neglected. For NRF transitions to lower excited states, which always lead to correlated γ rays, summing-out event losses of less than 1% are expected.

NRF transitions of carbon

In section 3.3 the mass loss of the CD_2 in the target was discussed and it was assumed that the carbon content is constant. It was tried to verify this assumption by comparing the summed count rates of the NRF transitions of carbon and aluminum in the first (I) and the second (II) half of the measurement. The ratio $(R_{\text{Al,II}}/R_{\text{C,II}})/(R_{\text{Al,I}}/R_{\text{C,I}})$ has been determined to 0.90 ± 0.13 for detector 1, to 1.09 ± 0.16 for detector 3, and to 0.99 ± 0.10 if the yields of both detectors are added. If the mass loss of the target was only caused by a reduction of carbon atoms, then a ratio of 1.0072 would have been expected. Thus, the statistical precision of the count rates is not sufficient to exclude this possibility or verify the assumption of constant carbon content.

3.4.3 HPGe efficiency

Calibration measurements

The full-energy-peak efficiency ε of the HPGe detectors is defined as the probability for the deposition of the full energy E_γ of γ rays, which are emitted isotropically at the target position, in the HPGe crystal. At certain energies below 2.8 MeV, ε was calibrated with radioactive ^{137}Cs , ^{60}Co , ^{88}Y , and ^{226}Ra sources, of which the reference activity A_0 was known with relative uncertainties of 0.5 %, 0.3 %, 0.6 %, and 1.7 %, respectively. The calibration measurements have been carried out when the beam was switched off before and after the experiment. The ^{60}Co sources used for event loss monitoring were only installed after the efficiency calibration with ^{60}Co .

The full-energy-peak efficiency is calculated from the peak area A determined with the integration method and the live time t_{live} by

$$\varepsilon(E_\gamma) = \frac{1}{\dot{N}_\gamma} \left(\frac{A + A_{\text{summing}}}{t_{\text{live}}} - \frac{A_{\text{bg}}}{t_{\text{live,bg}}} \right) \quad \dot{N}_\gamma = c_{\text{trans}} p A_0 e^{-\ln 2 \Delta t / T_{1/2}}. \quad (3.11)$$

The source strength \dot{N}_γ was calculated for each γ ray from the photon emission probability p , the half-life $T_{1/2}$, and the difference of reference time and measurement time Δt . Using atomic cross section data from [Berger2010], the photon transmission coefficient c_{trans} for the material surrounding the source has been calculated. The attenuation was about 5 % for the ^{226}Ra source, which is contained in a 6 mm thick plastic disc, and less than 0.4 % for the other sources. Count rate and relative dead time were nearly the same as in the background measurements. Therefore, losses due to pile-up of uncorrelated events are neglected. For ^{60}Co and ^{88}Y with their simple cascade decays, the small summing-out correction ($A_{\text{summing}}/A < 0.5$ %) was calculated as described in [Knoll1999, p. 322] using the total efficiency of the HPGe–BGO system (from the simulation described below) and the angular correlation between the photons. The summing-in correction for ^{88}Y is negligible. The background measurements have been checked for possible peaks at the same energy. Only for ^{226}Ra such background peaks have been observed and the count rate $A_{\text{bg}}/t_{\text{live,bg}}$ has been subtracted, which changed ε by less than 1 %.

The results are shown in figure 3.20. The relative uncertainties of the efficiency of detector 1 are 1.0 % for the γ ray of ^{137}Cs , 0.6 % for the γ rays of ^{60}Co , and 1.3 %, 1.5 %, and 10 % for the γ rays of ^{88}Y at 898 keV, 1836 keV, and 2734 keV, respectively. The γ rays of ^{226}Ra have relative uncertainties of 6 % at 2448 keV and 1.8–2.8 % at lower energies. They follow a similar energy dependence, but their normalization is a few percent lower compared to the other sources. Possible explanations for this deviation are event losses due to the high activity or an incorrect reference activity due to leaking of gaseous decay products. If summing corrections were applied for the γ rays of the ^{226}Ra source, which are mostly cascade transitions of the decay product ^{214}Po , it could still be used to determine the relative efficiency. The efficiency of detector 3 has similar energy dependence and uncertainties, but is 2–4 % lower at energies below 2 MeV. The dominant contributions to the uncertainty are from A and A_0 .

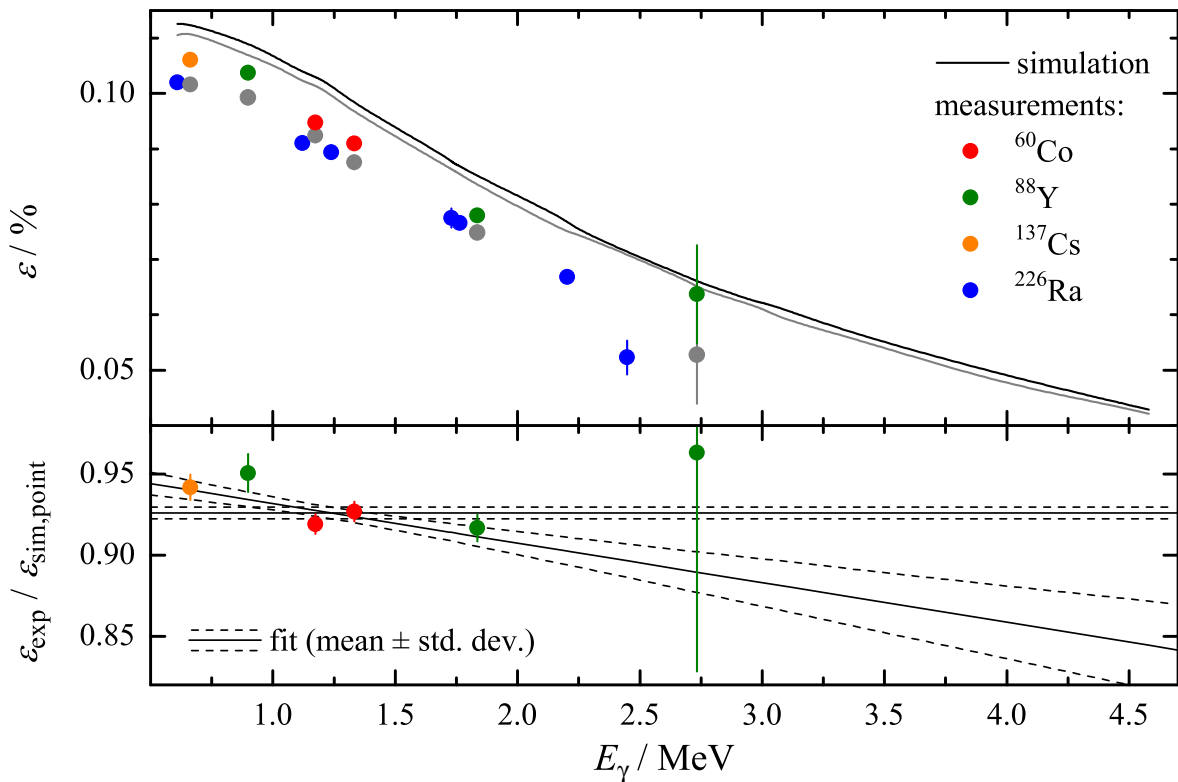


Figure 3.20: The upper panel shows the measured and simulated full-energy-peak efficiency of the HPGe detectors 1 (colored and black) and 3 (gray) for the detection of γ rays emitted from a point source at the target position. The lower panel shows a constant and a linear fit to the ratio of measured and simulated efficiencies of detector 1, in which the data points of ^{226}Ra have not been included.

The difference between the detectors comes very likely from the misalignment of detector 3, which was only recognized after the $d(\gamma,n)p$ experiment and which was related to a shifted reference point at the detector frame. The intersection points of the detector axes with the beam axis (z -axis) have been determined with a line laser. The target center is defined as the origin ($z_{\text{target}} = 0$). An analysis of the pictures in figure 3.21 results in $z_3 = 5$ mm and $z_1 = -1$ mm. From the small deviation between target center and detector 1, the precision of the alignment can be estimated to about 1 mm. Another approach, which is independent of the picture analysis, is a geometric calculation based on the shift of the reference point of detector 3. This results in an offset of $z_3 - z_1 = 6$ mm, too, and also reveals negligible changes of the angle $\vartheta_3 = (115 + 0.24)^\circ$ and the distance to the target center $d_3 = (245 + 0.01)$ mm of HPGe detector 3. To study how the efficiency was affected by the misalignment, some measurements with a ^{60}Co source that was placed in the xz -plane with up to 20 mm distance to the target center have been done. These measurements are compared to simulations later (see figure 3.23).

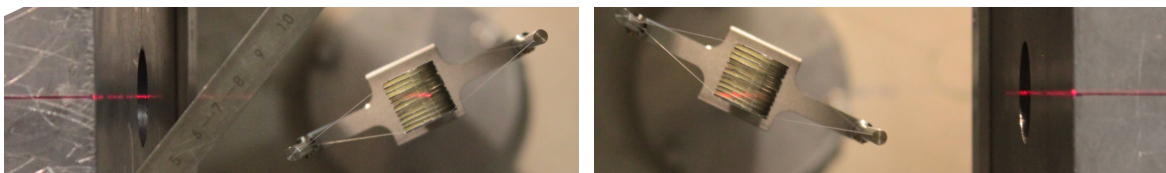


Figure 3.21: Pictures of target and collimator entrance holes of HPGe detector 1 (left) and 3 (right) taken from above. A red line laser has been used to check the alignment of the detector axes with the target after the $d(\gamma,n)p$ experiment.

GEANT4 simulation

For an experimental efficiency calibration at higher energies there are not many suitable γ -ray emitters and usually cascade transitions with known relative intensity from (n,γ) or (p,γ) reactions [Trompler2009] are used to determine efficiency ratios. For the determination of the photon flux, the efficiency must be known at the energies of the γ rays of ^{27}Al . Hence, apart from the extrapolation to higher energies, one must also interpolate between the measured data using a suitable analytic or simulated curve [Rusev2006, Nair2009]. A simulation has the advantage that also other effects such as the detector misalignment or the position dependence of the point of photon emission can be investigated.

An efficiency simulation with the software GEANT4 (version 9.4, patch-03) [Geant4-2003] has been done using an implementation of the detector geometry from [Rusev2006], which was modified by [Massarczyk2010]. Figure 3.22 shows the geometry, to which the target holder was added and in which the detectors were aligned as found after the experiment. A very important modification was an alternative implementation of the mount cup and the end cap of the HPGe crystals by using simple tubes (*G4Tubs*) rather than *G4Polycone* shapes because the latter resulted in a strong, unphysical reduction of detected events when photons were emitted off the detector axis. In the simulation, monoenergetic photons were started isotropically from the target center. The energy deposited in the HPGe crystal and in the BGO was stored for each event and put into histograms. The efficiency was calculated as the ratio of the number of full-energy events in the HPGe spectrum to the number of started photons. Figure 3.20 shows that the simulated efficiencies of detector 1 and 3 fit well to the energy dependence found in the calibration measurements, but are about 8 % higher. Deviations between measured and simulated efficiencies of similar setups have

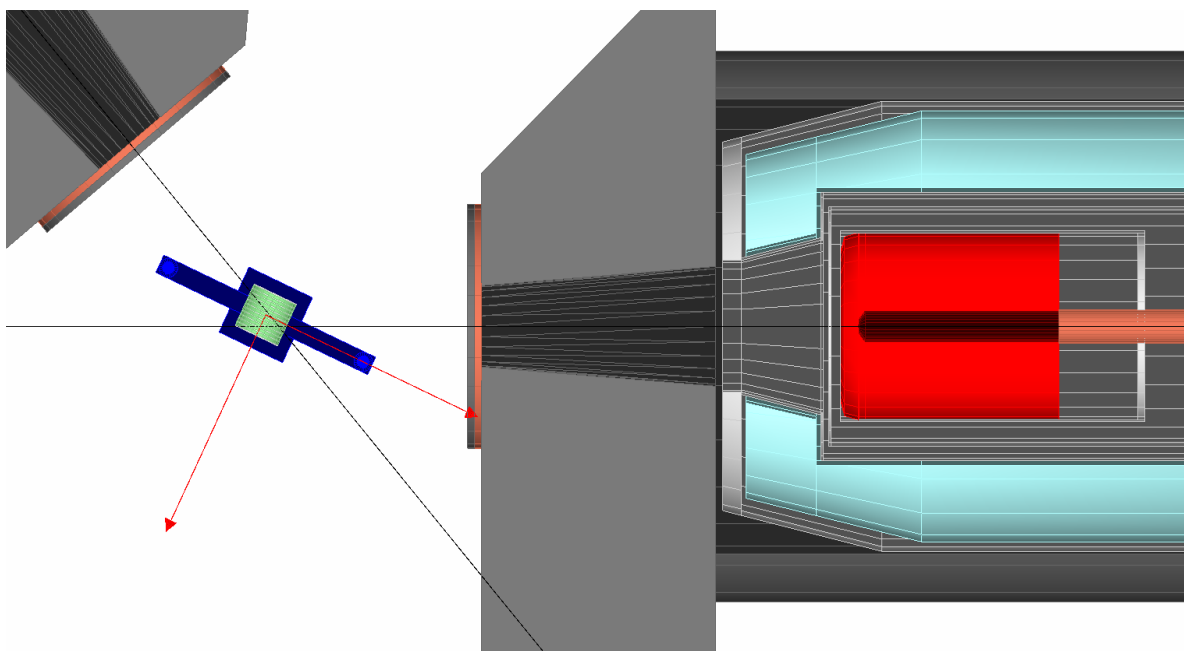


Figure 3.22: Geometry of efficiency simulation with GEANT4. For the picture, which shows a view from above ($y > 0$) in direction $(0, -1, 0)$, parts of the geometry with $y > 0$ were cut away. On the right, the closed-ended, coaxial HPGe detector 3 (red) is surrounded by aluminum (light gray), BGO (light blue), and lead (dark gray). The collimator and the absorber plates made of copper and lead are shown in the center (detector 3) and at the top on the left (detector 1). The target holder made of steel (dark blue) and the target are shown on the left, too. The z -axis (beam axis) and the x -axis are visualized by 10 cm long red arrows. The detector axes (black) visualize the misalignment. Target and axes were removed for the simulation.

been reported in [Rusev2006, Nair2009, Erhard2009, Wagner2013b], too. The reason could be an insufficient knowledge of the geometry. In [Wagner2013b] it was shown that modifications of the source–detector distance or the shape and size of the HPGc crystals can lead to better agreement. Increasing the source–detector distance in the simulation of the $d(\gamma,n)p$ experiment by 5 mm would decrease the efficiencies of detector 1 by about 4 %. Another explanation could be that the simulation relies on the simplification that an energy deposition leads to the same signal independent of the interaction position, i.e., that there is a uniform energy-to-charge conversion in the whole detector. In the simulation, only the lithium-doped contact layer is considered as a dead layer.

Scaling of simulated efficiency

As consequence of the deviations, the simulated efficiency curve for a point source at the origin was scaled to the efficiency measured with the ^{137}Cs , ^{60}Co , and ^{88}Y sources. The ratios of measured and simulated efficiencies were fitted with a constant f_0 as well as with a linear function $f_1 = a + bE_\gamma$, see figure 3.20. A least-squares minimization was used that treats the common systematic uncertainty of the source strength in the ^{60}Co and ^{88}Y data sets as correlation, although the effect of this correlation was found to be very small. The parameters and their uncertainties of the linear fit functions of detector 1 and 3 are similar. The deviation between constant and linear fit increases from 0 at $E_\gamma = 1.3$ MeV to about 10 % at $E_\gamma = 4.5$ MeV while over the same energy range the relative uncertainty of the linear scaling factors increases from 0.4 to 3.4 %. The scaling factor from the constant fit has a relative uncertainty of 0.4 %. The goodness of fit (weighted sum of squared residuals χ_i^2 from detector i divided by the number of degrees of freedom ν) favors the linear fit ($\chi_i^2/\nu \approx 1.1$) above the constant fit ($\chi_1^2/\nu \approx 2.8$, $\chi_3^2/\nu \approx 1.6$). Therefore the linear scaling factor f_1 has been used.

Position dependence

The efficiency was measured with point sources placed at the target center, but in the $d(\gamma,n)p$ experiment the target had a finite size (diameter and length of 20 mm). The position dependence of the efficiency was measured with a ^{60}Co source, which was placed on the x - and the z -axis up to 20 mm away from the target center and compared to the simulation. The resulting full-energy-peak efficiency profiles normalized to the target center are shown in figure 3.23. The simulated curves at different energies look nearly identical because the shape is mainly determined by the change of the solid angle, which is confined by the collimator. Apart from the effect of the misalignment (shifted mean values in z -direction), detector 3 is similar to detector 1. In y -direction (upwards) the efficiency forms a plateau between -10 and 10 mm and then drops to about 60 % at ± 25 mm. The efficiency profile in z -direction (beam direction) looks the same, but has a small asymmetry because of the detector angle of $\vartheta = 115^\circ$. In x -direction, which is close to the detector axes, the profile is linear. The relative uncertainties are about 2 % for the measurements and about 1 % for the simulations. Within these uncertainties the agreement between simulation and measurement is very good. Similar results for the position dependence of the efficiency of these and other HPGc detectors have been reported in [Trompler2009, Massarczyk2014].

For the photon flux determination that uses the NRF transitions of ^{27}Al , the efficiency must be known for γ rays emitted from the whole volume of the aluminum in the target. It was therefore obtained from the simulation for all twelve aluminum layers individually. The weighted average from these layers was calculated for each energy with the transmission coefficient of the incoming beam to the layer center as weighting factor. The resulting volume-source efficiency ϵ_{volume} of detector 1 is only 2 % less than that of a point source. For detector 3 this deviation is 3 %. Finally, the linearly scaled volume-source efficiency $\epsilon = f_1 \epsilon_{\text{volume}}$ has been used in equation (3.2) to determine the absolute photon flux.

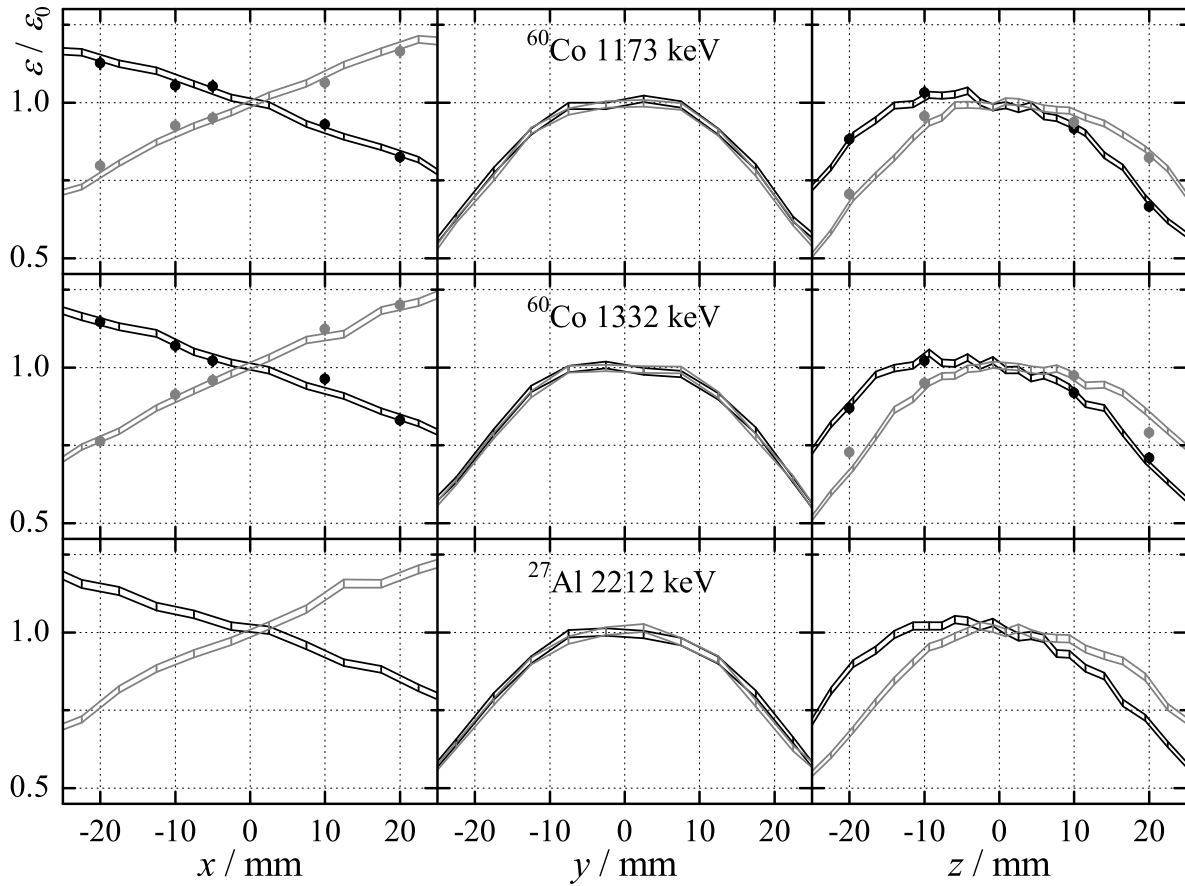


Figure 3.23: Position-dependent full-energy-peak efficiency ε of detectors 1 (black) and 3 (gray) normalized to the efficiency ε_0 at the origin (target center). In each column the position of the point source was varied on one axis while the other two coordinates were zero. The rows differ by the γ -ray energy, which is given in the central column. For the measurements (data points) the corrections for summing-out and absorption in the source were neglected because their variation with the position is negligible. The lines connect the error bars of the simulations.

3.4.4 Normalization and uncertainties

The results of the photon flux measurement are given in table 3.7 for detector 1. The total uncertainties are dominated by the uncertainties of the peak area A and the integrated scattering cross section I_S . For both detectors, the results are very similar, see figure 3.24. The ratio between the fluxes of both detectors, in which several systematic uncertainties cancel each other out, is compatible to 1 within the uncertainties for all transitions listed in table 3.7.

The ratio of the measured photon flux and the calculated photon flux from section 3.2.4 is used to determine the normalization constant N_{norm} , which then allows to calculate the photon flux at any energy by

$$\frac{d\Phi_\gamma(E_\gamma)}{dE_\gamma} = N_{\text{norm}} c_{\text{window}}(E_\gamma) \frac{d\sigma}{dE_\gamma}(E_\gamma). \quad (3.12)$$

Only the ground-state transitions from the levels at 2212, 2982, 3004, 3956, 4410, and 4580 keV, which cover the whole energy range of interest for the $d(\gamma,n)p$ reaction, have been used for the determination of N_{norm} . The transitions from the 2735 keV level to the ground state and from the 3956 keV level to the first excited state at 844 keV are compatible with these six transitions but have much larger uncertainties. The transitions, in which the second excited state is involved ($4410 \rightarrow 1014$, $2735 \rightarrow 1014$, $1014 \rightarrow 0$) have rather large uncertainties, too, and are systematically lower by a common factor of about 1.8 for unknown reasons. A constant C was fitted to the ratio of the

Table 3.7: Measured photon flux $d\Phi_\gamma/dE_\gamma / (\text{s}^{-1} \text{cm}^{-2} \text{eV}^{-1})$ for detector 1 and its relative uncertainty, for which the relative statistical and systematic uncertainties of the factors were combined quadratically. From the bold-printed data the normalization constant was determined. Transitions to excited state are marked with * (first) or ** (second).

E_γ / keV	photon flux	rel. unc.	rel. stat. unc. from		rel. syst. unc. from			
			A	ϵ_{volume}	I_S	c_{feed}	W	f_1
1014	15.92	32.2%	31.7%	0.3%	4.7%	2.8%	0.1%	0.4%
1720**	7.22	19.2%	12.2%	0.3%	14.5%	1.2%	2.0%	0.6%
2212	10.64	2.8%	1.7%	0.4%	1.8%	0.6%	0.3%	1.0%
2735	12.86	21.2%	14.6%	0.4%	15.1%	1.6%	0.7%	1.4%
2982	7.05	3.4%	1.9%	0.4%	2.3%	0.2%	0.1%	1.6%
3004	5.79	9.6%	7.1%	0.4%	6.2%	0.0%	0.0%	1.7%
3113*	5.97	30.8%	19.5%	0.4%	23.8%	0.0%	0.0%	1.8%
3396**	2.46	15.3%	6.8%	0.4%	13.5%	0.0%	0.3%	2.0%
3956	3.09	8.6%	4.7%	0.4%	6.7%	0.0%	0.4%	2.6%
4410	2.26	14.2%	5.5%	0.5%	12.7%	0.0%	0.4%	3.0%
4580	1.31	20.7%	16.5%	0.5%	12.0%	0.0%	0.2%	3.2%

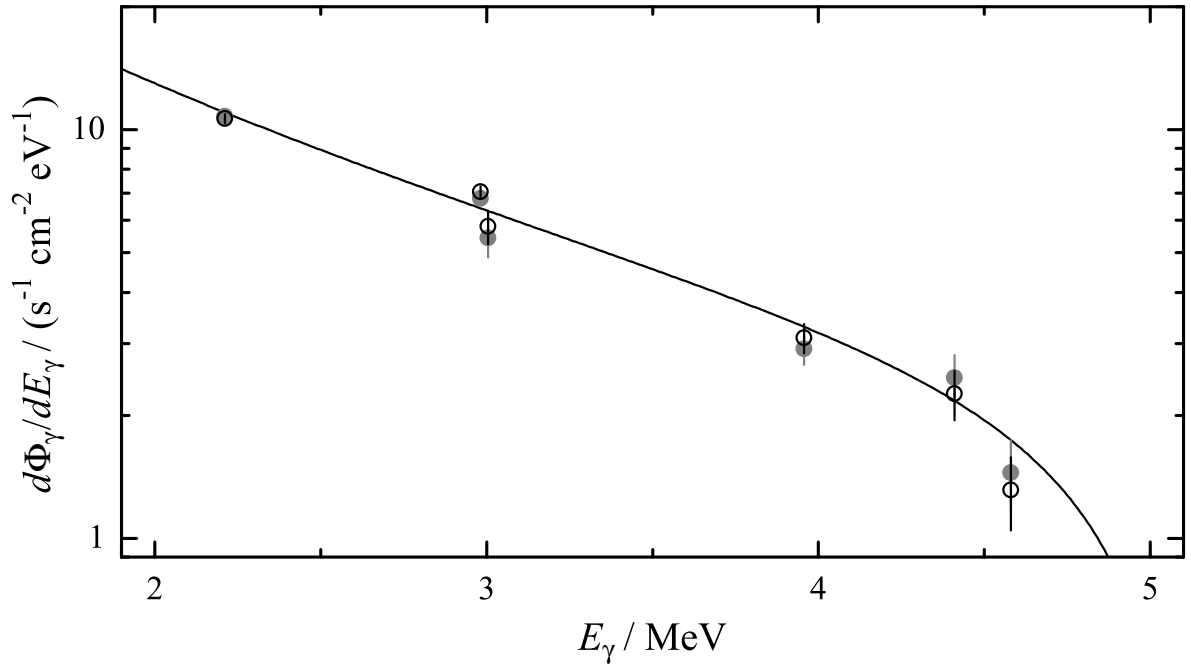


Figure 3.24: Measured and calculated photon flux. The measurements with detector 1 (black symbols) and 3 (gray symbols) are based on NRF transitions to the ground state. The calculation (black line) was fitted to the data from both detectors, see text for details.

2×6 data points and equation (3.12) with $N_{\text{norm}} = 1$. A combination of least-square minimization and Monte Carlo error propagation has been used to ensure that the correlations between the data points are taken into account. The statistical uncertainties, which come from A and ϵ_{volume} , served as the uncertainties for the least-square minimization while the mean values of I_S , c_{feed} , c_{loss} , and W as well as of the electron energy T_e and of the parameters a and b of the efficiency scaling factor f_1 were randomly sampled from a Gaussian distribution with a width given by their systematic uncertainties. For each Monte Carlo iteration the fit parameter C and its uncertainty ΔC are given by the least-square minimization. The mean values of their distributions are then N_{norm} and its statistical uncertainty σ_{stat} , while the systematic uncertainty σ_{syst} is given by the width of the

distribution of C :

$$N_{\text{norm}} = (2.372 \pm 0.021_{\text{stat}} \pm 0.045_{\text{syst}}) \frac{10^{-3} \text{ s}^{-1} \text{ cm}^{-2} \text{ eV}^{-1}}{\text{mb MeV}^{-1} \text{ per atom}}$$

$$\sigma_{\text{stat}}/N_{\text{norm}} = 0.9 \% \quad \sigma_{\text{syst}}/N_{\text{norm}} = 1.9 \% \quad \sqrt{\sigma_{\text{stat}}^2 + \sigma_{\text{syst}}^2}/N_{\text{norm}} = 2.1 \%$$

Equation (3.12) with this normalization constant is shown in figure 3.24. As a check for the correct energy dependence of the used calculation of the bremsstrahlung cross section, the ratio of measured and calculated photon flux was also fitted with a linear function. In this case, a slope compatible with zero was found.

3.5 Neutron detection

After the general description of the neutron detectors, their size, and their position in the setup on page 31, the detector properties and the analysis of the detector signals are explained in detail in this section.

3.5.1 Detection principle

Neutrons have no electric charge and belong to the group of indirectly ionizing radiation. Therefore, neutron detectors utilize nuclear reactions, which produce secondary radiation that can be detected more easily, e.g., protons, α particles, γ rays, fission fragments, or recoil nuclei. For a high detection efficiency the reactions should have large cross sections in the desired energy range. For slow neutrons the cross sections are usually higher, but their detection requires reactions with positive Q -values. In contrast, fast neutrons can transfer a measurable amount of kinetic energy to the reaction products. Neutron spectroscopy can be done by Bragg reflection (only for slow neutrons), calorimetric approaches, threshold activation, or the time-of-flight (tof) method. For a detailed discussion of the detection of slow and fast neutrons see [Knoll1999].

In the energy range relevant for BBN, the $d(\gamma,n)p$ reaction produces fast neutrons with kinetic energies between 10 and 100 keV. The maximum kinetic neutron energy in the $d(\gamma,n)p$ experiment at ELBE is about 1.5 MeV. Therefore, the proton-recoil detectors were used that had been developed for measurements at the neutron tof facility at ELBE (nELBE) in the energy range from 10 keV to 10 MeV by [Beyer2005]. Compared to lithium glass, zinc sulfide, lithium borate, or barium fluoride, plastic was the only scintillator material that fulfilled the requirement for tof measurements at nELBE, i.e., a low threshold, good time resolution, and high detection efficiency.

The detectors are made of the plastic scintillator EJ-200 manufactured by Eljen Technology, which is equivalent to Pilot F and BC-408. This material is based on polyvinyl toluene ($\text{C}_{27}\text{H}_{30}$). An electron that loses 1 MeV energy in EJ-200 causes the emission of about 10^5 scintillation photons with a most probable wavelength of 425 nm. The rise and decay times of the light emission are 0.9 ns and 2.1 ns, respectively.

Depending on their energy, fast neutrons can interact with the hydrogen and carbon nuclei in the scintillator in different ways [Knoll1999, pp. 553–565]. Nuclear reactions on carbon become important only for kinetic neutron energies above 6 MeV. Due to the small cross section, neutron interactions via the $p(n,\gamma)d$ reaction are negligible. The most important effect is elastic neutron scattering on protons. It has a high cross section (compare figure 2.6) and because of their similar masses the neutron can transfer its complete kinetic energy to the proton. Elastic neutron scattering on carbon nuclei is less efficient because the maximum fraction of transferred energy is only 28%. The energy transfer during elastic scattering depends on the scattering angle of the neutron, which

cannot be measured in these detectors. Thus, the kinetic neutron energy T_n must be calculated from the flight path l and the time of flight t with equation (2.13).

Each detector consisted of one or two 1000 mm long scintillator bars and two photomultiplier tubes (PMTs) that were mounted to the 42 mm \times (2 \times)11 mm large side surfaces of the scintillators, see figure 3.25. Compared to a readout by a single PMT there are two big advantages [Beyer2005]:

1. The difference of the two PMT time signals t_1 and t_2 allows a calculation of the detection position by $x = c_{\text{eff}}(t_1 - t_2)/2 + x_0$. The constant x_0 and the effective propagation velocity of the scintillation light c_{eff} are obtained from a position calibration with radioactive sources. The position information is important for
 - the discrimination of random coincidences, for which x can be outside the detector,
 - the subtraction of the propagation time of the scintillation light from the PMT time signal, by which the *tof* resolution improves,
 - the correct flight-path calculation, which is important for the energy resolution,
 - and the calculation of the angle of the photoneutron of the $d(\gamma,n)p$ reaction.

The *tof* can be calculated by $t = (t_1 + t_2)/2 + t_0$. The constant t_0 is obtained from signals that are assigned to photons, which travel with the speed of light. The *tof* spectra of the $d(\gamma,n)p$ experiment at ELBE are shown in figure 3.26.

2. The detection thresholds of each PMT can be decreased to values, at which even single scintillation photons are accepted. In the photocathode of the PMT, this photon can be converted to a single electron and thus has a signal amplitude as low as electronic noise. However, true signals can be discriminated from this noise by requesting a coincidence of both PMTs. The result is a stable, reproducible, and very low detection threshold for neutrons⁴.

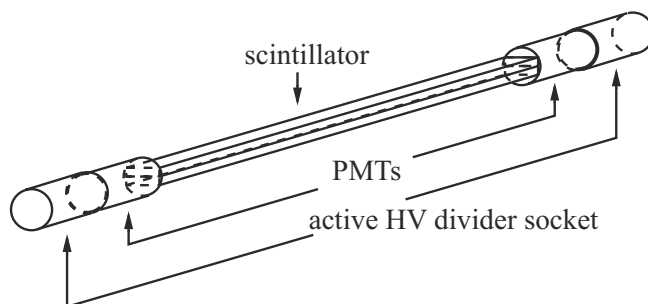


Figure 3.25: Layout of a neutron detector that consists of two scintillator bars on top of each other. In the $d(\gamma,n)p$ experiment at ELBE, this version was used at position 5 and 6, while the other four neutron detectors consisted of only one scintillator bar (compare page 31). Figure taken from [Beyer2007].

To prevent the escape of scintillation photons and the ingress of ambient light, the scintillators were wrapped with each one layer of Teflon tape, aluminum foil, and opaque tape (in that order). The optical coupling between the PMTs and the scintillator was realized by silicon grease, while for the mechanical fixing opaque heat shrink tube was used. Each detector was surrounded by a 10 mm thick lead shield to absorb bremsstrahlung photons that have been Compton-scattered in the target and ambient γ rays. In the $d(\gamma,n)p$ experiment, the lead-shielded detectors rested on a frame made from aluminum strut profiles in a way that the neutron flight paths were not blocked by any part of the setup, see figure 3.3.

The efficiency of prototypes of these detectors without lead shields has been measured by [Beyer2007], while the efficiency calibration of the lead-shielded detectors used in the $d(\gamma,n)p$ experiment is described in chapter 4. For other experiments there have been similar detector developments by [Langer2011, Kraeckmann2012, Perdikakis2012, Stuhl2014].

⁴ Due to the low threshold the unofficial name *Rosendorf Low-Amplitude-Neutron Detector (RoLAND)* was given to this detector type.

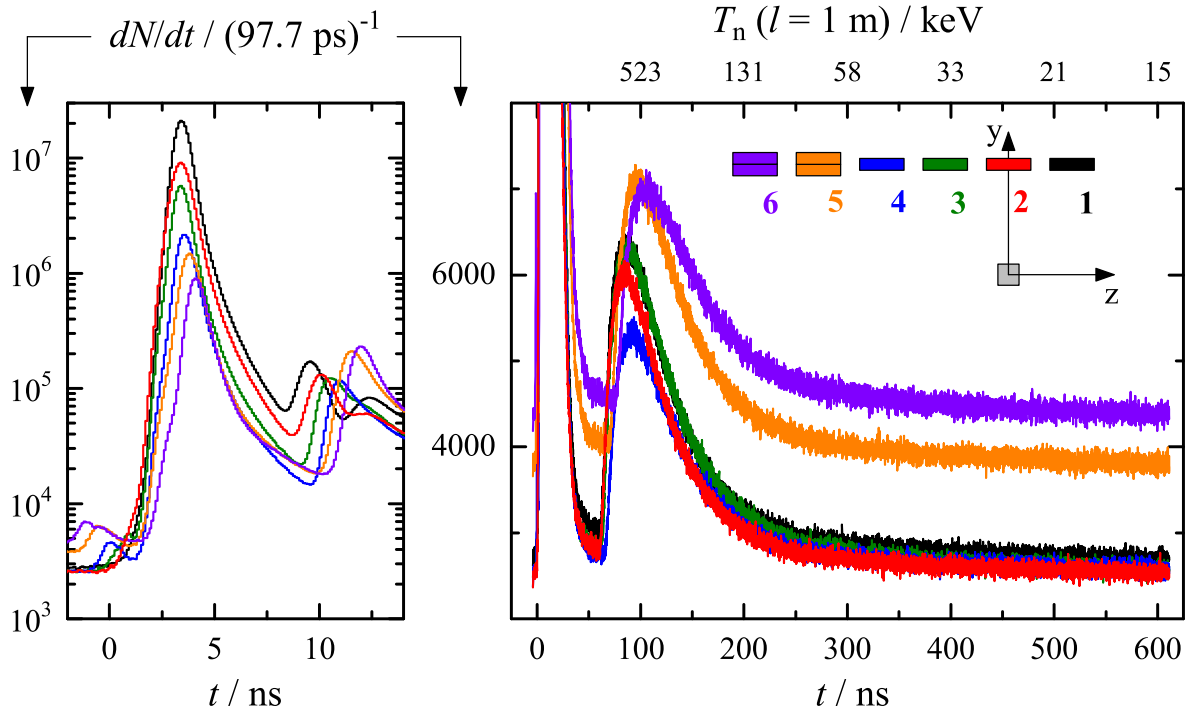


Figure 3.26: Time-of-flight spectrum of the $d(\gamma,n)p$ experiment at ELBE. The number of coincident events dN per TDC-channel width dt , which was measured in the real time $t_{\text{real}} = 123.0$ h, is shown for the six detectors as a function of the time of flight t . The left panel shows the part of spectrum containing bremsstrahlung photons that have been Compton-scattered in the target. This large photon-flash peak was used to fix the offset of t . The smaller peaks at $t \approx -1$ ns and $t \approx 10$ ns are photons scattered at the collimator exit and the beam dump, respectively. The right panel shows the whole spectrum and a sketch with the detector numbers and their position with respect to the target. The full width of the spectrum is just the micro-pulse period $t_{\text{acc}} = 615$ ns. Apart from the photon flash, the spectrum consists of a neutron distribution, which starts at $t \approx 60$ ns, and a constant background. The upper axis is labeled with the corresponding kinetic neutron energies T_n at a flight path $l = 1$ m. The detectors 5 and 6 consisted of two scintillator bars and thus had a higher detection efficiency.

3.5.2 Data acquisition and dead time

The principles of the data acquisition (DAQ) have been outlined in [Beyer2007, Hannaske2013], while elaborate descriptions of the use of this DAQ system in other experiments can be found in [Beyer2005, Beyer2013].

The 2" large *Hamamatsu R2059-01* PMTs were supplied with high voltage (HV) of up to 3 kV by the active HV divider sockets *iseg PHQ2059*. The high gain of the PMTs of up to 2×10^7 allowed to detect single-photoelectron events but also increased the afterpulse rate. Afterpulses are secondary signals that occur when rest gas in the evacuated PMTs gets ionized by the electron avalanche of a primary scintillation signal and positive ions drift back and hit the photocathode or a dynode.

The DAQ system of the neutron detectors was started and stopped synchronously to the separate DAQ system of the HPGe detectors. Events in the neutron detectors were measured in list mode with the *Multi-Branch-System*, which is a real-time data acquisition developed at GSI Darmstadt. This setup is optimized to control several VME bus crates with several front-end processors using a real-time operating system. The PMT output signals were fed into a *CAEN V874B* 4 Channel BaF₂-Calorimeter Read-Out Unit housing charge-to-digital converter (QDC) and constant-fraction discriminator (CFD) sections. A built-in veto time $\tau_{\text{CFD}} \approx 2.7$ μs in this module helped to suppress the rate of afterpulses. The QDC was used to adjust the discrimination threshold of the PMT signals

just below the single-photoelectron peak. The **CFD** output signals were fed into a *SIS 3820* scaler module to measure the detector count rates in intervals of 15 s and into the multi-hit multi-event time-to-digital converter (**TDC**) *CAEN V1190A* to determine the time information with a dispersion of 97.7 ps/channel. Within the so-called match window, which ranged from 2.2 μs before to 0.8 μs after the trigger, the **TDC** stored the time of all **CFD** signals and of the accelerator micro-pulse signals, which served as reference for the **tof** determination. A *CAEN V1495* FPGA module was used to identify coincidences of the 30 ns long **CFD** signals from the two **PMTs** of one detector and thus to trigger the **DAQ**. After each 31 events the internal memory of the modules was read out and the data was saved.

The trigger rate during the experiment was $R_{\text{trigger}} \approx 1700 \text{ s}^{-1}$, i.e., only about one out of one thousand accelerator pulses ($f_{\text{acc}} = 1.625 \text{ MHz}$) resulted in a coincident detector hit that triggered the **DAQ**. A trigger multiplicity ≥ 2 was observed in less than 0.1 % of all events, i.e., almost all triggers were generated by one detector alone. Although the match window was nearly five micro-pulse periods long, only in 0.2 % of all events there were coincident hits in more than one detector. The coincidence rates of the detectors 1, 2, 3, and 4–6, which were monitored with the scaler, were about 700, 400, 250, and each 150 s^{-1} , compare figure 3.9. As can be seen in the **tof** spectra in figure 3.26, these rates were dominated by photon and background events. In detector 2, e.g., the fractions of these events were 87.5 % and 10.5 %, while there were only 2 % neutron events.

The discrepancy between the trigger rate and the sum of the coincidence rates measured by the scaler ($\approx 1800 \text{ s}^{-1}$) was caused by the dead time of the **DAQ** system. Veto signals were sent from electronic modules that were busy to the trigger module. The longest veto signals were the **QDC** conversion time $\tau_{\text{QCD}} \approx 15 \mu\text{s}$ and the **DAQ** readout time $\tau_{\text{DAQ}} \approx 0.8 \text{ ms}$. The fraction of the real time, in which triggering was possible, can be estimated with the nonparalyzable model [Knoll1999, pp. 119–127] to $\alpha_{\text{DAQ}} = 1 - (30/31\tau_{\text{QCD}} + 1/31\tau_{\text{DAQ}})R_{\text{trigger}} \approx 0.93$. This relative live time was measured by comparing the vetoed and the free-running scaler rates of a 10 MHz pulser. Averaged over all analyzed data files one finds $\alpha_{\text{DAQ}} = 92.4 \%$. The real time was $t_{\text{real}} = 123.0 \text{ h}$, which is the same value as in the photon-flux measurement. Due to a defect of one **HV** divider, detector 5 measured ten hours less, compare figure 3.9.

The pulser–scaler method described above cannot always be used at pulsed neutron sources because there the dead-time correction can become **tof** dependent. Strong, steplike **tof** dependences are expected if the start and the length of the veto signal are described by distributions with sharp peaks and if the veto has a length comparable to the micro-pulse period. Both is true for **tof** measurements at **nELBE** (veto length: 15 μs , period 10 μs), in which the veto most often started at the photon-flash and thus stopped at a fixed **tof** in the middle of the next micro-pulse period. Thereby, deviations of the pulser–scaler method of up to 6 % were found [Hannaske2013]. In the $d(\gamma, n)p$ measurement, most of the veto signals also had a well defined start (photon flash) and length (**QDC** conversion time), but there was a much shorter micro-pulse period. Therefore, each veto stopping at a fixed **tof** was accompanied by many more fully vetoed periods, by which the **tof** dependence was drastically damped. Using the **tof** spectrum as veto start distribution and measurements of the veto length after each event over the whole $d(\gamma, n)p$ experiment, the **tof** dependence was calculated and found in very good agreement with the pulser–scaler method (deviations of $\leq 0.1 \%$).

Another source of dead time, which was not inhibiting the triggering on coincidences but their creation, was the **CFD** module with its built-in veto length $\tau_{\text{CFD}} \approx 2.7 \mu\text{s}$. The **CFD** can work much faster (signal length of 30 ns), but the veto was used to reduce the afterpulse rate of the **PMTs**. Because the **CFD** veto was shorter than the **QDC** veto, no further dead time is produced by coincident events. However, non-coincident events in one **PMT**, such as missed coincidences due to absorption of scintillation light or electronic noise, prevented the generation of another **CFD** signal from the same **PMT** and thus of coincidences during τ_{CFD} . For extreme changes of the total rates as shown figure 3.27 the effect becomes clearly visible.

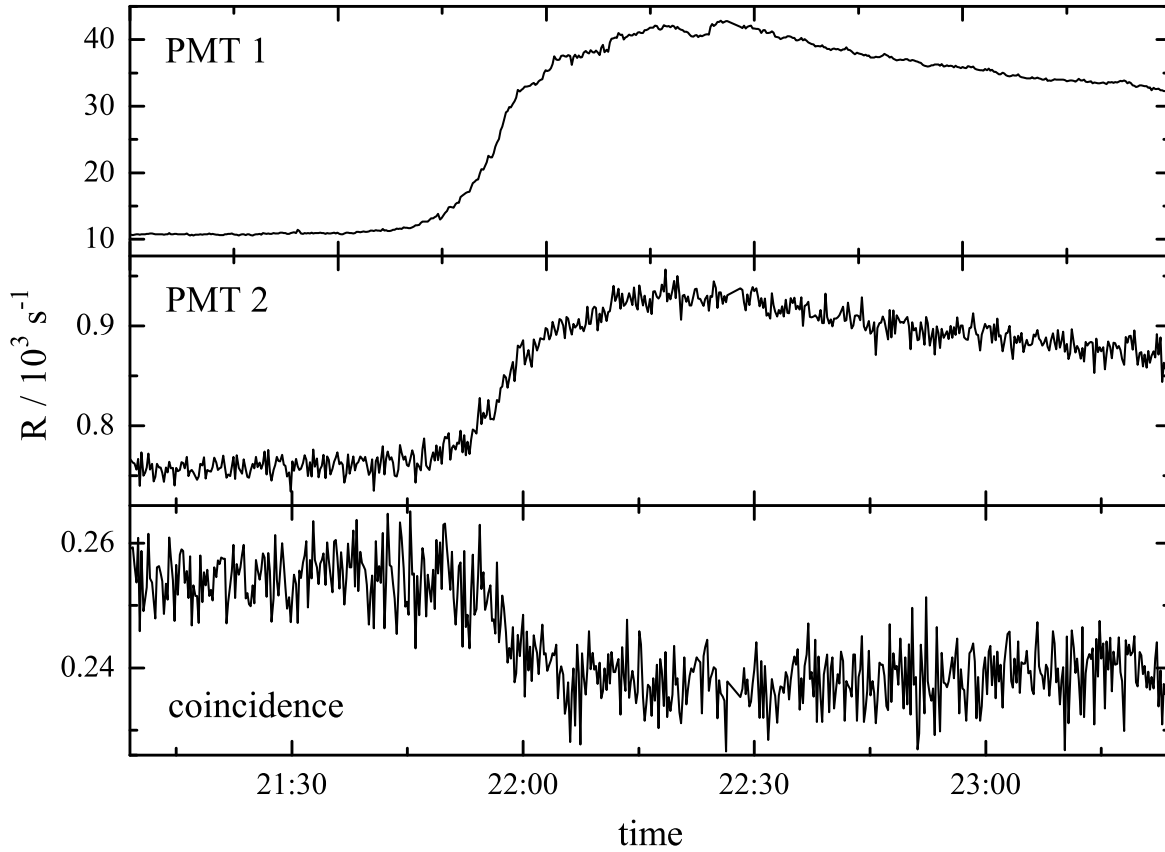


Figure 3.27: Total and coincidence count rates R_1, R_2 , and R_{12} of the PMTs of detector 3 measured in intervals of 15 s by the scaler. For reasons unknown, the total rate of PMT 1 started to increase strongly around 08.06.2010 21:45 up to 22:15. The scaler measurement of the coincident rate R_{12} has a relative live time $(1 - R_1 \tau_{\text{CFD},1}) \times (1 - R_2 \tau_{\text{CFD},2})$ that decreased from 97 to 89 %. This caused a reduction to $R_{12} \approx 255 \text{ s}^{-1} / 0.97 \times 0.89 \approx 234 \text{ s}^{-1}$. The coincidence rates of all detectors are also shown in figure 3.9.

To correct this dead-time effect it is necessary to know the length of the CFD veto, the number of non-coincident events, their *tof* distribution, and their distribution over the measurement time. The length of the CFD veto signals τ_{CFD} was considered as the shortest interval between two subsequent time signals of each PMT. The number of non-coincident events can be calculated from the total and coincidence count rates R_1, R_2 , and R_{12} that were measured in intervals of 15 s by the scaler. From their distributions over the whole experiment, the mean values \bar{R} and the relative standard deviation ε_R were determined. By analyzing the TDC data of those detectors that did not trigger an event, the rate of non-coincident signals was calculated in an alternative way (R_{TDC}). From the *tof* distribution of these events, the fraction that can be assigned to the photon flash or to neutrons was extracted ($c_{\gamma+n}$).

The obtained values are shown in table 3.8. The maximum deviation between the individual veto lengths is about 2.5 %. The PMTs did not show a uniform behavior as their rates strongly differed in their absolute scale and their fluctuations. The fluctuations of the coincidence count rates, which are mainly caused by beam intensity fluctuations, are much smaller and similar among the detectors. The absolute values of the coincidence count rate vary because of individual detection efficiencies and because the intensities of photons and neutrons from the target vary with distance and angle. The rates of non-coincident signals obtained from TDC data is quite similar to the rates measured with the scaler, which are mostly a little higher. In contrast to the coincident signals, the *tof* distribution of the non-coincident signals is mostly flat, i.e., it is dominated by signals that are uncorrelated to the time structure of the bremsstrahlung beam. Therefore, the highest fractions of signals from the photon flash or neutrons of about 15 % were only observed, if the total count

Table 3.8: Correction of dead time caused by the **CFD** veto. See text for explanation of symbols and discussion.

detector, PMT i	$\tau_{\text{CFD},i}$ (μs)	\bar{R}_i (10^3 s^{-1})	$\varepsilon_{R,i}$	\bar{R}_{12} (s^{-1})	$\varepsilon_{R,12}$	$\bar{R}_i - \bar{R}_{12}$ (10^3 s^{-1})	$\bar{R}_{\text{TDC},i}$ (10^3 s^{-1})	$c_{\gamma+n}$	α_{CFD}
1 / 1	2.69	6.19	29 %	696	5 %	5.50	5.39	1 %	0.971
1 / 2	2.74	5.26	33 %			4.57	4.54	1 %	
2 / 1	2.67	0.94	7 %	403	5 %	0.54	0.40	15 %	0.994
2 / 2	2.72	2.07	15 %			1.67	1.60	1 %	
3 / 1	2.69	13.93	80 %	253	6 %	13.68	13.35	0 %	0.941
3 / 2	2.72	0.78	12 %			0.52	0.45	5 %	
4 / 1	2.70	20.25	36 %	152	4 %	20.10	19.94	0 %	0.920
4 / 2	2.72	7.22	34 %			7.07	7.01	0 %	
5 / 1	2.71	1.18	7 %	175	4 %	1.01	0.89	3 %	0.988
5 / 2	2.69	3.54	8 %			3.37	3.36	1 %	
6 / 1	2.67	1.92	4 %	148	3 %	1.78	1.72	1 %	0.993
6 / 2	2.68	1.16	6 %			1.01	1.06	1 %	

rate was low. The resulting **tof** dependence of this dead-time correction was found to be negligible. Finally, the correction factor for the **CFD** dead time was calculated for each detector as

$$\alpha_{\text{CFD}} = \left(1 - \bar{R}_{\text{TDC},1} \tau_{\text{CFD},1}\right) \times \left(1 - \varepsilon_{R,1} \tanh\left(\varepsilon_{R,1} \bar{R}_{\text{TDC},1} \tau_{\text{CFD},1}\right)\right) \times \left(1 - \bar{R}_{\text{TDC},2} \tau_{\text{CFD},2}\right) \times \left(1 - \varepsilon_{R,2} \tanh\left(\varepsilon_{R,2} \bar{R}_{\text{TDC},2} \tau_{\text{CFD},2}\right)\right). \quad (3.13)$$

Dead-time related counting losses do not scale linearly and therefore the fluctuations of the count rates must be taken into account, which was done by the method by [Moore1980] in the terms with the tanh functions. Because the fluctuations of the coincidence count rates are low, this correction is negligible for the **DAQ** dead-time correction α_{DAQ} .

The choice of \bar{R}_{TDC} in equation (3.13) instead of the scaler rate was motivated by experiences with this correction method made with one of these detectors and a similar **DAQ** system in a neutron transmission experiment at **nELBE** [Hannaske2013]. In that experiment, the detector was positioned in a beam of photons and neutrons that was generated when a 30 MeV electron beam hit a liquid-lead target. The total and coincidence count rates of the **PMTs** measured by the scaler were $2 \times 10^4 \text{ s}^{-1}$ and $1 \times 10^4 \text{ s}^{-1}$, respectively. The analysis of non-coincident signals in the **TDC** revealed a strong **tof** dependence of the correction factor and a count rate that was only half the non-coincident scaler rate. Because the analysis of **TDC** data covers only periods before coincidences, it was suspected that a large fraction has to be assigned to afterpulses of these coincident signals. Nearly all of these afterpulses should occur within the **DAQ** busy time, so their **CFD** veto signals occur mainly in periods which are already considered as dead time and therefore only the non-coincident signals measured by the **TDC** should be used for the correction of the dead time caused by the **CFD** veto. In contrast to the transmission experiment at **nELBE**, the $d(\gamma,n)p$ experiment is characterized by much lower coincidence rates and (because of the lower electron energy) also by much lower signal amplitudes. Both result in a much lower afterpulse probability, which caused the smallness of the difference between non-coincident scaler and **TDC** rates.

In summary, relative live times of $\alpha_{\text{DAQ}} = 92.4 \%$ for all detectors due to the busy **DAQ** system and of $\alpha_{\text{CFD}} = 92.0 - 99.4 \%$ for the individual detectors due to the **CFD** veto have been determined. For α_{DAQ} a relative uncertainty of 0.1 % is estimated, which roughly corresponds to the time resolution of the pulser measurement as well as to the deviations between the pulser-scaler method and the event-wise calculation of the **tof** dependence. For the relative uncertainty of α_{CFD} a conservative estimate of 0.5 % will be used.

3.5.3 Background subtraction, energy resolution, and solid angle

Two sources of background have been detected together with the neutron signals: the photon flash and the *tof*-independent background. The photon flash, i.e., bremsstrahlung photons that have been Compton-scattered in the target, was discriminated by its well-defined *tof*, which was smaller than the neutron *tof*, see figure 3.26. Photons have also been detected after they were scattered first in the target and then in some other part of the setup. These photons had a longer flight path and thus a larger *tof*, which can be seen in additional peaks and a tail left of the photon flash. In an earlier version of this experiment, there was a comparison measurement between a deuterated and a normal polyethylene target to verify that this tail disappears before the neutron distribution starts and that the rest of the *tof* spectrum is constant [Hannaske2010]. The *tof*-independent background is related to ambient radiation, such as γ rays from the decay of ^{40}K or from the capture of thermalized neutrons. Because neutrons can be detected over the whole length of the detector, the flight path and thus the kinetic neutron energy must be calculated individually for each event. Therefore, it is not possible to subtract a constant from the *tof* spectrum before the conversion to an energy spectrum in this experiment. Instead, a scaled energy spectrum from a beam-off measurement was subtracted from the beam-on energy spectrum, whereas the scaling factor was the ratio of the constant background levels of the corresponding *tof* spectra. After normalizing beam-on and beam-off spectra to the same live time, the scaling factors were between 1.002 and 1.095.

The electron bunches were very short (≈ 2 ps) and thus the resolution of the *tof* measurement was dominated by the detectors. Their time signals vary due to the PMT properties and statistical fluctuations in the arrival time of the first scintillation photon. Therefore, a fast scintillator material with a high light yield and fast PMTs were chosen. The time and position resolution (FWHM) of the unshielded detectors had been determined with radioactive sources to 1 ns [Beyer2005, p. 56] and 5 cm [Beyer2007]. The photon-flash peaks shown in figure 3.26 have FWHM of about 1 ns and the peak position varied by less than 0.1 ns during the experiment. The relative *tof* uncertainty increases from 0.1 to 0.7 % from the lowest to the highest neutron energies. Including target and scintillator dimensions and the position resolution, flight path uncertainties between 6 mm (detector 2) and 10 mm (detector 6) are calculated, corresponding to relative uncertainties between 0.6 and 0.9 %. These values increase to 14–18 mm (1.2–1.6 %), if the lead shield is also considered as detector volume. The relative energy uncertainty is about the double of the quadratic sum of the relative *tof* and flight-path uncertainties, which follows from their propagation through equation (2.13). Without the lead shield it is 1.2 % (detector 2) and 1.7 % (detector 6) at $T_n = 15$ keV and 2.0 % at $T_n = 1.4$ MeV. These values have only a weak position dependence. Including the lead shield, the relative energy uncertainty is about 3 %. The worsening of the energy resolution due to neutron scattering in the lead shield has also been simulated for nELBE by [Beyer2013].

The angles, at which a neutron of a certain energy can be detected, are shown in figure 2.2. Neutrons from the target can directly reach the bottom face and except for the detector at $\theta = 90^\circ$ one side face of each detector. The solid angles have been determined analytically as well as by Monte Carlo integration with the same results, which are shown in table 3.9.

Table 3.9: Solid angles in 10^{-3} sr of the neutron detectors with (*) and without lead shields.

detector	1	2	3	4	5	6	1*	2*	3*	4*	5*	6*
bottom face	36.2	37.8	36.2	32.1	26.9	21.4	63.4	66.3	63.4	55.9	46.2	36.7
side face	1.5	0.0	1.5	2.8	7.2	7.8	6.2	0.0	6.2	12.6	16.5	18.0

4 Efficiency calibration of neutron detectors

4.1 Motivation and previous studies

For the absolute measurement of cross sections it is necessary to use detectors that have a well known detection efficiency, which depends on the counting geometry and the intrinsic efficiency of the detectors. The counting geometry, i.e., the solid angle, can usually be calculated (see section 3.5.3). The intrinsic efficiency, i.e., the probability that a neutron hitting the detector is registered by the DAQ system, is harder to determine. For some detectors, e.g., for uranium fission chambers with nearly 100 % detection efficiency for fission fragments, it can be calculated from nuclear data. If the detection process is more complex, e.g., if scintillation photons or interactions with structural materials have to be considered, the neutron detection efficiency can be obtained from simulation or from measurements in reference neutron fields, of which the energy distribution and the intensity are known.

In the feasibility study for the $d(\gamma,n)p$ experiment at ELBE by [Beyer2005] the neutron detection efficiency was measured with a ^{252}Cf source with a precision of 5–10 %. The γ rays from the spontaneous fission of that nuclide were detected in a close BaF_2 detector to have a reference for the tof of the neutrons measured in the plastic scintillation detector. The uncertainty of this method comes mainly from the efficiency of the reference detector, which could be strongly reduced by detecting fission fragments instead of photons, and from the counting statistics of the neutron detector, which can be a problem if the source is too weak or the detectors are too far away. The expected low counting statistics was the reason for not using this method in the $d(\gamma,n)p$ experiment.

The efficiencies of each three 11 mm and 22 mm thick detectors of the type described in section 3.5.1 have been calibrated at Germany's national metrology institute Physikalisch-Technische Bundesanstalt (PTB) Braunschweig at kinetic neutron energies of 24, 144, 250, 565, and 1200 keV by [Beyer2007]. Unlike in experiments at ELBE, where the detectors had lead shields and were only 1 m away from the target, at PTB there were no lead shields and the distances were 3 m and 4 m. Above kinetic neutron energies of 200 keV, efficiencies of about 20 % for the thin detectors and about 40 % for thick detectors were measured, while at 24 keV the efficiencies decreased to 10–15 %. The relative uncertainties were about 3 %, while the relative deviations between the individual detectors were up to 10 % for the thin detectors and up to 30 % for the thick detectors. The results of that calibration measurement were compared to simulations with NEFF7 [Dietze1982], a Monte Carlo code developed at PTB to be used for scintillation detectors at $T_n > 0.5$ MeV. Below that energy and especially close to the detection threshold there were large deviations between simulation and measurement. However, this was not unexpected, because NEFF7 was known to have deficits in the modeling of the light output function of the scintillator, the propagation of scintillation light with low intensities, and the coincident readout by two PMTs. A modified NEFF7 code that tried to improve these shortcomings showed smaller but still significant deviations. In a later experiment at nELBE, the efficiency of one shielded plastic scintillation detector was measured relative to a ^{235}U fission chamber. It agreed to the PTB calibration at 0.565 MeV and 1.2 MeV, but was significantly lower at lower energies, and also systematically higher at higher energies. A com-

parison of the measured and simulated efficiencies from the time before the $d(\gamma,n)p$ experiment is shown in figure 4.1 and discussed in [Beyer2014].

A better understanding of the discrepancies was important for the $d(\gamma,n)p$ measurement at BBN energies as well as for experiments at nELBE at energies up to 10 MeV. Furthermore, there was the need for a clarification of the influence of the lead shield and of the target–detector distance on the efficiency. Finally, since the PTB calibration in 2006 there were changes of scintillators or PMTs at some detectors. For all these reasons, a new calibration experiment was planned by [Beyer2011], which was performed and analyzed as a part of this dissertation.

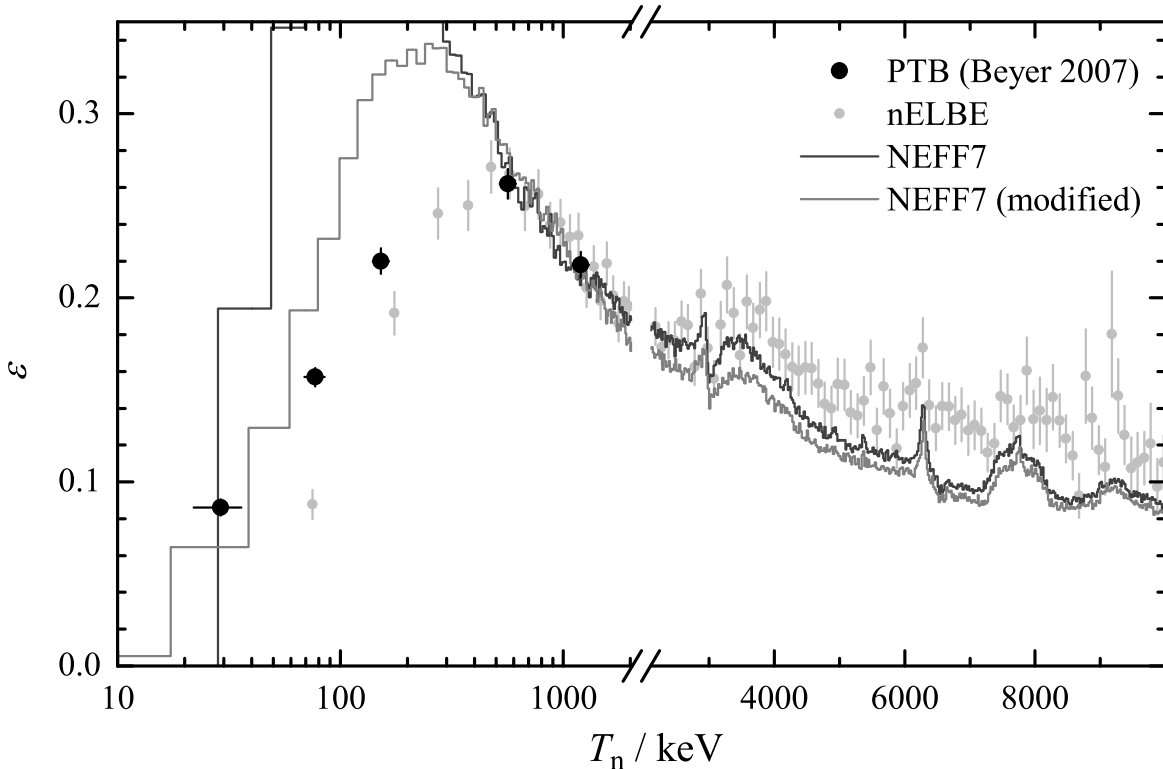


Figure 4.1: Measured (data points) and simulated (histograms) efficiency at the time before the $d(\gamma,n)p$ experiment. The PTB data is the mean of the results of the three thin detectors from [Beyer2007]. See text for details. Figure taken from [Beyer2011].

4.2 Experimental setup

For the new efficiency calibration, the shielded neutron detectors and their DAQ system were built up at the low-scatter facility at the PTB ion accelerator facility [Brede1980, Nolte2011a]. The low-scatter facility, which is shown in figure 4.2, has an area of $30\text{ m} \times 24\text{ m}$ and is 14 m high. The neutron-producing target is located 6.25 m above ground. Around it, there is a 10 m wide circular hole in the intermediate floor. This floor is made of an aluminum grid and is 4.5 m above ground. At the same height, the hole contains several movable stands, on which the plastic scintillation detectors have been mounted upright with their center on the height of the target. The $1000\text{ mm} \times 42\text{ mm}$ large detector sides faced the target. The large distances to the walls, the ground, and the ceiling as well as the avoidance of unnecessary and heavy installations strongly reduced the backscattering of neutrons to the detectors. This background was measured with shadow bars made of borated polyethylene, which absorb neutrons on the direct source–detector path, see figure 4.3. There were four different shadow bars formed like isosceles trapezoids, which shadowed either the whole detector including the lead shield or the scintillator only, and which were put up either at a distance of 1 m or 3 m. The stands of the detectors and shadow bars were moved by an electronic positioning system, which was used to adjust the distances and the angles.

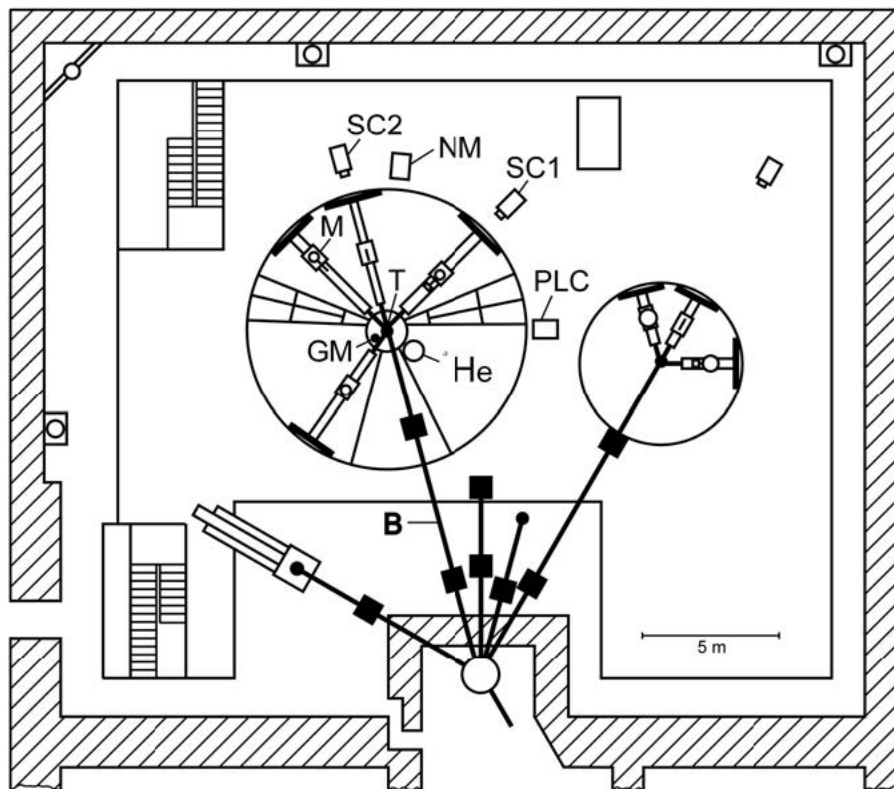


Figure 4.2: Layout (top view) of the low-scatter facility at the PTB ion accelerator facility. The abbreviations stand for the neutron-producing target (T), the movable mounting stands for detectors (M), the beam tube for charged particles (B), and several monitor detectors that are described in the text. Figure taken from [Nolte2011a].

A set of monoenergetic neutron reference fields with different mean neutron energies as specified in the ISO standard 8529-1 was used for the calibration [Nolte2011a]. Neutrons were produced at mean kinetic energies $\bar{T}_n(0^\circ)$ of about 5.0 MeV via the $D(d,n)^3\text{He}$ reaction, about 2.5 and 1.2 MeV via the $T(p,n)^3\text{He}$ reaction, and about 565, 250, and 144 keV as well as at $\bar{T}_n(76.5^\circ) \approx 24$ keV via the ${}^7\text{Li}(p,n){}^7\text{Be}$ reaction. The energy decreased with increasing angle. The reaction kinematics and the projectile energies are shown in figure 4.4. One D_2 gas target with a pressure of 0.85 bar and a beam stop made of gold as well as three solid targets with silver backing (LiF with an area density of $75 \mu\text{g}/\text{cm}^2$, Ti(T) with 1 and $2 \text{ mg}/\text{cm}^2$) have been used.

The p and d ions were accelerated by a Van-de-Graaff generator that had a nominal voltage of 3.75 MV and a typical energy resolution of 1.4 keV (FWHM) in pulsed mode [Brede1980]. The bunch length was about 1.2 ns (FWHM). Depending on the neutron energy, an accelerator frequency of 0.313 or 0.625 MHz was selected to avoid overlap of the slowest neutrons to the next pulse. A pick-up signal from the pulsed beam served as reference for the *tof*.

Because the measurement time was limited, only six neutrons detectors could be calibrated, which were chosen from all detectors used in experiments at ELBE. Among them were four shielded EJ-200 detectors from the $d(\gamma,n)p$ experiment, another detector of the same type, for which the PMTs of detector 5 from the $d(\gamma,n)p$ experiment were used, and one unshielded EJ-230 detector. All detectors were 11 mm thick. Before the beam-on measurements, there was a position calibration of each detector by fixing ${}^{137}\text{Cs}$ sources at $x = 0$ and $x = \pm 35$ cm. Three detectors were mounted in the low-scatter facility at the same time, usually at a distance of 3 m and at angles of 0 and 30° . For each of the seven nominal neutron energies described above, there was each one measurement with the wide shadow bar in front of one detector and one measurement without the shadow bar. Each measurement took between 20 and 90 minutes. There were some additional measurements, e.g., with switched detector positions, with the narrow shadow bar, at a distance reduced to 1 m, or with the 11 mm wide side of the EJ-230 detector facing the target.

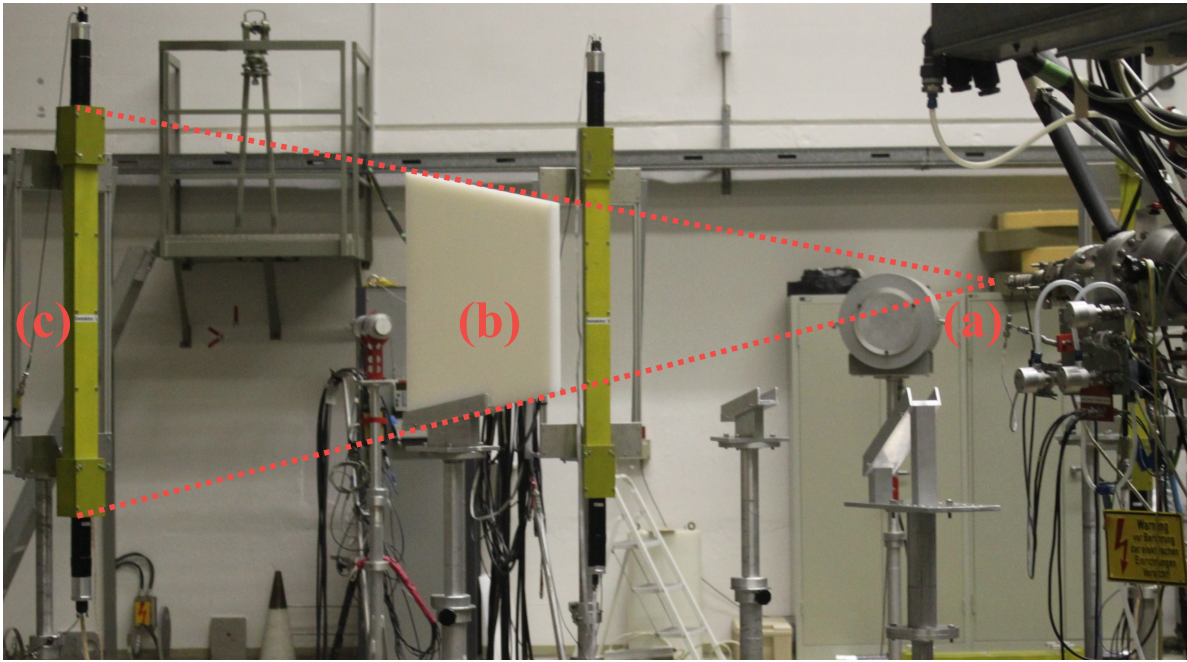


Figure 4.3: Experimental setup of the efficiency calibration at PTB Braunschweig. The dashed lines show the alignment of the neutron-producing target (a), the shadow bar used for background measurements (b), and a neutron detector at $\vartheta = 30^\circ$ (c). Another detector at the same angle can be hardly discerned right of the neutron-producing target, while the detector at $\vartheta = 0^\circ$ is shown in the center of the picture.

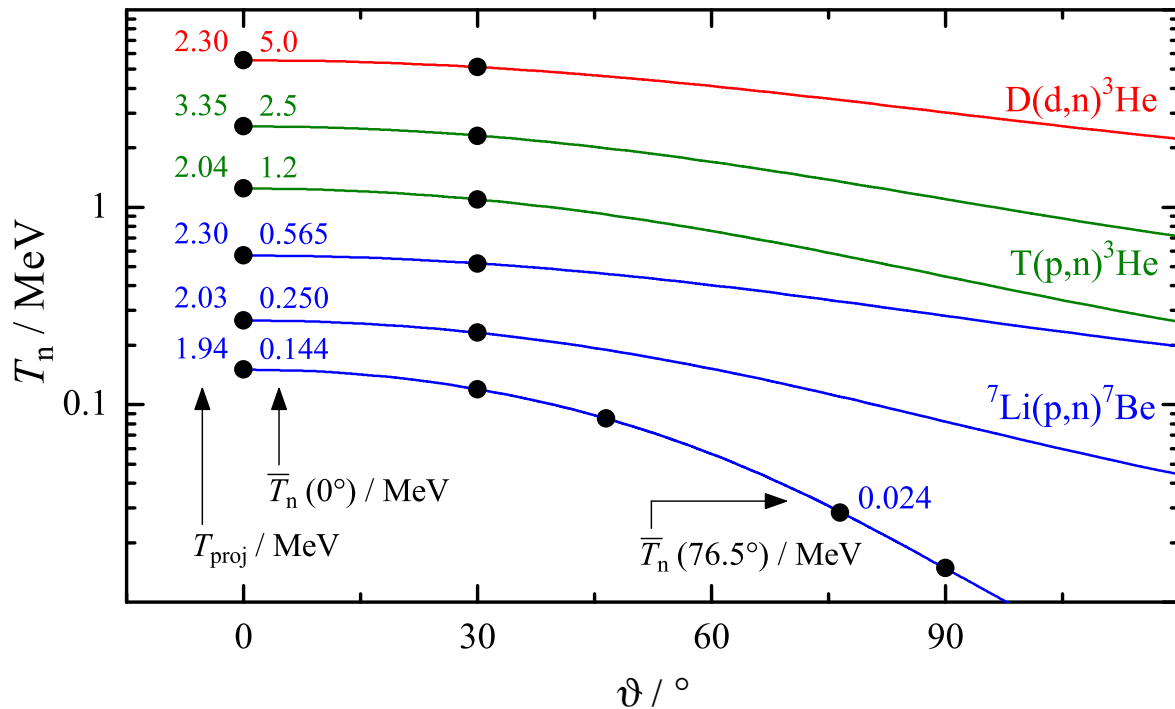


Figure 4.4: The lines show the kinematic relation between the angle ϑ and the kinetic neutron energy T_n in the lab frame for the neutron-producing reactions at the given kinetic projectile energies T_{proj} . The energy loss of the projectiles in the target was taken into account. The filled circles show the angles, at which the detectors were positioned. For some of these angles, the nominal kinetic neutron energy \bar{T}_n according to ISO standard 8529-1 is given.

4.3 Reference neutron flux

All measurements for the characterization of the neutron reference fields were performed and analyzed by [Nolte2011c]. The detector abbreviations refer to figure 4.2. The mean \bar{T}_n and the FWHM ΔT_n of the neutron energy distribution were measured with the *tof* method with scintillation detectors (SC) made of NE-102, NE-213, or lithium glass to check if the accelerator parameters were correct and the condition of the target was good. The neutron fluence was monitored during all measurements using a long counter with a ^3He proportional counter, which was called "new monitor" (NM), a De Pangher long counter with BF_3 counter (PLC), a ^3He proportional counter with moderator cap (He), a Geiger–Müller counter used as a photon monitor (GM), and a beam-charge integrator on the target. The monitor signals were counted by the scaler of the nELBE DAQ system. The monitor detectors have been calibrated using a direct current (dc) beam and reference instruments of well known efficiency [Schlegel2002a, Nolte2011b]. A recoil proton telescope [Schlegel2002b], a recoil proton proportional counter [Schlegel2002c], and an NE-213 liquid scintillator were used for these measurements, which were corrected for dead time, neutron scattering in the target, attenuation in air, and in-scattering of the reference instruments. Finally, the calibration factors of the "new monitor" f_{NM} , i.e., the number of unscattered neutrons emitted from the target in direction of the reference instrument per solid angle and per monitor count n_{NM} , have been used. Results are shown in table 4.1.

The number of incoming neutrons of a scintillation detector was calculated by

$$n_{\text{inc}} = n_{\text{NM}} f_{\text{NM}} f_{\text{att}} f_{\vartheta} \Omega, \quad (4.1)$$

in which Ω is the solid angle and f_{att} is the correction factor for neutron attenuation in air. The angular dependence of the neutron fluence is described by f_{ϑ} , which is calculated as the ratio of the differential cross sections of the neutron-producing reaction at ϑ_{det} and at the angle of the reference instrument ϑ_{ref} . The mean angle of the scintillation detector ϑ_{det} and its uncertainty were simulated with the Monte Carlo code that was also used to determine their solid angle assuming isotropically distributed neutrons. It is a little larger than the angle of the detector center, because the 1 m long detectors cover a small angular range. For the detectors positioned at a distance of 3 m and at angles ϑ of 0° , 30° , and 76.5° the mean angles ϑ_{det} were 4.7° , 30.4° , and 76.6° . At $\bar{T}_n = 144$ keV, neutron fluences have been measured at several angles and their ratios agreed well to the calculations of f_{ϑ} .

Table 4.1: The five leftmost columns are from the characterization measurements by [Nolte2011c]. The relative uncertainty of f_{NM} given in parentheses comes from the n-p scattering cross section, the calculation of the efficiency of the reference instrument, and at $\bar{T}_n = 20$ keV from the subtraction of γ -ray background. The fluence conversion factors $f_{\vartheta}(\vartheta)$ are given for a target–detector distance $d = 3$ m (^a $d = 2$ m, $\vartheta = 76.5^\circ$, ^b $d = 1$ m, $\vartheta = 90^\circ$). The three rightmost columns show typical scaler values of the total PMT rates, the coincidence rates, and the relative DAQ live time of the calibrated neutron detectors.

ϑ_{ref} ($^\circ$)	\bar{T}_n (MeV)	ΔT_n (keV)	f_{NM} (sr^{-1})	$f_{\vartheta}(0^\circ)$	$f_{\vartheta}(30^\circ)$	\bar{R}_i (10^3 s^{-1})	\bar{R}_{12}	α_{DAQ}
76.5	0.020	9	5760 (11.3%)	0.995 ^a	0.552 ^b	0.5	0.1	0.972
0	0.138	12	20190 (2.0%)	0.998	0.997	1.1	0.4	0.932
0	0.253	10	14938 (2.0%)	1.002	1.064	0.7	0.3	0.952
0	0.563	8	20534 (1.9%)	0.994	0.775	2.3	1.3	0.837
0	1.17	64	18311 (1.9%)	0.992	0.733	6.3	3.6	0.662
0	2.50	98	21185 (2.2%)	0.987	0.604	15.7	7.6	0.507
0	4.86	125	28010 (2.0%)	0.976	0.403	18.6	8.0	0.534

4.4 Data analysis and background

The number of detected neutrons n_{det} was determined by integrating the measured *tof* spectrum in an interval containing the neutron distribution, subtracting the constant background, and correcting all dead time effects. To subtract the fraction of neutrons scattered on the way from the target to the detector, the measurements with the shadow bar was analyzed in the same way and scaled to an equal number of monitor counts. In addition, the simulated fraction of neutrons scattered in the target was subtracted.

The detection principle and the **DAQ** system were similar to the $d(\gamma,n)p$ experiment at **ELBE**, see section 3.5. Data was acquired from three detectors at the same time. The count rates and the dead time, which depended on the intensity of the neutron reference field, increased with increasing \bar{T}_n , see table 4.1. Dead-time effects occurring with the used **DAQ** system have been described and discussed in section 3.5.2. At the time of the data analysis, the *tof* dependent dead-time correction was not yet developed and the pulser–scaler method was used. However, the *tof* dependence was only weak because the accelerator period of $1.6 \mu\text{s}$ was much shorter than the most frequent veto signal ($15 \mu\text{s}$). A later analysis of the *tof* dependence showed that the differences from the pulser–scaler method are between 0.001 at $\alpha_{\text{DAQ}} \approx 0.95$ and 0.01 at $\alpha_{\text{DAQ}} \approx 0.5$. The rate of non-coincident events observed in the **TDC** data was lower than the one observed by the scaler. This indicates that afterpulses occurred preferably in the **DAQ** dead time after a trigger. For a worst-case estimate of α_{CFD} , i.e., the correction factor of the dead time caused by **CFD** given by equation (3.13), the non-coincident scaler rate was used. Values of about 0.997, 0.995, 0.985, and 0.95 were found at \bar{T}_n of ≤ 0.250 , 0.565, 1.2, and ≥ 2.5 MeV. During the short measurements there were only negligible beam intensity fluctuations that had no influence on the dead-time correction in equation (3.13).

Typical *tof* spectra measured at **PTB** are shown in figure 4.5. The peak close to $t = 0$ is the photon flash and the other large peak comes from the monoenergetic neutrons. If only the scintillator was shadowed from the neutron-producing target by the 500 mm thick and 25 mm wide shadow bar, then the rate of detected neutrons decreased by about one order of magnitude. With the 40 mm wide shadow bar that also shadowed the lead shield, the reduction was about two orders of magnitude. In both cases, the reduction in the tail towards higher *tof* was much lower, i.e., these events come from neutrons that have not taken the direct flight path but must have been scattered into the detector. The *tof*-independent background is between two and four orders of magnitude lower than the maximum number of neutron events per bin. During the calibration measurements with $\bar{T}_n \leq 0.250$ MeV, the *tof*-independent background in the shielded **EJ-200** detectors was at the beam-off level of about 60 s^{-1} . It increased to about 500 s^{-1} at $\bar{T}_n \geq 1.2$ MeV. The *tof*-independent background level in shadow-bar measurements was usually about 5 % lower, but at 0.565 and at 5.0 MeV it was 13 % and 28 % lower, respectively, compare figure 4.5. An explanation for this reduction might be neutrons with kinetic energies below 20 keV after scattering in the target, which makes them slow enough to reach the 3 m distant detector in the next accelerator period $1.6 \mu\text{s}$ later.

Apart from the contributions of the photon flash, the neutrons, and the constant background, there are some more *tof* dependent events visible especially at higher energies. The original frequency of the accelerator of 2.5 MHz was reduced by factors of 4 or 8 by periodically deflecting the projectile beam away from an aperture. However, even when deflected away, the transmission through the aperture seems to be in the order of 0.1 %. This leads to weak neutron peaks delayed by integer multiples of 400 ns, which can be seen in the lower panel of figure 4.5. In that panel, there is also a small surplus of events at $t = 150$ ns when a shadow bar made of borated polyethylene of the neighboring detectors was used. These events are assigned to elastic neutron scattering on protons in that shadow bar, because the belonging *tof* can be calculated from the angle-dependent energy after the scattering and the longer flight path. The calculated *tof* of neutrons scattered in from the other detectors or their lead shields was much longer than that of unscattered neutrons.

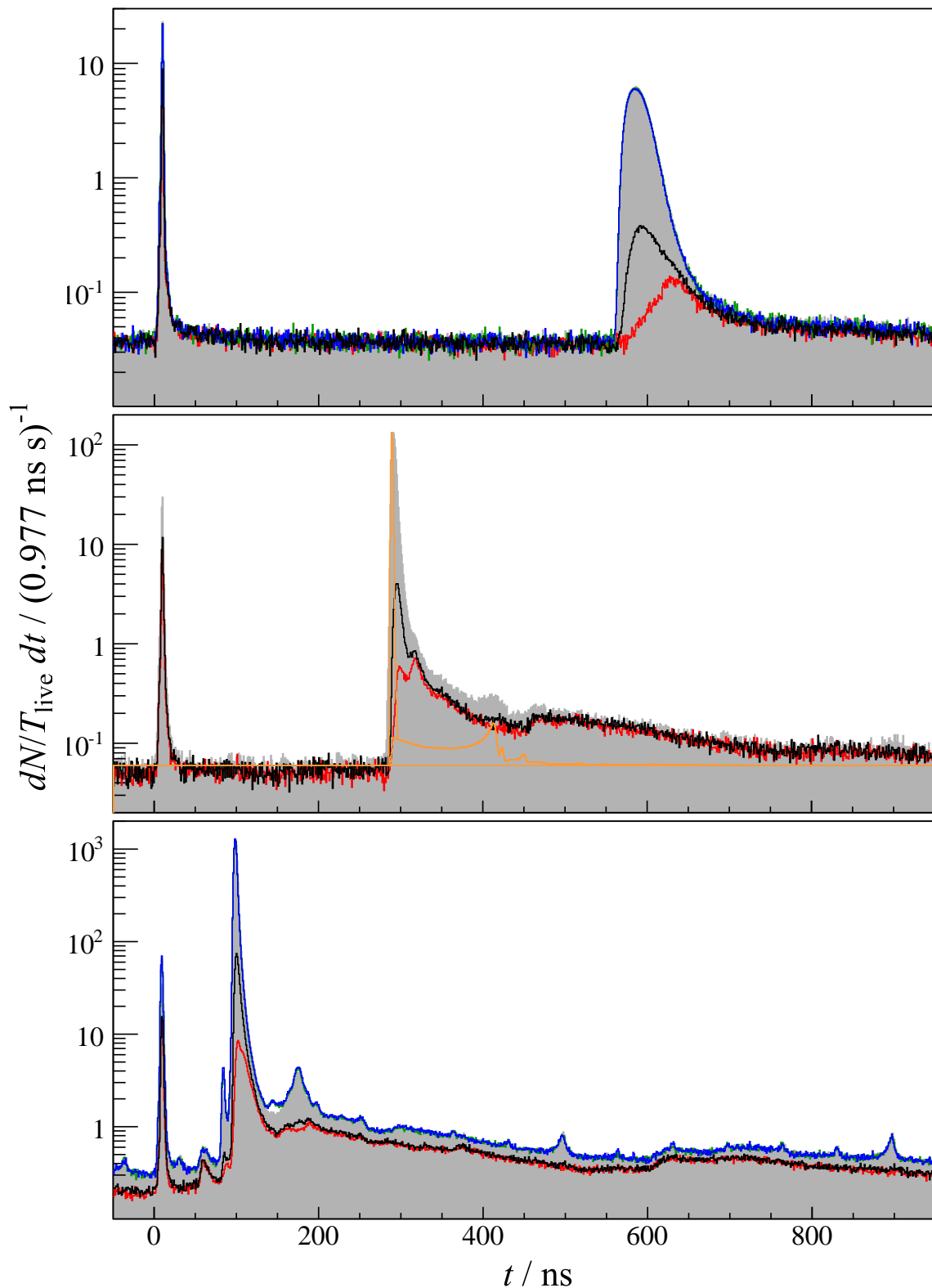


Figure 4.5: Time-of-flight spectra measured at PTB at mean kinetic neutron energies of about 144 keV (upper panel), 565 keV (middle panel), and 5 MeV (lower panel). In each panel, several measurements of detector 1 at an angle of 0° and at a distance of 3 m are shown: without any shadow bar (gray), with a narrow (black) and wide (red) shadow bar shading this detector, and with wide shadow bars shading one of the neighboring detectors at 30° (blue and green). For this picture, the measurements were normalized to their live time, but not to the neutron fluence, which differed by a few percent. The peak close to $t = 0$ is the photon flash, the other large peak comes from the monoenergetic neutrons. The three stacked orange histograms in the middle panel are the unscattered and scattered neutrons simulated with TARGET and a constant (all scaled to the measurement). See text for further discussion.

The Monte Carlo code TARGET [Schlegel2005], which was developed at PTB Braunschweig, has been used to simulate the neutron energy distribution including the background from neutrons interacting with parts of the target or with air. Such simulations are important for the energy measurements and the monitor calibration described in section 4.3, especially when the *tof* method could not be used together with a *dc* beam. For the detectors to be calibrated, the simulation offers an estimate of the background from neutrons scattered in the target.

The TARGET code uses a realistic geometry of the target cell and neutron cross section data of the neutron-producing materials, such as T or ^7Li , as well as of structural materials, such as Al or Ag. Straggling of the projectiles and the time resolution of the detector are taken into account. Due to technical problems, it was not possible to simulate the background from the D_2 gas target or to consider the length of the projectile pulses. Furthermore, the only available detector shape is a cylinder, to which the width (42 mm) and thickness (11 mm) of the scintillator bars was given. Simulated spectral fluences of scattered and unscattered neutrons as functions of *tof* or kinetic energy are shown in figures 4.5 and 4.6. It can be seen that the spectral fluence of neutrons scattered in the target is two to three orders of magnitude lower than for unscattered neutrons. Scattered neutrons have fractions between 1.5 and 5 % of the total fluence, but due to their different kinetic energy, most of them are well separable from the unscattered neutrons by their *tof*. The fraction of scattered neutrons having the same *tof* as the unscattered neutrons is negligible and a subtraction is not necessary, also because their flight path and thus their energy is similar.

Compared to the TARGET simulation, the measured *tof* spectra had a small shift towards lower energies and were broader. These difference could neither be explained by the time distribution of the projectile beam, which was obtained from a fit of the photon flash (1.6–3.1 ns FWHM), nor from the larger dimensions of the detector. It must be assumed that compared to the simulation the real neutron-producing target was thicker (e.g., due to diffusion into the backing) and covered by a dead layer. Similar findings were mentioned by [Nolte2011a, Nolte2011c].

4.5 Detection efficiency and uncertainties

The intrinsic neutron detection efficiency $\varepsilon = n_{\text{det}}/n_{\text{inc}}$ was calculated from the number of detected and incoming neutrons, which were described in sections 4.3 and 4.4. The results are shown in figure 4.7 and table 4.2. The efficiency curves of the five calibrated EJ-200 detectors have similar shapes, but differ strongly in their maximum efficiency and the energy at which the maximum is reached. For the extreme cases of the efficiencies of detectors 2 and 3 the largest ratio is $0.064/0.014 = 4.4$ at 20 keV, while towards higher energies the difference becomes smaller and reaches a minimum at 2.5 MeV. The slightly larger difference at 5 MeV is probably due to slightly different energies, at which such differences are also visible in the results from previous studies. Although detector 5n was constructed only a few months before this measurement, its efficiency is very similar to that measured with other detectors during the first PTB calibration and at energies above 0.5 MeV to the older nELBE measurement. No significant differences between the efficiencies of detector 1 calibrated at a target–detector distance of $d = 1$ m and those at larger distances were found, especially not for the precisely measured data points below 0.3 MeV. Due to the strong variation among the detectors, a comparison of their efficiencies to the result obtained by [Beyer2007] with the unshielded detectors is meaningless.

The mean \bar{T}_n and the width σ_T of the energy distributions were calculated from the measured values given in table 4.1, which were converted from their reference angle to the mean and the width of the angular distribution seen by the detector. The relative uncertainties of ε are about 2 % in the energy range $50 \text{ keV} \leq T_n \leq 1.2 \text{ MeV}$, about 3–5 % at higher energies, and about 12 % at lower energies. In measurements at target–detector distances of $d = 1$ m the uncertainties were a little larger at $T_n \leq 0.3 \text{ MeV}$, but by a factor 3–5 larger at higher energies. The dominating contribu-

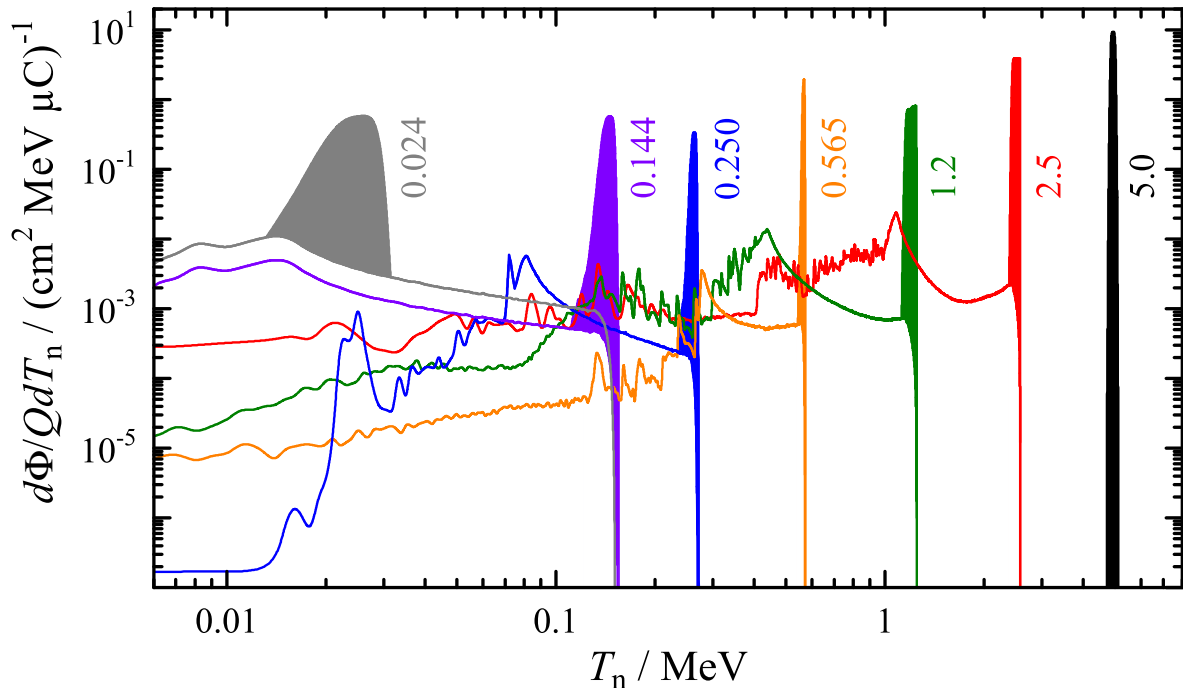


Figure 4.6: The spectral neutron fluence $d\Phi/dT_n$ simulated with TARGET and normalized to the accumulated projectile charge Q is shown for a detector (see text for geometry) at an angle of 0° and at a distance of 3 m (76.5° , 2 m for $\bar{T}_n = 0.024$ MeV). For each of the seven simulations labeled by \bar{T}_n , the unscattered neutrons are shown as a filled area stacked on the curve from scattered neutrons. At $\bar{T}_n = 5.0$ MeV no background was simulated due to technical problems.

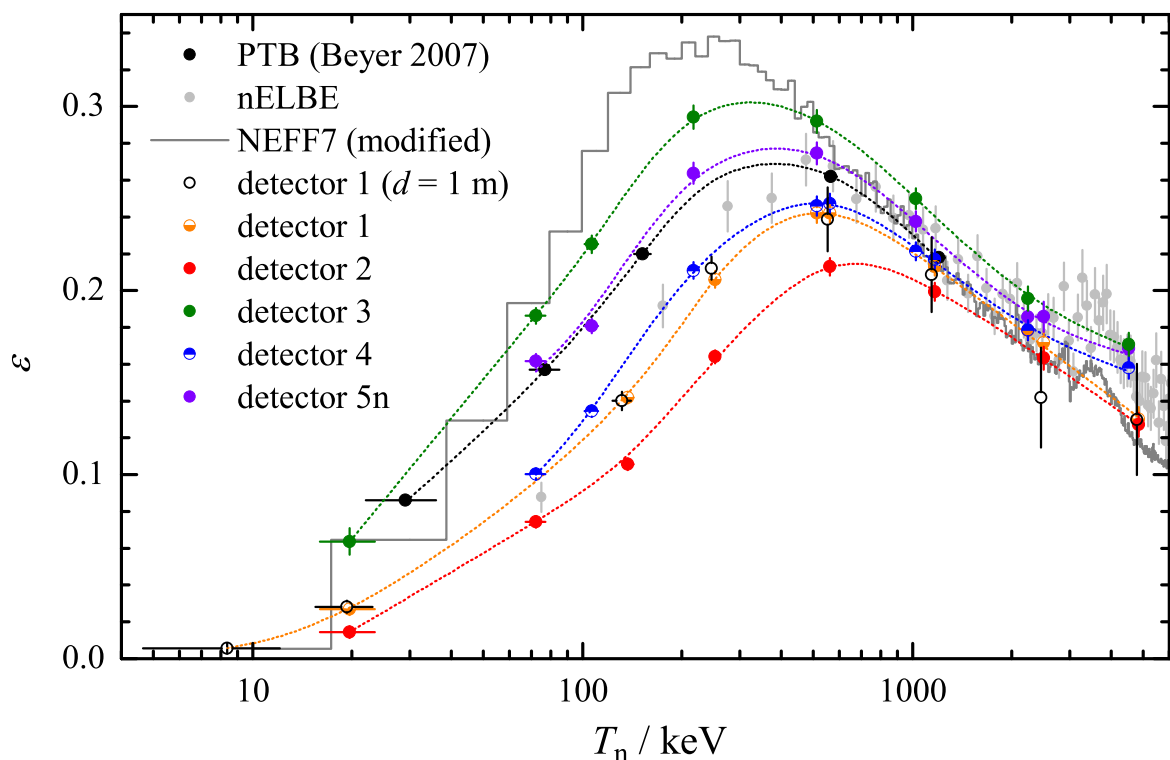


Figure 4.7: Results of the efficiency calibration of 11 mm thick EJ-200 plastic scintillation detectors at PTB Braunschweig in 2011. The detector numbers 1–4 are the same as in the $d(\gamma,n)p$ experiment at ELBE, compare figure 3.26. The dotted lines shall increase the readability of the figure. Horizontal error bars refer to the width σ_T of the energy distribution. Results from previous studies, which were shown in figure 4.1, are shown for comparison. Detector 1 was also used to study the influence of a target–detector distance d shorter than the usual 2 m at $T_n < 100$ keV and 3 m at higher energies.

Table 4.2: Measured neutron detection efficiencies ε of detector 1 with their relative uncertainties, for which the relative statistical and systematic uncertainties of the factors were combined quadratically. See text for explanations and discussion.

d (m)	\bar{T}_n (MeV)	σ_T (keV)	ε (%)	rel. unc.	rel. stat. unc. from		rel. syst. unc. from		
					n_{det}	n_{NM}	f_{NM}	f_{ϑ}	α
1	0.0084	3.7	0.6	13.4%	6.3%	0.5%	11.3%	3.4%	0.0%
2	0.0197	3.7	2.7	11.5%	1.0%	0.5%	11.3%	1.4%	0.3%
3	0.137	5	14.2	2.1%	0.1%	0.5%	2.0%	0.3%	0.4%
3	0.252	4	20.6	2.2%	0.2%	0.7%	2.0%	0.3%	0.3%
3	0.512	4	24.2	2.1%	0.1%	0.4%	1.9%	0.8%	0.4%
3	0.562	4	24.2	2.2%	0.1%	0.4%	1.9%	0.9%	0.4%
3	1.17	27	21.3	2.4%	0.1%	0.2%	1.9%	1.2%	0.8%
3	2.24	42	17.8	3.1%	0.1%	0.3%	2.2%	1.5%	1.5%
3	2.50	42	17.2	3.6%	0.1%	0.2%	2.2%	1.8%	2.2%
3	4.85	54	13.0	5.1%	0.0%	0.1%	2.0%	3.5%	3.1%

tions are the monitor calibration factors f_{NM} and (at higher energies or target–detector distances of $d = 1$ m) the fluence conversion factors f_{ϑ} and the dead time α (mainly from α_{CFD}). The statistical contributions from the number of detected neutrons n_{det} and the number of monitor counts n_{NM} are small. The uncertainty of the neutron attenuation in air is negligible. A relative uncertainty of the solid angle of about 1 % can be calculated using the uncertainties of the detector dimensions and the target-detector distance. However, the identical detectors are used in the $d(\gamma,n)p$ experiment, where only the distance is different. If only this is considered as uncertain, the relative uncertainty of the solid angle is 0.2 % and thus negligible. Improvements in the uncertainty budget are possible for the fluence conversion factors, for which rather coarse estimates were used, for the dead time effects at higher energies, for which a relative uncertainty of about 1 % is realistic, if the analysis method described in [Hannaske2013] is used, and for the reference flux at $\bar{T}_n = 24$ keV, if the $^{45}\text{Sc}(p,n)^{45}\text{Ti}$ reaction was available.

Possible explanations for the discrepancies between the five detectors shall be discussed in the following. An influence of specific signal cables or DAQ channels can be ruled out because there were several measurements with the same detector in the same neutron reference field at different positions, which agreed well to each other. The gains of the two PMTs of one detector were adjusted before the calibration by changing the high voltage until the positions of the single-photoelectron peaks observed in the beam-off QDC spectra were similar. Then the CFD threshold was set close below the single-photoelectron peak. There were detectors with different efficiencies that had similar single-photoelectron peaks and thresholds. Examples for beam-on QDC spectra at a kinetic neutron energy of about 72 keV are shown in figure 4.8 for the detectors 2 ($\varepsilon = 0.074$) and 3 ($\varepsilon = 0.186$). The positions of the single-photoelectron peak q_1 are identical for the PMTs of detector 3, while they differ by a factor 1.1 for detector 2. The widths of the single-photoelectron peak is larger for detector 2. The spectral shape is a result of the continuous energy spectrum of the recoil nuclei in the detector. The highest QDC value q_{max} , which is not related to the constant background, has its origin in a complete transfer of the kinetic neutron energy to recoil nuclei. These values are nearly identical for the two PMTs of detector 3, but differ by a factor 1.8 for detector 2. If this difference was the result of a different gain, than one would not expect that this affects the efficiency because the thresholds were properly adjusted and a variation of the gain of the PMTs over time has not been observed. The number of photoelectrons corresponding to the complete transfer of the kinetic neutron energy, which can be estimated as the ratio q_{max}/q_1 , is about 5 for PMT 1 of detector 2 and about 9 for the other three PMTs shown in figure 4.8. The maximum number of photoelectrons expected in one PMT from a 72 keV neutron can be estimated to 11 from the number of emitted scintillation photons (10^5 per MeV of deposited electron energy),

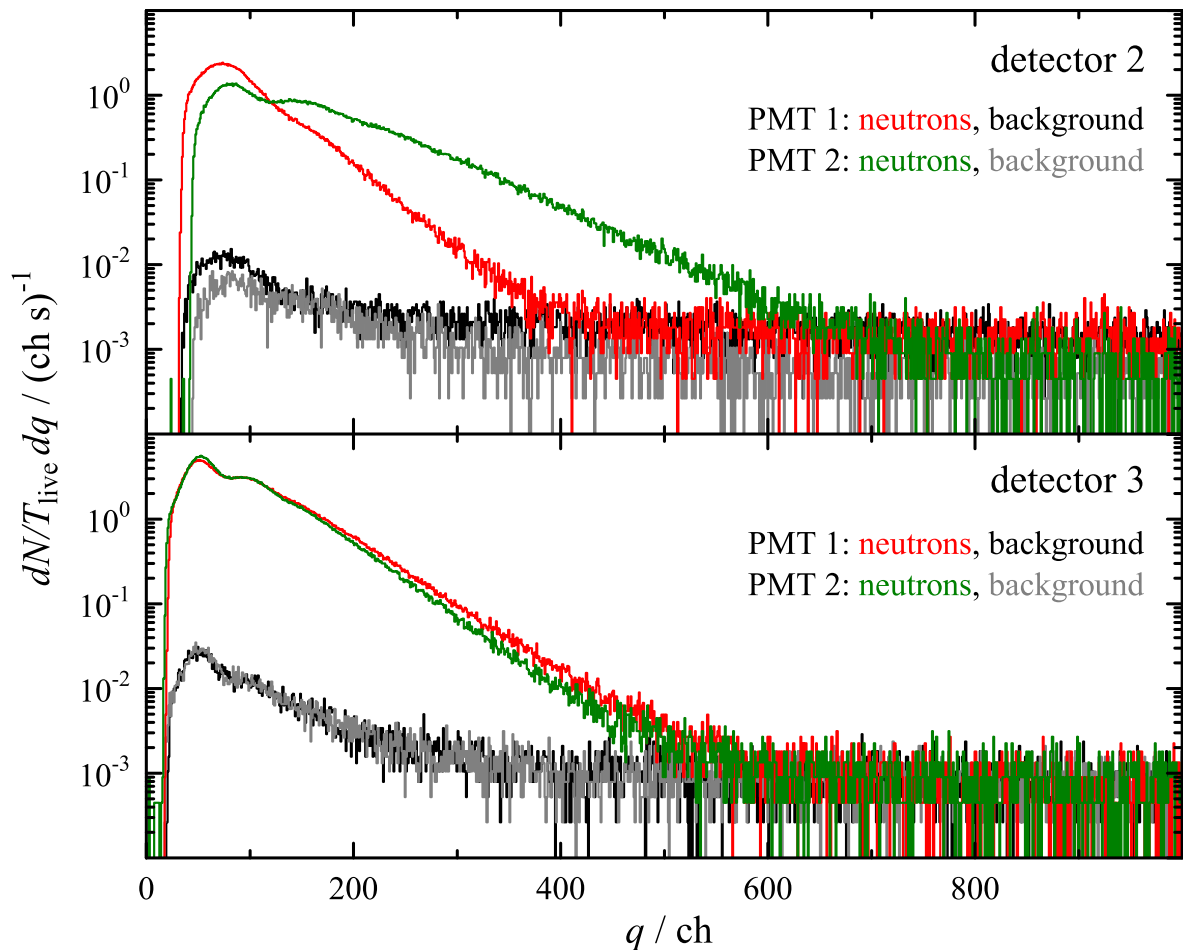


Figure 4.8: The discrete QDC signal q (unit: channels ch) is proportional to the charge of the PMT signal and therefore a measure of the number of photoelectrons emitted from the PMT's photocathode. The single-photoelectron peaks centered at channel $q_1 = 74, 82$ (detector 2), and 53 (detector 3) and the two-photoelectron peak centered at $2q_1$ are discernible. These spectra from the same calibration measurements at $\bar{T}_n(46.6^\circ) = 72$ keV were divided by the live time and normalized to the same length of the *tof* cut window, which either contained only constant background or neutrons plus constant background.

the relative response for protons (≈ 0.12 [Daub2013]), the fraction of photons emitted in direction of the PMT (≈ 0.5), and the quantum efficiency of the PMT (≈ 0.25).

The discrepancies of the efficiencies might be caused by deteriorations of properties of scintillator, PMTs, or their coupling. As some of the detectors were build quite a long time before the calibration, it seems possible that months and years of handling of the detectors within their heavy lead shields and their use in various experiments in horizontal or vertical position deteriorated the optical coupling between scintillator and PMT, which was made of silicon grease and mechanically fixed by opaque heat shrink tube. However, the highest efficiency was not measured for detector 5n, whose scintillator and PMTs were put together only a few months before the calibration, but for the older detector 3. The effect of a 50 % deterioration of the respective main properties of the scintillator material and the photocathode, i.e., the photon absorption length and the quantum efficiency, was simulated with NEFF7 by [Beyer2014] and gave an appropriate fit of the simulated efficiency to the older PTB calibration. As a possible mechanism it was implied, that already a deterioration of the photon absorption length in a wave-length range that contains the maximum of the quantum efficiency would have a large impact. However, it remains unclear, which processes can cause such deteriorations. Radiation damage by γ rays has been studied in [Li2005] and for the irradiation doses of 600 Gy and 14 kGy the light yield of EJ-200 reduced by 10 % and 100 %, respectively.

respectively. These doses are much larger than typical γ -rays doses of the detectors at nELBE, which are of the order of 10^{-4} Gy per year from background radiation and 10^{-2} Gy per week in transmission experiments. Furthermore, it is unlikely that only the signals of one PMT are affected by radiation damage.

5 Simulation of neutron interactions

5.1 Neutron interactions in the target

Photoneutrons from the $d(\gamma,n)p$ reaction can interact with the target before reaching the detector. To estimate the attenuation of the neutron flux seen by the detector a Monte Carlo simulation was written, which was also used for the determination of the solid angle in section 3.5.3. For the sake of simplicity the neutrons were started isotropically and uniformly distributed in a homogeneous target, i.e., this estimate neglects the true angular distribution, the attenuation of the incoming photon beam, and the layer structure of the target. For neutrons moving in direction of detector 2 (mean angle $\vartheta = 90^\circ$), the path length through the target l_{path} was calculated. The neutron attenuation was described by exponential distributions whose mean values were calculated from the number density of each atom species x (^1H , ^2H , $^{\text{nat}}\text{C}$, ^{27}Al) and their neutron total cross sections (ENDF/B-VII.0 [Nds]). From each distribution an attenuation length l_{att}^x was randomly sampled for each neutron. The neutron was regarded as absorbed by the atom species x with the smallest attenuation length, if $l_{\text{att}}^x < l_{\text{path}}$.

The fraction of absorbed neutrons is shown in the upper panel of figure 5.1 as a function of the neutron energy. The relative contributions of ^2H , $^{\text{nat}}\text{C}$, and ^{27}Al to the attenuation scale roughly with their number density because their neutron total cross sections are comparable in their absolute height, which is a few barn on average. The cross section of ^{27}Al has lots of resonances which cause differences by up to a factor of two in the total attenuation factor. Although the proton–hydrogen ratio of the target is only 2 %, ^1H has a two to five times larger cross section and thus also absorbs a discernible fraction of neutrons. The total attenuation is on average between 20 and 25 %, but up to 50 % at some narrow resonances below 0.2 MeV.

For neutrons not emitted in direction of the detectors, there is the possibility of in-scattering, i.e., the neutrons reach the detector only after scattering in the target. This effect was estimated with the Monte Carlo particle-transport code FLUKA [Ferrari2005, Battistoni2007, Ferrari2013], of which version 2011.2 was used. The same simplifications as for the attenuation estimate were used, i.e., neutrons were started isotropically and uniformly distributed in a homogeneous target. Another strong simplification was the assumption of the neutron energy distribution, because each of the variable-sized bins (FLUKA neutron groups) up to 1.4 MeV contained the same number of neutrons.

The number of neutrons reaching the detector was normalized bin-wise to the case without target interactions and is shown in the lower panel of figure 5.1. If only unscattered neutrons were accepted, than the FLUKA simulation gave similar results as the attenuation estimate described above (compare red line in upper panel of figure 5.1). If also scattered neutrons were accepted, than the number of neutrons increased the more, the lower their energy was (green line in upper panel of figure 5.1). In this estimate, the ratio of scattered to unscattered neutrons was about 25 % at 0.5 MeV and about 75 % at 0.1 MeV.

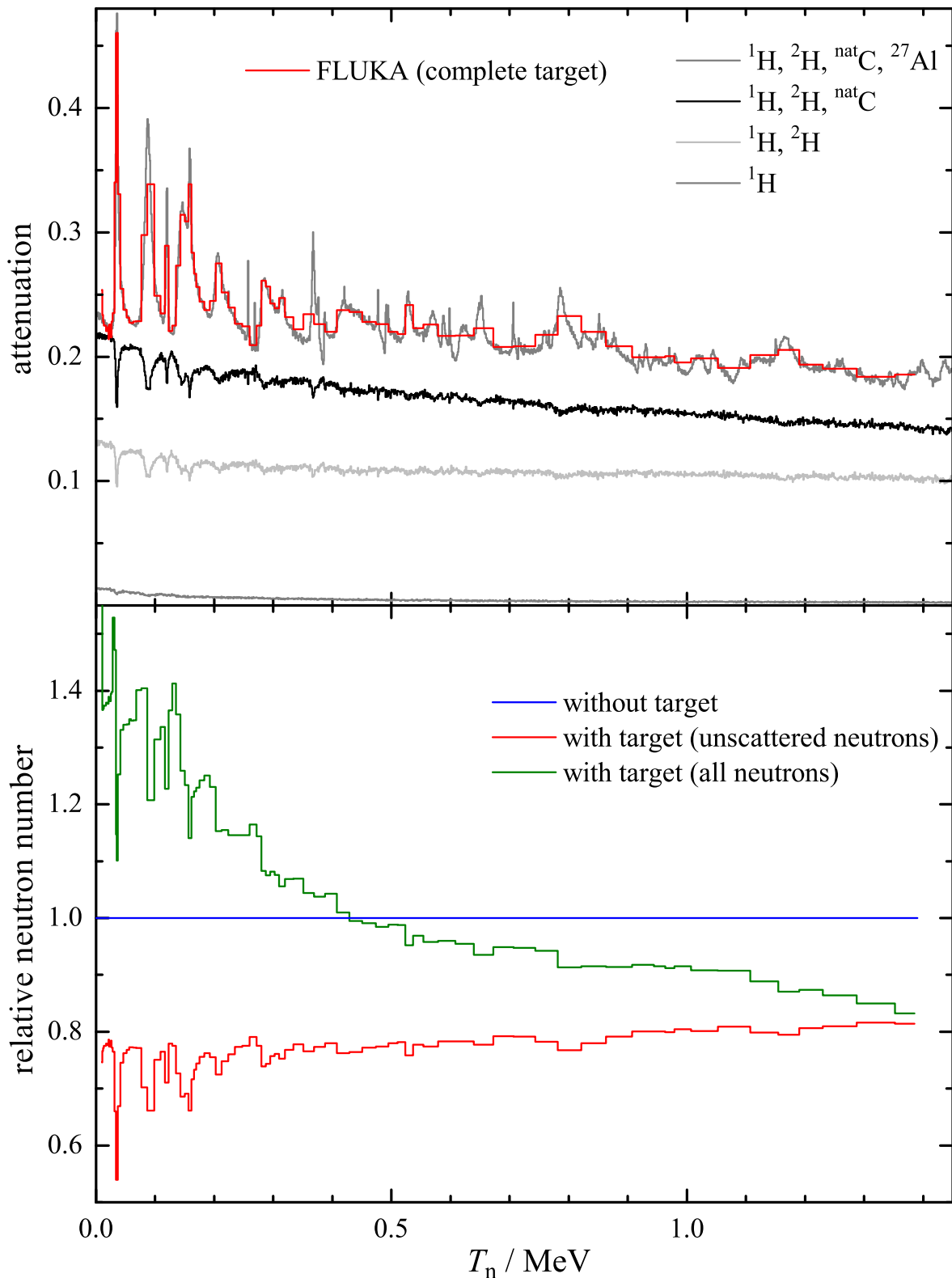


Figure 5.1: Estimated attenuation of neutrons in the target as function of neutron energy. The gray lines in the upper panel are the result of a simple Monte Carlo simulation, in which neutrons were absorbed based on the total ENDF/B-VII.0 cross section [Nds] of the atom species given in the legend. The lower panel shows the result of a FLUKA simulation, in which neutrons were registered in the detector depending on the type of target interactions. The red line in the upper panel is the relative number of unscattered neutrons not reaching the detector in that simulation. The bin width is 1 keV for the gray lines, while the colored lines have a variable bin width (FLUKA neutron groups).

5.2 Neutron interactions in the whole setup

The estimates in the previous section show that attenuation and in-scattering of neutrons change the neutron flux in the detectors significantly and make careful corrections necessary. Therefore, FLUKA (version 2011.2) was used to investigate, to what extent other parts of the experimental setup scatter neutrons from the target into the detectors.

5.2.1 Primary particle source

The attempt to use monoenergetic photons as primary particles failed because the angular distribution of the $d(\gamma,n)p$ reaction was not correctly reproduced by the FLUKA simulation. Instead, the number of neutrons per energy–angle interval emitted from the target in the lab frame was calculated by

$$\frac{dN}{dT_n d\vartheta} = \frac{d\Phi_\gamma}{dE_\gamma} \frac{dE_\gamma}{T_n} \frac{d\sigma}{d\Omega'} \frac{d\Omega'}{d\Omega} \frac{d\Omega}{d\vartheta}, \quad (5.1)$$

in which the first term is the photon flux from equation (3.12), the third term is the differential $d(\gamma,n)p$ cross section from equation (2.16) based on a spline interpolation of the theoretical calculations by [Chen1999] and [Rupak2000], and the other terms are kinematic factors described in appendix B. Because only simulations with and without material are compared to each other, the normalization of equation (5.1) is arbitrary, i.e., the results of the simulations do not depend on the absolute values of the $d(\gamma,n)p$ cross section or the photon flux, but only on their energy dependences. A table of the neutron distribution from equation (5.1) with a bin size of $5 \text{ keV} \times 1^\circ$ was used as primary particle source for the simulation. A FLUKA user routine implemented by [Ferrari2013] allowed a random sampling from the table. Figure 5.2 shows this neutron distribution with its maximum normalized to 1.

5.2.2 Geometry

The geometry of the FLUKA simulation was a simplified model of the real experimental setup (compare section 3.1). It is shown as a three-dimensional rendering in figure 5.3 as well as in the xz -plane at $y = 0$ together with the neutron fluence in figure 5.4. The most important parts were selected, which were either very large or close to target or detector:

- The target had the Al- CD_2 -multilayer structure and the correct composition. Neutrons were started in the whole target rather than only in the CD_2 layers.
- The neutron detectors consisted of the scintillator bars surrounded by the lead shields. The PMTs, the PMT lead shield, and the scintillator wrapping foils were not included.
- The two lead blocks (without collimator holes) shielding each one γ -ray detector from the target, the lead block (with beam-tube hole) shielding the room from the collimator exit, and the lead block (with entrance hole), that is the front face of the photon beam dump, were included.
- Walls, floor, and ceiling were made only 30 cm thick, because this saved computation time and neutrons reaching this depth have a negligible probability of re-entering the room. Normal concrete was chosen as material, although some parts consisted of heavy concrete.
- The experimental room was filled with air.

The geometry was implemented in the FLUKA input file by [Ferrari2013]. The importance of the selected parts is evaluated in the next section, while the inclusion of more parts is discussed in section 5.2.5.

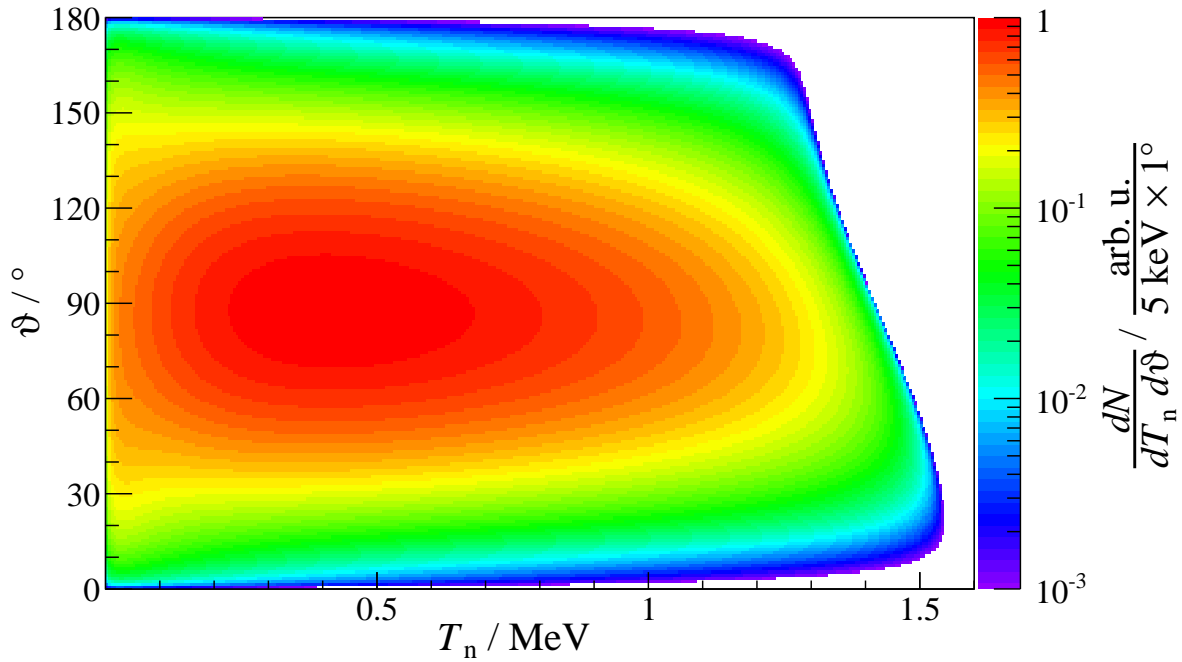


Figure 5.2: Neutron distribution from equation (5.1) with a bin size of $5 \text{ keV} \times 1^\circ$ that was used as primary particle source for the FLUKA simulation. Because the normalization is arbitrary, the maximum was normalized to 1. The ϑ asymmetry visible at high energies comes from the reaction kinematics. The ϑ independence of $d\sigma/d\Omega'$ (equation (2.16)) at low energies is covered by the term $d\Omega/d\vartheta \propto \sin \vartheta$.

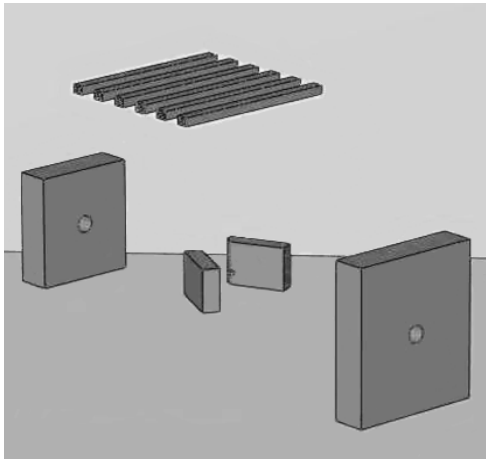


Figure 5.3: Three-dimensional rendering of the geometry of the FLUKA simulation. See text for details. Figure taken from [Ferrari2013].

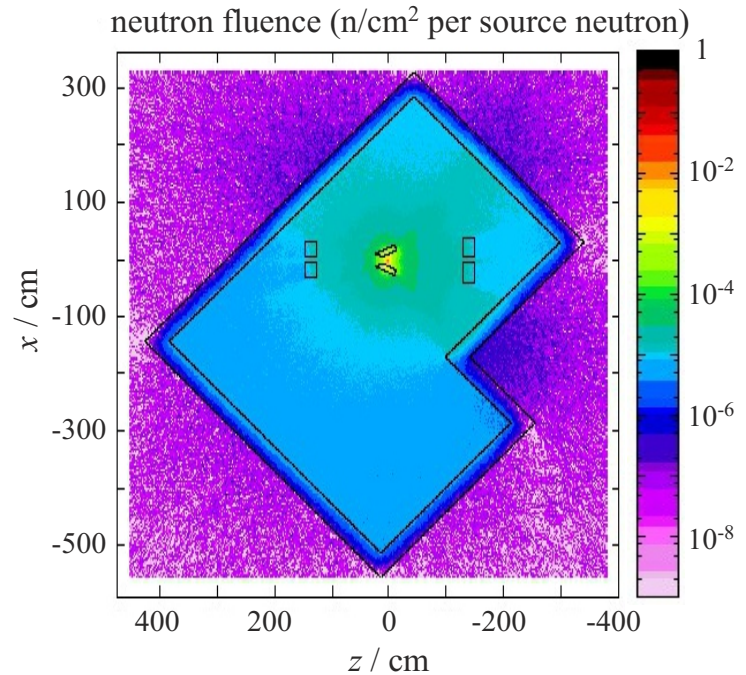


Figure 5.4: The geometry (black lines) and the neutron fluence (color scale) of the FLUKA simulation are shown in the xz -plane at $y=0$. The neutron fluence decreases with the distance to the target and due to interactions with the setup. Figure taken from [Ferrari2013].

5.2.3 Detection and tracking

Several quantities were saved for an event, if a particle entered the volume of neutron detector 2 located at $\vartheta = 90^\circ$. This volume included the scintillator bar, the lead shield, and the air between them. Beyond the quantities easily accessible in the FLUKA simulation, such as the type, position, direction, and energy of primary and detected particle, user routines were implemented by [Ferrari2013] that allowed to save the *tof* of the detected particles as well as the complete history of the event, i.e., all tracks and vertices of primary and secondary particles. Figure 5.5 shows an example for the tracking of particles. The event history allows to evaluate the importance of the parts included in the geometry, see table 5.1. Of all simulated particles reaching detector 2, one third are neutrons from the $d(\gamma,n)p$ reaction which had no interactions with any part of the setup. Another third of the detector hits had their previous interaction in the walls, the floor, or

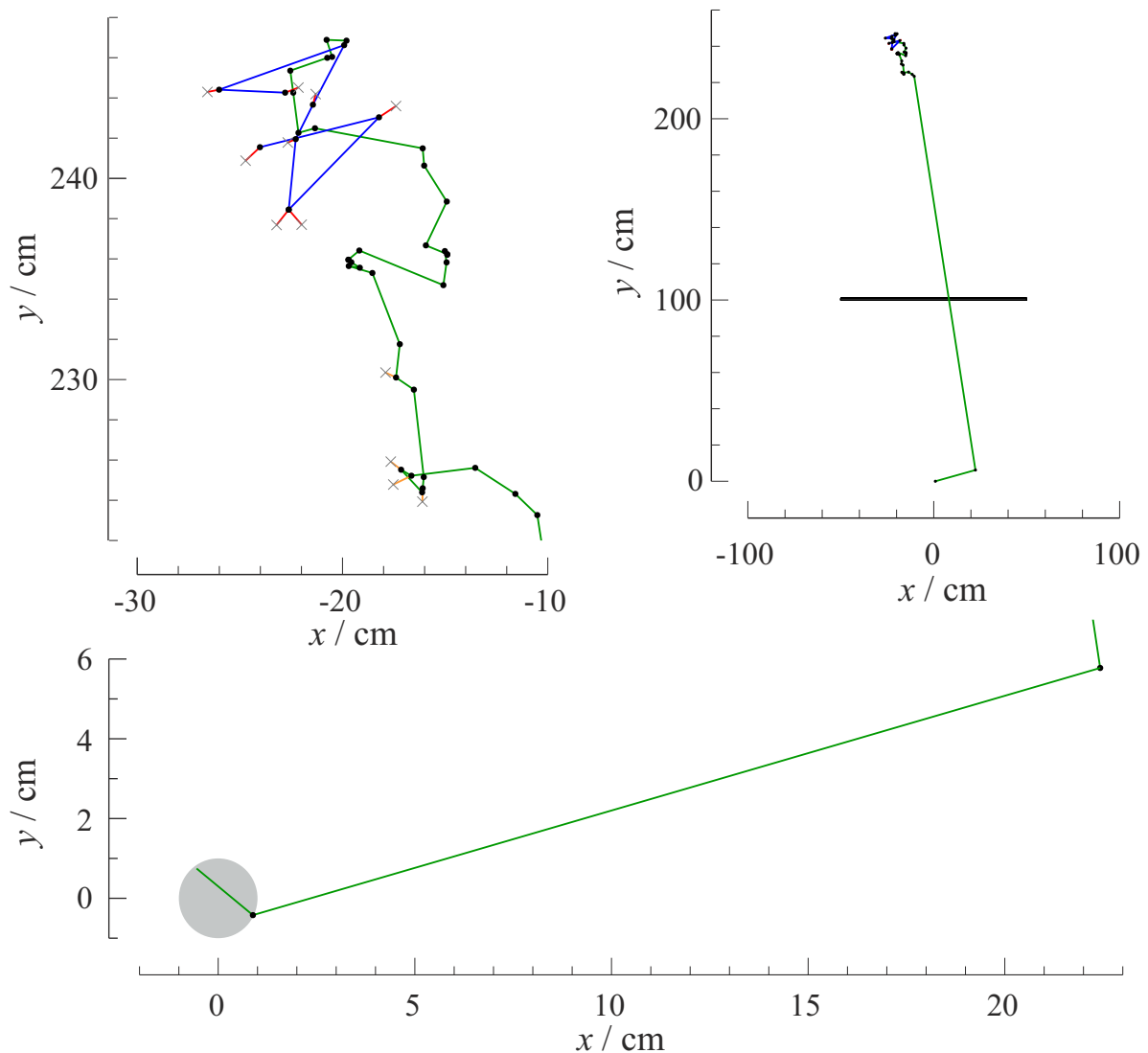


Figure 5.5: All panels show projections of particle trajectories (lines) and vertices (black dots) of the same event to the xy -plane. The lower panel shows in detail, how a neutron (green) is generated and scattered in the target (gray area) before it is scattered again in the lead shield of the γ -ray detector. The right panel shows that this neutron passes the detector (black rectangle) without interaction and reaches the concrete ceiling. The interactions there are shown in detail in the left panel. The neutron scatters on protons (orange) and other nuclei (not tracked) before it gets captured. Two capture γ rays (blue) are emitted and interact with electrons (red). After their creation, there is no further tracking of charged particles and the end of their tracks shown here is arbitrary (crosses).

Table 5.1: Relative abundance of simulated events hitting detector 2 depending on their previous interaction place. The absolute uncertainties of these values are between 0.4 % for the highest and 0.1 % for the lowest values. The relative abundance of events, in which the arriving particles are not neutrons, is given in parentheses, if > 0 .

previous interaction place	rel. abundance
no interaction	36.4 %
walls, floor, and ceiling	35.8 % (7.5 %)
lead shields of γ -ray detectors	9.8 %
CD_2 in target	4.9 %
lead shields of other neutron det.	4.4 % (0.2 %)
air	3.8 % (0.3 %)
aluminum in target	1.6 %
lead shield of beam dump front	1.6 %
scintillator of other neutron det.	0.9 %
lead shield of collimator exit	0.8 %

the ceiling. Other major sources of scattered neutrons are the lead shields of the γ -ray detectors, which are close to the target, the CD_2 in the target, the lead shield of the other detectors and the air. If the particle type is taken into account, one finds that one fifth of the detectors hits coming from particles from the walls, the floor, and the ceiling are photons, see table 5.1. These γ -rays are the result of capture reactions of neutrons that were slowed down by scattering. Because the tof is usually much longer than one accelerator period, they contribute to the constant background in the tof spectrum, which can be subtracted in the experiment, and are rejected in the simulation. Figure 5.6 shows, that neutrons reaching the detector after scattering in parts of the setup, which are far away from the target, have lost their energy– tof correlation given by equation (2.13). Many of the neutrons that interacted in the walls, the floor, or the ceiling hit the detector with energies

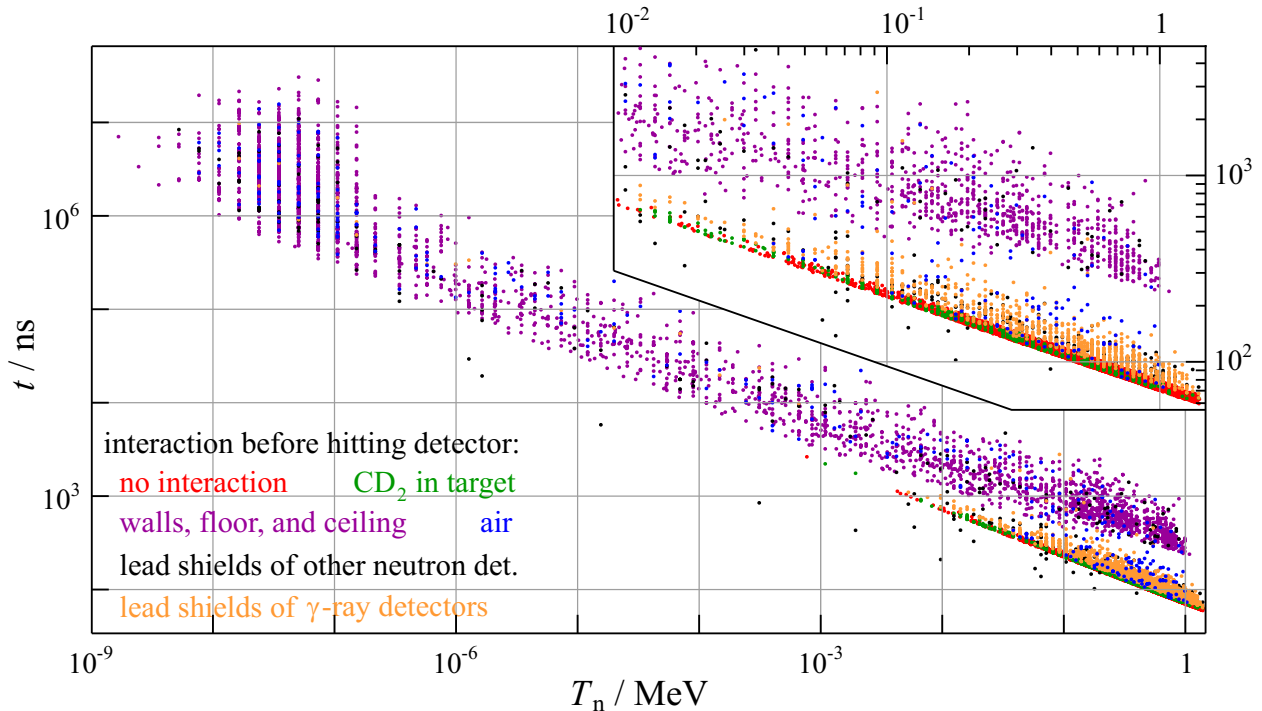


Figure 5.6: Correlation between kinetic energy T_n and time of flight t of neutrons hitting the detector. The colors denote the material, in which the last interaction happened before the neutron hit the detector volume. Scattered neutrons are plotted at the mean energy of the FLUKA energy group they belong to. The inset shows the energy range with sufficient detection efficiency and a tof range about 8 times larger than the accelerator period of 615 ns. Neutrons that traveled most of the time with the same energy on the direct target–detector path l , such as primary neutrons or neutrons scattered close to the target, maintained mostly the original relation (2.13). For neutrons scattered far away from target and detector t grows with the flight path. If the scattering took place close to the detector t can also be smaller.

between the thermal region and the detection threshold, while those above the threshold arrive at $t \gtrsim 240$ ns. This causes background signals at $T_n < 100$ keV, if $240 \text{ ns} < t < 615 \text{ ns}$, and in the whole energy range, if $t > 615$ ns (overlap into the next pulse). The neutrons in the energy range $T_n > 100$ keV are to 58 % primary particles, to 13 % from scattering in the lead shields of the γ -ray detectors, and to 13 % from scattering in the walls, the floor, or the ceiling.

5.2.4 Correction factor for the $d(\gamma, n)p$ measurement

In the analysis of the experiment, the neutron energy was calculated from the *tof* under the assumption the neutron took the direct flight path from the target to the detector. Thus, the energy assigned to scattered neutrons is wrong and an efficiency correction is not possible for such events. Therefore, the experimental detection efficiency described in chapter 4 was combined with the data from the simulation, in which the true energy and the *tof* were known. In principle, FLUKA could also be used to simulate the efficiency of the neutron detector. However, such simulations must include the production, the transport, and the coincident detection of scintillation light, which is rather difficult (compare discussion in section 4.1).

Each simulated event was filled in a histogram at the kinetic energy that was calculated from equation (2.13) with the simulated *tof* and flight path. The experimental energy resolution (see section 3.5.3) was not taken into account because it was smaller than the widths of the bins of the histogram, which were identical to the FLUKA neutron energy groups. The experimental efficiency ε at the simulated true energy was used as a weighting factor, which made a spline interpolation of the experimental data points ε_{exp} necessary. To normalize the simulated efficiency-corrected neutron energy spectrum, another FLUKA simulation was used, in which neutron source and detection volume were identical, but in which no material was present and the efficiency correction was not included. Using this normalization, a correction factor κ was calculated, which includes both the correction for the detection efficiency and for the simulated modification of the neutron spectrum from neutron interactions with the setup. From the comparison between κ and ε in the upper panel of figure 5.7 one sees that at $T_n > 1$ MeV the main effect is the neutron attenuation in the target. Below $T_n \approx 0.5$ MeV the in-scattering from the setup has a larger influence than the neutron attenuation. The ratio of κ/ε is about 3 at $T_n = 100$ keV and increases up to 100 at $T_n = 20$ keV, i.e., only 1 out of 100 neutrons registered by the detector in the experiment with an *tof* corresponding to $T_n = 20$ keV did not interact with the setup before.

A correct calculation of the relative uncertainties of ε between the data points of the experimental efficiency ε_{exp} would be complicated. On the one hand, the deviation between the interpolation function and the true efficiency curve, which is unknown, must be taken into account. In general, this deviation increases with the distance to the neighboring data points. On the other hand, the propagation of the relative statistical uncertainties of the two constraining data points leads to a decrease between them. Because both effects compensate each other to some extent, the relative uncertainties between the data points of the experimental efficiency have been estimated by a linear interpolation, which is shown in the lower panel of figure 5.7. To determine the systematic uncertainties $\Delta\kappa_{\text{sys}}$ of the simulated efficiency-corrected neutron energy spectrum, each event of the simulation was filled in a separate histogram, in which $\Delta\varepsilon$ was used as a weighting factor. The resulting relative systematic uncertainty $\kappa_{\text{sys}}/\kappa$ shown in the lower panel of figure 5.7 is similar to that of the efficiency interpolation at $T_n > 50$ keV. Below that energy it remains below 3 % because in most of these events the true simulated energy was much larger than the kinetic energy calculated from the *tof*.

The FLUKA simulations were run on a computer cluster [Ferrari2013]. In the simulation without material, 4.0×10^7 primary neutrons were started and 3.4×10^5 events were saved. In the simulation with material, which took much more computing time, only 7.8×10^5 primary neutrons

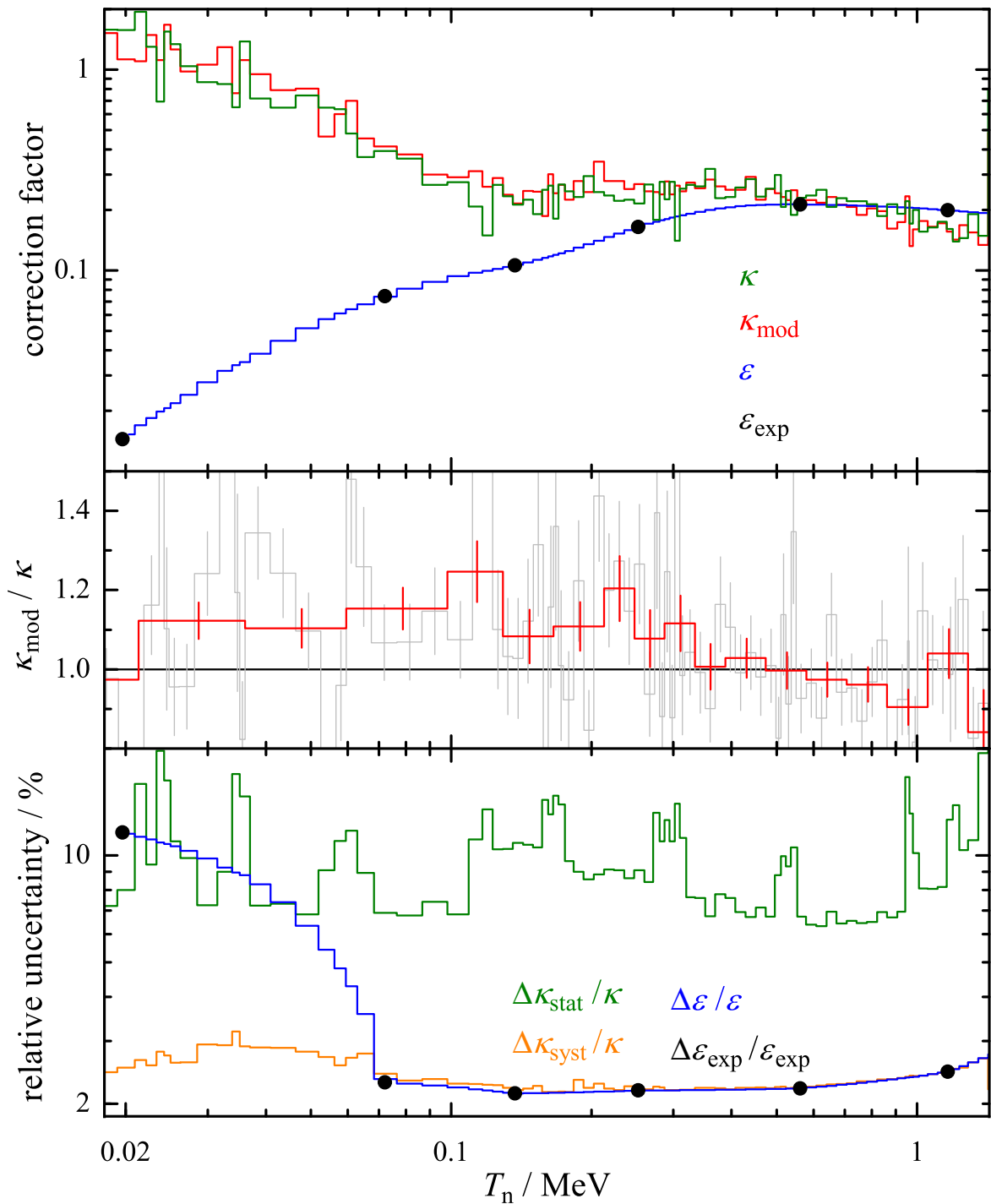


Figure 5.7: The upper panel shows the efficiency correction factor ε_{exp} of detector 2 that was measured at PTB in 2011 (black symbols, see chapter 4). The spline interpolation ε was used to calculate the correction factor κ that also includes the simulated modification of the neutron spectrum caused by neutron interactions with the setup. The correction factor κ_{mod} was estimated similarly from a simulation with a modified geometry, see section 5.2.5. The bin widths of the histograms is identical to the FLUKA neutron energy groups. Only for the red histogram in the middle panel, which shows the comparison of the original and the modified geometry, bins were combined to reduce the statistical uncertainty. The lower panel shows the relative uncertainties. The systematic uncertainty of κ is the result of the interpolated uncertainty of the efficiency. The statistical uncertainty of κ is related to the number of simulated events and therefore varies with the bin width.

were started and 1.3×10^4 events were saved. Therefore, the simulation with material dominates the statistical uncertainty. The relative statistical uncertainties $\Delta\kappa_{\text{stat}}/\kappa$ are between 7 and 20 %, see figure 5.7. They are calculated using the inverse square root of the number of events in a neutron energy group. The assumed Poisson statistic was verified by analyzing the variation between subsamples of the simulated data.

5.2.5 Outlook on improvements of the simulation

Obviously there is a large discrepancy between the statistical and systematic uncertainties of κ , which could be reduced by using more computation time. Before the start of such a long simulation, it was planned to include more parts and details in the geometry. The modified geometry is shown in figure 5.8. Based on the results shown in table 5.1, the following changes were made:

- The target holder made of steel, which is mounted on a aluminum strut profile, was included.
- The lead block shielding the room from the collimator exit was raised.
- The complete photon beam dump consisting of a large polyethylene block surrounded by thin cadmium sheets and lead was included.
- The lead blocks shielding the γ -ray detectors received conical collimator holes, which were covered by the absorber plates made of copper and lead.
- The γ -ray detectors including the **HPGe** crystals, the cooling fingers made of copper, the veto detectors made of **BGO**, the aluminum housing, and the radial lead shield were included with a simplified geometry.
- The lead shields of the **PMTs** were included with a simplified geometry as well as aluminum rings that surrounded the scintillator bars at both ends.

Furthermore, the primary neutrons were now only started in the **CD₂** layers of the target. There are results of test runs with this modified FLUKA simulation, in which unfortunately the size of the detection volume that triggers the event storage was reduced. The ratio of events per primary neutron of the modified and the original simulation is about 87 %, which is close to the geometric reduction of the detection volume. By analyzing the modified simulation as described in the previous section and normalizing the results to 100 %, a correction factor κ_{mod} was estimated, which is shown in figure 5.7. The energy dependence and the uncertainties of κ and κ_{mod} are very similar. The ratio $\kappa_{\text{mod}}/\kappa$, which is independent of the FLUKA simulation used for the normalization of both correction factors, is shown in the middle panel of figure 5.7. Between 20 and 300 keV, κ_{mod} is about 10 % larger than κ , while at higher energies there are no significant differences. An analysis of the last interaction place before the detector was hit (similar to that in table 5.1) for the modified simulation showed the small influence of some of the new parts, such as the radial lead shield (1.1 % of all events), the **BGO** (1.0 %), or the absorber plates (0.5 %), and the insignificance of others, such as the rest of the γ -ray detectors or the parts of the beam dump behind the front face (all < 0.1 %).

Up to now it was not possible to run one of the simulations for a longer time to reduce the relative statistical uncertainty or to obtain correction factors for the other detectors. If the relative statistical uncertainty was reduced significantly, it would become necessary to discuss the accuracy of such simulations in general and to estimate a systematic uncertainty for the simulation models. In that context it might be helpful to compare the results of the FLUKA simulation with other Monte Carlo codes, such as MCNP or GEANT4.

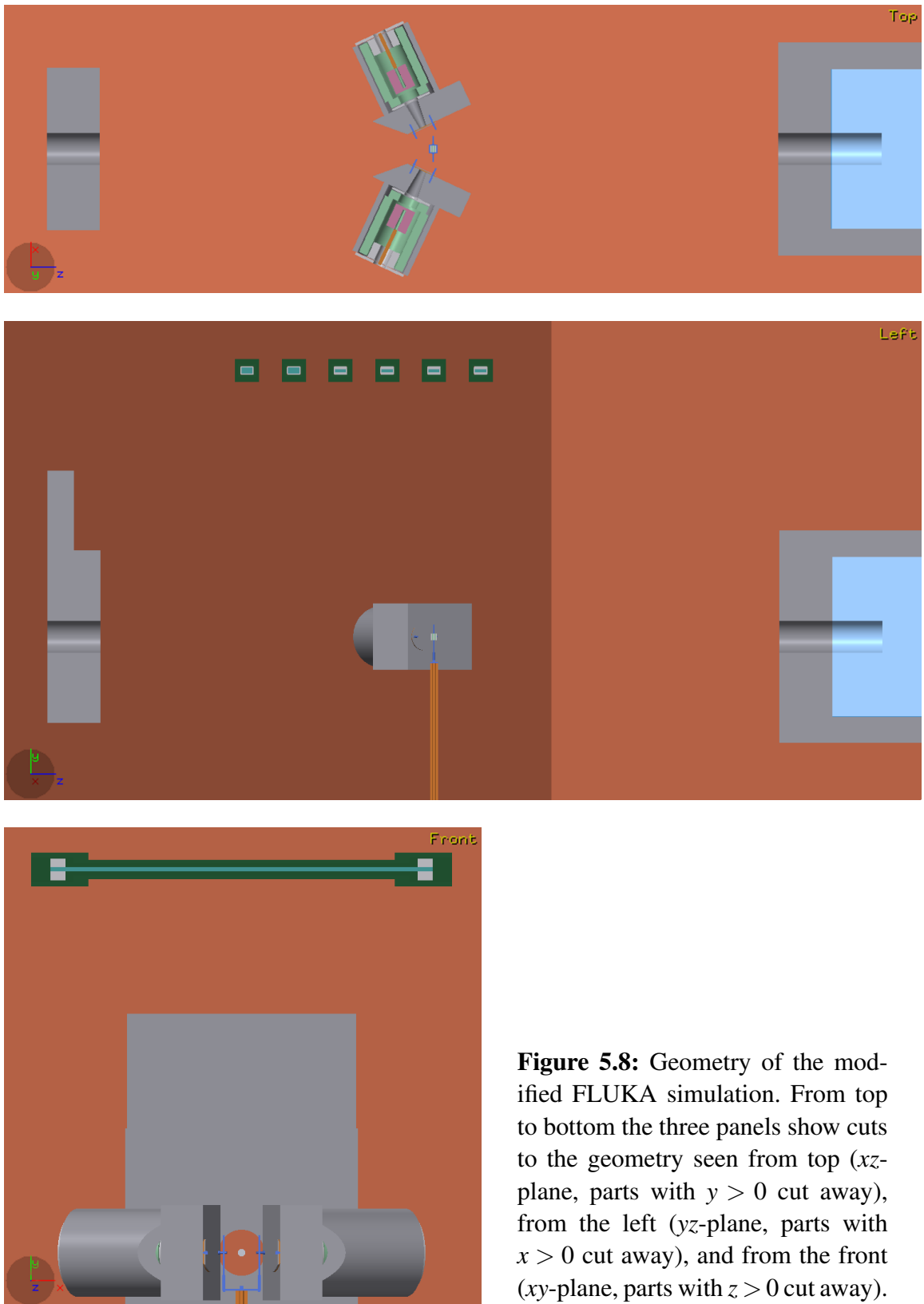


Figure 5.8: Geometry of the modified FLUKA simulation. From top to bottom the three panels show cuts to the geometry seen from top (xz -plane, parts with $y > 0$ cut away), from the left (yz -plane, parts with $x > 0$ cut away), and from the front (xy -plane, parts with $z > 0$ cut away).

6 Results and discussion

6.1 Cross section of the $d(\gamma,n)p$ reaction

The differential cross section of the $d(\gamma,n)p$ reaction in the center-of-mass (cm) frame at the cm kinetic energy T_{cm} was calculated by

$$\frac{d\sigma}{d\Omega'}(T_{\text{cm}}, \vartheta_n) = \frac{N_n(T_n, \vartheta_n)}{\kappa(T_n, \vartheta_n) \cdot N_\gamma(E_\gamma, \vartheta_n) \cdot N_d \cdot T_{\text{live}} \cdot \Omega(\vartheta_n) \cdot \frac{d\Omega'}{d\Omega}(T_{\text{cm}}, \vartheta_n)}, \quad (6.1)$$

in which the laboratory (lab) angle ϑ_n has one specific value for each of the six neutron detectors. The photon energy E_γ as well as T_{cm} were calculated using ϑ_n and the kinetic neutron energy T_n , which was calculated from the measured time of flight, see section 2.2. It should be called in mind, that the relations between T_n and T_{cm} as well as between ϑ_n and the cm neutron angle ϑ' are energy dependent, see figures 2.2 and 2.3.

The quantity in the numerator of equation (6.1), N_n , is the background-corrected number of neutrons (see section 3.5.3) in an energy interval that starts at $T_{n,1}$, ends at $T_{n,2}$, has the width ΔT_n , and has its center at T_n . In the measured neutron energy spectrum, all intervals were 0.1 keV wide. The correction factor κ , which includes both the measured neutron detection efficiency ε and the simulated modification of the neutron spectrum from neutron interactions with the setup, is given for intervals defined by the FLUKA neutron groups. Therefore, $T_{n,1}$ and $T_{n,2}$ were chosen as close as possible to the edges of the FLUKA groups. The number of incoming bremsstrahlung photons in an interval was calculated by

$$N_\gamma(E_\gamma, \vartheta_n) = \frac{d\Phi_\gamma}{dE_\gamma}(E_\gamma) \cdot c_{\text{trans}}(E_\gamma) \cdot \frac{dE_\gamma}{dT_n}(T_{\text{cm}}, \vartheta_n) \cdot \Delta T_n, \quad (6.2)$$

in which $d\Phi_\gamma/dE_\gamma$ is the photon flux from equation (3.12). The transmission factor c_{trans} describes the atomic attenuation of photons in the target and was calculated similarly to that in section 3.4. The kinematic factors dE_γ/dT_n and $d\Omega'/d\Omega$ are necessary for the transformation of the differential quantities, see appendix B. The further parameters in equation (6.1), which are independent of the energy, are the number of deuterium atoms in the target N_d (see section 3.3), the live time of the data acquisition of the neutron detectors T_{live} (see section 3.5.2), and the geometric solid angle of the neutron detector without lead shield in relation to the target Ω (see section 3.5.3).

The result⁵ of equation (6.1) is shown in figure 6.1 for the data measured with detector 2 at $\vartheta_n = 90^\circ$. To calculate a differential cross section from the data measured with the other three thin neutron detectors, further simulations of κ are necessary, while for the two thick detectors there is no experimental detection efficiency available. The comparison with the theoretical cross section calculated by [Arenhoevel2005] in figure 6.1 shows a reasonable agreement at $T_{\text{cm}} > 0.7$ MeV, where the ratio κ/ε is between 0.7 and 1.3 and thus the simulated correction of attenuation and in-scattering of neutrons is much smaller than at lower energies. The deviations from the theoretical curve of up to a factor of 2 in the energy range between 0.15 and 0.7 MeV decrease a little, if the same experimental data is corrected with the estimated κ_{mod} . With regard to the large in-scattering

⁵The preliminary results of the efficiency calibration, the FLUKA simulation, and the differential $d(\gamma,n)p$ cross section published in [Hannaske2016] are not identical to the final results in this dissertation.

correction (compare figure 5.7), the good agreement of the data points with the theory at energies below 150 keV is surprising and should be considered as dubious as long as the disagreement at higher energies is unsolved. The experimental energy resolution is much lower than the bin width that had to be chosen for the data points. At $T_{\text{cm}} > 0.2$ MeV, at least two FLUKA groups were combined to reduce the dominating statistical uncertainty coming from κ . This uncertainty is about 4–8 %, but could be reduced by longer simulations. The experimental statistical uncertainty is larger than 5 % at $T_{\text{cm}} < 0.2$ MeV and ranges down to about 0.7 % at $T_{\text{cm}} \approx 1.5$ MeV.

Equation (2.16) links the cross section $\sigma = \sigma_{\text{M1}} + \sigma_{\text{E1}}$ and the differential cross section by

$$\sigma(T_{\text{cm}}) = 4\pi \frac{d\sigma}{d\Omega'}(T_{\text{cm}}, \vartheta_n) \left[f_{\text{M1}}(T_{\text{cm}}) + \frac{3}{2} (1 - f_{\text{M1}}(T_{\text{cm}})) \sin^2 \vartheta'(T_{\text{cm}}, \vartheta_n) \right]^{-1}, \quad (6.3)$$

in which the relative M1 contribution to the $d(\gamma,n)p$ cross section $f_{\text{M1}} = \sigma_{\text{M1}}/\sigma$ is taken from the theoretical calculation of [Chen1999] shown in figure 2.9. The term in square brackets is constant and equal to 1 at $\vartheta' \approx 125^\circ$. For the measurement at $\vartheta_n = 90^\circ$, the term in square brackets increases from 1 at low energies to about 1.5 at the highest energy. The resulting $d(\gamma,n)p$ cross section is shown in figure 6.2 and in table 6.1 for $T_{\text{cm}} > 0.7$ MeV. As mentioned before, the simulated correction of attenuation and in-scattering of neutrons is less than 30 % in this energy range. The bin width from figure 6.1 was doubled to decrease the statistical uncertainty to about 3–5 %.

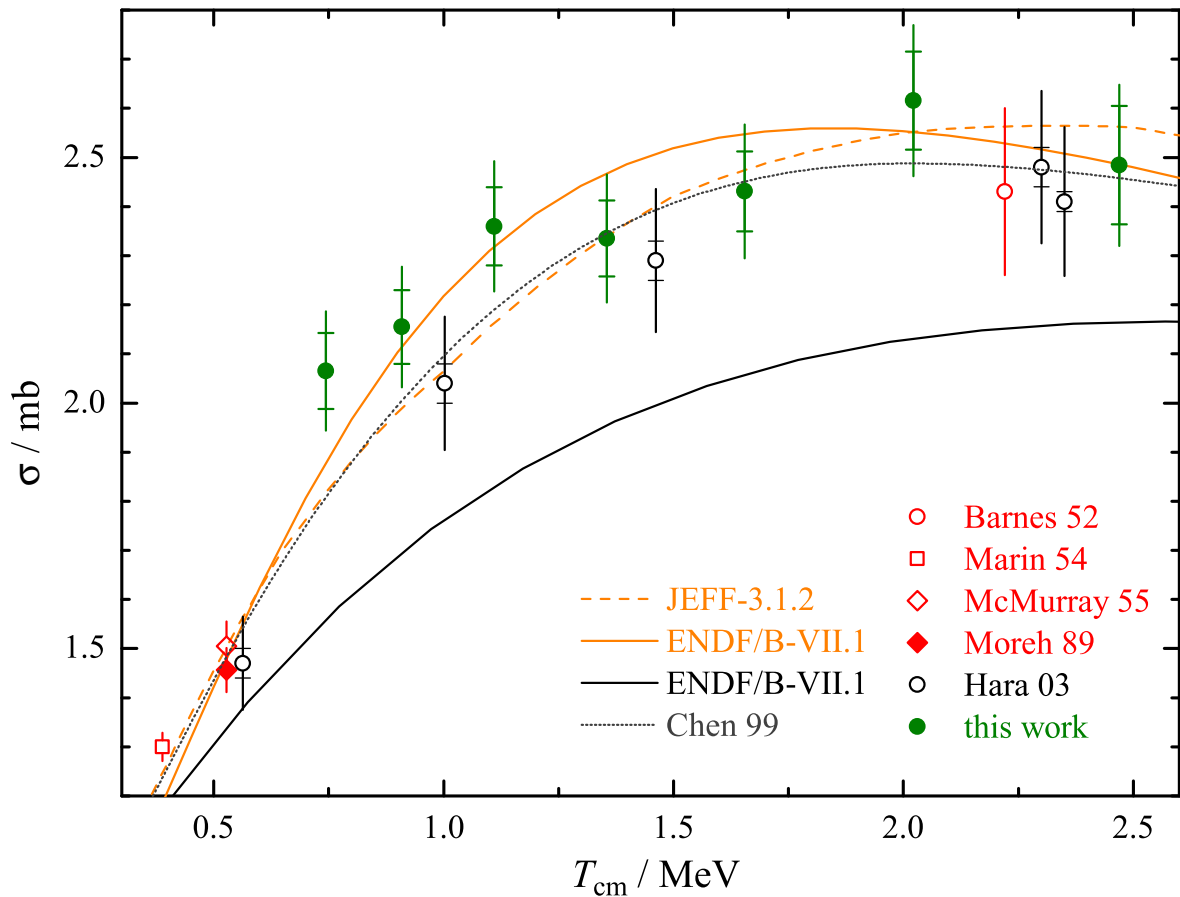


Figure 6.2: Comparison of $d(\gamma,n)p$ cross section measurements (symbols), evaluations (orange and black splines), and calculations (gray dotted spline, compare figure 2.4) in the energy range 0.3–2.6 MeV. A larger energy range with more experiments and the explanation of the colors are given in figure 2.8. The ELBE data (green symbols) were calculated from differential cross section measured at $\vartheta_n = 90^\circ$ and a theoretical $\sigma_{\text{M1}}/\sigma$ ratio. Below 0.7 MeV, the ELBE data need large corrections and are therefore not shown. All other bremsstrahlung experiments were at higher energies. Error bars without horizontal markers are total uncertainties, while error bars with horizontal markers are statistical uncertainties.

Table 6.1: $d(\gamma,n)p$ cross section data from ELBE shown in figure 6.2.

T_n (MeV)	ΔT_n (MeV)	E_γ (MeV)	T_{cm} (MeV)	$d\sigma/d\Omega'$ ($\mu\text{b}/\text{sr}$)	f_{M1}	σ (mb)	$\Delta\sigma_{stat}$ (mb)	$\Delta\sigma_{syst}$ (mb)
0.371	0.074	2.97	0.74	232	0.169	2.07	0.08	0.09
0.453	0.090	3.14	0.91	245	0.130	2.15	0.08	0.09
0.553	0.110	3.34	1.11	271	0.103	2.36	0.08	0.10
0.675	0.135	3.58	1.36	270	0.092	2.33	0.08	0.10
0.825	0.164	3.88	1.66	282	0.078	2.43	0.08	0.10
1.008	0.201	4.25	2.02	305	0.061	2.62	0.10	0.11
1.231	0.245	4.70	2.47	291	0.049	2.48	0.12	0.11

6.2 Systematic uncertainties

The relative systematic uncertainty is about 4.5 %, which is the quadratic sum of 4 contributions:

1. There is a systematic uncertainty of the correction factor of $\Delta\kappa_{syst}/\kappa = 2.2\text{--}3.0\%$ (see figure 6.1), which comes from the calibration of the neutron detection efficiency (see section 5.2.4). This uncertainty comes mainly from the monitor calibration factor f_{NM} and can hardly be reduced (compare tables 4.1 and 4.2).
2. The photon flux normalization in equation (6.2) leads to $\Delta N_\gamma/N_\gamma = 2.1\%$ (see section 3.4.4). This uncertainty comes mainly from the nuclear data input (energy-integrated scattering cross section I_S , see table 3.7). If there was better nuclear data, then the experimental statistical uncertainty as well as the efficiency scaling factor between experiment and simulation should be reduced. The former could at best be realized by a longer measurement time, while a larger target or a shorter target–detector distance would also increase the relative count rate loss due to larger dead time. The latter would require source measurements that are longer or at more energies.
3. The solid angle has an uncertainty of $\Delta\Omega/\Omega = 1.1\%$, for which only the flight path uncertainty was taken into account, because the identical detector was used in the efficiency calibration. A reduction of this contribution would also reduce the count rate because a target with reduced diameter, a thinner detector, or a longer flight path would be necessary.
4. The uncertainty of the number of deuterium atoms in the target of $\Delta N_d/N_d = 2.7\%$ is unexpectedly large due to a mass loss over time and an uncertain isotopic deuterium abundance (see section 3.3). In a measurement of the angular distribution of neutrons scattered from deuterium at nELBE, which was proposed, prepared, and analyzed by a group from Geel, a CD_2 sample enriched to 99.999 % with a mass of about 12 g and a relative mass uncertainty of 5×10^{-4} has been used [Nankov2014]. If such a low target uncertainty had been possible for the $d(\gamma,n)p$ experiment, the relative systematic uncertainty of the cross section would have been about 3.5 %

The deviations between simulation and reality, e.g., due to the incompleteness of the geometry or uncertainties of the nuclear data input, are difficult to estimate and therefore not included in κ_{syst} . The influence of the most important parts of the geometry was evaluated in sections 5.2.3 and 5.2.5. It was shown that with increasing level of detail of the geometry of the setup, the correction factor κ did not change much. At $T_{cm} > 0.7$ MeV, κ should be reliable to about 2 %. The accuracy of the results of the FLUKA simulation might be estimated from a comparison with other Monte Carlo codes, such as MCNP or GEANT4. An experimental verification might be possible for the attenuation of high-energy neutrons in the target by measurements and simulations with different

target diameters. A determination of the neutron fraction from in-scattering with the shadow-cone method seems not feasible in the compact setup because a shadow bar would change the neutron distribution seen by the close parts of the setup. In principle, the in-scattering of neutrons could be identified by measuring the *tof* and the kinetic energy independently for each event, e.g., with ${}^6\text{Li}$ glass detectors. However, such detectors can have other drawbacks, such as low efficiency, structures in the efficiency curve, or insufficient energy resolution in the relevant energy range.

An uncertainty for the calculation of the bremsstrahlung spectrum is also not included. For the data points in figure 6.2 at $T_{\text{cm}} > 2$ MeV, which correspond to $E_\gamma > 4$ MeV and are thus close to the endpoint energy, the cross section would increase by up to 5 % if the model of [Haug2008] was used instead of the model of [Schiff1951] (compare figure 3.12 and remember the normalization to photon flux measurements at $E_\gamma > 2$ MeV).

6.3 Conclusions and outlook

The experiment at ELBE described in this dissertation is the first absolute measurement of the $d(\gamma,n)p$ cross section at $T_{\text{cm}} < 5$ MeV that used bremsstrahlung. The seven data points that were obtained in the energy range $0.7 \text{ MeV} < T_{\text{cm}} < 2.5 \text{ MeV}$ are a little higher than the recent measurement by [Hara2003] that used a quasi-monoenergetic γ -ray source based on Laser-Compton scattering, see figure 6.2. These ELBE data points are consistent with recent cross section calculations and data evaluations except for the ENDF/B-VII.1 evaluation of the $d(\gamma,n)p$ data, which however is also not compatible with the ENDF/B-VII.1 evaluation of the $p(n,\gamma)d$ data after applying the principle of detailed balance (see section 2.3). The precision of the ELBE measurement is not sufficient to favor one evaluation or calculation, which are all rather similar in that energy range (compare also figure 2.4). The total uncertainties of the ELBE measurement of about 6.5 % come to similar parts from statistical and systematic uncertainties. The statistical uncertainty could be decreased from 3–5 % to about 1 %, if longer simulations of the correction factor κ were made. The systematic uncertainties of 4.5 % are mainly from the photon flux normalization, the neutron detection efficiency, and the target composition. It could be decreased to 3.5 %, if the measurement was repeated with better CD_2 target material. Similar total uncertainties were published by [Barnes1952] and [Hara2003] for their data points shown in figure 6.2, whereas the latter is dominated by systematic uncertainties. Unfortunately, the simulated correction of attenuation and in-scattering of neutrons becomes rather large at $T_{\text{cm}} < 0.7$ MeV. Therefore, the ELBE data can neither be compared to the high-precision measurements at $T_{\text{cm}} = 0.53$ MeV, which used the 2.76 MeV γ ray of ${}^{24}\text{Na}$, nor it covers the energy range relevant to Big Bang nucleosynthesis (BBN) at $T_{\text{cm}} \approx 20\text{--}200$ keV.

To reach the energy range relevant to BBN, the interactions of neutrons with the setup must be reduced. One possibility to do this, is to separate the CD_2 target from the ${}^{27}\text{Al}$ target. Such a setup has already been tested at ELBE, but with the ${}^{27}\text{Al}$ far behind the CD_2 target, which lead to a large background in the HPGe detectors, see page 32. A ${}^{27}\text{Al}$ target coming first in the photon beam would have the advantages, that there would be no resonant neutron absorption in the ${}^{27}\text{Al}$ (see figure 5.1) and that the interactions of neutrons in the lead shields of the HPGe detectors would be reduced (see table 5.1). The CD_2 target should than have a smaller diameter to ensure that it is completely shaded by the ${}^{27}\text{Al}$ target. It might also be possible to use “naked” HPGe detectors, i.e., without BGO or lead shields.

As shown in table 5.1 and figure 5.6, many neutrons that were scattered in the walls, the floor, or the ceiling are registered in the neutron detectors, but their time of flight (*tof*) corresponds to $T_{\text{cm}} < 200$ keV. Therefore, the *tof* of such neutrons must be prolonged to keep them out of the BBN energy range, which can be done in three ways:

1. A lower target–detector distance would reduce the *tof* of unscattered neutrons and prolong it for scattered neutrons. A deterioration of the energy resolution by the shorter distance would be acceptable, if the bin width was still as large as now (compare middle panel of figure 6.1). As the energy resolution is dominated by the flight path uncertainty and the time resolution of the detector (see section 3.5.3), the extremely short bunch length at ELBE would not limit a flight-path reduction.
2. A larger room would increase the flight path and thus the *tof* of scattered neutrons. The new neutron time-of-flight facility at ELBE (nELBE) offers a larger experimental area than the ELBE bremsstrahlung facility [Beyer2013, p. 162]. However, at nELBE it would only be possible to have bremsstrahlung emitted under an angle of about 90° from a thick target, for which the spectral distribution has to be simulated. It is also unclear, whether the kinetic electron energy at nELBE could be reduced to 5 MeV.
3. If the kinetic electron energy was lower, than both the spectrum of scattered and unscattered neutrons would be shifted towards lower energies. However, the kinetic electron energy of 5 MeV used in this dissertation was already at the lower limit of the ELBE accelerator, especially for the beam diagnostics.

In any case, the influence of changes in the experimental setup should be simulated *before* the measurement.

Appendix A Constant values used in this work

Table A.1: Values of constants used in this work. The uncertainties are given in parentheses in units of the last digit.

Quantity	Symbol	Numerical Value	Unit	Reference
Speed of light in vacuum	c	299.792458	mm ns^{-1}	[Mohr2012]
Electron mass	m_e	0.510998928(11)	MeV c^{-2}	[Mohr2012]
Proton mass	m_p	938.272046(21)	MeV c^{-2}	[Mohr2012]
Neutron mass	m_n	939.565379(21)	MeV c^{-2}	[Mohr2012]
Deuteron mass	m_d	1875.612859(41)	MeV c^{-2}	[Mohr2012]
Deuteron binding energy	B_d	2.22456614(41)	MeV	[Kessler1999]
Classical electron radius	r_e	2.8179403267(27)	fm	[Mohr2012]
Fine-structure constant	α	7.2973525698(24)	10^{-3}	[Mohr2012]

Appendix B Kinematics of the $d(\gamma,n)p$ reaction

Following the outline on kinematics in section 2.2, this chapter contains all definitions and the derivations of the relations between angles and energies in the two different frames. The equation numbers of section 2.2 are used here again.

The kinematics of the $d(\gamma,n)p$ reaction will be described in two reference frames. On the one hand, the laboratory (**lab**) frame is defined by a resting observer, i.e., all quantities are measured in this frame. It is assumed that the photon beam is parallel to the z -axis and that the deuteron is at rest in the **lab** frame. On the other hand, the center-of-mass (**cm**) frame is defined by a resting center of mass, i.e., the total momentum vanishes in this frame. This is the natural frame of the reaction. The velocity of the **cm** frame in the **lab** frame is v_{cm} . The following conventions will be used: The speed of light $c = 1$. If the frame is not denoted by an index, the prime symbol $'$ denotes the **cm** frame. Particles and coordinates are denoted by indices, too. The particle masses that have been used are listed in appendix A.

The relativistic relations between angles (or momentum coordinates p_x, p_y, p_z) and energies E in both frames can be calculated analytically using the momentum four-vector \mathbf{p} , the relativistic energy–momentum relation (including the mass m) and the Lorentz-transformation with its parameters β and γ :

$$\begin{aligned}
 \mathbf{p}_{\text{lab}} &= (E, p_x, p_y, p_z) & E' &= \gamma(E - \beta p_z) & E &= \gamma(E' + \beta p'_z) \\
 E^2 &= m^2 + p_x^2 + p_y^2 + p_z^2 & p'_x &= p_x & p_x &= p'_x \\
 \mathbf{p}_{\text{cm}} &= (E', p'_x, p'_y, p'_z) & p'_y &= p_y & p_y &= p'_y \\
 E'^2 &= m^2 + p_x'^2 + p_y'^2 + p_z'^2 & p'_z &= \gamma(p_z - \beta E) & p_z &= \gamma(p'_z + \beta E') \\
 & & \beta &= v_{\text{cm}} & \gamma &= (1 - \beta^2)^{-0.5}
 \end{aligned}$$

The initial state is described by

$$\begin{aligned}
 \mathbf{p}_{\gamma,\text{lab}} &= (E_\gamma, 0, 0, E_\gamma) & \mathbf{p}_{\gamma,\text{cm}} &= (E'_\gamma, 0, 0, E'_\gamma) \\
 \mathbf{p}_{\text{d},\text{lab}} &= (m_{\text{d}}, 0, 0, 0) & \mathbf{p}_{\text{d},\text{cm}} &= (E'_\text{d}, 0, 0, p'_{\text{d},z}) \\
 & & E'_\gamma &= (1 - \beta)\gamma E_\gamma \\
 & & E'_\text{d} &= \gamma m_{\text{d}} \\
 & & p'_{\text{d},z} &= -\beta\gamma m_{\text{d}}
 \end{aligned}$$

and the final state can be described in Cartesian or spherical coordinates by

$$\begin{aligned}
 \mathbf{p}_{\text{p},\text{lab}} &= (E_{\text{p}}, p_{\text{p},x}, p_{\text{p},y}, p_{\text{p},z}) = (E_{\text{p}}, p_{\text{p}} \sin \vartheta_{\text{p}} \cos \varphi_{\text{p}}, p_{\text{p}} \sin \vartheta_{\text{p}} \sin \varphi_{\text{p}}, p_{\text{p}} \cos \vartheta_{\text{p}}) \\
 \mathbf{p}_{\text{n},\text{lab}} &= (E_{\text{n}}, p_{\text{n},x}, p_{\text{n},y}, p_{\text{n},z}) = (E_{\text{n}}, p_{\text{n}} \sin \vartheta_{\text{n}} \cos \varphi_{\text{n}}, p_{\text{n}} \sin \vartheta_{\text{n}} \sin \varphi_{\text{n}}, p_{\text{n}} \cos \vartheta_{\text{n}}) \\
 p_{\text{p}/\text{n}} &\geq 0, \quad 0 \leq \vartheta_{\text{p}/\text{n}} \leq \pi, \quad 0 \leq \varphi_{\text{p}/\text{n}} < 2\pi \\
 \mathbf{p}_{\text{p},\text{cm}} &= (E'_{\text{p}}, p'_{\text{p},x}, p'_{\text{p},y}, p'_{\text{p},z}) = (E'_{\text{p}}, p'_{\text{p}} \sin \vartheta'_{\text{p}} \cos \varphi'_{\text{p}}, p'_{\text{p}} \sin \vartheta'_{\text{p}} \sin \varphi'_{\text{p}}, p'_{\text{p}} \cos \vartheta'_{\text{p}}) \\
 \mathbf{p}_{\text{n},\text{cm}} &= (E'_{\text{n}}, p'_{\text{n},x}, p'_{\text{n},y}, p'_{\text{n},z}) = (E'_{\text{n}}, p'_{\text{n}} \sin \vartheta'_{\text{n}} \cos \varphi'_{\text{n}}, p'_{\text{n}} \sin \vartheta'_{\text{n}} \sin \varphi'_{\text{n}}, p'_{\text{n}} \cos \vartheta'_{\text{n}}) \\
 p'_{\text{p}/\text{n}} &\geq 0, \quad 0 \leq \vartheta'_{\text{p}/\text{n}} \leq \pi, \quad 0 \leq \varphi'_{\text{p}/\text{n}} < 2\pi.
 \end{aligned}$$

Using momentum conservation in the **cm** initial state results in

$$\begin{aligned}
 0 &= p'_{\gamma,z} + p'_{\text{d},z} = E'_\gamma + p'_{\text{d},z} = (1 - \beta)\gamma E_\gamma - \beta\gamma m_{\text{d}} = E_\gamma - \beta(E_\gamma + m_{\text{d}}) \\
 \beta &= E_\gamma / (E_\gamma + m_{\text{d}}).
 \end{aligned} \tag{2.1}$$

With this, the **cm** photon energy is

$$E'_\gamma = (1 - \beta)\gamma E_\gamma = E_\gamma (1 + 2E_\gamma / m_{\text{d}})^{-0.5}. \tag{2.2}$$

In the initial state, the **cm** total energy \sqrt{s} , which is Lorentz invariant, can be calculated by

$$\sqrt{s} = E'_\gamma + E'_d = (1 - \beta)\gamma E_\gamma + \gamma m_d = m_d(1 + 2E_\gamma/m_d)^{0.5}. \quad (2.3)$$

The kinetic energy of the **cm** final state is then defined by

$$T_{\text{cm}} = \sqrt{s} - m_p - m_n. \quad (2.4)$$

Momentum conservation in the **cm** final state, i.e.,

$$0 = p'_{p,x} + p'_{n,x} \quad 0 = p'_{p,y} + p'_{n,y} \quad 0 = p'_{p,z} + p'_{n,z}$$

can be written in spherical coordinates as

$$p' := p'_n = p'_p \quad \vartheta' := \vartheta'_n = \pi - \vartheta'_p \quad \varphi' := \varphi'_n = \begin{cases} \varphi'_p + \pi & \varphi'_p < \pi \\ \varphi'_p - \pi & \varphi'_p \geq \pi. \end{cases}$$

The **cm** total energy calculated in the final state is

$$\sqrt{s} = E'_p + E'_n = (m_p^2 + p'^2)^{0.5} + (m_n^2 + p'^2)^{0.5}$$

and leads to the **cm** total momentum squared and the **cm** total neutron energy

$$p'^2 = [s - (m_p + m_n)^2][s - (m_p - m_n)^2]/(4s) \quad (2.5)$$

$$E'_n = (m_n^2 + p'^2)^{0.5} = (s + m_n^2 - m_p^2)/\sqrt{4s}. \quad (2.6)$$

The equations (2.1)–(2.6) show, that the velocity of the **cm** frame in the **lab** frame β , the **lab** photon energy E_γ , the **cm** photon energy E'_γ , the **cm** total energy \sqrt{s} , the **cm** kinetic energy T_{cm} , the **cm** total momentum p' , and the **cm** total neutron energy E'_n can be calculated, if one of these variables is known. Depending on the frame, in which neutron energy and angle are given, three cases are considered:

1. If E'_n and ϑ' are given, then the total energy E_n and the angle ϑ_n of the neutron in the **lab** frame are calculated by Lorentz back-transformation of the zeroth and the third component of $\mathbf{p}_{n,\text{lab}}$. One finds

$$E_n = \gamma(E'_n + \beta p' \cos \vartheta') = \gamma[(m_n^2 + p'^2)^{0.5} + \beta p' \cos \vartheta'] \quad (2.7)$$

$$\cos \vartheta_n = \gamma[p' \cos \vartheta' + \beta(m_n^2 + p'^2)^{0.5}]/(E'_n - m_n^2)^{0.5}. \quad (2.8)$$

2. If E'_n and ϑ_n are given, then the **lab** total neutron energy E_n and **cm** neutron angle ϑ' are calculated by Lorentz transformation of the zeroth and the third component of $\mathbf{p}_{n,\text{cm}}$. One finds

$$\begin{aligned} E'_n &= \gamma(E_n - \beta p_n \cos \vartheta_n) \\ E'_n/\gamma &= (p_n^2 + m_n^2)^{0.5} - \beta p_n \cos \vartheta_n \\ p_n^2 + m_n^2 &= E_n^2/\gamma^2 + 2p_n \cos \vartheta_n E'_n \beta/\gamma + \beta^2 p_n^2 \cos^2 \vartheta_n \\ 0 &= p_n^2(1 - \beta^2 \cos^2 \vartheta_n) + p_n(-2 \cos \vartheta_n E'_n \beta/\gamma) - E_n^2/\gamma^2 + m_n^2 \\ p_n^\pm &= \frac{\cos \vartheta_n E'_n \beta/\gamma \pm \sqrt{\cos^2 \vartheta_n E_n^2 \beta^2/\gamma^2 + (1 - \beta^2 \cos^2 \vartheta_n)(E_n^2/\gamma^2 - m_n^2)}}{1 - \beta^2 \cos^2 \vartheta_n} \\ &= \frac{\cos \vartheta_n E'_n \beta/\gamma \pm \sqrt{E_n^2/\gamma^2 - m_n^2(1 - \beta^2 \cos^2 \vartheta_n)}}{1 - \beta^2 \cos^2 \vartheta_n} \end{aligned} \quad (2.9)$$

$$\begin{aligned} T_{\text{cm}}^* &= \left[\frac{m_p^2 + \sqrt{m_p^4 - (1 - m_n^2/m_d^2) \left((m_p^2 - m_n^2)^2 - m_n^2 m_d^2 \right)}}{1 - m_n^2/m_d^2} \right]^{0.5} - m_p - m_n \\ &= 1.323 \text{ keV}. \end{aligned}$$

Because both solutions of equation 2.9 must be positive, T_{cm}^* is calculated from $p_n^- = 0$.

If $T_{\text{cm}} \geq T_{\text{cm}}^*$ then $\vartheta_n \in [0, \pi]$ and p_n^+ is the only solution.

If $T_{\text{cm}} < T_{\text{cm}}^*$ then $\vartheta_n \in [0, \arccos(\sqrt{1 - E_n'^2/(\gamma m_n)^2/\beta})]$ and p_n^+ and p_n^- are solutions.

This means, that p_n^- is irrelevant for BBN. Finally, one finds

$$E_n = (p_n^2 + m_n^2)^{0.5} \quad (2.10)$$

$$\cos \vartheta' = \gamma(p_n \cos \vartheta_n - \beta E_n)/p'. \quad (2.11)$$

3. If E_n and ϑ_n are given and only the case $T_{\text{cm}} \geq T_{\text{cm}}^*$ is considered, then the corresponding cm quantities are calculated by transforming p_n^+ from equation (2.9) into a function of only s and ϑ_n and solving it for s . This results in

$$s = m_d (Y_1 + Y_2) / Y_3 \quad (2.12)$$

$$Y_1 = p_n^2 (1 + \cos^2 \vartheta_n) m_d + p_n \cos \vartheta_n (m_p^2 - m_n^2 + m_d^2) + m_d m_p^2$$

$$Y_2 = \sqrt{p_n^2 + m_n^2} (2p_n \cos \vartheta_n m_d + (m_p^2 - m_n^2 + m_d^2))$$

$$Y_3 = p_n^2 (\cos^2 \vartheta_n - 1) + 2p_n \cos \vartheta_n m_d - m_n^2 + m_d^2$$

and E_n' and ϑ' can be calculated using equations (2.5), (2.6) and (2.11).

In all three cases, the relations between time of flight t_n , kinetic energy T_n and flight path l of a neutron are given by

$$t_n = l \frac{E_n}{p_n} = l \frac{T_n + m_n}{\sqrt{(T_n + m_n)^2 - m_n^2}} \Leftrightarrow T_n = m_n \left(\left(1 - \frac{l^2}{t_n^2} \right)^{-0.5} - 1 \right). \quad (2.13)$$

If there is a coordinate transformation between two one-dimensional variables $x \rightarrow y(x)$, then the chain rule has to be applied to differential quantities of $f(x)$, i.e., $df/dx = (df/dy) \cdot (dy/dx)$, in which dy/dx is the (1×1) -Jacobian-matrix of the transformation. The differential cross section in the lab frame and the cm frame are different because the solid-angle element $d\Omega = 2\pi \sin \vartheta d\vartheta = -2\pi d(\cos \vartheta)$ has to be transformed like

$$\frac{d\sigma}{d\Omega} = \frac{d\sigma}{d\Omega'} \frac{d\Omega'}{d\Omega} = \frac{d\sigma}{d\Omega'} \left(\frac{d}{d(\cos \vartheta')} \cos \vartheta_n \right)^{-1}$$

$$\frac{d}{d(\cos \vartheta')} \cos \vartheta_n = \frac{\gamma p' [(1 - \beta^2) \gamma^2 E_n' (\beta p' \cos \vartheta' + E_n') - m_n^2]}{[(\beta \gamma p' \cos \vartheta' + \gamma E_n')^2 - m_n^2]^{1.5}} = \frac{p' (E_n' E_n - \gamma m_n^2)}{p_n^3}. \quad (B.1)$$

The differential photon flux $d\Phi_\gamma/dE_\gamma$ has to be transformed to $d\Phi_\gamma/dT_{\text{cm}}$, $d\Phi_\gamma/dT_n$, or $d\Phi_\gamma/dt_n$. Using the terms Y_i from equation (2.12), the Jacobian matrices are

$$\frac{dE_\gamma}{dT_{\text{cm}}} = \frac{T_{\text{cm}} + m_p + m_n}{m_d} \quad (B.2)$$

$$\frac{dE_\gamma}{dT_n} = \frac{dE_\gamma}{ds} \frac{ds}{dp_n} \frac{dp_n}{dT_n} = \frac{1}{2m_d} \frac{m_d [d(Y_1 + Y_2)/dp_n Y_3 - (Y_1 + Y_2) dY_3/dp_n] E_n}{Y_3^2} \frac{E_n}{p_n} \quad (B.3)$$

$$\frac{dT_n}{dt_n} = m_n \frac{l^2}{t_n^3} \left(1 - \frac{l^2}{t_n^2} \right)^{-1.5}. \quad (B.4)$$

Appendix C Neutron sources

Table C.1: Comparison of several facilities offering neutron beams. At Tokyo Institute of Technology (TIT), University of Kentucky (UKY), and Los Alamos Neutron Science Center (LANSCE) there were measurements of the $p(n,\gamma)d$ cross section at Big Bang energies, while such measurements were planned at the neutron time-of-flight facility at ELBE (nELBE) and at the FRANZ neutron source (see section 2.6). At Physikalisch-Technische Bundesanstalt (PTB) Braunschweig, the efficiency of neutron detectors was calibrated (see chapter 4). T_{prim} , Δt_{prim} , and f_{prim} denote the kinetic energy, the bunch length, and the repetition rate of the primary-particle beam of the neutron-producing reaction. l is the distance from the neutron production target to the investigated sample. For $p(n,\gamma)d$ measurements, d is the sample thickness. T_n is the kinetic energy of the produced neutrons given as mean value or range.

facility, reference	neutron production	T_{prim} (MeV)	Δt_{prim} (ns)	f_{prim} (kHz)	l (m)	d (mm)	T_n (keV)
TIT, [Senoo1994]	${}^7\text{Li}(p,n)$	unpublished			0.08	2.0, 6.5, 10.2	10–30 30–50 50–80
TIT, [Suzuki1995b]	${}^7\text{Li}(p,n)$	1.9	1.5	2000	0.12	1, 2, 3, 4	20 40 64
TIT, [Tomyo2003]	${}^7\text{Li}(p,n)$	unpublished					110 148 180 344
TIT, [Nagai1997]	${}^7\text{Li}(p,n)$	2.3	1.5	4000	0.2	6.3, 10.5	550
UKY, [Daub2012]	${}^7\text{Li}(p,n)$ ${}^3\text{H}(p,n)$	2.23 1.62 2.0 2.5 3.0 3.5	1.0	1875	1.35	2	420 420 880 1450 1950 2500
LANSCE, [Daub2012]	p on W (spallation)	800	0.2	278, 556	15.45	2	$100-8 \cdot 10^5$
nELBE, [Beyer2013]	e^- on Pb (via (γ,n))	40	< 0.01	101, 203	5–7	-	$10-10^4$
FRANZ, [Reifarh2009]	${}^7\text{Li}(p,n)$	< 2.2	< 1	250	0.8	-	1–500
PTB, [Brede1980]	${}^7\text{Li}(p,n)$ ${}^3\text{H}(p,n)$ ${}^2\text{H}(d,n)$	1.94 1.94 2.03 2.30 2.10 3.35 2.30	1.2	625	1–3	-	24 144 250 565 1200 2500 5000

List of Acronyms and Abbreviations

ADC	analog-to-digital converter
AIST	National Institute of Advanced Industrial Science and Technology
BBN	Big Bang nucleosynthesis
BGO	bismuth germanate
BaF ₂	barium fluoride
CD ₂	deuterated polyethylene
CL	confidence level
cm	center of mass
CMB	cosmic microwave background radiation
CFD	constant-fraction discriminator
cw	continuous wave
DAQ	data acquisition
dc	direct current
EFT	effective field theory
ELBE	Electron Linac for beams with high Brilliance and low Emittance
FWHM	full width at half maximum
HIGS	High-Intensity Gamma-ray Source
HPGe	high-purity germanium
HV	high voltage
HZDR	Helmholtz-Zentrum Dresden-Rossendorf
lab	laboratory
LaBr ₃ (Ce)	cerium-doped lanthanum bromide
LANSCE	Los Alamos Neutron Science Center
LCS	Laser-Compton scattering
NaI(Tl)	thallium-doped sodium iodide
nELBE	neutron time-of-flight facility at ELBE
ndf	number of degrees of freedom
NN	nucleon–nucleon
NRF	nuclear resonance fluorescence
PMT	photomultiplier tube
PTB	Physikalisch-Technische Bundesanstalt
QDC	charge-to-digital converter
rf	radio frequency
S-DALINAC	Superconducting Darmstadt Linear electron Accelerator
TDC	time-to-digital converter
TIT	Tokyo Institute of Technology
tof	time of flight
UKY	University of Kentucky

List of Figures

0.1	Robert Herman, Ralph Alpher, and George Gamow	1
1.1	Nuclear reaction network of BBN	6
1.2	Calculated time-dependent mass fractions during BBN	7
1.3	Primordial abundances of light nuclei as function of η	7
2.1	Low-energy states of the NN system	9
2.2	Neutron angle as function of cm kinetic energy T_{cm}	11
2.3	Kinetic neutron energy T_n in the lab frame as function of T_{cm}	11
2.4	Calculated $d(\gamma,n)p$ cross sections at energies relevant to BBN	14
2.5	Calculated $d(\gamma,n)p$ differential cross sections at energies relevant to BBN	15
2.6	Previous $p(n,\gamma)d$ cross section measurements	16
2.7	Previous $p(n,\gamma)d$ cross section measurements at energies relevant to BBN	19
2.8	Previous absolute $d(\gamma,n)p$ cross section measurements	21
2.9	Previous measurements of the relative M1 contribution to the $d(\gamma,n)p$ cross section	21
3.1	Layout of ELBE in 2010	26
3.2	Layout of the $d(\gamma,n)p$ setup at ELBE	27
3.3	Setup of the $d(\gamma,n)p$ experiment at ELBE	28
3.4	Target and target holder	30
3.5	Self-leveling cross-line laser, movable scintillation detector, and photon beam dump	30
3.6	Technical drawing of the electron spectrometer	33
3.7	Measured spectra of the electron energy	34
3.8	Accelerator parameters logged during the $d(\gamma,n)p$ experiment	35
3.9	Detectors rates logged during the $d(\gamma,n)p$ experiment	35
3.10	Possible paths of the photon beam	36
3.11	Photon-beam profile measurements	36
3.12	Comparison of bremsstrahlung calculations	38
3.13	Al- CD_2 -multilayer target	41
3.14	Decrease of CD_2 layer mass over time	41
3.15	Level scheme of ^{27}Al	44
3.16	Fraction and maximum angle of Compton-scattered photons above B_d	46
3.17	Peaks in the γ -ray spectrum measured with an HPGe detector with beam on	48
3.18	γ -ray spectrum measured with an HPGe detector with beam on and off	49
3.19	Peak position stability and count rate losses	51
3.20	Measured and simulated full-energy-peak efficiency of the HPGe detectors	53
3.21	Alignment of detector axes with target	53
3.22	Geometry of efficiency simulation with GEANT4	54
3.23	Position-dependent full-energy-peak efficiency	56
3.24	Measured and calculated photon flux	57
3.25	Layout of a neutron detector	59
3.26	Time-of-flight spectrum of the $d(\gamma,n)p$ experiment at ELBE	60
3.27	Total and coincidence count rates of the PMTs of detector 3	62
4.1	Measured and simulated efficiency before the $d(\gamma,n)p$ experiment	66
4.2	Low-scatter facility at the PTB ion accelerator facility	67
4.3	Experimental setup of the efficiency calibration at PTB Braunschweig	68
4.4	Angle–energy relation of the neutron-producing reactions	68

4.5	Tof spectra with and without shadow bar	71
4.6	Spectral neutron fluence simulated with the TARGET code	73
4.7	Results of the efficiency calibration at PTB Braunschweig in 2011	73
4.8	QDC spectra measured at 72 keV	75
5.1	Estimated attenuation of neutrons in the target	78
5.2	Neutron distribution used as primary particle source for the FLUKA simulation	80
5.3	Three-dimensional rendering of the geometry of the FLUKA simulation	80
5.4	Geometry of the FLUKA simulation in the xz -plane at $y = 0$	80
5.5	Visualization of one event simulated with FLUKA	81
5.6	Correlation between kinetic energy and tof of neutrons hitting the detector	82
5.7	Correction factor for efficiency and simulated modification of the neutron spectrum	84
5.8	Geometry of the modified FLUKA simulation	86
6.1	Differential $d(\gamma,n)p$ cross section, energy resolution, and uncertainties	88
6.2	Cross section of the $d(\gamma,n)p$ reaction in the energy range 0.3–2.6 MeV	89

List of Tables

3.1	ELBE parameters	26
3.2	Previous experiments at the ELBE bremsstrahlung facility	27
3.3	Parameters of the measurements with the electron spectrometer	34
3.4	Parameters of the photon-beam profile measurements	37
3.5	Correction factors for the attenuation of photons in the target	45
3.6	Observed count rates with beam on and off	50
3.7	Results of the photon flux measurement	57
3.8	Correction of dead time caused by the CFD veto	63
3.9	Solid angles of the neutron detectors with and without lead shields	64
4.1	Measured energy and calibration factors	69
4.2	Results of the efficiency calibration	74
5.1	Relative abundance of simulated events depending on previous interaction place	82
6.1	$d(\gamma,n)p$ cross section data from ELBE shown in figure 6.2	90
A.1	Values of constants used in this work	93
C.1	Comparison of several facilities offering neutron beams	97

Bibliography

- [**Ahmed2008**] M. W. Ahmed et al., *Measurement of $d(\gamma,n)p$ reaction cross section*, in *TUNL XLVII Progress Report 1 September 2007 - 31 August 2008*, p. 100, Triangle Universities Nuclear Laboratory, 2008, <http://www.tunl.duke.edu/documents/public/tunlxlvii.pdf> cited on page(s) 23
- [**Ahrens1974**] J. Ahrens et al., *Photodisintegration of the deuteron at 15–25 MeV photon energy*, *Phys. Lett. B* **52** (1974) 49–50, doi:10.1016/0370-2693(74)90715-1 cited on page(s) 22
- [**AjzenbergSelove1990**] F. Ajzenberg-Selove, *Energy levels of light nuclei $A = 11-12$* , *Nucl. Phys. A* **506** (1990) 1–158, doi:10.1016/0375-9474(90)90271-M cited on page(s) 39
- [**Alpher1948a**] R. A. Alpher, H. Bethe and G. Gamow, *The Origin of Chemical Elements*, *Phys. Rev.* **73** (1948) 803–804, doi:10.1103/PhysRev.73.803 cited on page(s) 1
- [**Alpher1948b**] R. A. Alpher and R. Herman, *Evolution of the Universe*, *Nature* **162** (1948) 774–775, doi:10.1038/162774b0 cited on page(s) 1
- [**Alpher1950**] R. A. Alpher and R. C. Herman, *Theory of the Origin and Relative Abundance Distribution of the Elements*, *Rev. Mod. Phys.* **22** (1950) 153–212, doi:10.1103/RevModPhys.22.153 cited on page(s) 1
- [**Alpher1953**] R. A. Alpher, J. W. Follin and R. C. Herman, *Physical Conditions in the Initial Stages of the Expanding Universe*, *Phys. Rev.* **92** (1953) 1347–1361, doi:10.1103/PhysRev.92.1347 cited on page(s) 1
- [**Amaldi1936**] E. Amaldi and E. Fermi, *On the Absorption and the Diffusion of Slow Neutrons*, *Phys. Rev.* **50** (1936) 899–928, doi:10.1103/PhysRev.50.899 cited on page(s) 16
- [**Ando2006**] S. Ando et al., *Radiative neutron capture on a proton at big-bang nucleosynthesis energies*, *Phys. Rev. C* **74** (2006) 025809, doi:10.1103/PhysRevC.74.025809 cited on page(s) 8, 13, 106
- [**Arenhoevel1991**] H. Arenhövel and M. Sanzone, *Photodisintegration of the Deuteron - A Review of Theory and Experiment*, *Few-Body Systems*, Supplementum 3, Springer-Verlag, Wien, 1991 cited on page(s) 13, 15, 17, 20, 22, 23
- [**Arenhoevel2005**] H. Arenhövel, *Private communication*, Universität Mainz, 2005 cited on page(s) 13, 14, 87, 88
- [**Barnes1952**] C. A. Barnes et al., *The Photodisintegration of the Deuteron at Intermediate Energies. I*, *Phys. Rev.* **86** (1952) 359–372, doi:10.1103/PhysRev.86.359 cited on page(s) 20, 91
- [**Battistoni2007**] G. Battistoni et al., *The FLUKA code: description and benchmarking*, in M. Albrow and R. Raja (Editors), *Proceedings of the Hadronic Shower Simulation Workshop, Batavia, Illinois, USA, 06.-08.09.2006*, AIP Conf. Proc. **896** (2007) 31–49, doi:10.1063/1.2720455 cited on page(s) 77
- [**Baur1976**] G. Baur and D. Trautmann, *The break-up of the deuteron and stripping to unbound states*, *Phys. Rep.* **25** (1976) 293–358, doi:10.1016/0370-1573(76)90038-7 cited on page(s) 24
- [**Baur1986**] G. Baur, C. Bertulani and H. Rebel, *Coulomb dissociation as a source of information on radiative capture processes of astrophysical interest*, *Nucl. Phys. A* **458** (1986) 188–204, doi:10.1016/0375-9474(86)90290-3 cited on page(s) 24

- [**Berger2010**] M. J. Berger et al., *XCOM: Photon Cross Section Database (version 1.5)*, National Institute of Standards and Technology, Gaithersburg, MD, USA, 2010, <http://physics.nist.gov/xcom> cited on page(s) 39, 44, 52
- [**Bernabei1986**] R. Bernabei et al., *Total Cross Section for Deuteron Photodisintegration between 15 and 75 MeV*, Phys. Rev. Lett. **57** (1986) 1542–1545, doi:10.1103/PhysRevLett.57.1542 cited on page(s) 23
- [**Bertulani1988**] C. A. Bertulani and G. Baur, *Electromagnetic processes in relativistic heavy ion collisions*, Phys. Rep. **163** (1988) 299–408, doi:10.1016/0370-1573(88)90142-1 cited on page(s) 24
- [**Bethe1935**] H. Bethe and R. Peierls, *Quantum Theory of the Dipion*, Proc. R. Soc. Lond. A **148** (1935) 146–156, doi:10.1098/rspa.1935.0010 cited on page(s) 13
- [**Bethe1950**] H. A. Bethe and C. Longmire, *The Effective Range of Nuclear Forces II. Photo-Disintegration of the Deuteron*, Phys. Rev. **77** (1950) 647–654, doi:10.1103/PhysRev.77.647 cited on page(s) 13
- [**Beyer2005**] R. Beyer, *Aufbau und Entwicklung von Neutronen-Flugzeit-Detektoren für die Untersuchung astrophysikalisch relevanter (γ,n)-Reaktionen*, Diploma thesis, Friedrich-Schiller-Universität Jena, 2005, <http://www.db-thueringen.de/servlets/DerivateServlet/Derivate-8025> cited on page(s) 2, 22, 25, 27, 31, 32, 40, 58, 59, 60, 64, 65
- [**Beyer2007**] R. Beyer et al., *Proton-recoil detectors for time-of-flight measurements of neutrons with kinetic energies from some tens of keV to a few MeV*, Nucl. Instrum. Methods A **575** (2007) 449–455, doi:10.1016/j.nima.2007.02.096 cited on page(s) 59, 60, 64, 65, 66, 72
- [**Beyer2011**] R. Beyer, *Private communication*, Hemholtz-Zentrum Dresden-Rossendorf, 2011 cited on page(s) 66
- [**Beyer2013**] R. Beyer et al., *Characterization of the neutron beam at nELBE*, Nucl. Instrum. Methods A **723** (2013) 151–162, doi:10.1016/j.nima.2013.05.010 cited on page(s) 60, 64, 92, 97
- [**Beyer2014**] R. Beyer, *Inelastische Streuung schneller Neutronen an ^{56}Fe* , Dissertation (submitted), Technische Universität Dresden, 2014 cited on page(s) 66, 75
- [**Birenbaum1985**] Y. Birenbaum, S. Kahane and R. Moreh, *Absolute cross section for the photodisintegration of deuterium*, Phys. Rev. C **32** (1985) 1825–1829, doi:10.1103/PhysRevC.32.1825 cited on page(s) 20
- [**Bishop1950**] G. R. Bishop et al., *The Cross Section for Photo-Disintegration of the Deuteron at Low Energies*, Phys. Rev. **80** (1950) 211–222, doi:10.1103/PhysRev.80.211 cited on page(s) 20
- [**Bishop1951**] G. R. Bishop, L. E. Beghian and H. Halban, *The Angular Distribution in the Photodisintegration of the Deuteron at Low Energies*, Phys. Rev. **83** (1951) 1052–1053, doi:10.1103/PhysRev.83.1052 cited on page(s) 20
- [**Blaich1993**] T. Blaich and B. Dechant, *Performance of LAND studied by Deuteron Dissociation*, in U. Grundinger (Editor), *GSI Scientific Report 1992*, p. 375, Gesellschaft für Schwerionenforschung, Darmstadt, 1993, <http://repository.gsi.de/record/53539> cited on page(s) 24
- [**Boesgaard1985**] A. M. Boesgaard and G. Steigman, *Big Bang Nucleosynthesis: Theories and Observations*, Ann. Rev. Astron. Astrophys. **23** (1985) 319–378, doi:10.1146/annurev.aa.23.090185.001535 cited on page(s) 2

- [Brede1980] H. J. Brede et al., *The Braunschweig accelerator facility for fast neutron research: I: Building design and accelerators*, Nucl. Instrum. Methods **169** (1980) 349–358, doi:10.1016/0029-554X(80)90928-3 cited on page(s) 66, 67, 97
- [Browne1956] C. P. Browne and W. W. Buechner, *Broad-Range Magnetic Spectrograph*, Rev. Sci. Instrum. **27** (1956) 899–907, doi:10.1063/1.1715411 cited on page(s) 33
- [Brun1997] R. Brun and F. Rademakers, *ROOT – An Object Oriented Data Analysis Framework*, Nucl. Instrum. Methods A **389** (1997) 81–86, doi:10.1016/S0168-9002(97)00048-X, see also <http://root.cern.ch> cited on page(s) 47
- [Burbidge1957] E. M. Burbidge et al., *Synthesis of the Elements in Stars*, Rev. Mod. Phys. **29** (1957) 547–650, doi:10.1103/RevModPhys.29.547 cited on page(s) 1
- [Burles1999] S. Burles et al., *Sharpening the Predictions of Big-Bang Nucleosynthesis*, Phys. Rev. Lett. **82** (1999) 4176–4179, doi:10.1103/PhysRevLett.82.4176 cited on page(s) 8
- [Cameron1959] A. G. W. Cameron, *The origin of the elements*, Phys. Chem. Earth **3** (1959) 199–223, doi:10.1016/0079-1946(59)90006-0 cited on page(s) 1
- [Cerineo1961] M. Cerineo et al., *Capture of 14.4-Mev Neutrons by Protons and Deuterons*, Phys. Rev. **124** (1961) 1947–1948, doi:10.1103/PhysRev.124.1947 cited on page(s) 17
- [Chadwick1935] J. Chadwick and M. Goldhaber, *The Nuclear Photoelectric Effect*, Proc. R. Soc. Lond. A **151** (1935) 479–493, doi:10.1098/rspa.1935.0162 cited on page(s) 20
- [Chen1999] J.-W. Chen and M. J. Savage, *$np \rightarrow d\gamma$ for big-bang nucleosynthesis*, Phys. Rev. C **60** (1999) 065205, doi:10.1103/PhysRevC.60.065205, <http://arxiv.org/abs/nucl-th/9907042> cited on page(s) 13, 79, 89
- [Coc2010] A. Coc and E. Vangioni, *Big-Bang nucleosynthesis with updated nuclear data*, in *Proceedings of the 4th International Conference on Nuclear Physics in Astrophysics (NPA IV), Frascati, Italy, 08.-12.06.2009*, J. Phys. Conf. Ser. **202** (2010) 012001, doi:10.1088/1742-6596/202/1/012001 cited on page(s) 8
- [Coc2012] A. Coc et al., *Standard big bang nucleosynthesis up to CNO with an improved extended nuclear network*, Astrophys. J. **744** (2012) 158, doi:10.1088/0004-637X/744/2/158 cited on page(s) 6
- [Cokinos1977] D. Cokinos and E. Melkonian, *Measurement of the 2200 m/sec neutron-proton capture cross section*, Phys. Rev. C **15** (1977) 1636–1643, doi:10.1103/PhysRevC.15.1636 cited on page(s) 16, 17
- [Colgate1951] S. A. Colgate, *The Photodisintegration Cross Section of the Deuteron*, Phys. Rev. **83** (1951) 1262–1263, doi:10.1103/PhysRev.83.1262 cited on page(s) 20
- [Collie1950] C. H. Collie, H. Halban and R. Wilson, *Photoelectric Dissociation of the Deuteron*, Proc. Phys. Soc. A **63** (1950) 994–1009, doi:10.1088/0370-1298/63/9/307 cited on page(s) 20
- [Cox1965] A. E. Cox, S. A. R. Wynchank and C. H. Collie, *The proton-thermal neutron capture cross section*, Nucl. Phys. A **74** (1965) 497–507, doi:10.1016/0029-5582(65)90197-5 cited on page(s) 16, 17, 19
- [Cyburt2001] R. H. Cyburt, B. D. Fields and K. A. Olive, *The NACRE thermonuclear reaction compilation and big bang nucleosynthesis*, New Astron. **6** (2001) 215–238, doi:10.1016/S1384-1076(01)00053-7, <http://arxiv.org/abs/astro-ph/0102179> cited on page(s) 8

- [**Cybert2004**] R. H. Cybert, *Primordial nucleosynthesis for the new cosmology: Determining uncertainties and examining concordance*, Phys. Rev. D **70** (2004) 023505, doi:10.1103/PhysRevD.70.023505, <http://arxiv.org/abs/astro-ph/0401091> cited on page(s) 5, 8
- [**Cybert2005**] R. H. Cybert et al., *New BBN limits on physics beyond the standard model from ^4He* , Astropart. Phys. **23** (2005) 313–323, doi:10.1016/j.astropartphys.2005.01.005, <http://arxiv.org/abs/astro-ph/0408033> cited on page(s) 6
- [**Cybert2008**] R. H. Cybert, B. D. Fields and K. A. Olive, *An update on the big bang nucleosynthesis prediction for ^7Li : the problem worsens*, J. Cosmol. Astropart. Phys. **11** (2008) 012, doi:10.1088/1475-7516/2008/11/012, <http://arxiv.org/abs/0808.2818> cited on page(s) 6, 8
- [**Daub2012**] B. Daub, *Low energy neutron-proton interactions*, Dissertation, Massachusetts Institute of Technology, 2012, <http://dspace.mit.edu/handle/1721.1/76978> cited on page(s) 19, 97
- [**Daub2013**] B. H. Daub et al., *Response of BC-418 plastic scintillator to low-energy protons*, Nucl. Instrum. Methods A **701** (2013) 171–175, doi:10.1016/j.nima.2012.11.025 cited on page(s) 19, 75
- [**Descouvemont2004**] P. Descouvemont et al., *Compilation and R-matrix analysis of Big Bang nuclear reaction rates*, At. Data Nucl. Data Tables **88** (2004) 203–236, doi:10.1016/j.adt.2004.08.001 cited on page(s) 8
- [**Dietze1982**] G. Dietze and H. Klein, *NRESP4 and NEFF4 - Monte Carlo codes for the calculation of neutron response functions and detection efficiencies for NE 213 scintillation detectors*, Technical Report PTB-ND-22, Physikalisch-Technische Bundesanstalt Braunschweig, 1982 cited on page(s) 65
- [**Edwards1992**] G. W. R. Edwards et al., *Forward $p(n,d)\gamma$ cross sections above the pion production threshold*, Nucl. Phys. A **543** (1992) 685–702, doi:10.1016/0375-9474(92)90554-W cited on page(s) 17
- [**Elbe2013**] <http://www.hzdr.de/ELBE>, retrieved on 04.12.2013 cited on page(s) 25, 26
- [**Endt1990**] P. M. Endt, *Energy levels of $A = 21-44$ nuclei (VII)*, Nucl. Phys. A **521** (1990) 1–400, doi:10.1016/0375-9474(90)90598-G cited on page(s) 44
- [**Epelbaum2013**] E. Epelbaum, *Few-Body Physics in Chiral Effective Field Theory: Recent Developments*, Few-Body Syst. **54** (2013) 11–17, doi:10.1007/s00601-012-0326-1 cited on page(s) 14
- [**Erhard2009**] M. Erhard, *Photoaktivierung des p -Kerns ^{92}Mo am Bremsstrahlungsmessplatz von ELBE*, Dissertation, Technische Universität Dresden, 2009, <http://www.hzdr.de/publications/019255/19255.pdf> cited on page(s) 22, 27, 33, 47, 55
- [**Evans1955**] R. D. Evans, *The Atomic Nucleus*, McGraw-Hill Book Company, New York, 1955 cited on page(s) 10, 13, 15
- [**Fermi1935**] E. Fermi, *On the Recombination of Neutrons and Protons*, Phys. Rev. **48** (1935) 570, doi:10.1103/PhysRev.48.570 cited on page(s) 13
- [**Ferrari2005**] A. Ferrari et al., *FLUKA: a multi-particle transport code*, Technical Report CERN-2005-10, INFN/TC_05/11, SLAC-R-773, 2005, <http://www.slac.stanford.edu/cgi-wrap/getdoc/slac-r-773.pdf>, see also <http://www.fluka.org> cited on page(s) 77

- [**Ferrari2013**] A. Ferrari, HZDR, *Technical support and advice regarding all FLUKA simulations in this dissertation (writing of input files, implementation of user routines for neutron source and time of flight, running of simulations on a computer cluster)*, 2013
cited on page(s) 77, 79, 80, 81, 83
- [**Fields2006**] B. D. Fields and K. A. Olive, *Big bang nucleosynthesis*, Nucl. Phys. A **777** (2006) 208–225, doi:10.1016/j.nuclphysa.2004.10.033
cited on page(s) 5, 8
- [**Fields2011**] B. D. Fields, *The Primordial Lithium Problem*, Annu. Rev. Nucl. Part. Sci. **61** (2011) 47–68, doi:10.1146/annurev-nucl-102010-130445
cited on page(s) 5, 6
- [**Fiorentini1998**] G. Fiorentini et al., *Quantifying uncertainties in primordial nucleosynthesis without Monte Carlo simulations*, Phys. Rev. D **58** (1998) 063506, doi:10.1103/PhysRevD.58.063506
cited on page(s) 8
- [**Frisch1938**] O. R. Frisch, H. v. Halban, Jr. and J. Koch, *On the slowing down and capture of neutrons in hydrogenous substances*, Mathematisk-fysiske Meddelelser **15** (1938) 10, <http://www.sdu.dk/Bibliotek/matfys>
cited on page(s) 16
- [**Fuller2010**] G. M. Fuller and C. J. Smith, *Nuclear weak interaction rates in primordial nucleosynthesis*, Phys. Rev. D **82** (2010) 125017, doi:10.1103/PhysRevD.82.125017
cited on page(s) 6
- [**Gabriel2000**] F. Gabriel et al., *The Rossendorf radiation source ELBE and its FEL projects*, Nucl. Instrum. Methods B **161** (2000) 1143–1147, doi:10.1016/S0168-583X(99)00909-X
cited on page(s) 25, 26
- [**Geant4-2003**] GEANT4 collaboration, *GEANT4 – a simulation toolkit*, Nucl. Instrum. Methods A **506** (2003) 250–303, doi:10.1016/S0168-9002(03)01368-8, see also <http://www.geant4.org>
cited on page(s) 54
- [**Gericke2011**] M. T. Gericke et al., *Measurement of parity-violating γ -ray asymmetry in the capture of polarized cold neutrons on protons*, Phys. Rev. C **83** (2011) 015505, doi:10.1103/PhysRevC.83.015505
cited on page(s) 17
- [**Graeve1991**] A. D. Graeve et al., *The forward, backward and 90° deuteron photodisintegration between 7 and 19 MeV photon energy*, Nucl. Phys. A **530** (1991) 420–436, doi:10.1016/0375-9474(91)90811-J
cited on page(s) 22
- [**Graeve1992**] A. D. Graeve et al., *Absolute total cross sections for deuteron photodisintegration between 7 and 19 MeV*, Phys. Rev. C **45** (1992) 860–862, doi:10.1103/PhysRevC.45.860
cited on page(s) 22
- [**Hannaske2010**] R. Hannaske et al., *Towards a precision measurement of the photodissociation of the deuteron at energies relevant to Big Bang nucleosynthesis*, in *Proceedings of the 11th Symposium on Nuclei in the Cosmos (NIC XI), Heidelberg, Germany, 19.-23.07.2010*, Proc. Sci. **NIC XI** (2010) 090, http://pos.sissa.it/archive/conferences/100/090/NIC_XI_090.pdf
cited on page(s) 64
- [**Hannaske2013**] R. Hannaske et al., *Neutron total cross section measurements of gold and tantalum at the nELBE photoneutron source*, Eur. Phys. J. A **49** (2013) 137, doi:10.1140/epja/i2013-13137-1
cited on page(s) 60, 61, 63, 74
- [**Hannaske2016**] R. Hannaske et al., *Measurement of the photodissociation of the deuteron at energies relevant to Big Bang nucleosynthesis*, in *Proceedings of the 6th International Conference on Nuclear Physics in Astrophysics (NPA-VI), Lisbon, Portugal, 19.-24.05.2013*, J. Phys. Conf. Ser. **665** (2016) 012003, doi:10.1088/1742-6596/665/1/012003
cited on page(s) 87

- [**Hara2003**] K. Y. Hara et al., *Photodisintegration of deuterium and big bang nucleosynthesis*, Phys. Rev. D **68** (2003) 072001, doi:10.1103/PhysRevD.68.072001 cited on page(s) 23, 91
- [**Haug2004a**] E. Haug and W. Nakel, *The Elementary Process of Bremsstrahlung*, World Scientific Publishing, Singapore, 2004 cited on page(s) 37
- [**Haug2004b**] E. Haug, *Private communication*, Universität Tübingen, 2004 cited on page(s) 38
- [**Haug2008**] E. Haug, *Bremsstrahlung cross-section with screening and Coulomb corrections at high energies*, Rad. Phys. Chem. **77** (2008) 207–214, doi:10.1016/j.radphyschem.2007.10.003 cited on page(s) 38, 91
- [**Hayashi1950**] C. Hayashi, *Proton-Neutron Concentration Ratio in the Expanding Universe at the Stages preceding the Formation of the Elements*, Prog. Theor. Phys. **5** (1950) 224–235, doi:10.1143/ptp/5.2.224, <http://ptp.oxfordjournals.org/content/5/2/224> cited on page(s) 1
- [**Hetherington2014**] N. S. Hetherington and W. P. McCray, *Big Bang or Steady State?*, in S. R. Weart (Editor), *Cosmic Journey: A History of Scientific Cosmology*, Online exhibit, American Institute of Physics, Center for History of Physics, 2014, <http://www.aip.org/history/cosmology/index.htm> cited on page(s) 1, 2
- [**Hoyle1964**] F. Hoyle and R. J. Tayler, *The Mystery of the Cosmic Helium Abundance*, Nature **203** (1964) 1108–1110, doi:10.1038/2031108a0 cited on page(s) 2
- [**Iocco2009**] F. Iocco et al., *Primordial nucleosynthesis: From precision cosmology to fundamental physics*, Phys. Rep. **472** (2009) 1–76, doi:10.1016/j.physrep.2009.02.002, <http://arxiv.org/abs/0809.0631> cited on page(s) 5, 6
- [**Jenkins1994**] D. A. Jenkins, P. T. Debevec and P. D. Harty, *$^2H(\gamma,p)n$ cross section between 20 and 440 MeV*, Phys. Rev. C **50** (1994) 74–83, doi:10.1103/PhysRevC.50.74 cited on page(s) 20
- [**Johnson2001**] A. S. Johnson and G. M. Hale, *Recent R-matrix results for np-capture*, Nucl. Phys. A **688** (2001) 566–568, doi:10.1016/S0375-9474(01)00789-8, Data extracted from [**Ando2006**]. cited on page(s) 14
- [**Junghans2007**] A. R. Junghans, A. Wagner and E. Grosse, *Präzisionsmessung der Photodissoziation des Deuterons und der Umkehrreaktion bei Energien im Bereich der Big-Bang-Nukleosynthese*, 2007, <http://gepris.dfg.de/gepris/projekt/50561647> cited on page(s) 2, 19, 22, 25
- [**Kellogg1936**] J. M. B. Kellogg, I. I. Rabi and J. R. Zacharias, *The Gyromagnetic Properties of the Hydrogens*, Phys. Rev. **50** (1936) 472–481, doi:10.1103/PhysRev.50.472 cited on page(s) 9
- [**Kessler1999**] E. G. Kessler, Jr. et al., *The deuteron binding energy and the neutron mass*, Phys. Lett. A **255** (1999) 221–229, doi:10.1016/S0375-9601(99)00078-X cited on page(s) 9, 93
- [**Kii1998**] T. Kii et al., *Deuteron photodisintegration near threshold*, in N. Prantzos and S. Harissopulos (Editors), *Nuclei in the Cosmos V: Proceedings of the International Symposium on Nuclear Astrophysics, Volos, Greece, 06.-11.07.1998*, pp. 21–24, Atlantica Séguier Frontières, 1998 cited on page(s) 23
- [**Kii1999**] T. Kii, *Study of the Photodisintegration of Deuteron near threshold using Laser Compton Scattering gamma-rays*, Dissertation, Tokyo Institute of Technology, written in Japanese, 1999 cited on page(s) 23
- [**Kii2005**] T. Kii et al., *A time projection chamber for the study of nuclear photodisintegration*, Nucl. Instrum. Methods A **552** (2005) 329–343, doi:10.1016/j.nima.2005.07.003 cited on page(s) 23

- [**Kirkman2003**] D. Kirkman et al., *The Cosmological Baryon Density from the Deuterium-to-Hydrogen Ratio in QSO Absorption Systems: D/H toward Q1243+3047*, *Astrophys. J. Suppl. Ser.* **149** (2003) 1–28, doi:10.1086/378152 cited on page(s) 4
- [**Kneissl1996**] U. Kneissl, H. H. Pitz and A. Zilges, *Investigation of nuclear structure by resonance fluorescence scattering*, *Prog. Part. Nucl. Phys.* **37** (1996) 349–433, doi:10.1016/0146-6410(96)00055-5 cited on page(s) 43, 44
- [**Knoll1999**] G. F. Knoll, *Radiation Detection and Measurement*, John Wiley & Sons, New York, 3rd edition, 1999 cited on page(s) 31, 46, 52, 58, 61
- [**Koch1959**] H. W. Koch and J. W. Motz, *Bremsstrahlung Cross-Section Formulas and Related Data*, *Rev. Mod. Phys.* **31** (1959) 920–955, doi:10.1103/RevModPhys.31.920 cited on page(s) 37
- [**Kosev2007**] K. Kosev, *A High-Resolution Time-of-Flight Spectrometer for Fission Fragments and Ion Beams*, Dissertation, Technische Universität Dresden, 2007, <http://www.hzdr.de/publications/012023/12023.pdf> cited on page(s) 27
- [**Kraeckmann2012**] S. Kräckmann, *Kalibrierung und Aufbau eines LENA-Prototyps für R^3B* , Master thesis, Goethe-Universität Frankfurt am Main, 2012 cited on page(s) 59
- [**Landau1958**] C. Landau and Y. Smorodinsky, *Lectures on Nuclear Theory*, Springer Science+Business Media, New York, 1958, doi:10.1007/978-1-4899-6457-1 cited on page(s) 9
- [**Langer2011**] C. Langer et al., *Simulations and developments of the Low Energy Neutron detector Array LENA*, *Nucl. Instrum. Methods A* **659** (2011) 411–418, doi:10.1016/j.nima.2011.06.079 cited on page(s) 59
- [**Lehnert2007**] U. Lehnert, *NMR Magnetic Field Measurements and Beam Energy Calibration*, in *Wissenschaftlich-Technische Berichte FZD-473: Annual Report 2005/06 - Radiation Source ELBE*, p. 9, Forschungszentrum Dresden-Rossendorf, 2007, <http://www.hzdr.de/publications/010331/10331.pdf> cited on page(s) 33
- [**Leicht1981**] R. Leicht et al., *Monochromatic nuclear photon scattering experiment*, *Nucl. Instrum. Methods* **179** (1981) 131–139, doi:10.1016/0029-554X(81)91171-X cited on page(s) 22
- [**Li2005**] Z. Li et al., *Properties of plastic scintillators after irradiation*, *Nucl. Instrum. Methods A* **552** (2005) 449 – 455, doi:10.1016/j.nima.2005.06.075 cited on page(s) 75
- [**Machleidt2001**] R. Machleidt and I. Slaus, *The nucleon-nucleon interaction*, *J. Phys. G* **27** (2001) R69–R108, doi:10.1088/0954-3899/27/5/201 cited on page(s) 13
- [**Makosky1969**] L. M. Makosky, *Study of self-supporting deuterated polyethylene targets*, Master thesis, University of British Columbia, 1969, <http://hdl.handle.net/2429/35077> cited on page(s) 42
- [**Malaney1993**] R. A. Malaney and G. J. Mathews, *Probing the early universe: a review of primordial nucleosynthesis beyond the standard big bang*, *Phys. Rep.* **229** (1993) 145–219, doi:10.1016/0370-1573(93)90134-Y cited on page(s) 6
- [**Marcucci2006**] L. E. Marcucci et al., *Modern theories of low-energy astrophysical reactions*, *Nucl. Phys. A* **777** (2006) 111–136, doi:10.1016/j.nuclphysa.2004.09.008 cited on page(s) 13
- [**Marin1954**] P. Marin, G. R. Bishop and H. Halban, *The Absolute Standardization of the 2.615 MeV γ -rays of ThC'' and the Cross Section for the Photo Disintegration of the Deuteron at this Energy*, *Proc. Phys. Soc. A* **67** (1954) 1113, doi:10.1088/0370-1298/67/12/114 cited on page(s) 20

- [**Massarczyk2010**] R. J. Massarczyk, *Bestimmung der elektromagnetischen Dipolstärkeverteilung in mittelschweren Atomkernen mittels Kernresonanzfluoreszenz*, Diploma thesis, Technische Universität Dresden, 2010, <http://www.hzdr.de/publications/015458/15458.pdf> cited on page(s) 54
- [**Massarczyk2012**] R. Massarczyk et al., *Electromagnetic dipole strength of ^{136}Ba below the neutron separation energy*, Phys. Rev. C **86** (2012) 014319, doi:10.1103/PhysRevC.86.014319 cited on page(s) 27
- [**Massarczyk2014**] R. Massarczyk, *The effect of neutron excess and nuclear deformation on dipole strength functions below the neutron separation energy - nuclear resonance fluorescence experiments on $^{124,128,132,134}\text{Xe}$ at ELBE and HIγS*, Dissertation (submitted), Technische Universität Dresden, 2014 cited on page(s) 55
- [**Mayer-Kuckuk2002**] T. Mayer-Kuckuk, *Kernphysik / eine Einführung*, Teubner, Stuttgart; Leipzig; Wiesbaden, 7th edition, 2002 cited on page(s) 12
- [**McMurray1955**] W. R. McMurray and C. H. Collie, *The Radium Equivalent of ^{24}Na Sources and the Photodisintegration Cross Section of Deuterium*, Proc. Phys. Soc. A **68** (1955) 181–188, doi:10.1088/0370-1298/68/3/307 cited on page(s) 20
- [**Metzger1959**] F. R. Metzger, *Resonance fluorescence in nuclei*, in O. R. Frisch (Editor), *Progress in Nuclear Physics*, volume 7, pp. 53–88, Pergamon Press, New York, 1959 cited on page(s) 43
- [**Michel1989**] P. Michel et al., *Measurement of the capture reaction $H(n, d)\gamma$ at 25.6 MeV*, J. Phys. G **15** (1989) 1025–1032, doi:10.1088/0954-3899/15/7/010 cited on page(s) 17
- [**Mohr2012**] P. J. Mohr, B. N. Taylor and D. B. Newell, *CODATA recommended values of the fundamental physical constants: 2010*, Rev. Mod. Phys. **84** (2012) 1527–1605, doi:10.1103/RevModPhys.84.1527 cited on page(s) 9, 93
- [**Moore1980**] M. S. Moore, *Rate dependence of counting losses in neutron time-of-flight measurements*, Nucl. Instrum. Methods **169** (1980) 245–247, doi:10.1016/0029-554X(80)90129-9 cited on page(s) 63
- [**Moreh1989**] R. Moreh, T. J. Kennett and W. V. Prestwich, *$^2\text{H}(\gamma, n)$ absolute cross section at 2754 keV*, Phys. Rev. C **39** (1989) 1247–1250, doi:10.1103/PhysRevC.39.1247 cited on page(s) 20
- [**Musiol1988**] G. Musiol et al., *Kern- und Elementarteilchenphysik*, VCH, Weinheim; New York; Cambridge; Basel, 1988 cited on page(s) 12
- [**Nagai1997**] Y. Nagai et al., *Measurement of $^1\text{H}(n, \gamma)^2\text{H}$ reaction cross section at a comparable $M1/E1$ strength*, Phys. Rev. C **56** (1997) 3173–3179, doi:10.1103/PhysRevC.56.3173 cited on page(s) 18, 97
- [**Nair2009**] C. Nair, *Photodisintegration studies of astrophysically relevant p-nuclei*, Dissertation, Technische Universität Dresden, 2009, <http://www.hzdr.de/publications/019256/19256.pdf> cited on page(s) 22, 27, 33, 54, 55
- [**Nakayama2005**] S. Nakayama et al., *$M1$ cross section for the photodisintegration of deuterium using the $^2\text{H}(\gamma, ^7\text{Li}, ^7\text{Be})$ reaction*, Phys. Rev. C **72** (2005) 041001, doi:10.1103/PhysRevC.72.041001 cited on page(s) 24
- [**Nankov2014**] N. Nankov et al., *The Angular Distribution of Neutrons Scattered from Deuterium below 2 MeV*, in *Proceedings of the International Conference on Nuclear Data for Science and Technology, New York, USA, 04.-08.03.2013*, Nucl. Data Sheets **119** (2014) 98–103, doi:10.1016/j.nds.2014.08.028 cited on page(s) 90

- [Nds] Nuclear Data Section of the International Atomic Energy Agency, Evaluated Nuclear Data File online database, <https://www-nds.iaea.org/exfor/endl.htm> cited on page(s) 16, 19, 21, 77, 78
- [Nollett2000] K. M. Nollett and S. Burles, *Estimating reaction rates and uncertainties for primordial nucleosynthesis*, Phys. Rev. D **61** (2000) 123505, doi:10.1103/PhysRevD.61.123505 cited on page(s) 8
- [Nolte2011a] R. Nolte and D. J. Thomas, *Monoenergetic fast neutron reference fields: I. Neutron production*, Metrologia **48** (2011) S263, doi:10.1088/0026-1394/48/6/S04 cited on page(s) 66, 67, 72
- [Nolte2011b] R. Nolte and D. J. Thomas, *Monoenergetic fast neutron reference fields: II. Field characterization*, Metrologia **48** (2011) S274, doi:10.1088/0026-1394/48/6/S05 cited on page(s) 69
- [Nolte2011c] R. Nolte, *Private communication*, Physikalisch-Technische Bundesanstalt Braunschweig, 2011 cited on page(s) 69, 72
- [Okamura1994] H. Okamura et al., *Strong evidence of the Coulomb breakup of the deuteron at 56 MeV*, Phys. Lett. B **325** (1994) 308–312, doi:10.1016/0370-2693(94)90016-7 cited on page(s) 24
- [Olive2004] K. A. Olive and E. D. Skillman, *A Realistic Determination of the Error on the Primordial Helium Abundance: Steps toward Nonparametric Nebular Helium Abundances*, Astrophys. J. **617** (2004) 29–49, doi:10.1086/425170 cited on page(s) 5
- [Partovi1964] F. Partovi, *Deuteron photodisintegration and n-p capture below pion production threshold*, Ann. Phys. **27** (1964) 79–113, doi:10.1016/0003-4916(64)90084-3 cited on page(s) 13, 15
- [Pdg2013] Particle Data Group, *Review of Particle Physics*, Phys. Rev. D **86** (2012) 010001, doi:10.1103/PhysRevD.86.010001, and 2013 update for the 2014 edition (<http://pdg.lbl.gov>) Chapter 21. *Big-Bang cosmology*, revis. Sep. 2013 by K. A. Olive and J. A. Peacock Chapter 22. *Big-Bang nucleosynthesis*, revis. Oct. 2013 by B. D. Fields, P. Molaro and S. Sarkar Chapter 26. *Cosmic microwave background*, revis. Sep. 2013 by D. Scott and G. F. Smoot cited on page(s) 3, 4, 5, 6, 7
- [Peebles1966] P. J. E. Peebles, *Primordial Helium Abundance and the Primordial Fireball. II*, Astrop. J. **146** (1966) 542–552, doi:10.1086/148918 cited on page(s) 2
- [Penzias1965] A. A. Penzias and R. W. Wilson, *A Measurement of Excess Antenna Temperature at 4080 Mc/s*, Astrophys. J. **142** (1965) 419–421, doi:10.1086/148307 cited on page(s) 2
- [Perdikakis2012] G. Perdikakis et al., *LENDA: A low energy neutron detector array for experiments with radioactive beams in inverse kinematics*, Nucl. Instrum. Methods A **686** (2012) 117–124, doi:10.1016/j.nima.2012.05.076 cited on page(s) 59
- [Perdue2011] B. A. Perdue et al., *Cross sections for the three-body photodisintegration of ^3He at $E_\gamma = 12.8, 13.5, \text{ and } 14.7 \text{ MeV}$* , Phys. Rev. C **83** (2011) 034003, doi:10.1103/PhysRevC.83.034003 cited on page(s) 24
- [Phenneger1974] M. C. Phenneger and R. G. Winter, *Disintegration of the deuteron by 4 to 11 MeV electrons*, Nucl. Phys. A **219** (1974) 589–594, doi:10.1016/0375-9474(74)90119-5 cited on page(s) 24
- [Pietralla1995] N. Pietralla et al., *Absolute level widths in ^{27}Al below 4 MeV*, Phys. Rev. C **51** (1995) 1021–1024, doi:10.1103/PhysRevC.51.1021 cited on page(s) 39, 44

- [**Planck2013**] Planck collaboration, *Planck 2013 results. I. Overview of products and scientific results*, Astron. Astrophys. (2013) submitted, <http://arxiv.org/abs/1303.5062> cited on page(s) 3, 4, 7
- [**Pospelov2010**] M. Pospelov and J. Pradler, *Big Bang Nucleosynthesis as a Probe of New Physics*, Annu. Rev. Nucl. Part. Sci. **60** (2010) 539–568, doi:10.1146/annurev.nucl.012809.104521 cited on page(s) 5, 6
- [**R3b2011**] R³B collaboration, *Technical Report for the Design, Construction and Commissioning of NeuLAND: The High-Resolution Neutron Time-of-Flight Spectrometer for R³B*, 2011, <http://www.fair-center.de/fileadmin/fair/experiments/NUSTAR/Pdf/TDRs/NeuLAND-TDR-Web.pdf> cited on page(s) 24
- [**Reifarh2009**] R. Reifarh et al., *Opportunities for Nuclear Astrophysics at FRANZ*, Publ. Astron. Soc. Australia **26** (2009) 255–258, doi:10.1071/AS08061 cited on page(s) 19, 97
- [**Riska1972**] D. O. Riska and G. E. Brown, *Meson exchange effects in $n + p \rightarrow d + \gamma$* , Phys. Lett. B **38** (1972) 193–195, doi:10.1016/0370-2693(72)90376-0 cited on page(s) 13, 14
- [**Rudolph2012**] J. Rudolph, *Instruments and techniques for analysing the time-resolved transverse phase space distribution of high-brightness electron beams*, Dissertation, Universität Rostock, 2012, http://rosdok.uni-rostock.de/metadata/rosdok_disshab_000000000927 cited on page(s) 33
- [**Rupak2000**] G. Rupak, *Precision calculation of $np \rightarrow d\gamma$ cross section for big-bang nucleosynthesis*, Nucl. Phys. A **678** (2000) 405–423, doi:10.1016/S0375-9474(00)00323-7, <http://arxiv.org/abs/nucl-th/9911018> cited on page(s) 13, 79
- [**Rupak2013**] G. Rupak and D. Lee, *Radiative Capture Reactions in Lattice Effective Field Theory*, Phys. Rev. Lett. **111** (2013) 032502, doi:10.1103/PhysRevLett.111.032502, <http://arxiv.org/abs/1302.4158> cited on page(s) 14
- [**Rusev2006**] G. Rusev, *Dipole-strength distributions below the giant dipole resonance in ^{92}Mo , ^{98}Mo and ^{100}Mo* , Dissertation, Technische Universität Dresden, 2006, <http://www.hzdr.de/publications/010008/10008.pdf> cited on page(s) 22, 27, 36, 39, 47, 54, 55
- [**Ryezayeva2006**] N. Ryezayeva, *Search for the $p_{1/2}$ -Resonance in ^7He with the $^7\text{Li}(d, ^2\text{He})$ Reaction and Measurement of the Deuteron Electrodisintegration under 180° at the S-DALINAC*, Dissertation, Technische Universität Darmstadt, 2006, <http://elib.tu-darmstadt.de/diss/000762> cited on page(s) 24
- [**Ryezayeva2008**] N. Ryezayeva et al., *Measurement of the Reaction $^2\text{H}(e, e')$ at 180° Close to the Deuteron Breakup Threshold*, Phys. Rev. Lett. **100** (2008) 172501, doi:10.1103/PhysRevLett.100.172501 cited on page(s) 13, 24
- [**Sawatzky2005**] B. D. Sawatzky, *A Measurement of the Neutron Asymmetry in $d(\vec{\gamma}, n)p$ Near Threshold*, Dissertation, University of Virginia, 2005, http://nucleus.usask.ca/technical_reports/theses/sawatzky-final.pdf cited on page(s) 23
- [**Schiavilla2005**] R. Schiavilla, *Induced polarization in the $^2\text{H}(\gamma, \vec{n})^1\text{H}$ reaction at low energy*, Phys. Rev. C **72** (2005) 034001, doi:10.1103/PhysRevC.72.034001 cited on page(s) 13
- [**Schiff1951**] L. I. Schiff, *Energy-Angle Distribution of Thin Target Bremsstrahlung*, Phys. Rev. **83** (1951) 252–253, doi:10.1103/PhysRev.83.252 cited on page(s) 38, 91
- [**Schlegel2002a**] D. Schlegel and S. Guldbakke, *Key Comparison of Neutron Fluence Measurements in Monoenergetic Neutron Fields - Determination of Neutron Fluence and Monitor Calibration Factors*, Technical Report PTB-6.41-2002-01, Physikalisch-Technische Bundesanstalt Braunschweig, 2002 cited on page(s) 69

- [Schlegel2002b] D. Schlegel and S. Guldbakke, *Neutron Fluence Measurements with a Recoil Proton Telescope - Determination of Neutron Fluence*, Technical Report PTB-6.41-2002-03, Physikalisch-Technische Bundesanstalt Braunschweig, 2002 cited on page(s) 69
- [Schlegel2002c] D. Schlegel and S. Guldbakke, *Neutron Fluence Measurements with a Recoil Proton Proportional Counter - Determination of Neutron Fluence*, Technical Report PTB-6.41-2002-04, Physikalisch-Technische Bundesanstalt Braunschweig, 2002 cited on page(s) 69
- [Schlegel2005] D. Schlegel, *TARGET user's manual*, Technical Report PTB-6.42-05-2, Physikalisch-Technische Bundesanstalt Braunschweig, 2005 cited on page(s) 72
- [Schmitt1991] K.-M. Schmitt, P. Wilhelm and H. Arenhövel, *Deuteron photodisintegration at low energies*, *Few-Body Syst.* **10** (1991) 105–133, doi:10.1007/BF01083045 cited on page(s) 13
- [Schnorrenberger2014] L. Schnorrenberger et al., *Characterization of γ -ray detectors using the photon tagger NEPTUN for energies up to 20 MeV*, *Nucl. Instrum. Methods A* **735** (2014) 19–23, doi:10.1016/j.nima.2013.08.046 cited on page(s) 22
- [Schramm1998] D. N. Schramm and M. S. Turner, *Big-bang nucleosynthesis enters the precision era*, *Rev. Mod. Phys.* **70** (1998) 303–318, doi:10.1103/RevModPhys.70.303 cited on page(s) 2
- [Schreiber2000] E. C. Schreiber et al., *First measurement of the near-threshold $^2\text{H}(\vec{\gamma},n)p$ analyzing power using a free-electron laser based γ -ray source*, *Phys. Rev. C* **61** (2000) 061604, doi:10.1103/PhysRevC.61.061604 cited on page(s) 23
- [Schwengner2005] R. Schwengner et al., *The photon-scattering facility at the superconducting electron accelerator ELBE*, *Nucl. Instrum. Methods A* **555** (2005) 211–219, doi:10.1016/j.nima.2005.09.024 cited on page(s) 22, 27, 32
- [Schwengner2013a] R. Schwengner et al., *Pygmy dipole strength in ^{86}Kr and systematics of $N=50$ isotones*, *Phys. Rev. C* **87** (2013) 024306, doi:10.1103/PhysRevC.87.024306 cited on page(s) 27, 39
- [Schwengner2013b] R. Schwengner, *Private communication*, Hemholtz-Zentrum Dresden-Rossendorf, 2013 cited on page(s) 44
- [Seltzer1986] S. M. Seltzer and M. J. Berger, *Bremsstrahlung energy spectra from electrons with kinetic energy 1 keV-10 GeV incident on screened nuclei and orbital electrons of neutral atoms with $Z = 1-100$* , *At. Data Nucl. Data Tables* **35** (1986) 345–418, doi:10.1016/0092-640X(86)90014-8 cited on page(s) 38
- [Senoo1994] K. Senoo et al., *A Monte Carlo code for multiple neutron scattering events in a thick sample for (n,γ) experiments*, *Nucl. Instrum. Methods A* **339** (1994) 556–563, doi:10.1016/0168-9002(94)90193-7 cited on page(s) 17, 18, 97
- [Serpico2004] P. D. Serpico et al., *Nuclear reaction network for primordial nucleosynthesis: a detailed analysis of rates, uncertainties and light nuclei yields*, *J. Cosmol. Astropart. Phys.* **12** (2004) 010, doi:10.1088/1475-7516/2004/12/010 cited on page(s) 5, 8
- [Skorka1975] S. J. Skorka, *Nuclear resonance fluorescence*, in W. D. Hamilton (Editor), *The electromagnetic interaction in nuclear spectroscopy*, pp. 283–310, North-Holland Publishing Company, Amsterdam, 1975 cited on page(s) 45
- [Smit1987] F. D. Smit and F. D. Brooks, *Angular distribution of neutrons from $^2\text{H}(\gamma,n)^1\text{H}$ at $E_\gamma = 2.75$ MeV*, *Nucl. Phys. A* **465** (1987) 429–444, doi:10.1016/0375-9474(87)90357-5 cited on page(s) 20

- [**Smith1993**] M. S. Smith, L. H. Kawano and R. A. Malaney, *Experimental, computational, and observational analysis of primordial nucleosynthesis*, *Astrophys. J. Suppl. Ser.* **85** (1993) 219–247, doi:10.1086/191763 cited on page(s) 8
- [**Snell1950**] A. H. Snell, E. C. Barker and R. L. Sternberg, *Photo-Disintegration Cross Sections of Deuterium and Beryllium for the Gamma-Rays of Sodium 24 and Gallium 72*, *Phys. Rev.* **80** (1950) 637–642, doi:10.1103/PhysRev.80.637 cited on page(s) 20
- [**Steigman2007**] G. Steigman, *Primordial Nucleosynthesis in the Precision Cosmology Era*, *Annu. Rev. Nucl. Part. Sci.* **57** (2007) 463–491, doi:10.1146/annurev.nucl.56.080805.140437 cited on page(s) 5, 6
- [**Stephenson1987**] K. E. Stephenson et al., *Measurements of relative angular distributions for the $^2\text{H}(\gamma,n)\text{H}$ reaction below 18 MeV*, *Phys. Rev. C* **35** (1987) 2023–2027, doi:10.1103/PhysRevC.35.2023 cited on page(s) 22
- [**Stuhl2014**] L. Stuhl et al., *A neutron spectrometer for studying giant resonances with (p,n) reactions in inverse kinematics*, *Nucl. Instrum. Methods A* **736** (2014) 1–9, doi:10.1016/j.nima.2013.10.038 cited on page(s) 59
- [**Suzuki1995a**] T. S. Suzuki et al., *First direct measurement of a $p(n,\gamma)d$ reaction cross section at stellar energy*, in *Proceedings of the 3rd International Symposium on Nuclei in the Cosmos (NIC III), Assergi, Italy, 08-13.07.1994*, *AIP Conf. Proc.* **327** (1995) 145–148, doi:10.1063/1.47414 cited on page(s) 17
- [**Suzuki1995b**] T. S. Suzuki et al., *First measurement of a $p(n,\gamma)d$ reaction cross section between 10 and 80 keV*, *Astrophys. J.* **439** (1995) L59–L62, doi:10.1086/187744 cited on page(s) 18, 97
- [**Teichert2003**] J. Teichert et al., *Results of beam parameter measurement of the ELBE electron accelerator after commissioning*, *Nucl. Instrum. Methods A* **507** (2003) 354–356, doi:10.1016/S0168-9002(03)00918-5 cited on page(s) 26
- [**Timmes2009**] F. X. Timmes, *Astronomy codes: Nuclear reaction networks: Big Bang nucleosynthesis*, Arizona State University, 2009, http://cococubed.asu.edu/code_pages/net_bigbang.shtml cited on page(s) 7
- [**Tomyo2003**] A. Tomyo et al., *Measurement of the $p(n,\gamma)d$ reaction cross section between $E_n = 100$ and 350 keV*, in *Proceedings of the 7th International Symposium on Nuclei in the Cosmos (NIC VII), Fuji-Yoshida, Japan, 08.-12.07.2002*, *Nucl. Phys. A* **718** (2003) 401c–403c, doi:10.1016/S0375-9474(03)00814-5, EXFOR database: <http://www-nds.iaea.org/EXFOR/22774.002> cited on page(s) 18, 19, 23, 97
- [**Tornow2003**] W. Tornow et al., *Low-energy photodisintegration of the deuteron and Big-Bang nucleosynthesis*, *Phys. Lett. B* **574** (2003) 8–13, doi:10.1016/j.physletb.2003.08.078 cited on page(s) 23
- [**Trompler2009**] E. Trompler, *Messung des Wirkungsquerschnitts astrophysikalisch relevanter Kernreaktionen*, Diploma thesis, Technische Universität Dresden, 2009, <http://www.hzdr.de/publications/013364/13364.pdf> cited on page(s) 47, 54, 55
- [**Tytler2000**] D. Tytler et al., *Deuterium and the baryonic density of the universe*, *Phys. Rep.* **333–334** (2000) 409–432, doi:10.1016/S0370-1573(00)00032-6 cited on page(s) 4
- [**Wagner2013a**] A. Wagner et al., *Position-resolved Positron Annihilation Lifetime Spectroscopy*, *J. Phys. Conf. Ser.* **443** (2013) 012091, doi:10.1088/1742-6596/443/1/012091 cited on page(s) 27

- [Wagner2013b] L. Wagner, *Strahlungseinfang von Protonen im Bethe-Weizsäcker Zyklus*, Diploma thesis, Technische Universität Dresden, 2013 cited on page(s) 55
- [Wagoner1967] R. V. Wagoner, W. A. Fowler and F. Hoyle, *On the Synthesis of Elements at Very High Temperatures*, *Astrophys. J.* **148** (1967) 3–49, doi:10.1086/149126 cited on page(s) 2
- [Wauters1990] P. Wauters et al., *Total cross section for the $H(n,d)\gamma$ reaction at 39, 61, and 76 MeV*, *Few-Body Syst.* **8** (1990) 1–10, doi:10.1007/BF01078871 cited on page(s) 17
- [Weinberg2008] S. Weinberg, *Cosmology*, Oxford University Press, Oxford, 2008 cited on page(s) 3
- [Wustmann2006] W. Wustmann and B. Kämpfer, *Primordial Nucleosynthesis: Impact of the Reaction $pn \leftrightarrow D\gamma$* , in *Wissenschaftlich-Technische Berichte FZD-442: Annual Report 2005 - Institute of Nuclear and Hadron Physics*, p. 6, Forschungszentrum Rossendorf, 2006, <http://www.hzdr.de/publications/008551/8551.pdf> cited on page(s) 8
- [Xu1995] G. Xu et al., *Radiative capture of polarized neutrons by polarized protons at $T_n=183$ MeV*, *Phys. Rev. C* **52** (1995) 2859–2874, doi:10.1103/PhysRevC.52.2859 cited on page(s) 17
- [Zieger1986] A. Zieger, P. Grewer and B. Ziegler, *Forward photodisintegration of the deuteron at 10.74 MeV photon energy*, *Few-Body Syst.* **1** (1986) 135–141, doi:10.1007/BF01077004 cited on page(s) 22

Danksagung / Acknowledgement

Ich danke ...

... meiner Frau, die immer alles dafür getan hat, um mich zu unterstützen, sogar dann noch, als ich eigentlich alles hätte tun müssen, um sie zu unterstützen.

... Arnd Junghans für die motivierende und ausdauernde Betreuung, verbunden mit der ständigen Bereitschaft, die kompliziertesten Ideen zu diskutieren.

... Roland Beyer für die große Hilfe bei der Neutronen-Messtechnik, der Datenanalyse und dem PTB-Experiment.

... Andreas Wagner für die große Hilfe bei der Photonen-Messtechnik und die vielen Anregungen, meine eigene Arbeit kritisch zu hinterfragen und zu verbessern.

... Tom Cowan und René Reifarh für die Begutachtung der Dissertation.

... Burkhard Kämpfer und Antonio Hurtado für die Bereitschaft, mich im Rigorosum zu prüfen.

... Eckart Grosse dafür, dass er mich - auch aus seinem Ruhestand heraus - mit Hinweisen und Diskussionsbeiträgen unterstützte.

... Andreas Hartmann für die technische Unterstützung beim Aufbau der Experimente.

... Ronald Schwengner und Ralph Massarczyk für die effektive, effiziente und vor allem kompetente Beratung zum Thema Photonenfluss.

... Anna Ferrari für die umfangreichen FLUKA-Simulationen.

... Toni Kögler und Evert Birgersson für die Begleitung der Experimente an ELBE und PTB.

... Daniel Bemmerer, Mathias Kempe, Krasimir Kosev, Michele Marta, Andrija Matic, Klaus-Dieter Schilling, Georg Schramm, Manfred Sobiella, Daniel Stach und Dmitry Yakorev für die Begleitung des Experiments an ELBE

... den Mitarbeitern des ELBE- und des PTB-Beschleunigers, von letzterem besonders Ralf Nolte.

... allen meinen "alten" Kollegen der Abteilung Kernphysik, des Institutes für Strahlenphysik und des Helmholtz-Zentrums Dresden-Rossendorf, die sich an den vielen Diskussionen beteiligten und zur angenehmen Arbeitsatmosphäre beitrugen.

... allen meinen "neuen" Kollegen in der brandenburgischen Landesverwaltung, die mich dabei unterstützt haben meine Promotion parallel zu meiner neuen Tätigkeit abzuschließen.

... meinen Eltern, meiner Familie und meinen Freunden für ihre vielfältige Unterstützung.

... meiner Frau und meiner Tochter, dafür dass sie mir all die Entbehrungen und deren Nachwirkungen verzeihen, die meine Promotion für sie mit sich brachte.

Potsdam, 3. April 2016

Erklärung / Declaration

Hiermit versichere ich, dass ich die vorliegende Arbeit ohne unzulässige Hilfe Dritter und ohne Benutzung anderer als der angegebenen Hilfsmittel angefertigt habe. Die aus fremden Quellen direkt oder indirekt übernommenen Gedanken sind als solche kenntlich gemacht. Die Arbeit wurde bisher weder im Inland noch im Ausland in gleicher oder ähnlicher Form einer anderen Prüfungsbehörde vorgelegt. Die Arbeit wurde am Helmholtz-Zentrum Dresden-Rossendorf unter der wissenschaftlichen Betreuung von Prof. Dr. Thomas Cowan und Dr. Arnd R. Junghans angefertigt.

Ort und Datum der Abgabe

Unterschrift



Bautzner Landstr. 400
01328 Dresden, Germany
Tel. +49 351 260-3589
Fax +49 351 260-13589
a.junghans@hzdr.de
<http://www.hzdr.de>